IMPERIAL COLLEGE LONDON

Oral processing of micro-aerated chocolates: a computational mechanics, rheological and tribological study

Georgios F. Samaras

Department of Mechanical Engineering
Imperial College London

This thesis is submitted for the degree of
Doctor of Philosophy of Imperial College London

April 2022

Dedicated to the memory of my friend Alessio

Declaration of Originality

I hereby certify that the present thesis is in full the work of the author, with the work of others appropriately acknowledged. No part of the present work has been submitted to any other university or institution for any other degree or qualification.

Copyright Statement

Oral processing of micro-aerated chocolates: a computational mechanics, rheological and tribological study

Georgios F. Samaras

ABSTRACT

The emerging need to reduce the calorific value of foods, while simultaneously improving the consumer perception drives the quest for food structures that satisfy both criteria. Aiming to shed light on the influence that micro-aeration has on the breakdown of chocolate during the early stages of the oral processing, this study focuses on the investigation of the effect that micro-aeration has from a computational mechanics, rheological and tribological perspective. Firstly, several constitutive models are investigated and compared in both the explicit and implicit Finite Element (FE) frameworks and are calibrated using experimental results from mechanical testing conducted in a parallel PhD study. Afterwards, a non-local damage evolution law is presented providing mesh objectivity in both microscopic and macroscopic FE calculations. The constitutive model coupled with the non local damage model, implemented in an ABAQUS VUMAT subroutine, is then applied in a micromechanical model for the prediction of the elastic, plastic and fracture properties of micro-aerated chocolate using as input the properties of the non-aerated solid chocolate. Different boundary conditions are employed in both monodisperse and polydisperse dispersion of pores for the estimation of a representative volume element that is used for the estimation of the macroscopic properties. Overall, micro-aeration reduces the elastic, plastic and fracture properties of the chocolate, whereas the polydisperse dispersions provide a better estimation for the equivalent fracture strain at failure. The estimated values are applied in macroscopic FE simulations of the first bite, where the force displacement FE results match the experimental data obtained by a replicate of the first bite model with 3D printed molar teeth. The forces needed for the fragmentation of chocolate reduce with micro-aeration level as shown from the experiments and validated by the FE simulations, whereas the *in-vivo* and *in-vitro* fragmentation studies show that micro-aerated chocolate breaks into more and smaller pieces. Furthermore, the effect of the micro-aeration on the rheological properties of the molten chocolate with and without the influence of artificial saliva is investigated. Micro-aeration increases viscosity values while the storage and loss moduli decrease. From a tribological perspective, a new bench test rig to measure friction in the simulated tongue-palate contact is developed. The test was applied to molten chocolate samples with and without artificial saliva. Friction was measured over the first few rubbing cycles, simulating mechanical degradation of chocolate in the tongue-palate region. The coefficient of friction increases with cocoa solids

percentage and decreases with increasing micro-aeration level. The presence of artificial saliva in the contact reduced the friction for all chocolate samples, however the relative ranking remained the same. Finally, the link between structure, material properties and sensory perception is given through a comparison with data from sensory tests. The current study can be used as a cost efficient tool for the investigation of new food structures that reduce the calorific value while enhancing the taste perception.

Acknowledgements

Firstly, I would like to express my sincere gratitude to my supervisors, Prof. **Maria Charalambides**, Prof. **Philippa Cann**, Dr. **Marc Masen** and Prof. **Yannis Hardalupas** for giving me the opportunity to pursue a PhD at Imperial College London and for constantly providing valuable advice and support over the last four years. None of the research projects I brought to completion would have been possible without their enthusiasm and great support. Thank you very much for teaching me what true collaboration means.

Next, I would like to thank my industrial supervisors, Prof. **Christoph Hartmann** and Dr. **Josélio Vieira** for sharing their valuable inshights and expertise. I would, also, like to thank **Jamey German**, from Nestlé PTC York, for helping with the sample preparation.

Besides my advisors, I am thankful to my examiners Prof. **Daniele Dini** and Prof. **Alojz Ivankovic**. I appreciate their constructive feedback and their comments were very useful for improving the quality of my research. Also, special thanks go to my former Professors from the University of Thessaly and in particular Prof. **Gregory Haidemenopoulos**, Prof. **Spyros Karamanos** and Prof. **Nikolaos Aravas** for their great support and motivation during my undergraduate studies.

I further want to thank the fellow PhD student **Dimitrios Bikos** for our great collaboration and his friendship. His work ethic and determination led to outstanding results without which this thesis would not have been possible.

I am also extremely grateful to Dr. **Christos Skamniotis** for his help and guidance on my research during my PhD. Our discussions and exchange of ideas have contributed to a more complete research project.

I would also like to thank Dr. **Elze Porte** for helping me with the tribology experiments, Dr. **Rory McAllister** for training me in the rheometer, **Pavel Orzlowski** and Dr. **Ruth Brooker** for their help with the experimental work of this thesis. A thank you to **Val Crawford** for her constant availability and support in administrative matters. I would also like to thank **Ilias Bellas** for our valuable discussions regarding the computational aspects of this thesis.

On a more personal level, I am grateful to my friends who have been a great support throughout the years **Mitsos**, **Stelios**, **Stamatis** and **Konstantinos** thank you for your friendship and for always being beside me in both my happiest and most challenging mo-

ments. Moreover, I'm very fortunate for the friends I made along this journey. **Gabriele**, **Dimitris**, **Katerina** and **Christos** thank you for all the laughs, excursions, and unforgettable moments we shared together. You have made London feel like home, and nothing would have been the same without you. A big thank you to all my football teammates who made my Wednesdays special. Some honorable mentions to **Tom**, **Andrew**, **Adam**, **Gabs**, **Pras**, **Rich**, **Steve**, **Simo**, **Marc** and **Pablo**.

A sincere thank you to **Federica** for her enduring patience and understanding throughout the hardest final period of this study. This work would not have been possible without you.

Above all else, I want to express my deepest gratitude to my parents **Filippos** and **Anna** and to my brother **Dimitris** for their love and support.

Contents

List of Figures

List of Tables

Acronyms

ABS Acrylonitrile Butadiene Styrene.

ALLEL All elements part in ABAQUS.

B-SPH Bio- mechanical-smoothed particle hydrodynamics.

BFNU Body Flux Non Uniform.

BVP Boundary Value Problem.

CDM Continuum Damage Mechanics.

DFLUX User subroutine to define nonuniform distributed flux.

FE Finite Element.

FIM Fluid Immobilisation.

IOCCC International Office of Cocoa, Chocolate and Confectionery.

KUBC Kinematic Uniform Boundary Conditions.

PBC Periodic Boundary Conditions.

PDMS polydimethylsiloxane.

RSA Random Sequential Adsorption.

RVE Representative Volume Element.

SEM Scanning Electron Microscope.

TBC Traction Boundary Conditions.

TDS Temporal Dominance Sensations.

TPA Texture Profile Analysis.

UMAT User material subroutine in ABAQUS/Implicit.

VDFLUX User material subroutine for dynamic coupled thermal-stress analysis in ABAQUS/-Explicit.

VUEL User subroutine for user-defined elements in ABAQUS/Explicit.

VUMAT User material subroutine in ABAQUS/Explicit.

XRT X-Ray Tomography.

Nomenclature

Chapter 1

f	porosity measured as a fraction of the volume of voids over the total volume

Chapter 2

A	Johnson-Cook yield parameter
B	Johnson-Cook hardening parameter
C	Johnson-Cook rate dependent parameter
$\boldsymbol{D}$	deformation rate tensor
$\boldsymbol{D}^*$	virtual deformation rate tensor
E	Young's modulus
E_{ep}	elastic modulus of the elastic-plastic network
E_{ev}	elastic modulus of the elastic-viscous network
G	shear modulus
J_2	second invariant of the deviatoric stress
$\boldsymbol{L}^*$	virtual velocity gradient tensor
$\boldsymbol{I}$	identity tensor
$\boldsymbol{S}$	deviatoric part of the stress tensor
$\boldsymbol{S}^{tr}$	trial deviatoric part of the stress tensor
T	temperature
T_0	reference temperature
T_m	melting temperature

$\boldsymbol{W}^*$	anti-symmetric part of the virtual velocity gradient tensor
f_v	ratio between the elastic modulus of the elastic-viscous network to the total elastic modulus
m	Johnson-Cook temperature softening exponent
n	Johnson-Cook hardening exponent parameter
p	hydrostatic pressure
$\hat{\boldsymbol{t}}$	traction applied on the body
$\boldsymbol{u}$	displacement field
$\boldsymbol{v}$	velocity field
$\boldsymbol{v}^*$	virtual velocity field
γ	scalar representing the flow intensity
$\boldsymbol{\varepsilon}^e$	elastic strain tensor
$\dot{\boldsymbol{\varepsilon}}^p$	plastic strain rate tensor
ε_{eq}^p	equivalent plastic strain
$\dot{\varepsilon}_{eq}^p$	equivalent plastic strain rate
$\dot{\varepsilon}_{ep}$	elastic-plastic strain rate
$\dot{\varepsilon}_{ev}$	elastic-viscous strain rate
$\dot{\varepsilon}_0$	reference strain rate
λ	bulk modulus
ρ	density
$\boldsymbol{\sigma}$	stress tensor
σ_{eq}	von Mises equivalent stress
σ_{eq}^{tr}	trial von Mises equivalent stress
σ_{ep}	stress of the elastic-plastic part
σ_{ev}	stress of the elastic-viscous part
$\sigma_{y0,s}$	static yield stress
$\sigma_{y0,m}$	stress corresponds to the maximum strain observed in the monotonic tests

Chapter 3

$\bar{A}$	effective area
A_d	reduced cross-sectional area due to microvoids and microcracks
$\mathbb{C}$	fourth order stiffness tensor
G_f	fracture energy
G_f^I	mode *I* fracture toughness
G_f^{II}	mode *II* fracture toughness
I_1	first invariant of the stress tensor
c	specific heat
d	damage parameter
d_{cr}	damage parameter critical value for fracture
$\dot{d}$	damage evolution rate
e_{eq}^p	non-local equivalent plastic strain
k	thermal conductivity
l	internal length
l_{ch}	internal characteristic material length
r	heat supply per unit volume
Δt	time increment
Δl_{el}	size of the element
$\bar{\sigma}$	effective stress
$\hat{\varepsilon}_{eq}^p$	additional internal variable for Kuhn-Tucker conditions
$\varepsilon_{eq,i}^p$	equivalent plastic strain at damage initiation
$\varepsilon_{eq,f}^p$	equivalent plastic strain at damage failure
$\varepsilon_{eq,i}^{p,s}$	equivalent plastic strain at damage failure in shear
$\varepsilon_{eq,i}^{p,t}$	equivalent plastic strain at damage failure in tension
η	triaxiality

$\sigma^{p}_{eq,i}$	maximum stress corresponding to the equivalent plastic strain at damage initiation
σ_m	mean stress
$\sigma_{y,i}$	yield stress at the damage onset

Chapter 4

$\mathbb{C}^{eff}$	effective stiffness tensor
E_m	Young's modulus of the matrix
E_{HS}	Young's modulus calculated using the Hashin-Shtrikman bounds
L	edge length of the unit cell
N	number of pores
R	pores radius
k	bulk modulus
k^{eff}	effective bulk modulus
k_{HS}	bulk modulus calculated using the Hashin-Shtrikman bounds
$\boldsymbol{p}_i$	coordinates of a random point
$\overline{\boldsymbol{\varepsilon}}$	volumetric average macroscopic strain
μ	shear modulus
μ^{eff}	effective shear modulus
μ_{HS}	shear modulus calculated using the Hashin-Shtrikman bounds
ν_{HS}	Poisson's ratio calculated using the Hashin-Shtrikman bounds
$\overline{\boldsymbol{\sigma}}$	volumetric average macroscopic stress

Chapter 5

C^{NJ}	lamp capacitance matrix
F^{J}	internal flux vector
I^{J}	internal force vector
M^{NJ}	mass matrix

P^J	applied load vector
R^J	applied nodal source vector
δ	displacement of the lower jaw
$\dot{\delta}$	speed of the lower jaw
μ	coefficient of friction
θ_i^N	temperature at node N at the time increment i

Chapter 6

μ	coefficient of friction

Chapter 7

G'	storage modulus
G''	loss modulus
K	Power law time constant
K_H	Herschel–Bulkley time constant
K_{M}	Mizrahi time constant
K_{s}	Sisko time constant
q	Power law dimensionless exponent
q	Herschel–Bulkley dimensionless exponent
m	dimensionless Cross model parameter
n	dimensionless Carreau model parameter
n_{s}	Sisko dimensionless exponent
n_{M}	Mizrahi dimensionless exponent
α_c	dimensionless Cross model parameter
$\dot{\gamma}$	shear rate
η	viscosity
η_{CA}	Casson high shear viscosity

η_0	zero-shear viscosity
η_∞	infinite-shear-viscosity value
λ_c	dimensionless Carreau model parameter
τ	shear stress
$\tau_{0\mathrm{H}}$	Herschel–Bulkley yield stress
τ_{CA}	Casson yield stress
$\tau_{0\mathrm{M}}$	Mizrahi yield stress

1 Introduction

Topics

Multidisciplinary research has been conducted in the area of food oral processing in order to understand the different aspects that influence the food consumption leading to taste perception. Although the oral processing is only the first step in the food consumption process, followed by digestion, it is the phase that contributes the most to the sensory experience of the consumers. During oral processing the solid food is structurally broken down leading to a bolus that can be safely swallowed [1]. The need of the food industry to reduce the calorific value of the foods, while enhancing the taste perception has led to increased research for further understanding how the structure of the food influences the oral processing. This will allow to bridge the knowledge between food structure, sensory perception and calorific value and can lead to the design of healthier and more appealing to the consumer food products.

Micro-aeration is a procedure that has been examined by the food industry to achieve foods that are healthier but also more appealing. Although many foods can be considered as porous due to their cellular structure (for example bread and foamed chocolate [2]), in the current thesis micro-aeration is considered as a microstructural characteristic and two micro-aeration levels will be examined $f = 10\text{vol}\%$ and $f = 15\text{vol}\%$.

In the current thesis, the influence that micro-aeration has on the structural breakdown of chocolates will be investigated. Chocolate structure and physical properties are related to the composition and processing operations and influence the breakdown during oral processing [3]. Chocolate can be characterized as a suspension of solid particles, including cocoa particles, sugar and milk particles, in a continuous fat phase (Figure 1.1). There are different aspects that influence the oral perception of chocolates mainly involved with composition, processing operations and storage. The composition of the fat matrix phase plays an important role on how the chocolate samples behave in the oral cavity. Other im-

portant factors are the processing operation of chocolate, such as tempering, cooling, the storage temperature and the lipid composition. These characteristics influence the crystal morphology of the chocolate matrix. Hence, the physical attributes of the chocolate during the oral process are related to fragmentation, hardness and melting temperature and influence the mechanical, rheological and tribological properties. As the chocolate is broken down into smaller pieces due to the interaction with the teeth during the first bite and chewing, more chocolate surface is exposed to saliva and mouth temperature, leading to melting. It is evident that a change in chocolate structure, e.g. including micro-aeration, would influence all stages of oral processing, since it is expected that the mechanical properties will change leading to different fragmentation results affecting also the rheological and tribological properties [4].

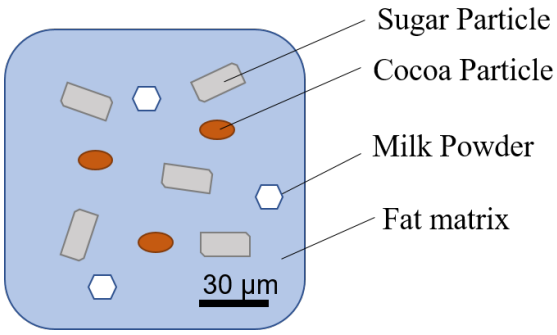

Figure 1.1: Schematic representation of the chocolate structure.

The food industry is interested in the oral processing, since it has been proven that the particle size distribution of the food fragments during mastication is related to numerous factors, such as the glycemic response [5], the taste perception [6] and flavour release [7]. Consequently, a great deal of attention has been given in investigating the breakdown of food during oral processing for improving the sensory and nutritional aspects of manufactured foods. The effect of oral processing on the sensory perception and digestion efficacy of foods, has led to major advances in the understanding of the food-related and human-related factors that influence the physico-chemical transformation of food in the mouth [8]. The mastication process and bolus properties have been related to texture perception in several studies in the literature [9, 6].

The general description of the oral processing is shown in Figure 1.2, where a schematic representation of food breakdown relating the length scale with the time scale is given. When the food specimen enters the oral cavity, it is in the centimeter length scale. At this point the food comes in contact with the teeth and is broken down into smaller pieces and mechanical and thermal loads dominate the food fracture at this stage. As the oral processing time evolves and the bolus formation takes place, rheology and tribology become dominant during the interaction of the food with the tongue and the palate.

The current thesis is part of an interdisciplinary research project at Imperial College

London and in collaboration with Nestlé. The schematic representations of Figure 1.2 acts as a guide for the topics covered in this thesis and the overall structure of the project. The computational mechanics part of stage *I* is studied in detail and particularly the constitutive and fracture modeling will be presented. The experimental part of stage *I*, related to the mechanical properties of chocolate, and the entire heat transfer study of stage *II* has been conducted by an accompanying PhD student and are presented in detail in the parallel PhD thesis of Bikos [10]. The experimental mechanical results, demonstrated in the work of Bikos et al. [11] will be used in this thesis (chapters 2-5) for the calibration and validation of the computational models. Finally, the rheological (stage *III*) and tribological (stage *IV*) aspects of the project are examined from an experimental point of view and presented in the current thesis.

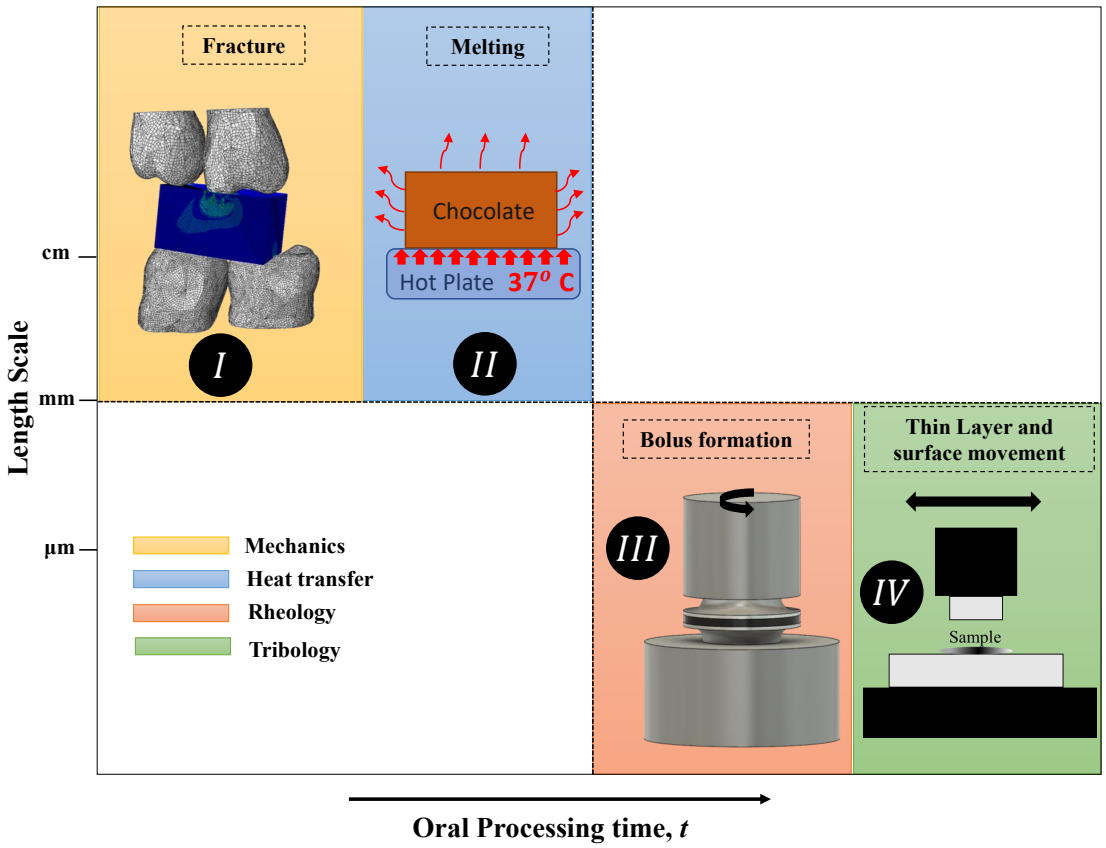

Figure 1.2: A qualitative schematic representation of the processes taking place during food breakdown.

1.1 Aims and objectives

Although micro-aeration reduces the calorific value of foods for a given product volume, at the same time it can be an important parameter for improving the taste perception of the consumers. For this reason, micro-aeration in foods is an important parameter that needs to be studied in detail. Therefore, quantifying the effect that micro-aeration has

on the mechanical, tribological and rheological properties of chocolate, using engineering principles, is important not only for marketing purposes but can also serve product development and optimisation.

Undoubtedly, the effect that micro-aeration has primarily on the mechanical and thermal properties of chocolate, influences the subsequent steps of oral processing leading to a different consumer experience. For example, a change in the mechanical properties of the chocolate will lead to different fragmentation that influence the surface area that is exposed to the mouth temperature. Subsequently, the rheological and tribological properties will change accordingly, both from the micro-aeration that exist in the fragmented particles but also from different fragment distribution as those defined from the interaction with mechanical and thermal loads.

The main aims of this thesis thesis are summarized in brief below:

1. Select and calibrate a constitutive material model based on the experimentally determined stress-strain curves.
2. Develop a multiscale computational mechanics model, validated by the experiments, to estimate the fragmentation behaviour of chocolate as a function of structure.
3. Perform tribological and rheological experiments to measure the coefficient of friction and the viscosity as a function of micro-aeration.
4. Provide a fundamental engineering approach and use the experimentally determined mechanical properties to explain the changes in sensorial attributes.
5. Qualitatively link the main findings to sensory perception data available from the food industry.
6. Create the basis of chocolate engineering to understand oral processing towards tailoring the chocolate's properties according to consumer attributes.

This thesis can be used as a design tool, by the food industry, to quantify how micro-aeration can be applied in order to achieve desirable properties of the end product. The design of an engineering tool for controlling the sensory perception attribute is the main novelty of the present thesis. It is the first time that, a conclusive engineering analysis is used in chocolate to explain the difference is sensory perception. The engineering tools used towards this scope, and in particular mechanics, tribology and rheology involved techniques that have not been applied before in the oral processing literature. The main novelties applied in each topics are summarised below:

1. In the computational mechanics part, a more sophisticated damage model based on the non-local damage theory, is applied whereas previous studies [12, 13, 14] used more simple damage models when simulating the chewing process.

2. In tribology, a flat on flat configuration is used in contrary to the ball on flat configuration that most of the studies in the field use [15]. This allows for the isolation of the samples under investigation avoiding entertainment of new sample in the testing area.
3. In rheology experiments, the main novelty attributes to achieving reliable and repeatable results at 37 °C. Previous studies focus on higher temperatures ($\sim$ 40 °C) [16]. In addition to that the effect of artificial saliva was included in the experiments.

A thorough description of the methodologies followed to develop reliable computational models and experiments is given in the chapters of this thesis.

1.2 Thesis overview

This thesis is divided in nine chapters, with chapter **1** being the Introduction. Figure 1.3 depicts the stages of the oral processing, with the numbers indicating the chapters of the current thesis where each process is studied. Chapter **2** deals with constitutive models that can be used to characterise the mechanical behaviour of the solid chocolate. The Johnson-Cook constitutive model is presented and the steps followed to implement it in both the explicit and the implicit solver of ABAQUS are given. In addition, the two-layer viscoplastic model is presented as an alternative constitutive model that can be calibrated with experimental data.

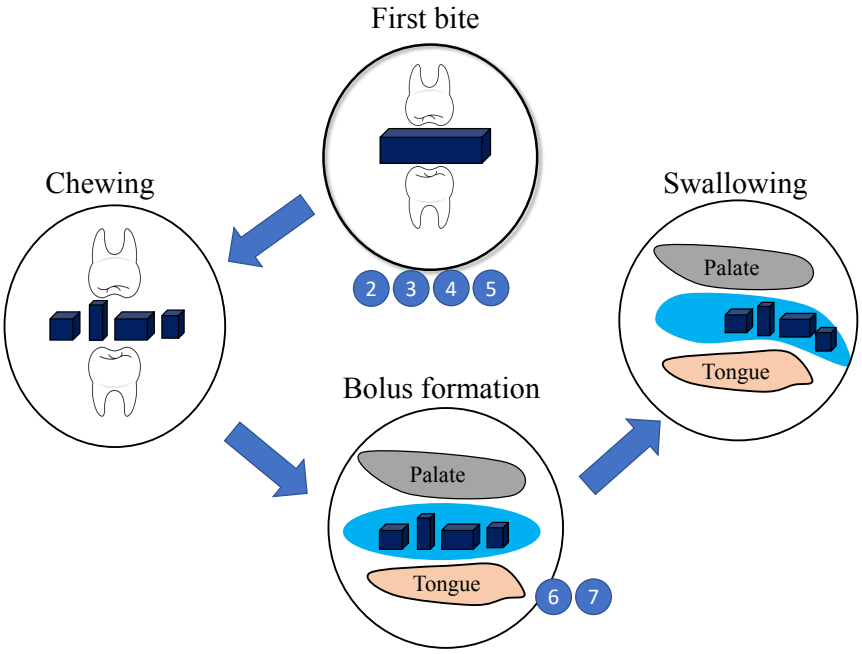

Figure 1.3: Stages of the oral processing and schematic representation of the thesis. Numbers indicate chapters in this thesis.

Chapter **3** starts with a general review of the continuum damage theory. The continuum damage models are widely used to model fracture with arbitrary crack paths, although a main limitation of this theory is that the results obtained by the Finite Element (FE) simulations are mesh dependent. For this reason, the theory of the non-local damage models is presented and the methodology for the implementation into ABAQUS using a VUMAT subroutine is also given. Finally, results from two benchmark tests are provided to highlight the mesh independence of the results.

In chapter **4**, a micromechanical model for the prediction of the elastic, plastic and fracture properties of the micro-aerated chocolate is presented. The methodology for the generation of monodisperse and polydisperse porous unit cells and the meshing technique followed is outlined. Initially, the size of the representative volume element is estimated and the elastic, plastic and fracture properties are calculated for the chocolate of two different porosity levels $f = 10\text{vol}\%$ and $f = 15\text{vol}\%$ and compared with the experimental data from the parallel PhD study [10].

Chapter **5** presents the experimental and computational work for the simulations of the first bite. A 3D printed pair of molar teeth are used in the experimental set up. These experimental data are compared against a FE model of the first bite where the constitutive model is coupled with the non-local damage model in the ABAQUS/Explicit solver. Also, the fragmentation of the different micro-aerated samples obtained from the experiments is compared with *in vivo* mastication tests.

In chapter **6** a new bench test to measure friction in the simulated tongue-palate contact is presented. The test consists of a flat polydimethylsiloxane (PDMS) disk, representing the tongue loaded and reciprocating against a stationary lower glass surface representing the palate. The test is applied to molten chocolate samples with and without artificial saliva. Friction is measured over the first few rubbing cycles, simulating mechanical degradation of chocolate in the tongue-palate region. The effects of chocolate composition (cocoa solids content ranging between 28 wt% and 85 wt%) and structure (micro-aeration/non-aeration 0-15 vol%) will be shown.

The rheology experiments are described in chapter **7**, where the viscosity and the storage and loss moduli of the micro-aerated and commercial samples are measured at a temperature of 37 °C. Analytical models are also used for fitting the viscosity results.

The micro-aeration influences the mechanical properties, the coefficient of friction and the viscosity of the samples. In chapter **8**, a link between the findings presented in the previous chapters and sensory perception through data available from a sensory panel is given. Finally, the main conclusions of this dissertation are provided in chapter **9**, along with perspectives for future research.

Due to the multidisciplinary nature of the project, a literature review for each topic is presented at the Introduction of the respective chapter.

2 Constitutive model

Topics

2.1 Introduction

This chapter presents possible constitutive models that can be used to characterize the mechanical response of the solid chocolate matrix.

Due to the lack of literature in the mechanical characterisation of chocolates, several models were studied and the most appropriate will be shown in this chapter. Experimental results, shown in the study of Bikos et al. [11], showed a complex material behaviour that depends upon different parameters, i.e. strain rate, triaxiality and loading history. The need of implementing the constitutive model in the FE simulation of the first bite, imposed additional challenges on the chosen material for this study. A constitutive model is defined through a mathematical relation that correlates stress and strain as a function of field variables, such as temperature and strain rate. Most of the commercially available FE software, like ABAQUS [17] that will be used in this study, already provide a big variety of constitutive models that can be easily applied directly in the model. One of the built-in constitutive models used to describe strain rate dependent materials is the Johnson-Cook

model. Although, the built-in Johnson-Cook model can be calibrated and used for the characterisation of the solid chocolate, the limitation of having a mesh independent simulation of the first bite, drives the implementation of the model through a user subroutine. ABAQUS allows the user to advance the existing built-in constitutive models though external material subroutines, such as the UMAT subroutine in the ABAQUS/Implicit solver and the VUMAT subroutine in the ABAQUS/Explicit solver [18, 19].

Initially, the general theory of the Johnson-Cook constitutive law is presented. Afterwards the von Mises plasticity theory is used as the basis for the implementation of the model in the implicit and explicit solvers. The radial return mapping algorithm, which is an implicit scheme for solving the plasticity equations, is also presented [20], followed by the methodology for the development of the VUMAT and UMAT subroutines [21]. The VUMAT is compared with the UMAT and the built-in Johnson-Cook model through stress-strain results from one element compression FE simulations. In addition, the two-layer viscoplastic constitutive model is presented and is calibrated to the experimental data.

2.2 The Johnson-Cook constitutive law

The Johnson-Cook constitutive equation relates the yield stress of the material with the equivalent plastic strain, ε_{eq}^{p}, the equivalent plastic strain rate, $\dot{\varepsilon}_{eq}^{p}$, and the temperature, T. The dependence on these three parametes can be expressed by the following generalized equation:

$$\sigma_y = \sigma_y^{\varepsilon}\left(\varepsilon_{eq}^{p}\right)\sigma_y^{\dot{\varepsilon}}\left(\dot{\varepsilon}_{eq}^{p}\right)\sigma_y^{T}(T) \tag{2.1}$$

In equation (2.1), σ_y^{ε}, represents the strain hardening, which is expressed as:

$$\sigma_y^{\varepsilon}(\varepsilon_{eq}^{p}) = (A + B\varepsilon_{eq}^{p^n}) \tag{2.2}$$

Equation (2.2) describes the flow stress of the material under the reference conditions. Therefore, parameters A, B and n are calibrated using the data from the mechanical experiments conducted at the lowest strain rate. The second term of equation (2.1), $\sigma_y^{\dot{\varepsilon}}\left(\dot{\varepsilon}_{eq}^{p}\right)$ describes the dependence of the yield stress on the plastic strain rate, $\dot{\varepsilon}_{eq}^{p}$, and is expressed as:

$$\sigma_y^{\dot{\varepsilon}}\left(\dot{\varepsilon}_{eq}^{p}\right) = 1 + C\ln\left(\frac{\dot{\varepsilon}_{eq}^{p}}{\dot{\varepsilon}_0}\right) \tag{2.3}$$

where, $\dot{\varepsilon}_{eq}^{p}$ is the equivalent plastic strain rate, $\dot{\varepsilon}_0$ is the reference strain rate and C is a dimensionless parameter controlling the strengthening of the material due to the plastic strain rate. The third term of equation (2.1), $\sigma_y^{T}(T)$, represents the temperature dependence of the yield stress. If $T < T_0$ there is no temperature dependence, and if $T \geq T_m$ the material is assumed to behave as a liquid. The temperature dependence function is

written as:

$$\sigma_y^T(T) = \begin{cases} 1 - \left(\frac{T-T_0}{T_m-T_0}\right)^m & \text{if} \quad T_0 \leq T < T_m \\ 1 & \text{if} \quad T < T_0 \\ 0 & \text{if} \quad T \geq T_m \end{cases} \tag{2.4}$$

where T_0 and T_m are the reference and melting temperature respectively and m is an exponent which characterises the material softening due to heating. It is worth noting that in the current study, the effect of temperature is not considered and the term $\sigma_y^T(T)$ is not implemented in the VUMAT, as the models are calibrated using mechanical test data at a room temperature of 20° [11]. So, the Johnson-Cook model is being used taking into account only the effect of plastic strain and plastic strain rate. In the current study, the assumption is that the mouth temperature does not influence the fragmentation of the food during the first bite. Furthermore, in both micromechanical and macromechanical simulations where the non local damage model is applied, temperature is used through a VDFLUX subroutine but has no physical meaning. As it will be explained in section 3.5, the temperature is used for the calculation of the non local equivalent plastic strain.

Overall a simplified version of the Johnson-Cook constitutive model, without the temperature effect, was implemented in the current study and is expressed by the following equation:

$$\sigma_y = \left[A + B\left(\varepsilon_{eq}^p\right)^n\right]\left[1 + C\ln\left(\frac{\dot{\varepsilon}_{eq}^p}{\dot{\varepsilon}_0}\right)\right] \tag{2.5}$$

2.3 J_2 plasticity theory

In this section the J_2 plasticity theory for rate independent plasticity will be presented, and will be used as the basis for the formulation of the rate dependent plasticity [21]. The J_2 plasticity theory assumes that the stress state of the material depends on the yield surface which is defined through a scalar yield function f. Figure 2.1 represents how the yield surface defines the stress state. If the yield function is less than zero then the stress state is purely elastic. Plasticity is defined when the yield function is equal to zero and stress state is characterised as non admissible for positive values of the yield surface.

The stress tensor, $\boldsymbol{\sigma}$, is decomposed in two parts:

$$\boldsymbol{\sigma} = p\boldsymbol{I} + \boldsymbol{S} \tag{2.6}$$

where $\boldsymbol{I}$ is the identity tensor, p is the hydrostatic pressure given by:

$$p = \frac{1}{3}\mathrm{tr}[\boldsymbol{\sigma}] \tag{2.7}$$

where $\mathrm{tr}\{\bullet\}$ denotes the trace of a second order tensor, and $\boldsymbol{S}$ is the deviatoric part of the

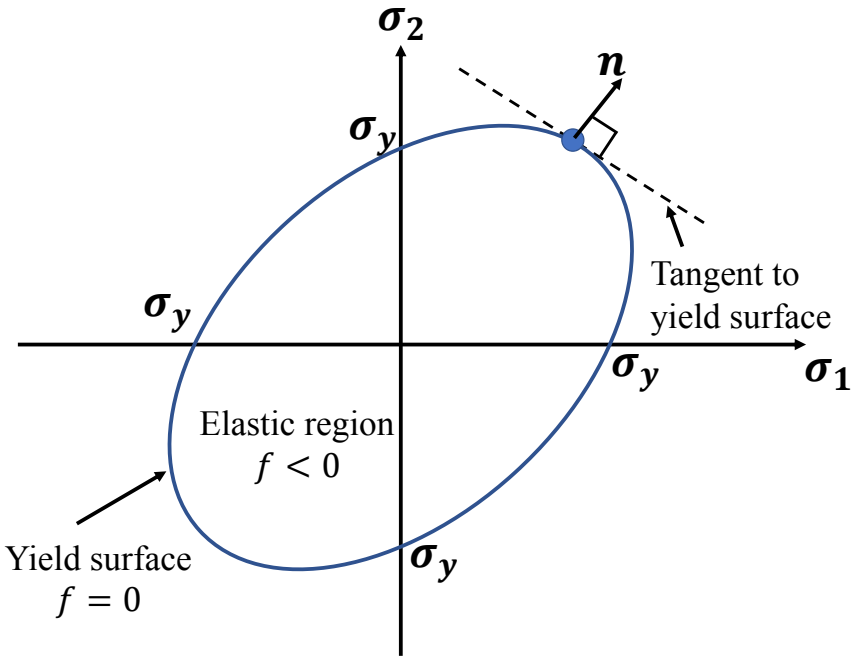

Figure 2.1: Yield surface with vector $\boldsymbol{n}$ tangent to the the yield surface. Re-sketched from Dunne and Petrinic [21].

stress tensor, given by:

$$\boldsymbol{S} = \boldsymbol{\sigma} - \frac{1}{3}\mathrm{tr}[\boldsymbol{\sigma}]\boldsymbol{I} \tag{2.8}$$

The yield function, f, is, then, defined as:

$$f = \sigma_{eq} - \sigma_y(\varepsilon^p_{eq}, \dot{\varepsilon}^p_{eq}) \tag{2.9}$$

where σ_{eq} is the von Mises equivalent stress defined from the deviatoric stress as:

$$\sigma_{eq} = \sqrt{\frac{3}{2}\boldsymbol{S} : \boldsymbol{S}} \tag{2.10}$$

and $\sigma_y(\varepsilon^p_{eq}, \dot{\varepsilon}^p_{eq})$ is the yield stress of the material, defined according to equation (2.5), which depends on the equivalent plastic strain, ε^p_{eq}, and the equivalent plastic strain rate, $\dot{\varepsilon}^p_{eq}$, which are calculated as:

$$\begin{aligned} \dot{\varepsilon}^p_{eq} &= \sqrt{\frac{2}{3}\dot{\boldsymbol{\varepsilon}}^p : \dot{\boldsymbol{\varepsilon}}^p} \\ \varepsilon^p_{eq} &= \int_0^t \dot{\varepsilon}^p_{eq} dt \end{aligned} \tag{2.11}$$

where $\dot{\boldsymbol{\varepsilon}}^p$ is the plastic strain rate tensor. The associative plastic flow rule introduces the assumption that the increment of the plastic strain tensor, $\Delta\boldsymbol{\varepsilon}^p$, is normal to the tangent of

the yield surface (Figure 2.1). This is expressed by:

$$\Delta\boldsymbol{\varepsilon}^p = \Delta\gamma\boldsymbol{n} \quad \text{or} \quad \dot{\boldsymbol{\varepsilon}}^p = \dot{\gamma}\boldsymbol{n} \tag{2.12}$$

where $\dot{\gamma}$ is a scalar representing the flow intensity of the plastic strain rate and $\boldsymbol{n}$ is a second order tensor normal to the yield function representing the flow direction, and is given by:

$$\boldsymbol{n} = \frac{\boldsymbol{S}}{\sqrt{\boldsymbol{S}:\boldsymbol{S}}} = \frac{3}{2}\frac{\boldsymbol{S}}{\sigma_{eq}} \tag{2.13}$$

The increment of the equivalent plastic strain, $\Delta\varepsilon^p_{eq}$, is expressed as:

$$\Delta\varepsilon^p_{eq} = \left(\frac{2}{3}\frac{3}{2}\Delta\gamma\frac{\boldsymbol{S}}{\sigma_{eq}} : \frac{3}{2}\Delta\gamma\frac{\boldsymbol{S}}{\sigma_{eq}}\right)^{1/2} = \frac{\Delta\gamma}{\sigma_{eq}}\sqrt{\frac{3}{2}\boldsymbol{S}:\boldsymbol{S}} \tag{2.14}$$

Combining equations (2.10) and (2.14), it turns out that for a von Mises material:

$$\Delta\varepsilon^p_{eq} = \Delta\gamma \quad \text{and} \quad \dot{\varepsilon}^p_{eq} = \dot{\gamma} \tag{2.15}$$

which implies that for a von Mises material, the increment of the scalar parameter γ is equal to the increment of the equivalent plastic strain. By rewritting equation (2.12) taking into account equation (2.13), the following equation is derived, which relates the plastic strain increment with the increment of the equivalent plastic strain, :

$$\Delta\boldsymbol{\varepsilon}^p = \frac{3}{2}\frac{\boldsymbol{S}}{\sigma_{eq}}\Delta\varepsilon^p_{eq} \tag{2.16}$$

Finally, if the second invariant of the deviatoric stress is defined as:

$$J_2 = \frac{1}{2}\boldsymbol{S}:\boldsymbol{S} \tag{2.17}$$

then equation (2.9) can be rewritten as:

$$f = \sqrt{3J_2} - \sigma_y(\varepsilon^p_{eq}, \dot{\varepsilon}^p_{eq}) \tag{2.18}$$

which is the reason why the von Mises yield criterion is also referred to as J_2 plasticity.

At this point it is worth mentioning that there are two integration schemes, namely implicit and explicit, that can be used for the integration of the momentum balance, or equilibrium, in FE simulations. This scheme should not be confused with the implementation of the plasticity equations which can be employed with either implicit or explicit methods. Therefore, the overall solution process can be obtained by a combination of implicit and explicit methods. FE methods which employ implicit integration schemes for the integration of the momentum balance, or equilibrium equations, regardless of the scheme

that is used for the integration of the plasticity equations, are called implicit FE methods (e.g. ABAQUS Standard). On the other hand, the finite element methods that used the explicit schemes for the integration of the momentum balance, or equilibrium equations are referred to as explicit FE methods (e.g. ABAQUS Explicit). Both implicit and explicit methods are available in ABAQUS known as ABAQUS Standard and ABAQUS Explicit respectively. In the following sections the radial return mapping algorithm [20] which is an implicit integration scheme of the plasticity equations will be presented followed by the implementation in the explicit and implicit solver of ABAQUS through VUMAT and UMAT subroutines respectively. It can be seen that the implicit scheme offers the more robust overall approach, because of the iteration necessary in order to achieve convergence [21]. Explicit schemes, however, will be used in the macroscopic simulation of the first bite, since they can often produce more rapid solutions, and are more appropriate for dynamic analyses [17]. Care has to be taken, however, in choosing time step size and ensuring the calculated solution does not drift away from the true solution. In the current chapter both methodologies are presented. The comparison between explicit and implicit schemes will verify that the constitutive model of the VUMAT is appropriately implemented and can be safely used for the simulations including fracture.

2.3.1 Radial return mapping algorithm

The radial return mapping algorithm, introduced by Simo and Taylor [20], is a method to determine the plastic strain that is required in order to return the stress state on the yield surface after a trial stress is applied. In the return mapping algorithm, the strain increment between time t_n and t_{n+1} is assumed to be $\Delta\boldsymbol{\varepsilon}$, which can be decomposed to the elastic strain increment, $\Delta\boldsymbol{\varepsilon}^e$, and the plastic strain increment, $\Delta\boldsymbol{\varepsilon}^p$, and the deviatoric stress tensor at t_n is $\boldsymbol{S}_n$. The elastic strain, $\boldsymbol{\varepsilon}^e$, at the end of the increment can be calculated as:

$$\boldsymbol{\varepsilon}^e_{n+1} = \boldsymbol{\varepsilon}^e_n + \Delta\boldsymbol{\varepsilon}^e = \boldsymbol{\varepsilon}^e_n + \Delta\boldsymbol{\varepsilon} - \Delta\boldsymbol{\varepsilon}^p \tag{2.19}$$

so that

$$\boldsymbol{\sigma}_{n+1} = 2G\left(\boldsymbol{\varepsilon}^e_n + \Delta\boldsymbol{\varepsilon} - \Delta\boldsymbol{\varepsilon}^p\right) + \lambda\,\mathrm{tr}\left[\boldsymbol{\varepsilon}^{\mathrm{e}}_n + \Delta\boldsymbol{\varepsilon} - \Delta\boldsymbol{\varepsilon}^p\right]\boldsymbol{I} \tag{2.20}$$

and so:

$$\boldsymbol{\sigma} = \underbrace{2G\left(\boldsymbol{\varepsilon}^e_n + \Delta\boldsymbol{\varepsilon}\right) + \lambda\,\mathrm{tr}\left[\boldsymbol{\varepsilon}^e_n + \Delta\boldsymbol{\varepsilon}\right]\boldsymbol{I}}_{\text{Elastic predictor}} - \underbrace{2G\Delta\boldsymbol{\varepsilon}^p}_{\text{Plastic corrector}} \tag{2.21}$$

since $\mathrm{Tr}\left(\Delta\boldsymbol{\varepsilon}^p\right) = 0$ depicting that the volume remains constant during plastic deformation. Also, the subscript $n+1$ has been dropped to simplify the equation. This notation is adopted for the rest of this chapter. The elastic predictor, known as trial stress is written as:

$$\boldsymbol{\sigma}^{\mathrm{tr}} = 2G\left(\boldsymbol{\varepsilon}^e_n + \Delta\boldsymbol{\varepsilon}\right) + \lambda\,\mathrm{tr}\left[\boldsymbol{\varepsilon}^e_n + \Delta\boldsymbol{\varepsilon}\right]\boldsymbol{I} \tag{2.22}$$

Knowing that for a von Mises material equation (2.16) can be applied and by combining it with equation (2.21), the following equation is derived:

$$\boldsymbol{\sigma} = \boldsymbol{\sigma}^{\mathrm{tr}} - 2G\Delta\varepsilon^{p}_{eq}\frac{3}{2}\frac{\boldsymbol{S}}{\sigma_{\mathrm{eq}}} \tag{2.23}$$

where $\Delta\varepsilon^{p}_{eq}$ is the increment of the equivalent plastic strain. As shown in equations (2.6)-(2.8), the stress tensor can be expressed in terms of the deviatoric and the mean stress. Substituting equations (2.6)-(2.8) in equation (2.23) the following is obtained:

$$\boldsymbol{S} + \frac{1}{3}\mathrm{tr}[\boldsymbol{\sigma}]\boldsymbol{I} = \boldsymbol{\sigma}^{tr} - 3G\Delta\varepsilon^{p}_{eq}\frac{\boldsymbol{S}}{\sigma_{eq}} \tag{2.24}$$

and after rearrangement:

$$\left(1 + 3G\frac{\Delta\varepsilon^{p}_{eq}}{\sigma_{eq}}\right)\boldsymbol{S} = \boldsymbol{\sigma}^{tr} - \frac{1}{3}\mathrm{tr}[\boldsymbol{\sigma}]\boldsymbol{I} \tag{2.25}$$

Now, by expanding the right hand side of equation (2.25) using equation (2.22), the following can be shown [21], where K is the elastic bulk modulus:

$$\begin{aligned}\boldsymbol{\sigma}^{tr} - \frac{1}{3}\mathrm{tr}[\boldsymbol{\sigma}]\boldsymbol{I} &= 2G\left(\boldsymbol{\varepsilon}^{e}_{n} + \Delta\boldsymbol{\varepsilon}\right) + \lambda\left(\boldsymbol{\varepsilon}^{e}_{n} + \Delta\boldsymbol{\varepsilon}\right)\boldsymbol{I} - K\mathrm{tr}[\boldsymbol{\varepsilon}^{\mathrm{e}}_{n} + \Delta\boldsymbol{\varepsilon} - \Delta\boldsymbol{\varepsilon}^{p}]\boldsymbol{I} \\ &= 2G\left(\boldsymbol{\varepsilon}^{e}_{n} + \Delta\boldsymbol{\varepsilon}\right) + \left(\lambda - K\right)\left(\boldsymbol{\varepsilon}^{e}_{n} + \Delta\boldsymbol{\varepsilon}\right) : \boldsymbol{I} \equiv \boldsymbol{S}^{tr}\end{aligned} \tag{2.26}$$

Therefore, combining equations (2.25) and (2.26), the following is obtained:

$$\left(1 + 3G\frac{\Delta\varepsilon^{p}_{eq}}{\sigma_{eq}}\right)\boldsymbol{S} = \boldsymbol{S}^{tr} \tag{2.27}$$

After some algebra the following relation is obtained:

$$\left(1 + 3G\frac{\Delta\varepsilon^{p}_{eq}}{\sigma_{eq}}\right)^{2}\boldsymbol{S} : \boldsymbol{S} = \boldsymbol{S}^{tr} : \boldsymbol{S}^{tr} \tag{2.28}$$

Taking into account equation (2.10)

$$\left(1 + 3G\frac{\Delta\varepsilon^{p}_{eq}}{\sigma_{eq}}\right)\sigma_{eq} = \left(\frac{3}{2}\boldsymbol{S}^{tr} : \boldsymbol{S}^{tr}\right)^{1/2} \equiv \sigma^{tr}_{eq}. \tag{2.29}$$

Leads to:

$$\sigma_{eq} + 3G\Delta\varepsilon^{p}_{eq} = \sigma^{tr}_{eq} \tag{2.30}$$

At time t_{n+1} the trial stress needs to be checked whether it is admissible or not, through the yield function:

$$f = \sigma^{tr}_{eq} - \sigma_{y}(\varepsilon^{p}_{eq,n}, \dot{\varepsilon}^{p}_{eq,n}) = \sigma^{tr}_{eq} - \sigma_{y,n} \tag{2.31}$$

where $\sigma_{y,n}$ is the yield stress at the beginning of the increment, $t = t_n$. The next step is to check the sign of the yield function f leading to two possible scenarios:

- If $f \leq 0$ then the step is fully elastic and the stress tensor at $t = t_{n+1}$ is equal to the trial stress tensor, $\boldsymbol{\sigma} = \boldsymbol{\sigma}^{tr}$.

- If $f > 0$ then the step is plastic and plastic correction should be applied in order to bring the stress on the surface of the yield function. This is schematically represented in Figure 2.2.

The plastic corrector is calculated through forcing the yield surface equation to be zero at t_{n+1}, through the following non linear equation:

$$f = \sigma_{eq}^{tr} - 3G\Delta\varepsilon_{eq}^{p} - \sigma_y = 0 \tag{2.32}$$

where $\Delta\varepsilon_{eq}^{p}$ is the main unknown of the non linear equation. The Newton Raphson method is applied to solve equation (2.32) and once $\Delta\varepsilon_{eq}^{p}$ is obtained, the equivalent stress at time, t_{n+1}, is updated through equation (2.30), the trial deviatoric stress from equation (2.27) and the elastic strain tensor increment is given by:

$$\Delta\boldsymbol{\varepsilon}^{e} = \Delta\boldsymbol{\varepsilon} - \Delta\boldsymbol{\varepsilon}^{p} \tag{2.33}$$

And finally the stress increment is updated from:

$$\Delta\boldsymbol{\sigma} = 2G\Delta\boldsymbol{\varepsilon}^{e} + \lambda\Delta\boldsymbol{\varepsilon}^{e}\boldsymbol{I} \tag{2.34}$$

The method described so far for updating the stress tensor is called radial return mapping algorithm and is schematically depicted in Figure 2.2.

According to ABAQUS manual [17], if the step is assumed as quasi-linear, then $\Delta\varepsilon_{eq}^{p}$ can be explicitly calculated as:

$$\Delta\varepsilon_{eq}^{p} = \sqrt{\frac{3}{2}}\frac{\sigma_{eq}^{tr} - \sigma_{y,0}}{3G + h} \tag{2.35}$$

where $h = d\sigma_{y,n}/d\varepsilon_{eq,n}^{p}$ is the hardening slope at the current point. This is generally adopted in VUMAT material models when a small time increment is used in ABAQUS/ Explicit. According to Ming et al. [22] this leads to many instabilities because the non linear terms of the constitutive equation become important. For this reason, similar to the approach of Zaera et al. [23], a Newton-Raphson method is applied to calculate the roots of equation (2.32).

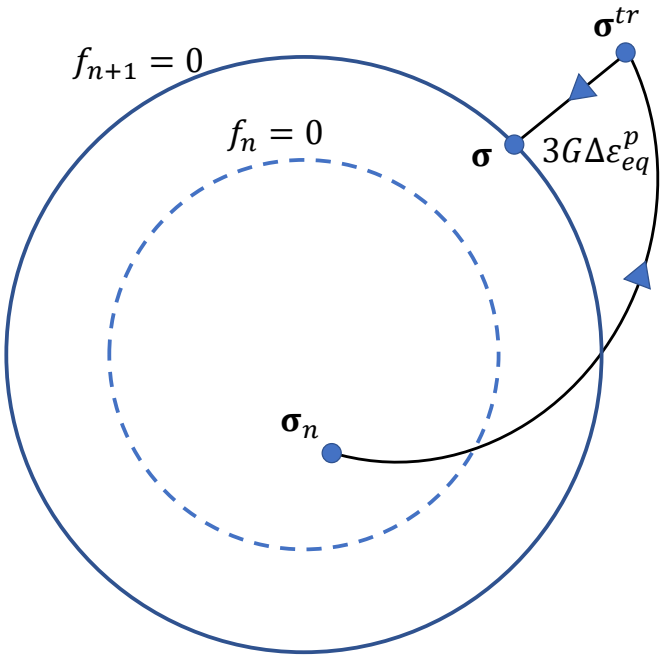

Figure 2.2: Schematic representation of the radial return mapping algorithm depicting the transition from t_n to t_{n+1}.

2.3.2 The Newton-Raphson method

The Newton-Raphson method is used to define the roots of a non linear function, g, and it requires the calculation of the first derivative $g'(x)$. Applying Taylor series expansion in function $g(x)$ around x, gives:

$$g\left(x_{i+1}\right) = g\left(x_i\right) + g'\left(x_i\right)\left(x_{i+1} - x_i\right) + \mathscr{O}\left(x_{i+1} - x_i\right)^2 \tag{2.36}$$

Assuming that x_{i+1} is a root of $g(x) = 0$, then:

$$g\left(x_i\right) + g'\left(x_i\right)\left(x_{i+1} - x_i\right) + \mathscr{O}\left(x_{i+1} - x_i\right)^2 = 0 \tag{2.37}$$

If x_i is close to x_{i+1} the term $\mathscr{O}\left(x_{i+1} - x_i\right)^2$ can be ignored and equation (2.37) becomes:

$$x_{i+1} = x_i - \frac{g\left(x_i\right)}{g'\left(x_i\right)} \tag{2.38}$$

which is known as the Newton-Raphson formula. Equation (2.38) defines the iterative process followed for the calculation of the root, which is repeated until the following convergence criterion is met:

$$\left|x_{i+1} - x_i\right| \leq \text{error} \tag{2.39}$$

where error defines the tolerance of the Newton-Raphson method. The derivative of the

yield function, f, given in equation (2.32), is calculated as:

$$f'(\Delta\varepsilon_{eq}^{p}) = -3G - \frac{d\sigma_y(\Delta\varepsilon_{eq}^{p})}{d\Delta\varepsilon_{eq}^{p}} \tag{2.40}$$

with:

$$\begin{aligned}\frac{d\sigma_y(\Delta\varepsilon_{eq}^{p})}{d\Delta\varepsilon_{eq}^{p}} &= \frac{\partial\sigma_y}{\partial\varepsilon_{eq}^{p}}\frac{d\varepsilon_{eq}^{p}}{d\Delta\varepsilon_{eq}^{p}} + \frac{\partial\sigma_y}{\partial\dot{\varepsilon}_{eq}^{p}}\frac{d\dot{\varepsilon}_{eq}^{p}}{d\Delta\varepsilon_{eq}^{p}} \\ &= \sqrt{\frac{2}{3}}\left(\frac{\partial\sigma_y}{\partial\varepsilon_{eq}^{p}} + \frac{1}{\Delta t}\frac{\partial\sigma_y}{\partial\dot{\varepsilon}_{eq}^{p}}\right)\end{aligned} \tag{2.41}$$

According to Ming et al. [22] the calculation of the derivatives using an analytical method is difficult. For this reason, a numerical solution is used as an alternative approach, by adding a small increment to the equivalent plastic strain and the equivalent plastic strain rate, in order to calculate the partial derivatives of equation (2.41) as:

$$\frac{\partial\sigma_y}{\partial\varepsilon_{eq}^{p}} = \frac{\sigma_y\left(\varepsilon_{eq}^{p} + \Delta\varepsilon_{eq}^{p}, \dot{\varepsilon}_{eq}^{p}\right) - \sigma_y\left(\varepsilon_{eq}^{p}, \dot{\varepsilon}_{eq}^{p}\right)}{\Delta\varepsilon_{eq}^{p}} \tag{2.42}$$

$$\frac{\partial\sigma_y}{\partial\dot{\varepsilon}_{eq}^{p}} = \frac{\sigma_y\left(\varepsilon_{eq}^{p}, \dot{\varepsilon}_{eq}^{p} + \Delta\dot{\varepsilon}_{eq}^{p}\right) - \sigma_y\left(\varepsilon_{eq}^{p}, \dot{\varepsilon}_{eq}^{p}\right)}{\Delta\dot{\varepsilon}_{eq}^{p}} \tag{2.43}$$

2.4 Johnson-Cook implementation in VUMAT

This section describes the steps followed to implement the radial return mapping algorithm for the Johnson-Cook constitutive law using a VUMAT subroutine in ABAQUS/Explicit. Since the main purpose of the current thesis is the simulation of the first bite, which includes contact, it is preferable to use the Explicit solver of ABAQUS, which handles better problems with contact [17].

The algorithm developed by Ming et al. [22] was used in the current study, and the required steps for the VUMAT implementation in ABAQUS/Explicit are presented here as well. The variables passed in the VUMAT are the following:

- The strain increment tensor, $\Delta\boldsymbol{\varepsilon}$, at each material point (strainInc).
- The stress tensor at the beginning of the increment (stressOld).
- The state variables at each material point at the beginning of the increment (stateOld). Here, the state variables are the plastic strain, ε_{eq}^{p}, the plastic strain rate, $\dot{\varepsilon}_{eq}^{p}$, the plastic corrector $\Delta\varepsilon_{eq}^{p}$ and the stress triaxiality η.

ABAQUS then combines this information with the material properties of the constitutive law and initially calculates the deviatoric trial elastic stress, $\boldsymbol{S}^{tr}$, and afterwards the

trial von Mises yield stress, σ_{eq}^{tr}. The initial stress $\boldsymbol{\sigma}_n$ is decomposed to the hydrostatic pressure and the deviatoric stress $\boldsymbol{S}_n$ as follows:

$$\begin{aligned} p_n &= \frac{1}{3}\,\mathrm{tr}\,[\boldsymbol{\sigma}_n] \\ \boldsymbol{S}_n &= \boldsymbol{\sigma}_n - p_n \boldsymbol{I} \end{aligned} \tag{2.44}$$

The hydrostatic stress, p_1, and the trial deviatoric stress, $\boldsymbol{S}^{tr}$, at the end of the increment are given by:

$$\begin{aligned} p_1 &= p_n + K\,\mathrm{tr}[\Delta\boldsymbol{\varepsilon}] \\ \boldsymbol{S}^{tr} &= \boldsymbol{S}_n + 2G(\Delta\boldsymbol{\varepsilon} - \frac{1}{3}\,\mathrm{tr}[\Delta\boldsymbol{\varepsilon}]\boldsymbol{I}) \end{aligned} \tag{2.45}$$

The von Mises yield stress, σ_{eq}^{tr}, is calculated using equation (2.29) and is compared against the yield stress at the beginning of the increment, $\sigma_y(\varepsilon_{eq,n}^p, \dot{\varepsilon}_{eq,n}^p)$. The two possible scenarios are listed below:

- If $\sigma_{eq}^{tr} \leq \sigma_y(\varepsilon_{eq,n}^p, \dot{\varepsilon}_{eq,n}^p)$ then the step is fully elastic and the deviatoric stress at $t = t_1$ is equal to the trial deviatoric stress ($\boldsymbol{S} = \boldsymbol{S}^{tr}$), and the plastic corrector equals to zero ($\Delta\varepsilon_{eq}^p = 0$).

- If $\sigma_{eq}^{tr} > \sigma_y(\varepsilon_{eq,n}^p, \dot{\varepsilon}_{eq,n}^p)$ then plasticity takes place and the stress state of the material at $t = t_{n+1}$ lies outside the surface of the yield function. The plastic corrector, $\Delta\varepsilon_{eq}^p$, needs to be calculated by enforcing equation (2.32) to be zero.

The plastic corrector $\Delta\varepsilon_{eq}^p$ is calculated using the Newton-Raphson method to find the roots of equation (2.32). According to Ming et al. [22] the interval of the plastic corrector is initialized so that $\Delta\varepsilon_{eq}^p \in \left[0, \sigma_{eq}^{tr}/3G\right]$. Then, the equivalent plastic strain, ε_{eq}^p, and the equivalent plastic strain rate, $\dot{\varepsilon}_{eq}^p$ at the end of the increment, t_{n+1}, are calculated according to equation (2.46).

$$\varepsilon_{eq}^p = \varepsilon_{eq,n}^p + \sqrt{\frac{2}{3}}\Delta\varepsilon_{eq}^p \tag{2.46}$$

Afterwards, the yield stress, $\sigma_{y,1}$, the yield function, $f(\Delta\varepsilon_{eq}^p)$, and its derivative, $f'(\Delta\varepsilon_{eq}^p)$, are computed and the convergence is checked through the increment of $\Delta\varepsilon_{eq}^p$.

$$\delta\Delta\varepsilon_{eq}^p = -\frac{f(\Delta\varepsilon_{eq}^p)}{f'(\Delta\varepsilon_{eq}^p)} \tag{2.47}$$

The derivative of function f is derived in equation (2.41) and is calculated through equations (2.42) and (2.43). For the Johnson-Cook constitutive law these equations are written as:

$$\frac{\partial\sigma_y}{\partial\varepsilon_{eq}^p} = nB{\varepsilon_{eq}^p}^{(n-1)}\left[1 + C\ln\left(\frac{\dot{\varepsilon}_{eq}^p}{\dot{\varepsilon}_0}\right)\right] \tag{2.48}$$

$$\frac{\partial \sigma_y}{\partial \dot{\varepsilon}^p_{eq}} = \begin{cases} \frac{C\left(A+B\varepsilon^{p^n}_{eq}\right)}{\varepsilon^p_{eq}} & \text{if} \quad \dot{\varepsilon}^p_{eq} \geq \dot{\varepsilon}_0 \\ 0 & \text{if} \quad \dot{\varepsilon}^p_{eq} < \dot{\varepsilon}_0 \end{cases} \tag{2.49}$$

2.5 Implementation of Johnson-Cook model in UMAT

For the implementation of a constitutive law using a UMAT subroutine in the implicit solver of ABAQUS, a range of values is passed into relating to both the beginning and the end of the time increment. In particular, strain and deformation gradient are provided at the beginning and the end of the time increment whereas stress is provided only at the beginning. Afterwards, the stresses at the end of the time increment are determined through the material Jacobian, or tangent stiffness, which is also be provided. Finally, all the state variables, e.g. equivalent plastic strain, triaxiality, are updated at the end of the time increment [21].

The implementation of the constitutive equations within the ABAQUS implicit FE code requires the determination of the Jacobian, which comprises both the tangent stiffness matrix and the load stiffness matrix. The tangent stiffness matrix depends mainly on the constitutive equations. It is therefore necessary to provide the material tangent stiffness matrix in addition to the integration of the constitutive equations. For the implementation of the constitutive equations in the ABAQUS implicit solver (ABAQUS/Standard), a UMAT subroutine is needed which contains the constitutive equations together with the material Jacobian.

2.5.1 The Principle of Virtual Work

The principle of virtual work forms the basis for the implementation of non linear finite element approximation and will be discussed in this section. Consider a deformable continuum body, which occupies a volume V_0 with boundary surface S and has a mass density ρ_0 in its reference state at $t = 0$. The body is then loaded with body forces $\boldsymbol{b}$ per unit mass together with a traction $\hat{\boldsymbol{t}}$ applied on a part of the boundary S_t and by prescribed displacements on the rest of the boundary (S_u)[1], as shown in Figure 2.3 [24].

After a time period Δt, the body is deformed occupying a volume V with a mass density ρ surrounded by surface S. The loading induces a Cauchy stress σ_{ij} and the equilibrium is expressed as:

$$\frac{\partial \sigma_{ij}}{\partial x_j} + \rho b_i = 0 \tag{2.50}$$

[1]Note that $S_u \cap S_t = \emptyset$ and $S_u \cup S_t = S$

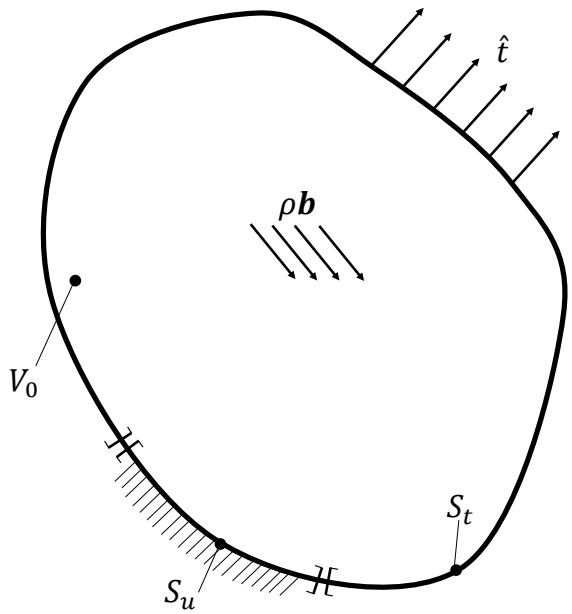

Figure 2.3: Continuum body of volume V subjected to traction and displacement boundary conditions

with boundary conditions for applied forces and displacements in the boundary ∂S:

$$\boldsymbol{u} = \hat{\boldsymbol{u}} = \text{known} \quad \text{on } S_u \tag{2.51}$$

$$\hat{\boldsymbol{t}} = \boldsymbol{\sigma} \cdot \boldsymbol{n} = \text{known} \quad \text{on } S_t \tag{2.52}$$

when $\boldsymbol{n}$ is a vector normal to the surface boundary ∂S_t. The problem is completed by the kinematical relationships:

$$D_{ij} = \frac{1}{2}\left(\frac{\partial v_i}{\partial x_j} + \frac{\partial v_j}{\partial x_i}\right) \tag{2.53}$$

where D_{ij} is the deformation rate tensor that corresponds to the velocity field v_i.

Equations (2.50-2.53) constitute the strong formulation of the boundary value problem. The principle of virtual work is based in rewriting the equations of equilibrium in the weak formulation. To express this equation, a kinematically admissible virtual velocity field, $\boldsymbol{v}^*$, is defined on S_u and then integrating over the entire volume of continuum body the following is derived:

$$\int_V \left[\frac{\partial \sigma_{ij}}{\partial x_j} + \rho b_i = 0\right] v_i^* dV = 0 \tag{2.54}$$

Applying the chain rule:

$$\frac{\partial \sigma_{ij}}{\partial x_j} v_i^* = \frac{\partial}{\partial x_j}\left(\sigma_{ij} v_i^*\right) - \sigma_{ij}\frac{\partial v_i^*}{\partial x_j} \tag{2.55}$$

and making use of the divergence theorem, the following is derived:

$$\begin{aligned}\int_V \frac{\partial \sigma_{ij}}{\partial x_j} v_i^* dV &= \int_V \left[\frac{\partial}{\partial x_j} \left(\sigma_{ij} v_i^* \right) - \sigma_{ij} \frac{\partial v_i^*}{\partial x_j} \right] dV \\ &= \int_{S_t} n_j \sigma_{ij} v_i^* dS - \int_V \sigma_{ij} \frac{\partial v_i^*}{\partial x_j} dV \\ &= \int_{S_t} t_i v_i^* dS - \int_V \sigma_{ij} L_{ij}^* dV \end{aligned} \tag{2.56}$$

where L_{ij}^* is the virtual velocity gradient the components of which are given by:

$$L_{ij}^* = \frac{\partial v_{ij}^*}{\partial x_j} \tag{2.57}$$

this can be decomposed into the symmetric D_{ij}^* and antisymmetric part W_{ij}^* and taking advantage of the symmetry of $\boldsymbol{\sigma}$, the following equation is derived:

$$\sigma_{ij} L_{ij}^* = \sigma_{ij} \left(D_{ij}^* + W_{ij}^* \right) = \sigma_{ij} D_{ij}^* + \sigma_{ij} W_{ij}^* = \sigma_{ij} D_{ij}^* \tag{2.58}$$

Combining equations (2.54), (2.56) and (2.58) the weak form of the boundary value problem is written as:

$$\int_V \sigma_{ij}^* D_{ij}^* dV - \int_{S_t} t_i v_i^* dS - \int_V \rho b_i v_i^* dV = 0 \tag{2.59}$$

Equation 2.59 is known as the weak formulation of the boundary value problem (BVP) and forms the basis for the FE approximation introduced in the following section.

2.5.2 FE for the solution of the weak formulation BVP

In this section the Johnson-Cook material model that was introduced in section 2.2 will be implemented in the FE code. In FE analysis the displacement field is discretised by choosing to calculate the displacement field in a set of n nodes. The solution is developed incrementally by applying a displacement increment $\Delta u(\boldsymbol{x})$, which is the main unknown of the problem. The unknown displacement vector at each nodal point is denoted by u_i^α, where the superscript α ranges from 1 to n, with n representing the number of nodes. In the viscoplastic case the displacements vary as a function of time, so $u_i^\alpha = u_i^\alpha(t)$. The displacement $u_i^\alpha(t)$ is assumed to be known at the end of each step and unknown is the $u_i^\alpha(t+\Delta t)$. The displacement field is summarised as:

$$u_i^\alpha(t+\Delta t) = u_i^\alpha(t) + \Delta u_i^\alpha$$

and is solved by calculating the displacement field Δu_i^α. By discretising the continuum body into finite elements, the displacement increment, $\Delta \boldsymbol{u}$ and the virtual displacement,

$\boldsymbol{v}^*$, can be expressed as an interpolation function within each element as:

$$\Delta u(\boldsymbol{x})_i = \sum_{i=1}^{n} N^{\alpha}(\boldsymbol{x}) \Delta u_i^{\alpha} \tag{2.60}$$

$$v_i^*(\boldsymbol{x}) = \sum_{i=1}^{n} N^{\alpha}(\boldsymbol{x}) {v_i^*}^{\alpha} \tag{2.61}$$

where, $\boldsymbol{x}$, denotes the coordinates of an arbitrary point in the solid and N_i are the shape functions. The symmetric part, D_{ij}^* , of the virtual velocity field is expressed as:

$$D_{ij}^* = \frac{1}{2}\left(\frac{\partial v_i^*}{\partial x_j} + \frac{\partial v_j^*}{\partial x_i}\right) = \frac{1}{2}\sum_{i=1}^{n}\left(\frac{\partial N^{\alpha}}{\partial x_j}{v_i^*}^{\alpha} + \frac{\partial N^{\alpha}}{\partial x_i}{v_j^*}^{\alpha}\right) \tag{2.62}$$

By using the constitutive law, the stress field caused by the strain in the time increment Δt can be calculated as function of the strain increment and the time increment due to the strain rate effect. The stress can be expressed as:

$$\sigma_{ij} = \sigma_{ij}\left(\Delta u_i^{\alpha}, \Delta t\right) \tag{2.63}$$

Substituting into the principle of virtual work of equation (2.59):

$$\left[\int_V \sigma_{ij}\left(\Delta u_i^{\alpha}, \Delta t\right)\frac{\partial N^{\alpha}}{\partial x_j} dV - \int_V \rho b_i N^{\alpha} dV - \int_{S_t} t_i N^{\alpha} dS_t\right] {v_i^*}^{\alpha} = 0 \tag{2.64}$$

and because this must hold for all ${v_i^*}^{\alpha}$:

$$\int_V \sigma_{ij}\left(\Delta u_i^{\alpha}, \Delta t\right)\frac{\partial N^{\alpha}}{\partial x_j} dV - \int_V \rho b_i N^{\alpha} dV - \int_{S_t} t_i N^{\alpha} dS_t = 0 \tag{2.65}$$

Equation (2.65) is a set of non linear equations to be solved for Δu_i^a using Newton's method. Thus, the expression of the Jacobian matrix, that is used for the solution of the problem, needs to be derived.

2.5.3 Calculation of the Jacobian

The linearization of the return mapping algorithm is needed for the calculation of the Johnson-Cook Jacobian. Doghri and Ouaar [25] showed that the Jacobian at $t = t_{n+1}$ can be written as [26]:

$$\frac{\partial \Delta\boldsymbol{\sigma}^{(n+1)}}{\partial \Delta\boldsymbol{\varepsilon}^{(n+1)}} = \lambda^* \boldsymbol{I}\otimes\boldsymbol{I} + G^*[\boldsymbol{I}\overline{\otimes}\boldsymbol{I} + \boldsymbol{I}\underline{\otimes}\boldsymbol{I}] + \left[\frac{h}{1+\frac{h}{3G}} - 3G^*\right]\frac{\boldsymbol{S}^{(n+1)}}{\sigma_{eq}^{n+1}}\otimes\frac{\boldsymbol{S}^{(n+1)}}{\sigma_{eq}^{n+1}} \tag{2.66}$$

where:

$$G^* = G\frac{\sigma_y^{(n+1)}}{\sigma_{eq}^{tr(n+1)}}, \quad \lambda^* = K - \frac{2}{3}G^*, \quad h = \frac{\partial \sigma_y^{(n+1)}}{\partial \varepsilon_{eq}^{p(n+1)}} + \frac{\partial \sigma_y^{(n+1)}}{\partial \dot{\varepsilon}_{eq}^{p(n+1)}}\frac{1}{\Delta t} \tag{2.67}$$

The same notation as in the paper of Achour et al. [26] is followed here as well where the symbols $\boldsymbol{I}\overline{\otimes}\boldsymbol{I}$ and $\boldsymbol{I}\underline{\otimes}\boldsymbol{I}$ indicate the two special dyadic products of the identity tensor, $\boldsymbol{I}$, and are defined as:

$$[\boldsymbol{I}\overline{\otimes}\boldsymbol{I}]_{ijkl} = \delta_{ik}\delta_{jl}, \quad [\boldsymbol{I}\underline{\otimes}\boldsymbol{I}]_{ijkl} = \delta_{il}\delta_{jk} \tag{2.68}$$

where δ_{ij} is the delta Kronecker. The detailed derivation of equation (2.66) is provided in Appendix A.1. The terms $\frac{\partial \sigma_y^{(n+1)}}{\partial \varepsilon_{eq}^{p(n+1)}}$ and $\frac{\partial \sigma_y^{(n+1)}}{\partial \dot{\varepsilon}_{eq}^{p(n+1)}}$, of the hardening parameter h in equation (2.67), have been already calculated in equations (2.48) and (2.49).

2.6 Two-layer viscoplasticity

Besides the Johnson-Cook material model, the two-layer viscoplastic model which is implemented in the material library of ABAQUS, is used for the characterisation of the chocolate matrix. The two-layer viscoplastic model divides the material behaviour in elastic, plastic and viscous parts. Such laws can be represented, in one dimension, using a combination of spring, dashpots and sliding elements. Figure 2.4 depicts this material idealisation, with the elastic-plastic and the elastic-viscous networks connected in parallel.

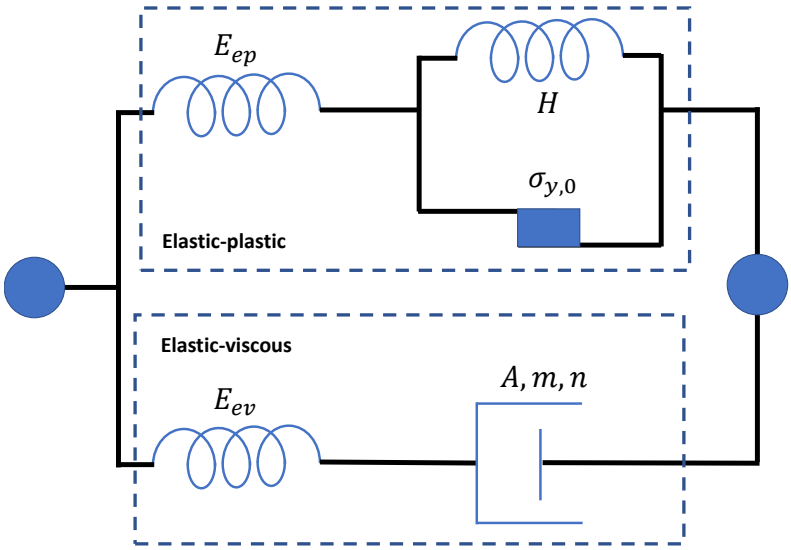

Figure 2.4: One dimensional representation of the two-layer viscoplastic model.

The springs represent the elastic part of the response using a linear elastic isotropic definition. The ratio between the elastic modulus of the elastic-viscous network (E_{ev}) to

the total elastic modulus ($E_{ev}+E_{ep}$), with E_{ep} defining the elastic modulus of the elastic-plastic network, is a user specified ratio given by:

$$f_v = \frac{E_{ev}}{E_{ev}+E_{ep}} \tag{2.69}$$

The elastic-plastic branch is based on the the von Mises yield condition and describes the time independent material behaviour. The elastic-plastic layer consists of a spring with elastic modulus E_{ep} which is connected in series with a sliding element with a yield stress σ_{y0} and strain hardening parameter H. The material behaviour regarding the elasto-plastic time independent behavior depends on whether the material exceeds the yield stress or not and is described by the following equations:

$$\sigma_{\text{ep}} = \begin{cases} \varepsilon E_{\text{ep}}, & \text{if} \quad \varepsilon E_{\text{ep}} \leq \sigma_{\text{yo}} \\ \sigma_{\text{yo}} + H\left(\varepsilon - \frac{\sigma_{\text{yo}}}{E_{\text{ep}}}\right), & \text{if} \quad \varepsilon E_{\text{ep}} > \sigma_{\text{yo}} \end{cases} \tag{2.70}$$

The elastic-viscous part of Figure 2.4 is characterized by a spring, with elastic modulus E_{ev} and a dashpot, with parameters A, n and m connected in series. This combination is known as a generalised Maxwell element and introduces the strain rate dependency in the model. The viscous parameters A, n and m are called Norton Hoff rate parameters [17] and must satisfy the following conditions:

$$A, n > 0 \quad \text{and} \quad -1 \leq m \leq 0 \tag{2.71}$$

The elastic-viscous stress is calculated according to the following equation:

$$\sigma_{\text{ev}}(t) = A^{-\frac{1}{n}} t^{\left(-\frac{m}{n}\right)} \dot{\varepsilon}_{\text{v}}(t)^{\left(\frac{1}{n}\right)} \tag{2.72}$$

Equation (2.72) can be rearranged so that, the strain rate of the dashpot, $\dot{\varepsilon}_{\text{v}}(t)$, is obtained as:

$$\dot{\varepsilon}_{\text{v}}(t) = A\sigma_{\text{ev}}(t)^n t^m \tag{2.73}$$

Taking into account the parallel connection of the elastic-plastic and elastic-viscous branches the below relations can be written:

$$\dot{\varepsilon} = \dot{\varepsilon}_{ep} = \dot{\varepsilon}_{ev} \tag{2.74}$$

$$\sigma = \sigma_{ep} + \sigma_{ev} \tag{2.75}$$

The elastic-plastic strain rate, $\dot{\varepsilon}_{ep}$, and the elastic-viscous strain rate, $\dot{\varepsilon}_{ev}$, can be further

decomposed to the following:

$$\dot{\varepsilon}_{ep} = \dot{\varepsilon}_p + \dot{\varepsilon}_{ep,e} \tag{2.76}$$

$$\dot{\varepsilon}_{ev} = \dot{\varepsilon}_v + \dot{\varepsilon}_{ev,e} \tag{2.77}$$

where $\dot{\varepsilon}_p$ is the plastic strain rate, $\dot{\varepsilon}_{ep,e}$ is the elastic strain rate of the elastic plastic branch, $\dot{\varepsilon}_v$, is the viscous strain rate and $\dot{\varepsilon}_{ev,e}$ is the elastic strain rate of the elastic-viscous branch.

Substituting equations (2.70) and (2.72) into (2.75) the following equation of the overall stress of the two-layer viscoplastic model is obtained:

$$\sigma = \begin{cases} \varepsilon E_{ep} + A^{-\frac{1}{N}} t^{-\frac{m}{n}} \dot{\varepsilon}_v^{\frac{1}{N}}, & \text{if} \quad \varepsilon E_{ep} \leq \sigma_{y0} \\ \sigma_{y0} + H' \left(\varepsilon - \frac{\sigma_{y0}}{E_{ep}} \right) + A^{-\frac{1}{N}} t^{-\frac{m}{n}} \dot{\varepsilon}_v^{\frac{1}{N}}, & \text{if} \quad \varepsilon E_{ep} > \sigma_{y0} \end{cases} \tag{2.78}$$

The viscous strain rate, $\dot{\varepsilon}_v$, is unknown. According to ABAQUS manual [17] this parameter can be estimated by considering $m = 0$, implying steady state conditions, which result in $\sigma_{ev} = A^{-\frac{1}{N}} \dot{\varepsilon}_v^{\frac{1}{N}}$. According to Skamniotis [27] this leads to severe limitations in the chewing application, which includes high strain rates. To overcome this limitation, the methodology introduced in [27] will be applied here as well. The decomposition of the viscous strain rate of the dashpot, $\dot{\varepsilon}_{ev}$, as shown in equation (2.77), will be used for the calculation of the elastic viscous strain rate $\dot{\varepsilon}_v$. An explicit approach is applied, where the current elastic strain, $\varepsilon^i_{ev,e}$, is calculated by differentiating equation (2.73) between t^{i-1} and t^i and using the stress of the previous increment σ^{i-1}_{ev}, which is known and can be found from the spring response as $E_{ev}\varepsilon^{i-1}_{ev,e}$. The procedure is summarised bellow:

$$\begin{aligned} \sigma^{i-1}_{ev} &= E_{ev}\varepsilon^{i-1}_{ev,e} \\ \varepsilon^i_{ev,e} &= \varepsilon^{i-1}_{ev,e} + \Delta\varepsilon - \Delta t A \left(\sigma^{i-1}_{ev}\right)^n t^m \\ \varepsilon^i_v &= \varepsilon^i - \varepsilon^i_{ev,e} \end{aligned} \tag{2.79}$$

The calibration starts from $t = 0$ where the strains are zero and using equation (2.79) the elastic strain of the elastic-viscous layer, $\varepsilon_{ev,e}$, is computed. Afterwards, the viscous strain rate, $\dot{\varepsilon}_v$, is calculated using equation (2.77) and subsequently the total stress is found by substituting in equation (2.78).

The methodology described so far, together with equations (2.79) was implemented in an MS EXCEL spreadsheet and the parameters A, N, m, f, H' and σ_{y0} were calibrated. The stress-strain monotonic compression experimental data [11] were used and an instantaneous, $E_{ep} + E_{ev}$, of 100 MPa was applied for the non-aerated chocolate samples. The hardening parameter H' was calculated as the gradient between two stress values. These two stress data points were selected as the onset of plastic deformation, also known as the static yield stress, $\sigma_{y0,s}$ and the stress, $\sigma_{y0,m}$ that corresponds to the maximum strain

observed from the monotonic compression experiments at strain rate $\dot{\varepsilon} = 0.01\,\mathrm{s}^{-1}$. The maximum strain value for the non aerated chocolate was found to be 0.21 (shown in Figure 2.5). The slope of the plastic region at $\dot{\varepsilon} = 0.01\,\mathrm{s}^{-1}$ strain rate was used to calculate the values of $\sigma_{y0,s}$ and $\sigma_{y0,m}$.

2.7 Summary of experimental results

The experimental data used for the calibration of the constitutive models, are presented in detail in the study of Bikos et el. [11]. In this thesis, the experimental results from monotonic compression and tension are presented and the reader is advised to read the study of Bikos et al. [11] for details regarding the experimental set up, the instrumentation and the geometry of the samples used. Figure 2.5 depicts the stress-strain results from monotonic compression (black dashed line) and from monotonic tension (red dashed lined) for three strain rates $\dot{\varepsilon} = 0.01, 0.1, 1\,\mathrm{s}^{-1}$.

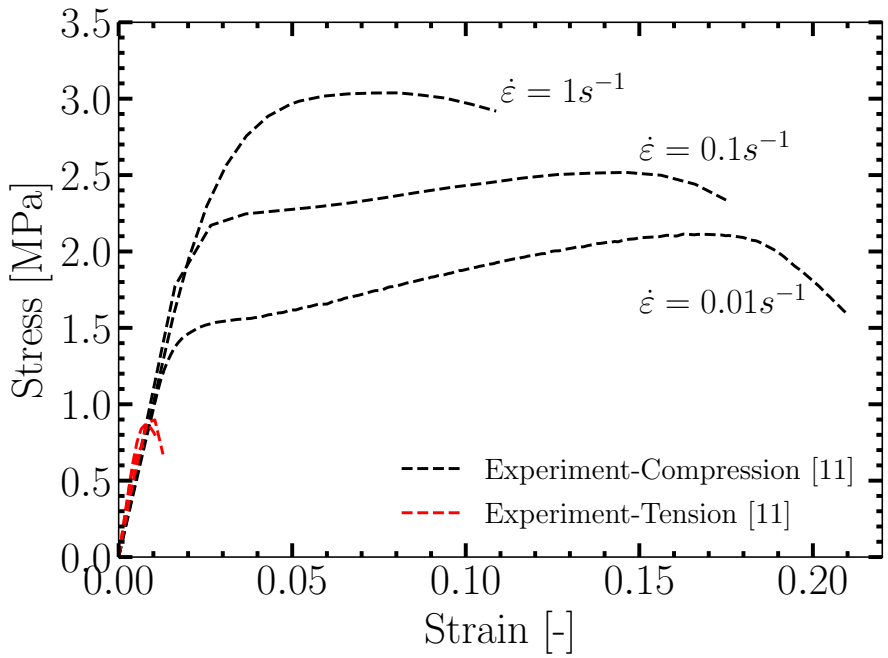

Figure 2.5: Comparison between monotonic compression and tension experimental data [11].

It is evident that for the monotonic compression tests, the material behaviour is rate dependent and the elastic, plastic and softening regions are visible. On the other hand, the results from the tension experiments show a different behaviour. Although the Young's modulus is comparable with the respective value obtained by the compression experiment, the tension results reveal that the yield stress in tension is smaller than in compression. It is worth noting that, due to the nature of the material, it is difficult to create straight tensile specimens without flows. This misalignment can cause severe problems resulting

in unreliable results leading to premature failure. For this reason, in the current thesis, only the compression experiments will be used for the estimation of the Young's modulus, the Poisson's ratio and the calibration of the experimental data and the estimation of the plastic strain at the initiation of failure (chapter 3).

2.8 Comparison of constitutive models

The constitutive models presented so far were implemented in ABAQUS, calibrated against experimental data [11] and a comparison is given in this section. All FE simulations were conducted in a single element and the stress-strain curves were calculated for the different constitutive models. In this section, the compression experimental data of Figure 2.5 will be used for the calibration of the model parameters. Also, the part of the curve until the maximum stress point at each strain rate is considered, excluding the softening part, since the damage has not considered in the models so far. The entire stress-strain curves will be considered in chapter 3, where the softening part will be used for the calibration of the parameters that are involved in the damage evolution law.

Initially, the Johnson-Cook material model was calibrated. The Young's modulus, E, was calculated from the gradient of the elastic region of Figure 2.5 and the Poisson's ration, ν, was adapted from the study of Bikos et al. [11], where a detailed calculation methodology is provided. The parameters A, B and n were estimated using the lower strain rate $\dot{\varepsilon} = 0.01$. The parameter A represents the yield point, the parameter B influences the hardening and the parameter n characterises the curvature of the plastic region at this rate. The parameter C corresponds to the rate dependency. All the calibrated parameters are given in Table 2.1

Table 2.1: Calibrated parameters of the Johnson-Cook model

Parameter	**Value**
Elastic modulus, E [MPa]	100
Poisson's ratio, ν [-]	0.49
A [MPa]	1.35
B [MPa]	3.5
C [-]	0.05
n [-]	0.8
$\dot{\varepsilon}$ [s^{-1}]	0.01

Figure 2.6 depicts a comparison of the stress-strain data obtained from compression experiments and data calculated from the FE analysis of one element subjected to compression. The Johnson-Cook model calibrated according to Table 2.1 lies in good agreement with the experimental data. The different implementations of the modified Johnson-

Cook constitutive model provide the same stress-strain response. In the graph the three curves obtained from the FE calculations overlap and this is the reason why the ABAQUS UMAT data are not visible.

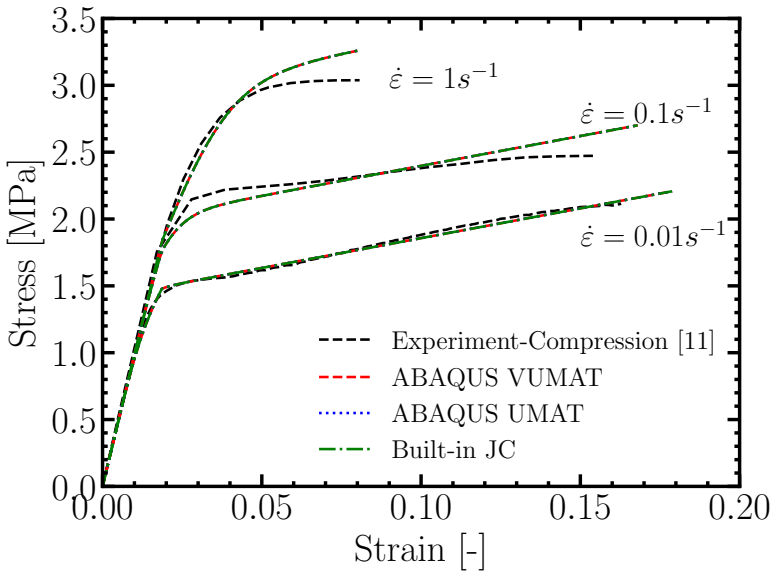

Figure 2.6: Comparison between the Johnson-Cook model implemented in VUMAT, UMAT and ABAQUS built-in and the experimental data in compression [11].

The calibrated parameters of the two-layer viscoplastic model are presented in Table 2.2. Figure 2.7 shows the stress-strain graph of the two-layer viscoplastic law for different strain rates. There is a good agreement between the simulation and experimental data in compression. It is worth noting that, the two-layer viscoplastic law is only available in the implicit solver of ABAQUS [17], which limits its utility in the chewing model, as it will be explained in chapter 5. Note that the experimental data, presented in Figures 2.6 and 2.7, include only the part of the curve before softening occurs. Softening is examined for the calibration of the damage parameters and the calculation of the strain at the fracture initiation.

Table 2.2: Calibrated parameters of the two-layer viscoplastic model

Parameter	**Value**
Elastic modulus, E [MPa]	100
Poisson's ratio, ν [-]	0.49
$\sigma_{yo,s}$ [MPa]	0.8
$\sigma_{yo,m}$ [MPa]	1.8
A [MPa$^{-\mathrm{n}}$s$^{-1-\mathrm{m}}$]	0.04
n [-]	0.8
m [-]	-0.01
f [-]	0.57

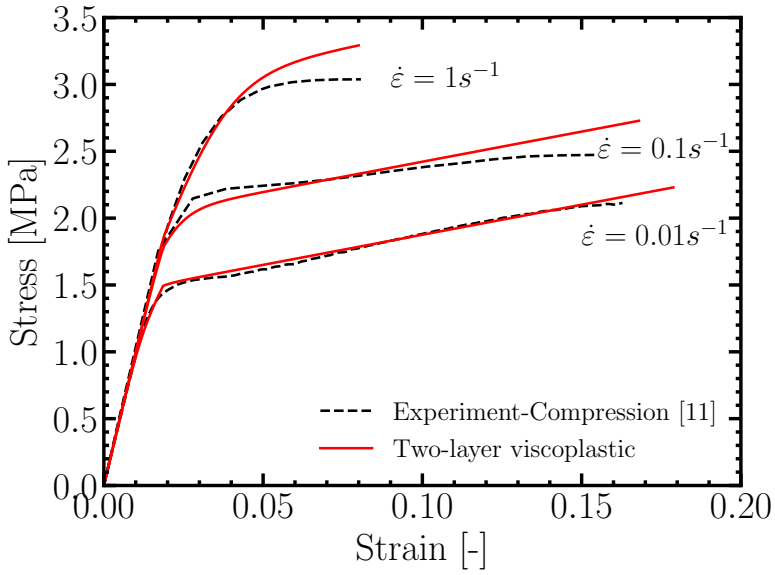

Figure 2.7: Comparison between the two-layer viscoplastic model and the experimental data in compression [11].

2.9 Conclusions

This chapter investigated material models available in ABAQUS with the potential to model the solid chocolate matrix. ABAQUS provides several built-in material models that can be used for the purposes of this theses. However, as it will be shown in chapter 3, the built-in damage laws that are compatible with these material models suffer from mesh dependency, which is a crucial aspect when simulating the food fracture during the first bite. For this reason, the material model needs to be coupled with an appropriate damage model though a user material subroutine.

Initially, the Johnson-Cook constitutive model was presented followed by the radial return mapping algorithm which defines an implicit algorithm for the solution of the constitutive equations. The Johnson-Cook material model was implemented in both the Implicit (UMAT) and Explicit (VUMAT) solver of ABAQUS and the methodology followed was presented. Although, the macroscopic first bite simulations will be conducted in ABAQUS Explicit, since it handles better simulations that involve contact [17], the VUMAT was compared against the same constitutive model implemented in a UMAT subroutine and the built-in Johnson-Cook material model. The finite element simulations were conducted in a single element and the stress-strain curves showed that the three different implementations of the model overlap. This proved that the VUMAT has been successfully implemented in the finite element model and can be used in conjunction with the damage model for the simulations that will be presented in chapters 4 and 5.

In addition to that, the built-in two-layer viscoplastic model was calibrated for the experimental data of the solid chocolate matrix. The results showed that the model can be

successfully applied and can provide an alternative constitutive model that can be used in the simulations of the first bite.

3 Implementation of non-local damage model

Topics

3.1 Introduction

Like many engineering materials, foods contain microstructural flaws that decrease their strength. Modeling damage that is driven through discontinuities in the matrix, for the non-aerated chocolate, and pores, in the case of micro-aerated chocolate, is the field that Continuum Damage Mechanics (CDM) is concerned with [28, 29]. The heterogeneous nature of the matrix causes strain localisation phenomena which appear initially as shear bands leading to the formation of cracks. As a result of strain localisation, softening in the material takes place leading to reduction of stresses while strains are increasing. A model that predicts correctly the formation of shear bands is of crucial importance, since it will secure the accurate prediction of fracture which is an important aspect in the prediction of fragmentation during the first bite.

The theory of CDM aims to describe and analyse the damage and fracture properties from a continuum mechanics point of view [30, 31]. The changes in the microstructure due to growth, nucleation and coalescence of voids and other defects lead to loss of stiffness that influences that macromechanical behaviour of the material.

In order to characterise the effect of the discontinuities that are present in the micro-scale by means of continuum mechanics, the microscopic micro-homogeneities must be

homogenised and represent them as a homogeneous macroscopic field. Figure 3.1 represents defects that are present at a material point P. According to the principle of local state [32], a state variable at a point can be used to describe the thermodynamic state (damage state). In CDM an internal state variable, known as damage variable $d(x)$, is used to describe the damage state at a material point.

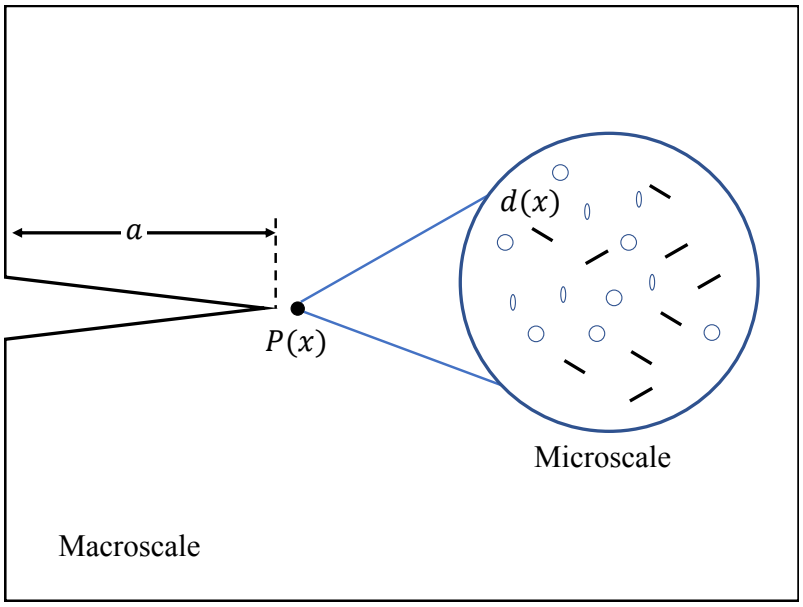

Figure 3.1: The damage parameter $d(x)$ is calculated taking into account the defects around a material point P in front of a crack with lenght a.

In the so called local CDM model (e.g. ductile damage model in ABAQUS [17]) the damage parameter depends only on the strain state at each material point. This causes the numerical simulations to exhibit a pathological mesh dependence and the damage parameter tends to increase as the mesh is refined leading to unreliable results [33]. The limitation is derived from the fact that when investigating the shear band formation using classical continuum mechanics, the numerical solutions suffer from ill-posed mathematics and the governing partial differential equations (PDEs) lose ellipticity (from elliptic to hyperbolic) [34]. The absence of an internal material length in the classical continuum theory, causes the characteristic element length to become the material length.

The FE calculation using local CDM has no physical meaning as the predictions of the shear band width and crack propagation depend on the element size and not a material property, i.e. an internal length scale. As it will be shown in section 3.6, the width of the shear band decreases as the mesh becomes more refined. A technique to resolve the mesh dependency problem is by extending the classic CDM theory to include a characteristic length of the material, that is related to inter-void distance or the grain size of the material's microstructure [34]. Such extension is done through strain gradient or non-local models [35]. In non-local models, the microstructure interaction around a material point is introduced, where the stress response of a material point is assumed to depend on the

state of its neighborhood. A non-local variable is defined as weighted average at a point and the size of the neighborhood that is assumed to influence the state of the material point is defined through the internal material length. Kröner [36] and Eringen and Edelen [37] applied the non-local theory for an elastic material. This theory was further developed and applied into continuum damage mechanics by the work of Pijauder-Cabot and co-workers [38]. The direct averaging procedure of the non-local models requires a lot of computational effort making these models inefficient to use.

Strain gradient theories are used as an approximation to the non-local models. The strain gradient theory approximates the non-local models by Taylor expanding the integral form that averages the strain field over the surrounding volume of a material point [39]. Strain gradient theories have been used to simulate a variety of material instabilities. Bammann and Aifantis [40, 41] and Aifantis [42, 43] applied the strain gradient theory to describe plastic instabilities including dislocation patterning and spatial characteristics of shear bands. Subsequent articles by Aifantis and co-workers [44, 45, 46, 47, 48] have shown the potential of using the gradient approach to a variety of material instability problems ranging from metal fatigue and polycrystal/soil shear banding to the failure of concrete. The gradient approach has also been extended to problems of size effect [49, 50, 51] when investigating such problems as micro-bending [52] and micro-torsion [49, 53]. Computational issues of the gradient theory for plasticity [54, 55, 51, 56], damage [38, 51, 57, 58], and coupled damage-plasticity [59, 39, 48] have been discussed extensively in the literature. Besson [60] provides a detailed review of the non-local methods used to solve the mesh dependence problems of the local damage models.

The chapter is organised as follows. Initially, the basic theory of CDM is provided. Then the non-local model developed to overcome the mesh dependency is presented. Following that, the steps followed for the implementation of the non-local model in ABAQUS using a VDFLUX subroutine are presented. Finally, a comparison between the local and the non-local models is provided using two benchmark tests.

3.2 Isotropic continuum damage mechanics theory

Damage models rely on an internal variable to characterise the degradation of the material due to defects, e.g. microcracks or microvoids. In order to understand the basis of defining the internal damage variable, first the one dimensional case is used to define the effective properties through a scalar damage variable. Figure 3.2 represents a continuum body where imperfections are present. The apparent (observed) stress applied to the body is $\sigma = F/A$, where F is the force applied over the area A. This body contains defects such as microvoids and microcracks, reducing the cross sectional area by A_d and the effective area, $\bar{A}$, is given by:

$$\bar{A} = A - A_d \tag{3.1}$$

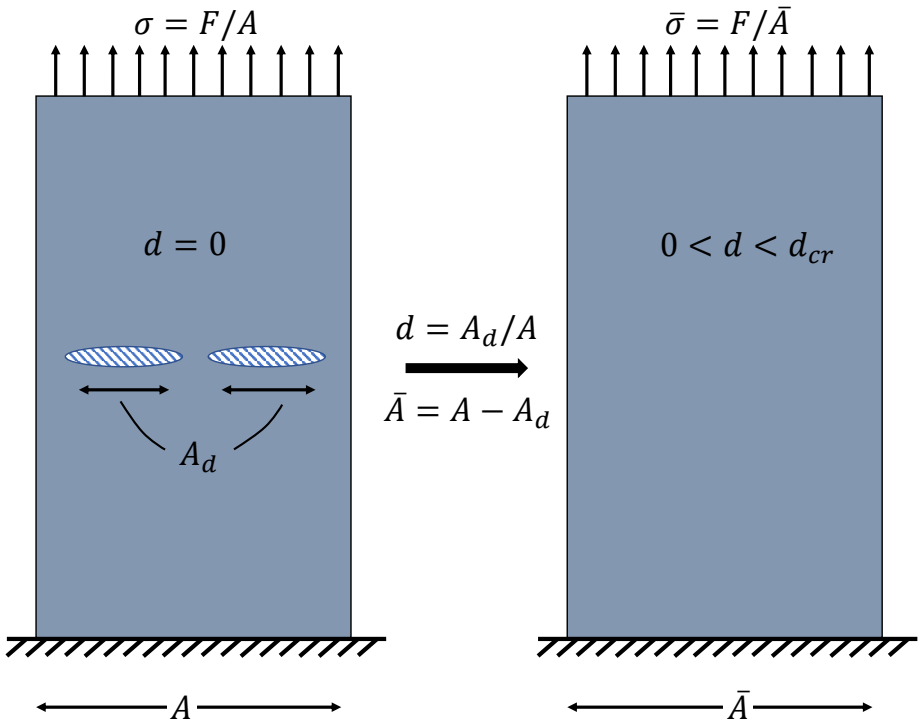

Figure 3.2: Continuum damage mechanics concept. Transition from real microstructure containing defects to a fictitious undamaged microstructure characterised by the damage variable d.

The effective undamaged material is defined through the equilibrium of forces that must exist between the damaged and the (fictitious) undamaged configuration:

$$F = \sigma A = \bar{\sigma}\bar{A} \tag{3.2}$$

So the apparent (observed) stress is calculated as:

$$\sigma = \frac{\bar{A}}{A}\bar{\sigma} = \frac{A - A_d}{A}\bar{\sigma} = (1 - \frac{A_d}{A})\bar{\sigma} \tag{3.3}$$

The damage amplitude for a given plane is defined through the scalar damage variable which is defined as the density defects and according to Kachanov et al. [61] can be written as:

$$d = \frac{A_d}{A} \tag{3.4}$$

The damage variable, d, for the undamaged material is $d = 0$ leading to $\bar{A} = A$. As soon as the damage initiates, the damage variable grows until the complete degradation of the material, which is characterised by the asymptotic limit $d = d_{cr}$ (usually $d_{cr} = 1$), where the effective area is reduced to zero.

For the simple case of an isotropic elastic material the effective stress is give by:

$$\bar{\sigma} = E\varepsilon \tag{3.5}$$

where E is the Young's modulus of the undamaged material. Combining Equations (3.3) and (3.5), it is evident that the apparent stress, σ, takes the following form:

$$\sigma = (1-d)E\varepsilon \tag{3.6}$$

Equation (3.6) describes how stresses are influenced by damage through the damage variable d. A damage evolution law is needed for the one dimensional problem presented so far to be complete. The damage evolution law relates the damage variable with the applied strain as:

$$d = g(\varepsilon_{eq}^{p}), \quad 0 \leq \mathrm{d} \leq d_{cr} \tag{3.7}$$

where function $g(\varepsilon_{eq}^{p})$ affects the softening part of the stress strain graph.

A qualitative stress-strain graph of an elastic-plastic material with and without damage is presented in Figure 3.3. Once the loading exceeds the yield stress, σ_y, of the material, plasticity takes place. Unloading from point **A** would result in an unloading path with an undamaged Young's modulus, E, leading to an equivalent plastic strain $\varepsilon_{eq,A}^{p}$. Damage starts at point **B** initiating the degradation of the Young's modulus. The damage onset equivalent plastic strain, $\varepsilon_{eq,i}^{p}$, is a model parameter which depends on the equivalent strain rate, $\dot{\varepsilon}_{eq}$, and the stress triaxiality, η. It is related to the strain where the shear bands become visible in the compression experiments [11], and are calculated following the methodology presented in section 3.3. The equivalent plastic strain at the damage onset is used in the damage evolution equation. After point **B** stresses start to decrease according to Equation (3.6) and the dashed line of $\bar{\sigma}$ represents the stress-strain response in the absence of damage. Damage parameter, d increases from $d = 0$ at the damage onset, until point **D** where the damage parameter reaches a critical value, $d = d_{cr}$, calculated from the damage evolution law corresponding to complete material failure (element deletion in the FE framework). The equivalent plastic strain at failure $\varepsilon_{eq,f}^{p}$ is calculated indirectly from the damage evolution law through the fracture energy, G_f, which is specified from the experimental data [11]. Figure 3.4a depicts the fracture energy parameter, which is calculated through a stress-displacement law, instead of a stress-strain law, after the damage initiation (blue area under the graph). In Figure 3.4a the displacements are linked to the equivalent strain through the characteristic length, l, presented in section 3.4, as $u_i = l\varepsilon_{eq,i}$ and $u_f = l\varepsilon_{eq,f}$. This methodology is followed by ABAQUS [17] to alleviate the mesh dependency during ductile damage and will be used in the current study as well. The way that the damage parameter, d, monotonically increases from $\varepsilon_{eq,i}^{p}$ to $\varepsilon_{eq,f}^{p}$ is determined by the damage evolution law. Unloading from point **C** (in the damaged

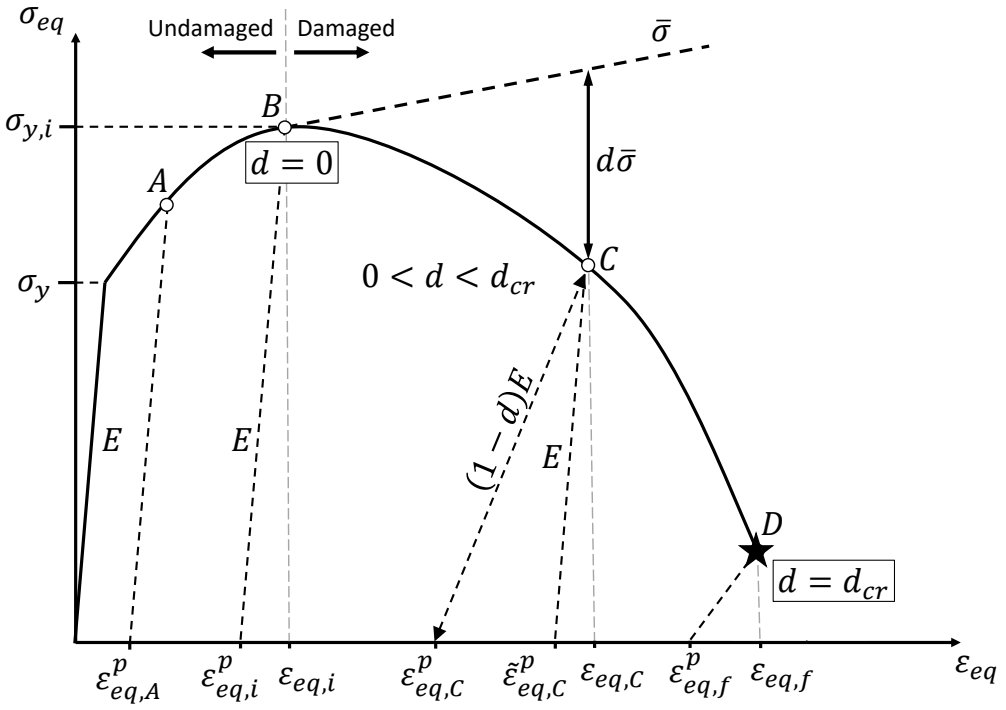

Figure 3.3: Qualitative graph of equivalent stress, σ_{eq}, versus equivalent strain, ε_{eq}, coupled with ductile damage [17].

state) would result in an equivalent plastic strain $\varepsilon^p_{eq,C}$ driven by an unloading modulus $(1-d)E$, instead of $\tilde{\varepsilon}^p_{eq,C}$ which represents the unloading in the case that damage is not considered.

A qualitative graph representing the damage evolution of the damage parameter d is shown in Figure 3.4b. Damage variable initiates for an equivalent plastic strain $\varepsilon_{eq,i}$ and before that is zero indicating no damage in the material. After damage initiation microcracks and microvoids are supposed to be formed in the microstructure and damage evolves in a linear way until complete failure is reached when $d = d_{cr}$.

These models are relatively simple and are often used to describe strain localisation phenomena that take place during failure. However, when the damage parameter depends only on the strain state, damage propagation through element deletion is expected to depend on the characteristic element size, implying mesh dependent results. This is a characteristic behavior of the local damage models, lacking to reliably predict the thickness of the strain localization band, leading to results that are highly dependent on the mesh density of the model. The strains tend to concentrate across a line of the shear band decreasing its thickness as the mesh becomes more refined. This is evident in the schematic force-displacement graph, where the response of the softening part is influenced by the mesh density (Figure 3.5).

Special care should be given to the loading unloading path of point **C** in Figure 3.3. When the material is deformed up to the strain $\varepsilon_{eq,C}$, this results in damage $d_1 = g(\varepsilon_{eq,C})$

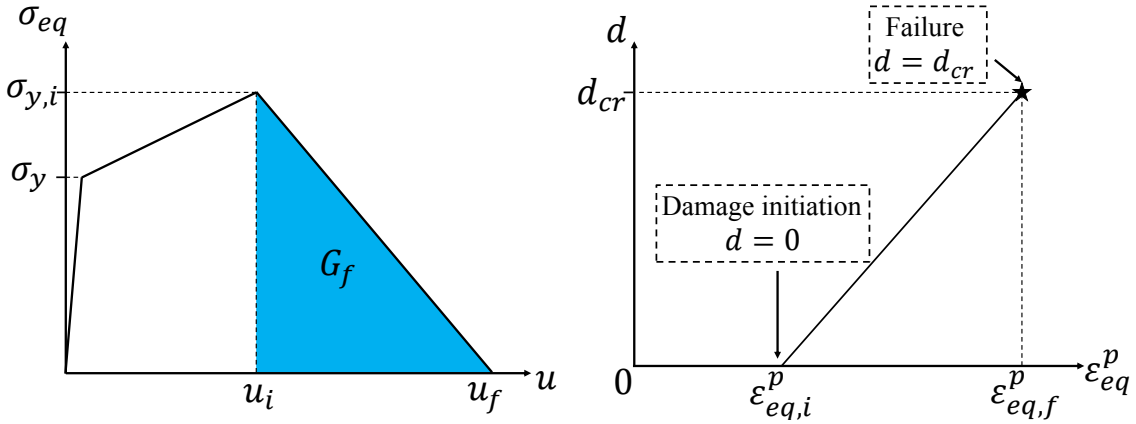

Figure 3.4: Qualitative graph for a single element in tension: (a) equivalent stress, σ_{eq} versus effective displacement, u, with the corresponding fracture energy, G_f depicted as the blue area under the graph, (b) linear evolution of damage variable d versus equivalent plastic strain ε^p_{eq}.

and the stresses decrease due to the degradation of the Young's modulus $E_1 = (1-d_1)E$. During unloading there is no evolution of the damage parameter and during reloading the damage parameter must continue from the highest strain reached in the strain history. To ensure that, an additional internal variable $\hat{\varepsilon}^p_{eq}$ is introduced that characterises the maximum strain reached in the material during loading up to a time t and is defined as:

$$\hat{\varepsilon}^p_{eq}(t) = \max\left\{\hat{\varepsilon}^p_{eq,i}, \max\left\{\varepsilon^p_{eq}(\tau) \mid 0 \leq \tau \leq t\right\}\right\} \tag{3.8}$$

Equation (3.8) introduces the additional material property, $\hat{\varepsilon}^p_{eq,i}$, which is the damage threshold and represents the strain at which the damage starts. The damage evolution of equation (3.7) is then rewritten as:

$$d = g(\hat{\varepsilon}^p_{eq}) \quad \text{with} \begin{cases} g(\hat{\varepsilon}^p_{eq}) = 0 & \text{if} \quad \hat{\varepsilon}^p_{eq} = \hat{\varepsilon}^p_{eq,i} \\ 0 < g(\hat{\varepsilon}^p_{eq}) \leq 1 & \text{if} \quad \hat{\varepsilon}^p_{eq} > \hat{\varepsilon}^p_{eq,i} \end{cases} \tag{3.9}$$

which ensures that the CDM law remains valid both for loading and unloading. An alternative approach to equation (3.8) is defining a loading function $f(\varepsilon^p_{eq}, \hat{\varepsilon}^p_{eq}) = \varepsilon^p_{eq} - \hat{\varepsilon}^p_{eq}$ and enforce the loading-unloading conditions in the Kuhn-Tucker form:

$$f \leq 0; \quad \dot{\hat{\varepsilon}}^p_{eq} \geq 0; \quad \dot{\hat{\varepsilon}}^p_{eq} f = 0 \tag{3.10}$$

The first condition indicates that $\hat{\varepsilon}^p_{eq}$ cannot be smaller than ε^p_{eq}, while the second condition restricts the $\hat{\varepsilon}^p_{eq}$ to only increase. The last condition of equation (3.10) implies that $\hat{\varepsilon}^p_{eq}$ can grow only if the current values of ε^p_{eq} and $\hat{\varepsilon}^p_{eq}$ are equal.

The theory presented so far can be easily transformed to the general three dimensional

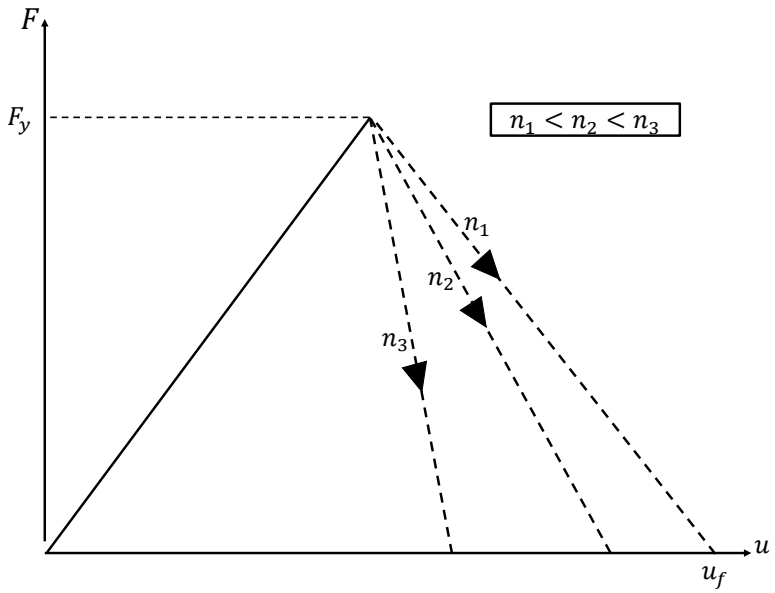

Figure 3.5: Force displacement graph for different n_i mesh densities.

case. The damage variable d is usually considered as a second order tensor, but in the current thesis isotropic damage is considered and the damage variable is chosen as scalar. The stress-stain relation is given as:

$$\boldsymbol{\sigma} = (1-d)\mathbb{C}\boldsymbol{\varepsilon} \tag{3.11}$$

where $\mathbb{C}$ is the fourth order stiffness tensor of the undamaged material, $\boldsymbol{\sigma}$ is the stress tensor and $\boldsymbol{\varepsilon}$ is the strain tensor. Equation (3.11) can be used to derive the effective constitutive equations of the damaged material by simply replacing the stress tensor $\boldsymbol{\sigma}$ by the effective stress tensor $\bar{\boldsymbol{\sigma}} = \frac{\boldsymbol{\sigma}}{(1-d)}$ in the constitutive equations presented in Chapter 2.

Similarly to the one dimensional case, a loading function in defined as:

$$f(\varepsilon^p_{eq}, \hat{\varepsilon}^p_{eq}) = \varepsilon^p_{eq}(\boldsymbol{\varepsilon}) - \hat{\varepsilon}^p_{eq} \tag{3.12}$$

The evolution function now depends on the strain vector $\boldsymbol{\varepsilon}$ and on the scalar variable $\hat{\varepsilon}^p_{eq}$. The scalar variable $\hat{\varepsilon}^p_{eq}$ can be interpreted in a similar way to the one dimensional case, as the largest equivalent plastic strain reached in the loading history. Equation (3.12) and the Kuhn-Tucker condition of Equation (3.10) define the problem for the general three dimensional case.

3.3 Estimation of the fracture strain

Before introducing the local damage theory, the estimation of the fracture strain of the solid chocolate from experimental data will be presented. Both compression and tension results obtained at different strain rates from uniaxial tests, are available from

a parallel PhD study [10], and will be used for the estimation of the fracture strain at the initiation of failure. The tensile and compressive experimental data are presented in Figure 3.6. It is evident that the chocolate experiences anisotropy in compression and tension and different fitting parameters of the Johnson-Cook model are needed to fit the two experiments. In the compression experimental results, presented in detail in the paper of Bikos et al. [11], shear bands were present during the experiment indicating clearly the initiation of damage. In the stress-strain compression curves there is a clear elastic part followed by plasticity until a maximum value of stress (red hexagons in Figure 3.6). The strain at the initiation of fracture corresponds to the point of maximum stress followed by softening. As it will be presented in section 3.4 the equivalent plastic strain is needed in the damage evolution law. The equivalent plastic strain, for the different strain rates, is calculated as:

$$\varepsilon^{p}_{eq,i} = \varepsilon_{eq,i} - \frac{\sigma_{eq,i}}{E} \tag{3.13}$$

with the index i indicating the damage initiation and the values of $\varepsilon_{eq,i}$ and $\sigma_{eq,i}$ correspond to the red hexagonal marks of Figure 3.6. The values of the equivalent plastic strain at the initiation of failure are given in Table 3.1.

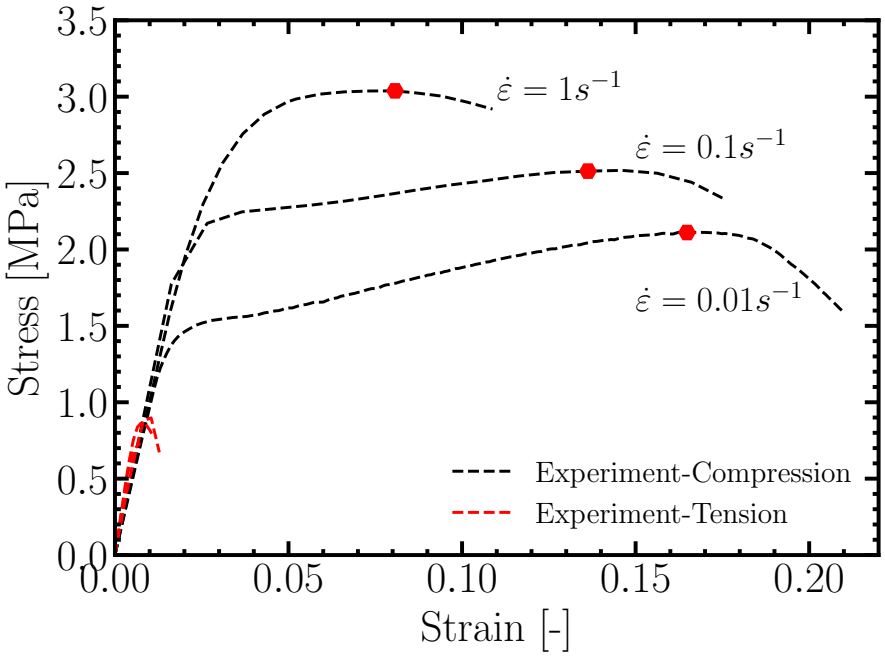

Figure 3.6: Comparison between compression and tension experimental data. The red hexagons indicate the initiation of fracture. Data adopted from the study of Bikos et al. [11]

At this point it is worth noting that, due to the nature of chocolate that imposed difficulties in creating samples for tension experiments, an assumption is made for the estimation of the fracture strain at the fracture initiation. The fact that, shear bands were visible during the compression experiment (Figure 3.7), and appear at 45° allows the assumption

that the premature failure is caused due to tension. For this reason the equivalent plastic stain at failure initiation, shown in table 3.1 and calculated from the compression data of Figure 3.6, will be assumed to be associated to tension.

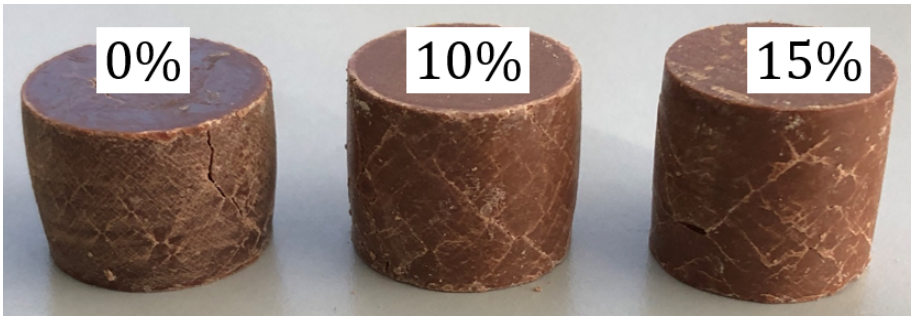

Figure 3.7: Fractured specimens after monotonic compression experiments at $\dot{\varepsilon} = 1\,\mathrm{s}^{-1}$ for different micro-aeration levels. The white marks represent the cracks at 45°. Adapted from [10].

Table 3.1: Equivalent plastic strain at damage onset for different strain rates for the solid chocolate samples. Values calculated from compression experiments, but used to initiate damage in tension.

$\varepsilon^p_{eq,i}$	$\dot{\varepsilon}(\mathrm{s}^{-1})$	η
0.152	0.01	1/3
0.12	0.1	1/3
0.05	1	1/3

Similar approach has been adopted in the literature and especially in studies regarding the fracture of cement and metallic glass, both of which exhibit failure anisotropy in compression and tension, similar to the chocolate [62]. The equivalent plastic strain at the end of failure is calculated through the damage evolution law that is driven from the fracture toughness, G_f, as it will be discussed in detail in section 3.4.

3.4 Local damage evolution law

As presented in section 3.2, The evolution of the scalar variable, d, is dictated by the function $g(\varepsilon^p_{eq})$. According to Wu et al. [63], three main damage evolution models exist in the literature: micromechanically motivated porous plasticity models [64, 65, 66, 67], CDM models derived from thermodynamic considerations [61, 68], and macroscopic phenomenological strain-based failure models, which consider a stress-state-dependent strain to failure which is influenced by stress triaxiality and the Lode angle parameter [69, 70]. Since, little information is known for the mechanism causing the fracture of chocolate, the latter approach is adopted in this thesis, taking into consideration only the

effect of the stress triaxiality. The stress triaxiality, which is a dimensionless parameter, is defined as the ratio of the mean stress to the equivalent stress:

$$\eta = \frac{\sigma_m}{\sigma_{eq}} = \frac{I_1}{\sqrt{3J_2}} \tag{3.14}$$

with the two invariants of the stress tensor and its deviatoric part respectively calculated as:

$$I_1 = \frac{1}{3}\mathrm{tr}[\boldsymbol{\sigma}] \tag{3.15}$$

$$J_2 = \frac{1}{2}\boldsymbol{S} : \boldsymbol{S} \tag{3.16}$$

The von Mises equivalent stress is defined through the second deviatoric stress invariant as:

$$\sigma_{eq} = \sqrt{3J_2} \tag{3.17}$$

A simplified version of the modified damage model of Bai and Wierzbicki [71] is adopted. For a direct comparison with the built-in ductile damage model of ABAQUS, the same linear dissipation-energy-based damage evolution law is applied [17]:

$$\dot{d} = \frac{\sigma_{y,i} l}{2G_f}\dot{\varepsilon}^p_{eq} \tag{3.18}$$

where $\sigma_{y,i}$ is the yield stress at the damage onset, l is an internal length and G_f is the fracture energy with dimensions of energy per unit surface area [$\mathrm{J/m^2}$]. Complete damage is achieved when the damage parameter d reaches a critical value given by:

$$d_{cr} = \int_{\varepsilon^p_{eq,i}}^{\varepsilon^p_{eq,f}} \frac{\sigma_{y,i} l}{2G_f}\, \mathrm{d}\varepsilon^p_{eq} \tag{3.19}$$

Overall the damage evolution law is controlled by a damage initiation equivalent plastic strain and an energy based evolution law, and including the triaxiality parameter it is written as:

$$d = \begin{cases} 0; & \varepsilon^p_{eq} \leq \varepsilon^p_{eq,i} \\ \int_{\varepsilon^p_{eq,i}}^{\varepsilon^p_{eq,f}} \frac{\sigma_{y,i} l}{2G_f}\, \mathrm{d}\varepsilon^p_{eq}; & \varepsilon^p_{eq,i} < \varepsilon^p_{eq} < \varepsilon^p_{eq,f} \quad \text{and} \quad \eta \geq \eta_{\mathrm{cr}} \\ d_{cr} & \varepsilon^p_{eq} = \varepsilon^p_{eq,f} \end{cases} \tag{3.20}$$

The critical value of the damage parameter d_{cr} needs to be calibrated against the experimental data. The calibration methodology used by Lian et al. [72] is also applied in the present study. The fracture toughness, G_f, was calculated from single edge notched bending (SENB) tests in three different speeds of $0.02\,\mathrm{mm\,s^{-1}}$, $0.2\,\mathrm{mm\,s^{-1}}$ and $2\,\mathrm{mm\,s^{-1}}$ and a detailed description is provided in the study of Bikos et al. [11]. The G_f value of

the non aerated samples is in the range 8-12 $\mathrm{J/m^2}$ for the different speeds and an average value of $10\,\mathrm{J/m^2}$ is adopted for the damage evolution law of equation (3.20). The latter together with the equivalent plastic strain at the onset of damage, calculated in section 3.13 from the experimental data for different strain rates, provide a direct connection to material properties that are independently measured and used to define damage evolution.

The influence of triaxiality on the damage evolution should be considered as well, since during chewing there are multiple stress states [73]. The damage onset equivalent plastic strain should be related to the respective stress state. The experimental data available for the compression experiments of the non aerated chocolate samples are used for the calculation of the onset equivalent plastic strain in tension ($\eta = 1/3$), as presented in section 3.3. Although, data for shear failure strain are not available, 45° shear bands were visible in the compression experiments [11] and the damage criterion will be extended to include the equivalent plastic strain in shear, $\varepsilon^{p,s}_{eq,i}$, for each strain rate $\dot{\varepsilon}$. The methodology of section 3.3 will be used in a similar manner, such that damage onset occurs for the maximum principal strain, ε_1. Therefore, the equivalent plastic strain in shear ($\eta = 0$) is approximated using equation (3.21) substituting $\varepsilon^p_2 = 0$ and $\varepsilon^p_1 = -\varepsilon^p_3 = \varepsilon^{p,t}_{eq,i}$, with $\varepsilon^{p,t}_{eq,i}$ representing the equivalent plastic strain at the damage onset in tension (presented already in table 3.1). The correlation between the equivalent plastic strain in shear at the damage onset $\varepsilon^{p,s}_{eq,i}$, and the equivalent plastic strain in tension at the damage onset is then calculated as $\varepsilon^{p,s}_{eq,i} = \frac{2}{\sqrt{3}}\varepsilon^{p,t}_{eq,i}$. The equivalent plastic strains at the damage onset for different strain rates and stress triaxiality values are shown in Table 3.2.

$$\varepsilon^p_{eq} = \frac{\sqrt{2}}{3}\left[\sqrt{\left(\varepsilon^p_1 - \varepsilon^p_2\right)^2 + \left(\varepsilon^p_2 - \varepsilon^p_3\right)^2 + \left(\varepsilon^p_3 - \varepsilon^p_1\right)^2}\right] \tag{3.21}$$

Table 3.2: Equivalent plastic strain at damage onset for different stress states and strain rates.

$\varepsilon^p_{eq,i}$	η	$\dot{\varepsilon}(\mathrm{s^{-1}})$
0.175	0	0.01
0.152	1/3	0.01
0.134	0	0.1
0.12	1/3	0.1
0.058	0	1
0.05	1/3	1

It is worth mentioning that the fracture toughness value was acquired from SENB experiments which represent a mode *I* fracture. Since the damage will be applied in the more general chewing simulations (shown in chapter 5), where multiple fracture modes take place, the assumption of fracture toughness isotropy should be considered. In the study of Skamniotis et al. [12] a detailed methodology is provided where the influence that stress triaxiality has on the fracture toughness is considered by calculating the ra-

tio of the maximum principal stress and maximum principal strain at the damage onset. This is implemented in the FE simulation through a VUSDFLD subroutine. This approach was applied to model the behaviour of a starch based food with a mode *I* fracture toughness equal to $G_f^I = 930\,\mathrm{J/m^2}$ and the mode *II* fracture toughness is approximated as $G_f^{II} = \frac{2}{\sqrt{3}} G_f^I = 1820\,\mathrm{J/m^2}$. Comparing the fracture toughness values of the starch based food with the respective ones of the chocolate, it is evident that the energy dissipation is one order of magnitude higher for the starch based food, playing a crucial role in the damage behavior. Since the fracture toughness for chocolate has a relatively low value, an isotropic fracture toughness behaviour is assumed and more care is given on the implementation of the non-local damage law though the calculation of the non-local equivalent plastic strain (shown in section 3.5).

According to Skamniotis et al. [74] the element deletion for compressive states ($\eta = -1/3$) leads to unreasonably increased element removal from the FE simulation. This is crucial in the FE simulation of the first bite, since the mass of the fragmented food at the end of the simulation should be close to the initial mass before the fragmentation [73]. To avoid this phenomenon, the initiation of fracture is not allowed for compressive stress states and an additional condition is added allowing damage to initiate and evolve for $\eta \geq 0$ ($\eta_{cr} = 0$ in equation (3.20)). This is also depicted in Figure 3.8.

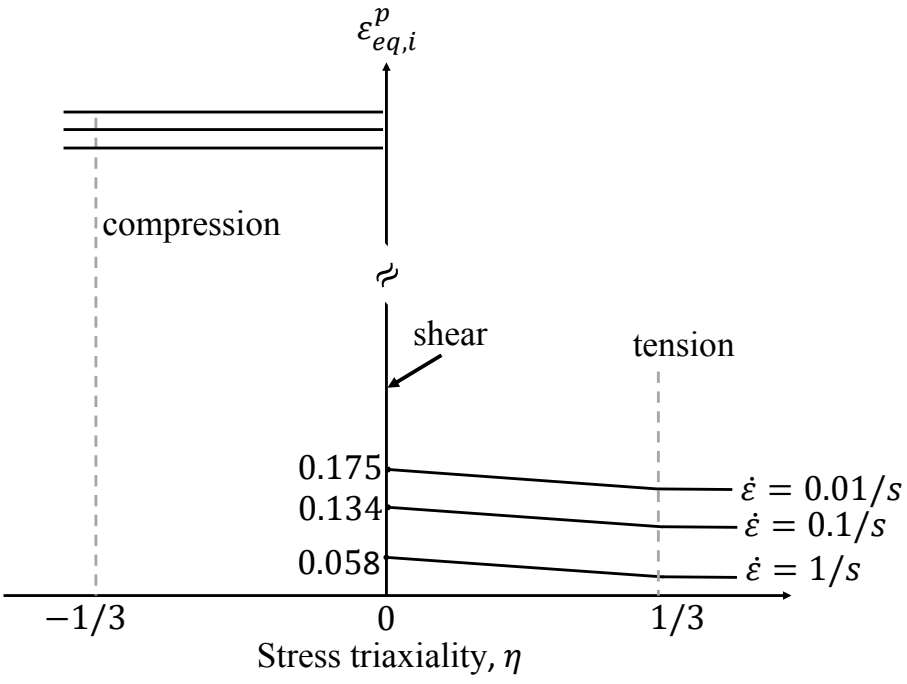

Figure 3.8: Equivalent plastic strain at damage onset, $\varepsilon^p_{eq,i}$ versus different triaxiality values, η. The y-axis has been broken to indicate that the equivalent plastic strain in compression is intentionally selected much higher than the respective values in shear and tension to avoid unreasonable element removal.

The damage law of equation (3.20) needs to be calibrated against the parameters d_{cr} and l. These two parameters are related with the damage propagation and can be cal-

ibrated by fitting the stress-strain curves from simulations to the experimental data. It is worth noting that existing studies in the literature use the damage evolution law of equation (3.4) and the fracture toughness is used as a calibration parameter [63] or it is normalised to the element length and written as a material parameter with dimensions of energy per unit volume [75]. In the present study, the fracture toughness has a physical meaning and is not used as a calibration parameter. A single 3D element was subjected to tension and is used for the calibration of the d_{cr} and l. The experimental and numerical stress-strain curves are compared in Figures 3.9a and 3.9b. The constitutive model is in good agreement with the experimental curve until the damage initiation and softening. The numerical stress-strain curves for different l values and $d_{cr} = 1$ are shown in Figure 3.9a and a value of $l = 0.08\,\text{mm}$ predicts well the softening branch of the curve. Afterwards, the same simulations were repeated keeping constant the already calibrated value of l and changing the value of the d_{cr} (Figure 3.9b), which controls the equivalent plastic strain at failure (element deletion). A value of $d_{cr} = 0.1$ is considered sufficient for the proper calibration. Both values are calibrated for the highest stain rate, $\dot{\varepsilon} = 1\,\text{s}^{-1}$, that was experimentally tested, since as it will be shown in chapter 5, the chewing rates existing in the mouth during first bite are even higher than the available experimental data. The FE results for $\dot{\varepsilon} = 0.01\,\text{s}^{-1}$ and $0.1\,\text{s}^{-1}$ strain rates are compared with the experimental data and there is a good fit, although the parameters l and d_{cr} are calibrated using the $\dot{\varepsilon} = 1\,\text{s}^{-1}$ strain rate.

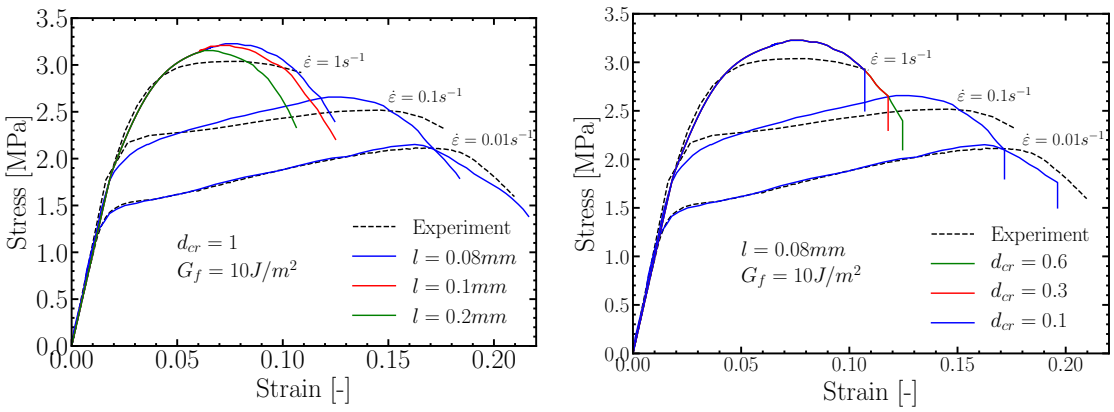

Figure 3.9: Comparison between experimental [11] data and FE stress-strain results. For the numerical results, the VUMAT has been coupled with the local damage model for a single element in tension at three strain rates, for (a) the calibration of parameter l (b) the calibration of parameter d_{cr}.

3.5 Non-local damage model

The CDM model presented so far belongs to the so called local damage models. The mesh dependency that is present when using this models is an important problem for the simulation of the first bite, since the simulation results aim to provide a reliable tool to study the fragmentation of food. The mesh dependency of the results is more intense in the softening region of the stress-strain graph. The main reason is that the mathematical equations that describe the problem lose ellipticity and the boundary value problem becomes ill-posed [34]. To overcome this difficulty, the local CDM model needs to be extended, introducing an internal characteristic length that is related to the material microstructure, such as the grain size in polycrystals or the void size or spacing in porous materials [75]. In the following sections the non-local equivalent plastic strain, e^p_{eq}, will be calculated, the additional equations needed to be solved will be presented and the non-local version of damage evolution law of section 3.4 will be shown. It is worth mentioning that the non-local equivalent plastic strain is usually represented as $\bar{\varepsilon}^p_{eq}$. In this thesis, $\bar{\varepsilon}$ symbol is used for the macroscopic strain in the micromechanical analysis which is presented in chapter 4. To avoid confusion, the non-local equivalent plastic stain will be represented as e^p_{eq}, similar to the work of Papadioti et al. [75], as opposed to the local equivalent plastic strain ε^p_{eq}.

3.5.1 Non-local theory

The non-local approach introduces an internal characteristic material length, in addition to the internal length of section 3.4, that accounts for the microstructural interaction of the defects around this material point. Figure 3.10 shows a material point $\mathbf{x}$ and a close up view around this point, including the defects that are present in the area around the point. The internal characteristic material length, l_{ch}, can be physically interpreted as the radius of the circle (or sphere for the three dimensional case) over which the plastic equivalent strain is averaged, taking into account how the material points included in this fictitious area are influenced by damage. The non-local equivalent plastic strain e^p_{eq} is defined as a weighted average of the local equivalent plastic strain ε^p_{eq} over a volume V around the material point $\boldsymbol{x}$ at a distance $\boldsymbol{s}$, and is calculated as:

$$e^p_{eq} = \frac{1}{V}\int_V \varepsilon^p_{eq}(\boldsymbol{x}+\boldsymbol{s})dV \tag{3.22}$$

Equation (3.22) can be generalised for anisotropic materials by including a weighting function, $h(s)$, in the integral. In the current thesis, the weighting function will be considered to be the identity tensor, since the chocolate is considered to be isotropic.

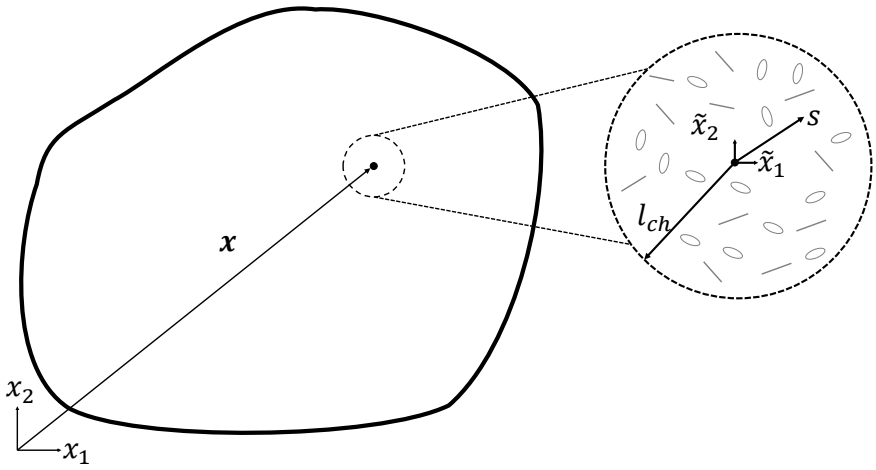

Figure 3.10: The internal characteristic material length, l_{ch}, introduces the effect that the surrounding microstructural defects, around a material point **x**, have on the mechanical properties.

3.5.2 Explicit gradient formulation

Following Peerlings et al. [76] and Engelen et al. [77] equation (3.22) is approximated by initially Taylor expanding the local equivalent plastic strain as:

$$\varepsilon^p_{eq}(\boldsymbol{x}+\boldsymbol{s}) \approx \varepsilon^p_{eq} + \nabla\varepsilon^p_{eq}\cdot\boldsymbol{s} + \frac{1}{2!}\nabla^{(2)}\varepsilon^p_{eq}\cdot\boldsymbol{s}\otimes\boldsymbol{s} + \cdots \tag{3.23}$$

Substituting equation (3.23) into (3.22) results in the strain gradient formulation [78]:

$$e^p_{eq} = \varepsilon^p_{eq} + c_2\nabla^{(2)}\varepsilon^p_{eq} + c_4\nabla^{(4)}\varepsilon^p_{eq} + \cdots \tag{3.24}$$

where $\nabla^{(i)}$ represents the i-th order gradient operator and $c_2 = \frac{1}{2}l^2_{ch}, c_4 = \frac{1}{8}l^4_{ch}$. The odd derivative terms of equation (3.24) vanish as a result of the isotropy of the weighting function [76] and by neglecting terms of fourth order and higher:

$$e^p_{eq} = \varepsilon^p_{eq} + c_2\nabla^{(2)}\varepsilon^p_{eq} \quad \text{in} \quad V \tag{3.25}$$

with V representing the volume occupied by the body. Equation (3.25) explicitly expresses the non-local equivalent plastic strain in terms of the local equivalent plastic strain and its second derivatives. The steps presented to approximate equation (3.22) through the explicit formulation of equation (3.25) describe the transition from a non-local to a gradient model.

3.5.3 Implicit gradient formulation

Equation (3.25) can be further analysed by applying a Laplacian operator and multiply by c_2. If the result is subtracted from equation (3.25), and higher order terms are neglected, the following equation is derived:

$$e^p_{eq} - c\nabla^{(2)} e^p_{eq} = \varepsilon^p_{eq} \quad \text{in} \quad V \tag{3.26}$$

where the index of c_2 has been dropped. Equation (3.26) is a Helmhotz type equation and a boundary condition must be provided in order to fix the solution. As proposed by Peerlings et al. [76], the following natural boundary condition is introduced and solved together with equation (3.26).

$$\frac{\partial e^p_{eq}}{\partial n} \equiv \mathbf{n} \cdot \nabla e^p_{eq} = 0 \quad \text{on} \quad \partial V \tag{3.27}$$

where $\mathbf{n}$ is the unit outward normal vector to the surface ∂V. Equation (3.26) defines the non-local equivalent plastic strain implicitly in terms of the local plastic strain and together with the boundary condition of equation (3.27) formulate the boundary value problem that needs to be solved. The methodology followed for the implementation in ABAQUS/Explicit is presented in section 3.5.4.

The approximation of the non-local equation in either the explicit or implicit form in known as the gradient plasticity formulations. Despite the efficiency of the gradient plasticity models, a unified interpretation of the physical meaning of the internal length scale and a direct link with the material microstructure is still missing [79]. The internal characteristic length scale is usually implemented in the model as another parameter calibrated through experimental data. Table 3.3 presents a range of length scales found in the literature.

Table 3.3: Internal length scales reported in the literature for different materials [80].

Authors	Material	Internal characteristic length l_{ch}
Nix & Gao [81]	Cu	5.84 μm
Shotriya et al. [82]	Al	5.6 μm
Ro et al. [83]	Al2024	0.2 μm
Guo et al. [84]	Cu	85.21 μm
Iliev et al. [85]	In	93.34 μm

3.5.4 Implementation to ABAQUS through VDFLUX subroutine

The detailed implementation of the additional non-local equations withing the FE framework and the solution for the displacement field **u(x)** and the non-local equivalent

plastic strain , $e^p_{eq}(\mathbf{x})$, requires the generation of user elements through the VUEL subroutine of ABAQUS for the Explicit solver. A detailed analysis of this approach can be found in the studies of Mediavilla et al. [86] and Papadioti et al. [75].

In the current thesis the methodology developed by Seupel et al. [87] and also applied by Korsunsky [88] for the estimation of the residual stresses and by Papadioti et al. [75] in the ABAQUS/Explicit solver will be presented. According to this methodology, the similarities between equation (3.26) and the transient heat transfer equation for isotropic materials can be used to solve for the non-local equivalent plastic strain using a dynamic temperature displacement analysis step. The transient heat transfer equation is given by:

$$k\nabla^{(2)}T + r(\Delta\boldsymbol{\varepsilon}, T) = \rho c\dot{T} \tag{3.28}$$

where c is the specific heat, T is the temperature, k is the thermal conductivity, r is the heat supply per unit volume, $\Delta\boldsymbol{\varepsilon}$ is a strain increment [17] and ρ is the density.

The transient heat transfer equation (3.28) is already implemented in the VDFLUX subroutine which can be coupled with the constitutive equations in the VUMAT as this presented in chapter 2. Comparing equations (3.26) and (3.28) there is a direct correlation between the non-local equivalent plastic strain and the temperature. It is, then, possible to use the VDFLUX subroutine, to solve the non-local problem, by adjusting the following parameters:

$$T \leftrightarrow e^p_{eq}, \quad k \leftrightarrow \frac{1}{2}l^2_{ch}, \quad r(\Delta\boldsymbol{\varepsilon}, T) \leftrightarrow \varepsilon^p_{eq} - e^p_{eq} \tag{3.29}$$

To overcome the limitation that the heat supply, r, cannot be defined in the VUMAT, the command *DFLUX ALLEL, BFNU is added to the loading section in the input file before the analysis set to run [75]. ALLEL is a set that contains all the elements in the mesh and BFNU (Body Flux Non Uniform) allows for a user defined heat supply r [17]. The VDFLUX is modified as $r = \varepsilon^p_{eq} - e^p_{eq}$, with e^p_{eq} defined as the temperature and ε^p_{eq} passed from the VUMAT via a user introduced common block. The VDFLUX subroutine is provided in appendix A.2.

The term on the right hand side of equation (3.28) should be chosen in order to be small. The term $\rho c\dot{e^p}_{eq}$ (temperature is the non-local equivalent plastic strain) depends on the density, which is a material property, the strain rate and the specific heat. From these variables only the specific heat has no physical meaning for the simulation and has to be chosen in order to minimise the right hand side term of equation (3.28). At this point it should be considered that the minimum time increment, that ensures stability, depends on the specific heat according to:

$$\Delta t > \frac{\rho c}{6k}\Delta\ell^2_{el} \tag{3.30}$$

where Δt is the time increment and $\Delta\ell_{el}$ is the size of the element. It is evident that the

choice of the specific heat influences the time step and a very small number will result in a large number of increments. In order to calculate the appropriate specific heat value, the approach of Papadioti et al. [75] is applied, according to which, the spatial uniform solution is considered, where $\nabla^2 T = \nabla^2 e^p_{eq} = 0$, leading to $\varepsilon^p_{eq} - e^p_{eq} = \rho c \dot{e}^p_{eq}$. The exact solution is $\varepsilon^p_{eq} = e^p_{eq}$ and the error is given by $\rho c \dot{e^p}$ which should be minimised according to:

$$\rho c \dot{e}^p_{eq} < \text{TOL} \tag{3.31}$$

where $\text{TOL} < 10^{-4}$ is a reasonable value for simulations where the elastic strain rates are small [75]. Therefore, it should be clarified that the specific heat does not have any physical meaning, but it is selected in order to satisfy equation (3.31), taking into account the material density and the applied strain rate.

3.5.5 Non-local damage evolution law

The non-local damage evolution is derived from the local damage evolution law (equation (3.20)), by directly replacing the equivalent plastic strain with the non-local equivalent plastic strain. Therefore, equation (3.20) is rewritten as:

$$d = \begin{cases} 0; & e^p_{eq} \leq e^p_{eq,i} \\ \int_{e^p_{eq,i}}^{e^p_{eq,f}} \frac{\sigma_{y,i} l}{2G_f} \, \mathrm{d}e^p_{eq}; & e^p_{eq,i} < e^p_{eq} < e^p_{eq,f} \quad \text{and} \quad \eta \geq \eta_{\text{cr}} \\ d_{cr} & e^p_{eq} = e^p_{eq,f} \end{cases} \tag{3.32}$$

At this point, it is worth noting that the internal length, l, should not be confused with the internal characteristic length, l_{ch}. The internal length is a parameter in the damage evolution law that is calibrated against the experimental data to capture the softening branch of the stress strain graph of Figure 3.9a. The internal characteristic length is introduced in the model to calculate the non-local equivalent plastic strain, e^p_{eq}, and the physical meaning is related with the radius around a material point that is taken into account in the calculation of the integral of equation (3.22). The local damage model is derived for $l_{ch} = 0$, since for this value $e^p_{eq} = \varepsilon^p_{eq}$.

3.6 Benchmark tests - numerical examples

To demonstrate the efficiency of the non-local damage model, two examples of shear band formation in a plane strain bar with geometric non linearity (Figure 3.11a) and a plane strain bar with material imperfection (Figure 3.11b) will be presented. The objective of this study is to describe the numerical implementation of the constitutive model in two simplified geometries using the same material and damage properties as those used in the more complicated first bite simulation. All the material properties are listed in Table

3.4. All simulations were conducted for a strain rate $\dot{\varepsilon} = 1\,\mathrm{s}^{-1}$, and taking into account that the material density is $\rho = 1\,\mathrm{kg\,m}^{-3}$, the specific heat is chosen as $c = 10^{-4}\,\mathrm{s}/(\mathrm{kg}/\mathrm{m}^3)$, in order to satisfy the criterion of equation (3.31). The geometries are subjected to tension to aid the shear band formation and four-node bilinear displacement and temperature, reduced integration with hourglass control (CPE4RT) elements are used. It is worth reminding that the elements used contain temperature as an additional degree of freedom, since the step that is used is a dynamic temperature-displacement step for the implementation of the non-local damage through the VDFLUX subroutine. In the following section, the FE results, comparing the non-local and the local damage law, will be presented. The local damage law is retrieved for $l_{ch} = 0$, whereas the internal characteristic length was selected as $l_{ch} = 0.1\,\mathrm{mm}$. This value was chosen, so that the shear band width remains constant while the mesh is refined.

Table 3.4: Material properties for the FE simulations of the benchmark tests. The internal characteristic length is $l_{ch} = 0.1\,\mathrm{mm}$.

Parameter	**Value**
Density, ρ [$\mathrm{kg\,m}^{-3}$]	1
Elastic modulus, E [MPa]	100
Poisson's ratio, ν [-]	0.49
A [MPa]	1.35
B [MPa]	3.5
C [-]	0.05
n [-]	0.8
$\dot{\varepsilon}$ [s^{-1}]	0.01
internal length, l [mm]	0.08
d_{cr}	0.1
specific heat, c [$\mathrm{s}/(\mathrm{kg}/\mathrm{m}^3)$]	10^{-4}

3.6.1 Tension of a bar with geometrical imperfection

The geometry of Figure 3.11a is used to demonstrate the shear band formation due to a geometry non linearity. The damage evolution law is applied and the local ($l_{ch} = 0$) and the non-local case are compared. Figure 3.12 depicts the shear band formation for two different mesh densities, 250 and 3800 elements. The contour plot represents the normalised damage variable (d/d_{cr}) for the local case ($l_{ch} = 0$ and $\varepsilon^p_{eq} = e^p_{eq}$). The shear band width tends to localise into a thin line as the mesh becomes more refined. In addition, as the shear band becomes thinner the damage variable increases. This simulation illustrates how mesh size influences the calculation of the damage variable, potentially leading to unreliable fragmentation results when applied to the macroscopic FE simulation of the first bite.

Therefore, the same simulation was repeated taking into account the non-local equiv-

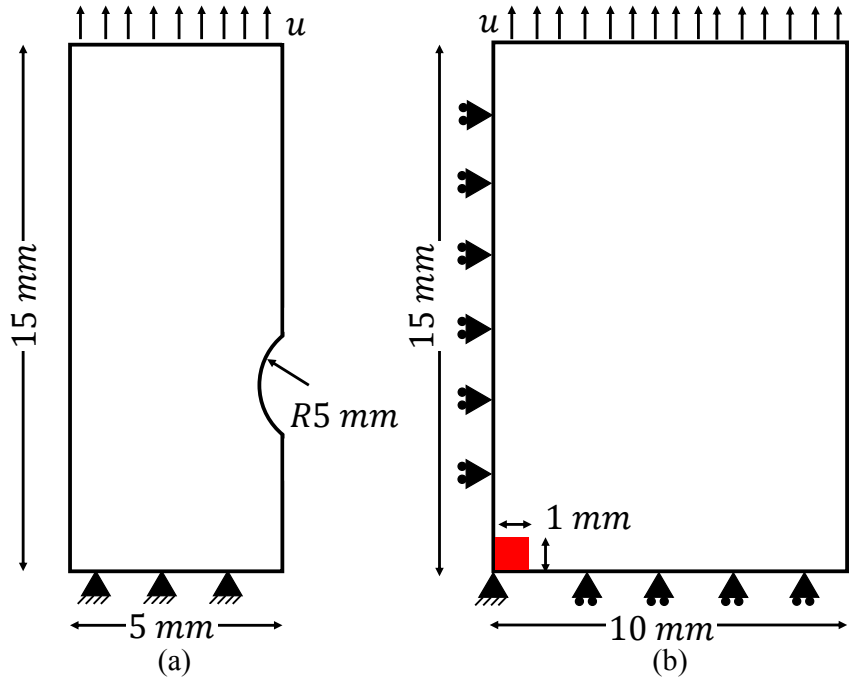

Figure 3.11: Geometries with induced shear band formation to comparison between the local and the non-local damage model. Shear band due to (a) geometric non-linearity [87] and (b) material imperfection at the lower left corner of the the geometry [75].

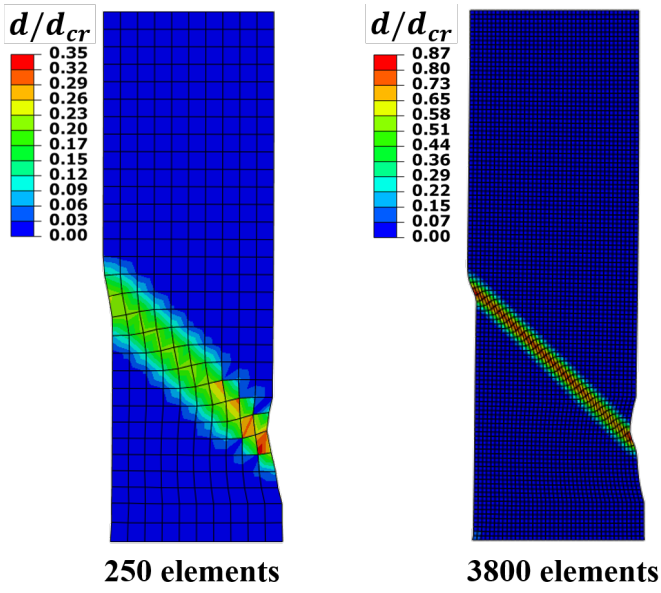

Figure 3.12: Shear band formation due to geometry non linearity for different mesh densities. The shear band width decreases and the normalised damage parameter increases with mesh refinement. Two different mesh densities are depicted, 250 and 3800 elements.

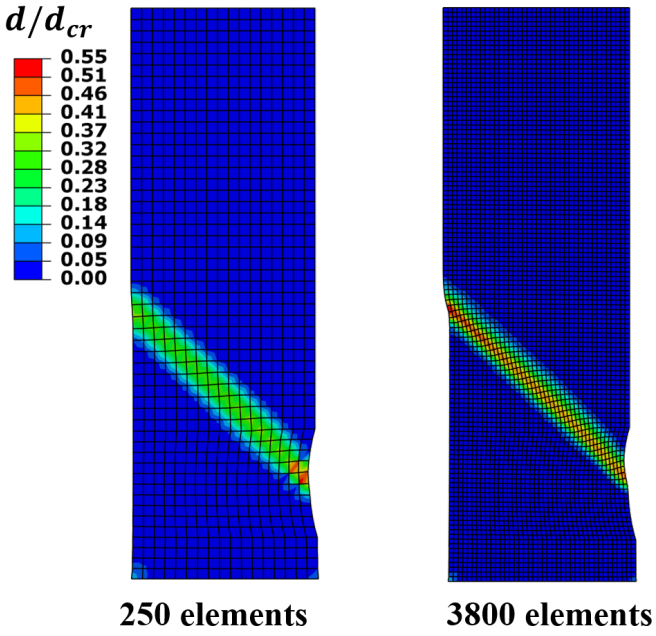

Figure 3.13: Contour plot of the normalised damage parameter using the non-local damage model. Two different mesh densities are depicted, 250 and 3800 elements.

alent plastic strain in the damage evolution law. The results of Figure 3.13 show that the shear band thickness is not affected by the mesh size, and indicates that the non-local damage model is efficient, can produce reliable results and can be confidently applied in the macromechanical simulation of the first bite. A comparison between the local and non-local model is also provided in Figure 3.14 where the force displacement curve is plotted. Until the damage initiation the two models have identical behaviour. As soon as softening starts, the local damage model provides softening branches that are mesh dependent, whereas the non-local model is consistent for different mesh refinements.

3.6.2 Shear band due to material imperfection

Figure 3.11b depicts a material imperfection that triggers the non-uniform deformation in the specimen leading to the formation of a shear band. The imperfection at the lower left part of the specimen has a square shape with side length of 1 mm and yield point 98% less that the rest of the matrix. Due to symmetry, only one quarter of the specimen is simulated and symmetric boundary conditions are applied on the lower and left surfaces.

Results are presented for both the local and the non-local damage models. Figure 3.15 shows the shear band formation initiated from the material imperfection. Two different mesh densities are presented for 247 and 3836 elements. A similar trend with the results presented using the geometric imperfection is observed. Although, the initiation at the onset of localization is captured correctly, the shear band tends to localise in a plane and

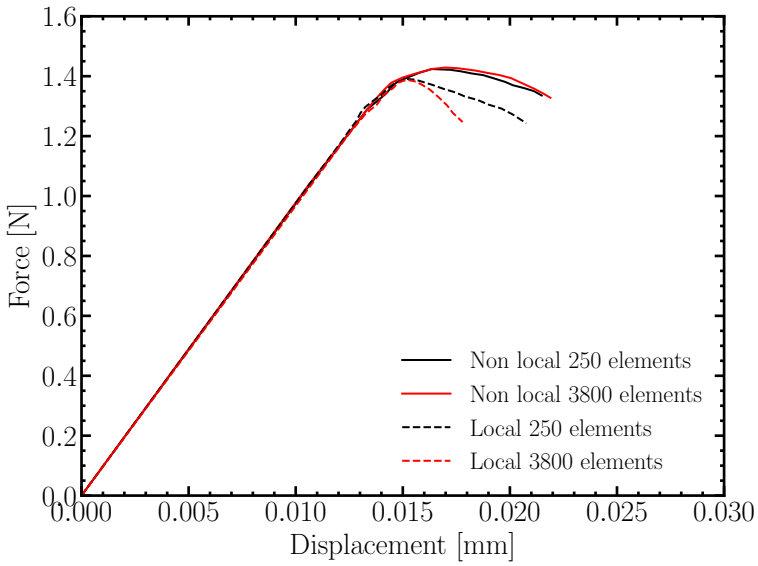

Figure 3.14: Force displacement curves comparing the local (dashed lines) and the non-local (continuous lines) damage evolution law for different mesh densities.

the normalised damage parameter increases as the mesh becomes more refined. Figure 3.16 shows contour plots of the normalised damage parameter for the non-local model. The width of the shear band is constant for the different mesh densities, implying that the non-local damage law restores the ellipticity in the constitutive equations and the solution is continuous [89].

3.7 Conclusions

In the present chapter the damage evolution law was presented. Initially, the general theory of continuum damage mechanics was presented and the local damage evolution law based on a linear dissipation energy law was applied. Afterwards, the mesh dependency problem of the local damage models was alleviated though the implementation of the non-local damage models. A new internal characteristic length scale was introduced in the model which takes into account the contribution of the material points in the neighborhood of a material point that damage has initiated. Explicit and implicit gradient formulations of the non-local model were presented and the similarities of the latter with the transient heat transfer equation made possible the direct implementation of the implicit gradient formulation into ABAQUS/Explicit through a VDFLUX subroutine. The methodology for coupling the VUMAT with the VDFLUX subroutine was discussed and the non-local damage evolution law was given.

The non-local damage evolution law was tested in two benchmark geometries, one with a geometric imperfection and one with a material imperfection. The goal of these benchmark tests was to validate the damage law in a simplified case where only one shear

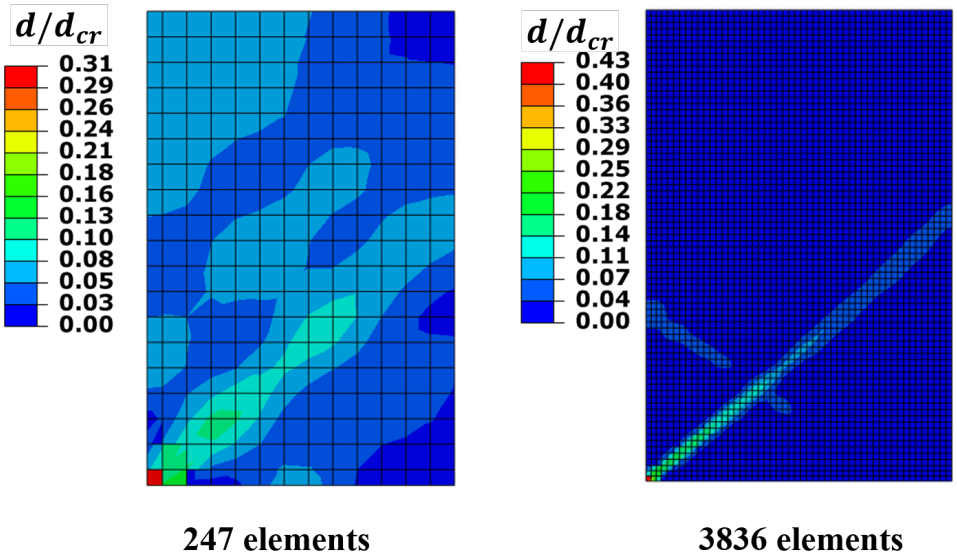

Figure 3.15: Shear band formation due to material imperfection using the local model. Two different mesh densities are depicted, 247 and 3836 elements.

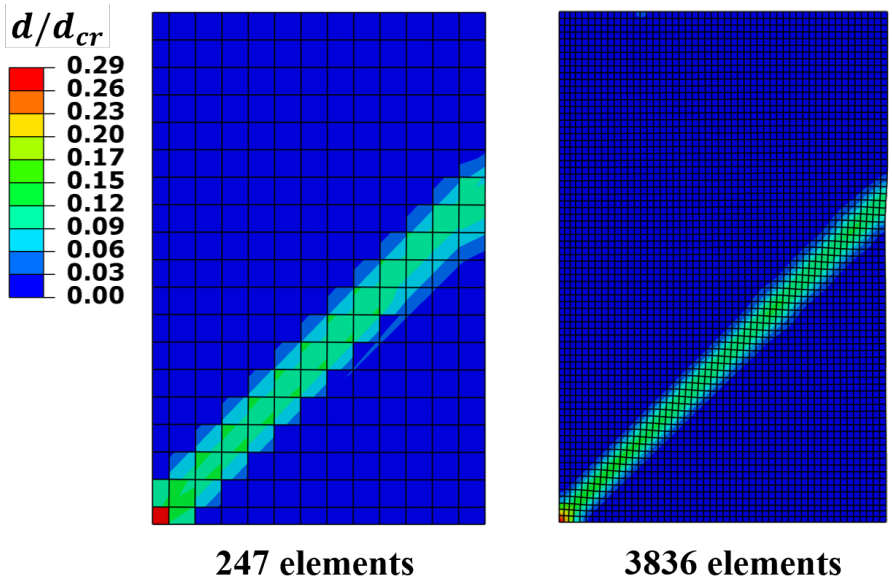

Figure 3.16: Shear band formation due to material imperfection using the non-local model. Two different mesh densities are depicted, 247 and 3836 elements.

band is generated, instead of multiple shear bands and cracks that are present in the first bite simulation. The results showed that the models are not mesh dependent and both the shear band width and the damage parameter remain constant for different mesh densities for the case of the non-local model. This non-local damage model will be used in chapters 4 and 5 for micromechanical simulations and the macromechanical simulations of the first bite respectively.

4 Micromechanical model for the prediction of the elastic, plastic and fracture properties in aerated products

Topics

4.1 Introduction

The purpose of this chapter is to present the methodology followed to calculate the elastic, plastic and fracture properties of the micro-aerated chocolate samples, based on the mechanical properties of the non-aerated samples. The goal of this chapter is to provide a numerical tool that allows the estimation of the material properties that will be used in the macromechanical simulation of the first bite.

The change in the mechanical behaviour of materials when pores are introduced in the matrix and the calculation of the effective properties is performed through the theory of computational homogenisation. Computational homogenisation has been used to derive the effective properties of heterogeneous materials, by knowing the properties of their constituents. Homogenisation can also be applied for non-linear properties and it has been the field of research in many papers e.g. [90, 91, 92]. In the current thesis, homogenisation will be used for porous materials, where the air will be considered as the second phase of the heterogeneous material.

The theory of computational homogenisation will be applied to random porous microstructures, which will be developed through a Random Sequential Adsorption (RSA) algorithm [93] and to geometries generated from 3D reconstruction of X-Ray Tomography (XRT) images. The study on the random microstructure aims to provide the geometric characteristics in terms of size and number of pores, which is sufficient to represent the macroscopic properties. This statistically homogeneous unit cell is known as the Representative Volume Element (RVE) and it will be used for the computational homogenisation.

In addition to computational homogenisation, several theoretical models exist for the estimation of the effective behaviour of linear elastic composite materials. The simplest models that provides a rough estimate of the effective mechanical properties are the Voigt [94] and Reuss [95] models, which assume uniform strain and stress field, respectively over the entire composite volume. The results of these simplistic models provide upper and lower bounds of the effective material properties. Eshelby [96] solved the problem of an ellipsoidal inclusion in an infinite elastic matrix. Based on Eshelby's work, Hashin [97] extended the theory for non-dilute porous media and proposed an exact solution for linear elastic composites subjected to hydrostatic loading. Hashin and Shtrikman [98, 99, 100] extended the Voigt and Reuss bounds by assuming that the constituent phases of the composite are isotropically distributed in the volume of the composite. Hershey [101] and Kröner [102] introduced the self consistent approximation and was applied to elastic polycrystals and Willis [103, 104, 105] applied a generalisation of these results in terms of variational principles. The simplistic Voigt and Reuss bounds that take into account only the volume fractions, will be presented together with the more sophisticated Hashin and Shtrikman bounds [100]. These analytical bounds will be compared against the elastic properties as those calculated both from the experiments and the homogenisation method.

The converged RVEs will be used for the calculation of the yield and fracture properties using the constitutive model presented in Chapter 2 coupled with the non local damage model as this shown in Chapter 3. The purpose of this study is to investigate how the plastic and fracture properties are influenced by the micro-aeration, assuming that the matrix of the micro-aerated samples has the same properties as the non aerated samples. For this reason the l_{ch} parameter remains constant for all micro-aeration levels, since it can be related to the sugar crystal size, which lies in the same length scale (10-40 μm) and is present in both micro-aerated and non aerated chocolate. The sugar crystals are visible in Figure 4.1.

The current chapter is organised as follows. Section 4.2 provides information about the microscopic structure as those defined from Scanning Electron Microscope (SEM) and XRT images. This information will be the basis for the artificially generated microstructures using the RSA algorithm. In addition the elastic properties of both micro-aerated and non aerated chocolates, as those calculated from experiments [11], are given in the

same section. The RVE notion is introduced in section 4.3 including a literature review regarding different definitions in subsection 4.3.1. The boundary conditions and the Hill-Mandel condition, which are crucial for the mathematical formulation of the Boundary Value Problem (BVP), are presented in subsection 4.3.2 followed by the convergence criterion in section 4.3.3. In section 4.4 the RSA method for the generation of the random porous microstructures and the steps followed for the mesh generation of the generated unit cells are presented. The estimation of the effective elastic properties is presented in section 4.5 followed by the analytical models. Finally, the stress-strain graphs for the estimation of the plastic and fracture properties are given in the results' section 4.7 followed by the conclusions in section 4.8.

4.2 Microstructures and elastic properties of non-aerated and micro-aerated samples

The microstructure of both micro-aerated and non micro-aerated samples was investigated though the Scanning Electron Microscope (SEM). Figures 4.1a and 4.1b show the microstructure of the non micro-aerated samples and $f = 15\text{vol}\%$ micro-aerated samples respectively. Besides pores, which are clearly seen in Figure 4.1b, sugar particles are also visible. The sugar particles appear as crystals and their size ranges between 10 μm to 40 μm [11], which is in agreement with values reported in the literature [106].

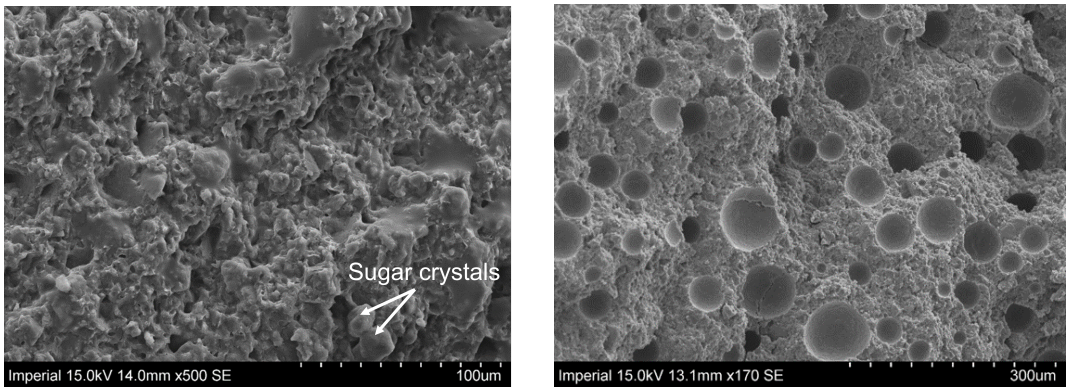

(a) (b)

Figure 4.1: SEM images of (a) non micro-aerated and (b) $f = 15\text{vol}\%$ micro-aerated samples. More details about the SEM images and additional information appearing in them, e.g. sugar crystals, can found in the paper published by Bikos et al. [11]

To better characterise the microstructure of the micro-aerated samples, XRT images were taken and are shown in Figure 4.2. The average pore size distribution was calculated by using both the SEM and the XRT images and the distribution is plotted in Figure 4.3. The 2D SEM images led to an average pore diameter of 38 μm and the average pore diameter calculated through the 3D XRT image was 45 μm for both micro-aerated samples

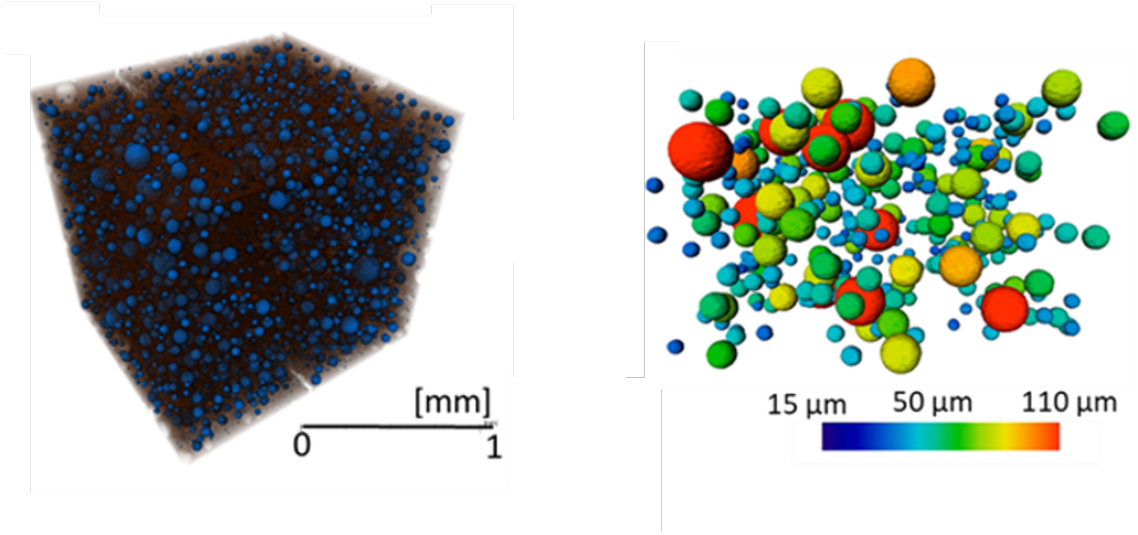

(a) (b)

Figure 4.2: (a) 3D reconstruction of $f = 15$vol% porosity samples, the blue spheres represent the pores in the brown matrix which represents the chocolate, (b) 3D contour plot of the pore diameters processed from the XRT images [11].

with $f = 10$vol% and $f = 15$vol% micro-aeration [11]. The later mean value of 45 µm will be used for the generation of monodisperse and polydisperse porous geometries for the study of the mechanical properties, as will be presented in section 4.4.

Figures 4.2a and 4.2b depict the pore distribution in the matrix. It is evident that bigger pores of diameter higher than 100 µm are present in the aerated samples, which is also shown in the plot of Figure 4.3. These bigger pores are believed to appear in the matrix, and therefore are also present in the non-aerated chocolate, due to the manufacturing process, where were trapped in the matrix and are hence not considered as part of the micro-aeration process [11]. The bigger pores will be excluded from the micromechanical study and only geometries with mean pore size of 45 µm will be considered.

4.3 The Representative Volume Element (RVE)

As stated in section 4.1, the main purpose of this chapter is the determination of a Representative Volume Element (RVE) size, in which the linear and non linear properties of the porous microstructures will be calculated and used in the homogeneous macroscopic simulations of the first bite in chapter 5. A widely used approach for modeling materials with heterogeneous microstructure is to perform calculations in a micro-scale sample which contains detailed information of the microstructure. This leads to estimation of global macroscopic material properties, and the micro-scale sample is known as the RVE. The RVE has the advantage of describing the macroscopic structure performing calculations in much smaller specimens in less computational time by applying the appropriate

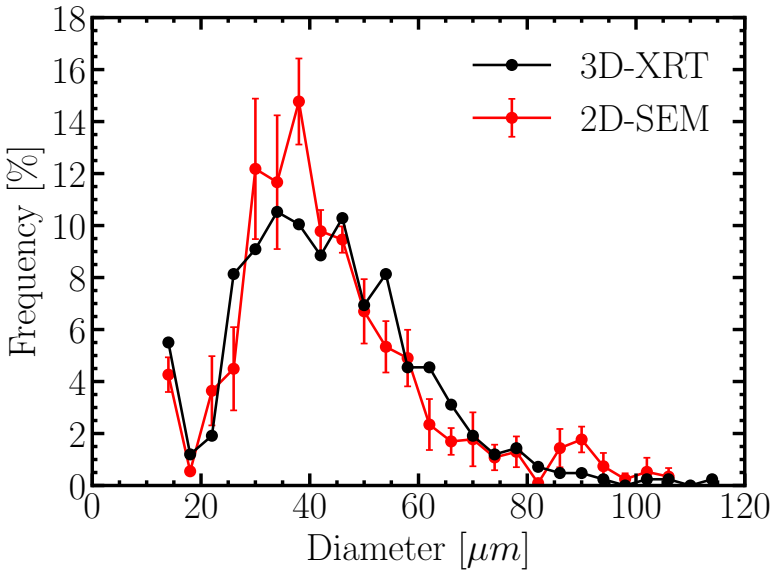

Figure 4.3: Size distribution of pores as calculated from 2D SEM and 3D XRT images for $f = 15$vol% [11].

boundary conditions in the micro-problem which satisfy the Hill-Mandel condition [107]. In this section different definitions of the RVE found in the literature will be provided, the boundary conditions that are used in the micro-problem will be presented and the criterion for the RVE size determination will be determined.

The transition between the micro-scale and the macro-scale is conducted though averaging properties calculated in the RVE. The size of the RVE has to be large enough in order be characterised as statistically uniform and also small enough to be able to run simulations in sufficient time. However the existence and the size determination of an RVE is a question addressed by many researchers; different definitions have been suggested and these will be presented in the following subsection.

4.3.1 Literature review of RVE definitions

According to Kanit et al. [108] two different conditions are being used for the RVE definition in the mechanics of heterogeneous materials. The first one states that the RVE should be sufficiently large to be considered as statistically representative of the composite material, meaning that it should include a variety of microstructural characteristics, i.e. voids, grains, etc. The second one is based on statistical properties, which according to Kanit et al. [108] is stated as "*the RVE must ensure a given accuracy to the estimated property obtained by spatial averaging of the stress, the strain, or the energy fields in a given domain.*"

There has been a lot of research on the field of RVEs and more definitions are listed below:

– According to Hill [107], RVE is "*a sample that (a) is structurally entirely typical of the whole mixture on average, and (b) contains a sufficient number of inclusions for the apparent overall moduli to be effectively independent of the surface values of traction and displacement, so long as these values are macroscopically uniform*".

– According to Hashin [109], the RVE should be statistically homogeneous containing enough information of the microstructure, but smaller than the macroscopic scale.

– Drugan and Willis [110] stated that, the RVE "*is the smallest material volume element of the composite for which the usual spatially constant (overall modulus) macroscopic constitutive representation is a sufficiently accurate model to represent mean constitutive response.*"

According to Gitman et al. [111] larger sized microstructural cells behave in a consistent way, whereas smaller microstructural cells provide values that differ to each other, which will be considered as one of the criteria for determination of the RVE size in section 4.3.3. Another important finding was by Ostoja-Starzewski [112] who noted that the RVE is perfectly defined for periodic microstrures and volumes containing a large number of microstrucrural heterogeneities as shown in Figure 4.4.

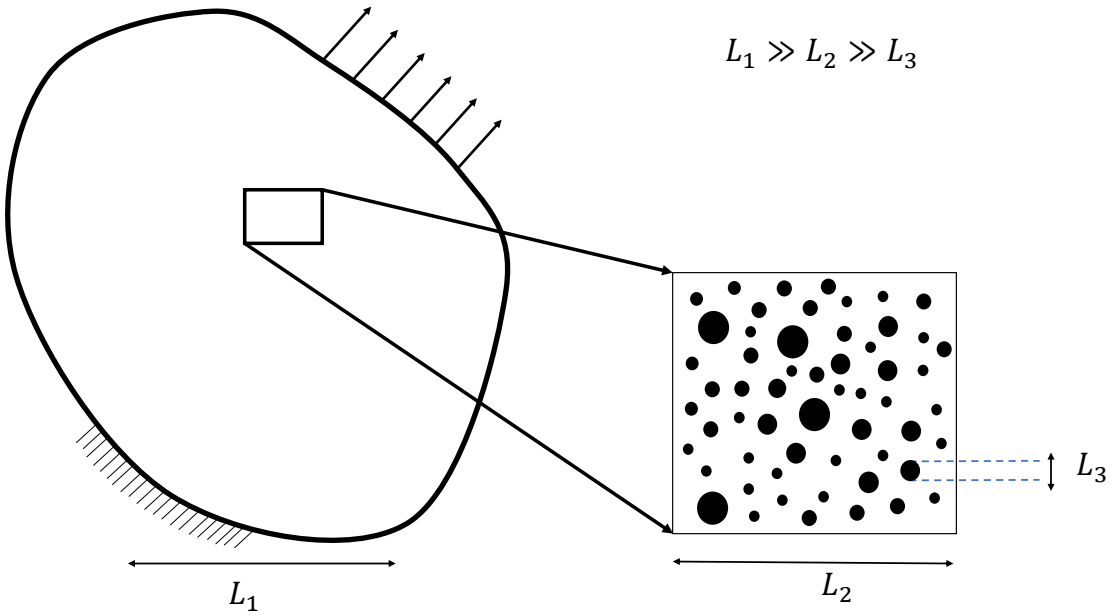

Figure 4.4: The different legth scales in the material. Image re-sketched from [28].

4.3.2 Boundary conditions and the Hill-Mandel condition

As stated in the previous section, the volume averages should be calculated in a microstructural volume, V, that contains sufficiently enough microstructural information to

be considered as statistically homogeneous. The transition from the microscopic to the macroscopic scale relies on volume averaging relations and is mathematically expressed through the Hill-Mandel condition [107]:

$$\overline{\boldsymbol{\sigma}} : \overline{\boldsymbol{\varepsilon}} = \frac{1}{V} \int_V \boldsymbol{\sigma} : \boldsymbol{\varepsilon} \, \mathrm{d}V \tag{4.1}$$

where $\boldsymbol{\sigma}$ and $\boldsymbol{\varepsilon}$ define the microscopic stress and strain respectively and $\overline{\boldsymbol{\sigma}}$ and $\overline{\boldsymbol{\varepsilon}}$ define the volumetric average macroscopic stress and strain respectively given by:

$$\overline{\boldsymbol{\sigma}}(\mathbf{x}) = \frac{1}{V} \int_V \boldsymbol{\sigma}(\mathbf{x}) \, \mathrm{d}V \tag{4.2}$$

$$\overline{\boldsymbol{\varepsilon}}(\mathbf{x}) = \frac{1}{V} \int_V \boldsymbol{\varepsilon}(\mathbf{x}) \, \mathrm{d}V \tag{4.3}$$

In linear elasticity, the Hill-Mandel condition relates the micro-scale with the macro-scale strain energy densities and is satisfied by a variety of boundary conditions. The Kinematic Uniform Boundary Conditions (KUBC) and Traction Boundary Conditions (TBC), also known as Dirichlet and Neumann respectively, are the most common boundary conditions used in the literature and are usually referred as homogeneous boundary conditions. Both types of boundary conditions have limitations when considering the physics of the problem. The TBC result in a compliant response (provide a lower bound to stiffness), whereas the KUBC result in a stiffer response (upper bound) [113]. As an alternative, the Periodic Boundary Conditions (PBC) provide an estimation that is bounded by the two homogeneous boundary conditions. The last statement will be used as the second criterion for the RVE size determination. For the purpose of this thesis only the KUBC and PBC are applied for the analysis presented in the following sections.

Equation (4.4) describes the KUBC, where an average strain $\overline{\boldsymbol{\varepsilon}}$ is applied at any material point $\mathbf{x}$ of the boundary of the unit cell ∂V and the displacement field $\mathbf{u}(\mathbf{x})$ is:

$$\mathbf{u}(\mathbf{x}) = \overline{\boldsymbol{\varepsilon}} \cdot \mathbf{x} \tag{4.4}$$

KUBC overconstrains the unit cell providing an overestimation of the effective elastic properties. KUBC are considered as the opposite to the TBC where a traction $\mathbf{t}$ is applied to all surfaces of the unit cell, resulting in an underestimation of the elastic modulus [114]. In ABAQUS [17], the KUBC are included by selecting all surfaces of the unit cell and applying a displacement field which is dependent on the the position of the material point. For example, for the simple case of a uniaxial tension in the y direction, the displacement field should be defined as $\mathbf{u}(\mathbf{y}) = (y, 0, 0)$, by creating an expression field in the "Analytical Field" option of the boundary condition tab in ABAQUS [17]. A schematic representation the KUBC is provided in Figure 4.5.

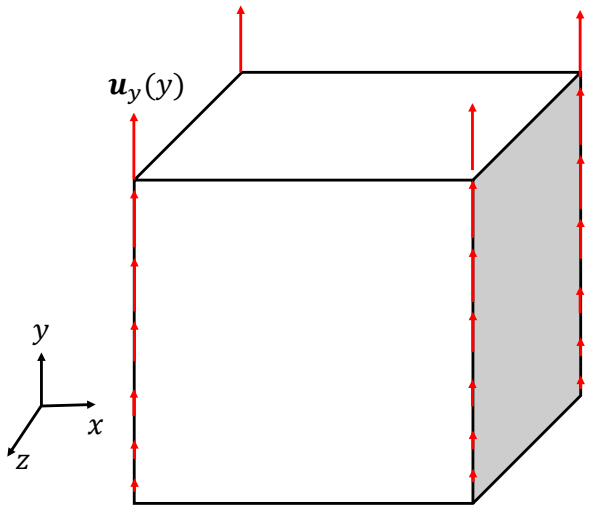

Figure 4.5: Schematic representation of KUBC.

PBC are imposed on the opposite boundaries of the unit cell as described by Mbiakop et al. [115] and the displacement field $\mathbf{u}(\mathbf{x})$ is given by:

$$\mathbf{u}(\mathbf{x}) = \overline{\boldsymbol{\varepsilon}} \cdot \mathbf{x} + \mathbf{u}^*(\mathbf{x}) \tag{4.5}$$

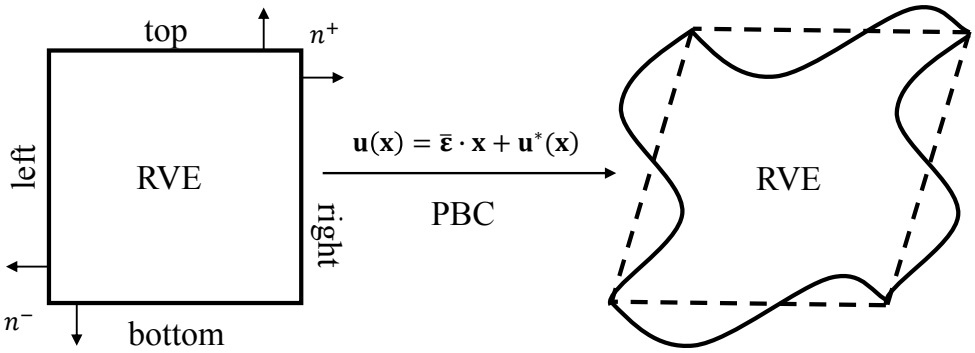

Figure 4.6: Schematic representation of PBC.

The implementation of PBC introduces the assumption that the structure of the porous material is periodic. However, as already presented in section 4.2, the internal material structure is random. It is a common assumption in the literature [111], to consider a periodic RVE when computational homogenisation is applied in materials with random microstructures. Figure 4.7 depicts the internal structure of a random porous material and different RVEs that can be selected for the micromechanical analysis. As has been

already mentioned, the RVE should be representative of any part of the material meaning that the macroscopic structure can be created by repeating this RVE structure in the three dimensional space. It is possible to create the macroscopic structure using samples **A, B, D** and **E**, in Figure 4.7, by assuming that the sample is infinitely long. This assumption is valid for the material under consideration since the pores' diameter is three orders of magnitude less than the length of the macroscopic material. On the contrary samples **C** and **F** are on the boundary so one or more sides cannot be crossed by pores [111]. In this thesis, RVEs where pores are allowed to intersect their boundaries will be considered.

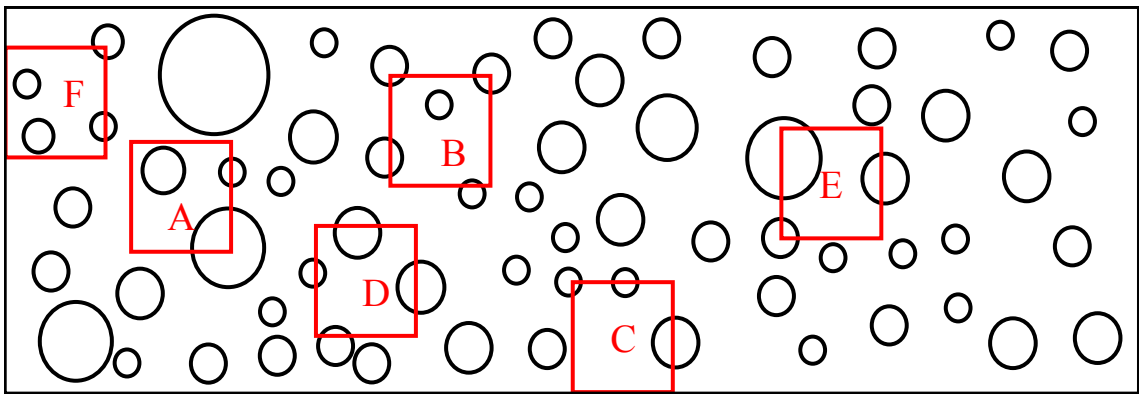

Figure 4.7: Different RVE selection in 2D microstructure with random pore distribution. Re-sketched from [111].

4.3.3 Criterion for determination of RVE size

According to Ostoja-Starzewski [117], the definition of statistical homogeneity relies on the Hill-Mandel condition [107]. Another way of expressing the homogeneity criterion is to state that the RVE response should be independent of the boundary conditions applied to it. In this thesis, an extension of Ostoja-Starzewski [117] statement will be used for the determination of the RVE size. The convergence criterion introduced by Zerhouni et al. [118] will be used, which states the following:

- the difference between the effective properties calculated by applying KUBC and PBC should be less than 2% and
- further increase of the size of the unit cell does not fluctuate the effective properties calculated by KUBC by more than 0.1%

The criterion for the RVE size determination is better explained through the qualitative graph in Figure 4.8. The PBC is the most efficient in terms of convergence rate with increasing RVE size, whereas the KUBC provides a wrong prediction of the effective property for small RVEs and converges to an asymptotic value of the averaged property for bigger volumes. The convergence of apparent properties to the effective ones as the

size of the unit cell increases, has been investigated by Huet [114, 119], Ostoja-Starzewski [112, 120], Pecullan et al. [121] and Terada et al. [122].

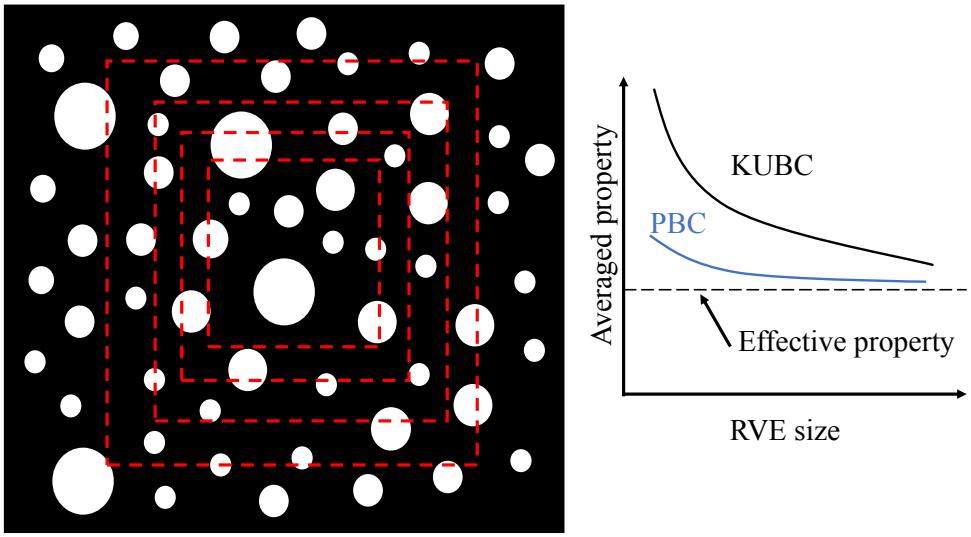

Figure 4.8: Qualitative graph of the predictions provided by different boundary conditions and RVE sizes.

4.4 Generation and meshing of periodic RVEs

4.4.1 The Random Sequential Adsorption method

In this section the methodology for the generation of the random 3D porous microstructures will be presented. The virtual porous microstrucrture contains randomly distributed non overlapping pores of the same (monodisperse) or different (polydisperse) radius. The pores are randomly generated according to the Random Sequential Adsorption (RSA) algorithm [93], and are randomly placed in a unit cell of edge size, L. In addition, the unit cell is periodic, meaning that the opposite surfaces of the cube have identical faces. In this study, the estimation of the elastic effective properties was initially conducted in monodisperse unit cells and then extended to polydisperse configurations as the latter is closer to the real microstructure observed in the SEM and XRT images (Figure 4.3). The monodisperse microstructure is a 3D cubic unit cell of length L, containing N identical non overlapping pores of radius R. For cubic unit cells and spherical voids the porosity f of microstructures generated using the RSA algorithm is given by:

$$f = \frac{4}{3} N \pi \left(\frac{R}{L} \right)^3 \tag{4.6}$$

Both monodisperse and polydisperse microstructures were generated following the

procedure described by Rintoul and Torquato [93]. The procedure followed is described below:

– Initially the center of the first pore is placed at a random point $\boldsymbol{p_i}$ that represents the center of a pore with radius R_i. Then a second pore, with radius R_j is placed and the non-overlapping of the spheres is achieved through satisfying the following relation:

$$\left\|\boldsymbol{p}_i - \boldsymbol{p}_j\right\| \geq \left(R_i + R_j\right) \tag{4.7}$$

if equation (4.7) is not satisfied, then the pore with radius R_j is rejected and a new sphere is placed in the domain. The remaining pores are placed in a sequential process. As proposed by Fritzen et al. [123] a minimum distance between the centers of the pores equal to 2.5% of the mean diameter is applied in order to guaranty FE discretisation.

– In addition, according to Zerhouni et al. [118] in order to generate easier to mesh microstructrures, pores that lie very close to the faces of the cube are also rejected from the configuration. The following equation must also be satisfied:

$$\left\|p_i^k - R\right\| \geq 0.05R \quad \text{and} \quad \left\|p_i^k + R - L\right\| \geq 0.05R, \quad (k = 1,2,3) \tag{4.8}$$

It has been reported in the literature [124, 125] that the maximum porosity that can be achieved using the RSA and satisfying the criteria introduced by equations (4.7) and (4.8) is limited to $f = 61.5\text{vol}\%$ for both monodisperse and polydisperse microstructures. This is not a limiting factor for the current study as the maximum porosity examined is $f = 15\text{vol}\%$.

The open source code Mote3D [126] is capable of generating random particulate microstructures with periodic surfaces and is used for the generation of both monodisperse and polydisperse porous microstructures with porosities $f = 10\text{vol}\%$ and $f = 15\text{vol}\%$. Representative porous microstructrures of increasing volume are depicted in Figure 4.9.

It is worth noting that, 3D XRT geometry, available only for the $f = 15\text{vol}\%$ porosity was also analysed. The geometry, presented in Figure 4.2, was imported into ABAQUS and the spheres were subtracted from a cube with edge side $L = 1.5\,\text{mm}$ to create the porous unit cell. Afterwards, it was meshed in ABAQUS with C3D10 elements and only KUBC were applied, since the outer opposite surfaces are not periodic to allow the implementation of PBC.

4.4.2 Meshing randomly generated unit cells

Mote3D outputs the center coordinates and radii of the pores, which is then processed by a Python script to generate a readable file by the commercial software NETGEN [116]

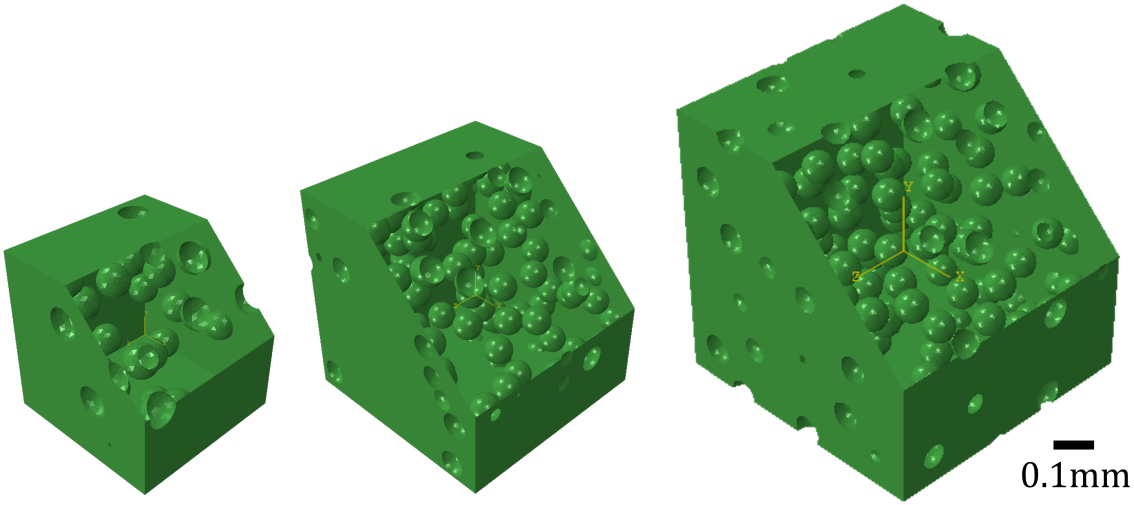

Figure 4.9: Unit cells of $f = 15$vol% micro-aeration, generated with the RSA algorithm. The increasing size of the cubes is accommodated with increased number of pores in order the porosity to remain constant.

which is used for meshing the microstructures. NETGEN [116] is capable of creating periodic meshes, which is required in the current study, by creating identical surface meshes at opposite surfaces of the unit cell. This allows the use of the "EQUATION" command in order to apply the PBC in the ABAQUS general purpose FE code [17] where all calculations were conducted. Three dimensional ten-node quadratic tetrahedral elements

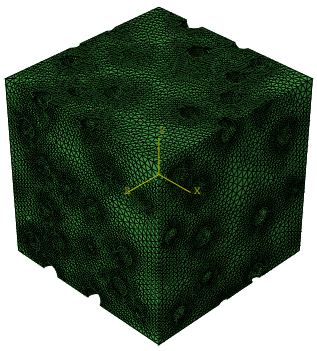

(a) (b) (c)

Figure 4.10: Meshed microstructures using the commercial software NETGEN [116]. The monodisperse unit cells consist of $N = 100$ voids, edge size $L = 0.36$ mm and radius $R = 22.5\,\mu$m, resulting in a porosity of $f = 10$vol%. The microstructrures are meshed with three different mesh densities: (a) coarse mesh of 51,063 elements, (b) fine mesh of 322,049 elements, (c) very refined mesh of 1,931,492 elements.

It is worth noting that another important issue that should be considered is the refinement of the unit cells, as finer meshes will result in more accurate results but will also increase the computational time. For the unit cells studied in the current thesis, fine mesh

densities (200,000 to 500,000 elements depending on the size of the unit cell) found to provide a good compromise between accuracy and computational time and the results presented later are based on discretisations with mesh refinement as presented in Figure 4.10(b).

4.5 Estimation of effective elastic properties and size of RVE

4.5.1 Determination of effective elastic properties and RVE size

The steps followed to calculate the effective elastic properties and the size of the RVE will be presented in this section. Four different sizes of periodic unit cells with gradually increasing size of edge length L and number of pores N (to keep the porosity constant) were examined for both porosities of $f = 10\text{vol}\%$ and $f = 15\text{vol}\%$. Detailed information about the unit cells generated with the RSA algorithm is presented in Table 4.1.

Table 4.1: Sizes of unit cells, for the two examined porosities, used for the computation of RVE. The sizes correspond to both monodisperse and polydisperse microstructure, and the radius (mean radius for the polydisperse unit cells) is $R = 22.5\,\mu\text{m}$.

	$f = 10\text{vol}\%$	$f = 15\text{vol}\%$
N	L[mm]	L[mm]
30	0.24	0.21
50	0.28	0.25
100	0.36	0.31
150	0.42	0.36

The two types of boundary conditions presented above were implemented to the generated microstructures and linear elastic FE simulations were conducted, where the matrix was modeled as a linear isotropic material with Young's modulus $E_m = 100\,\text{MPa}$ and Poisson's ratio $\nu = 0.49$, which are properties calculated from experiments conducted to the non-aerated chocolate samples. More details regarding the experimental procedure can be found in the work of Bikos et al. [11].

The homogenised stiffness tensor is calculated from the volume average stress and volume average strain fields using the constitutive equation:

$$\overline{\boldsymbol{\sigma}}(\mathbf{x}) = \mathbb{C}^{eff} : \overline{\boldsymbol{\varepsilon}}(\mathbf{x}) \tag{4.9}$$

where $\mathbb{C}^{eff}$ is the effective stiffness tensor.

According to Kanit et al. [108] the homogenised stiffness tensor is calculated by imposing six average strain fields in different directions in order to calculate all the six columns of $\mathbb{C}^{eff}$. According to Anoukou et al. [127] microstructures generated with the

RSA method can be considered as isotropic. For isotropic materials, the elastic properties can be described by the bulk modulus, k, and the shear modulus, μ. By applying specific average strain fields as the following:

$$\overline{\boldsymbol{\varepsilon}}_k = \begin{pmatrix} \frac{1}{3} & 0 & 0 \\ 0 & \frac{1}{3} & 0 \\ 0 & 0 & \frac{1}{3} \end{pmatrix}, \quad \overline{\boldsymbol{\varepsilon}}_\mu = \begin{pmatrix} 0 & \frac{1}{2} & 0 \\ \frac{1}{2} & 0 & 0 \\ 0 & 0 & 0 \end{pmatrix} \tag{4.10}$$

The effective bulk modulus k^{eff} and the effective shear modulus μ^{eff} are calculated as:

$$k^{eff} = \overline{\boldsymbol{\sigma}} : \overline{\boldsymbol{\varepsilon}}_k = \frac{1}{3}\,\mathrm{trace}(\overline{\boldsymbol{\sigma}}) \tag{4.11}$$

$$\mu^{eff} = \overline{\boldsymbol{\sigma}} : \overline{\boldsymbol{\varepsilon}}_\mu = \overline{\boldsymbol{\sigma}}_{12} \tag{4.12}$$

Micromechanical analysis is also conducted for the 3D reconstructed geometry of Figure 4.2a and since the geometry is not periodic, only KUBC are applied on the boundaries.

Regarding the estimation of the yield and fracture points, the constitutive model coupled with the non-local damage evolution law is used in compression FE simulations for different strain rates using the converged RVE geometries. The material properties are the same as the ones used for the benchmark tests in section 3.6 and are given in Table 3.4. It is worth noting that the internal characteristic length, l_{ch} remains the same although the geometry changes. Different mesh refinements were tested for both the polydisperse and the monodisperse microstructures, and the value of $l_{ch} = 0.06$ provided mesh independent results without making the FE simulations computationally expensive. The stress-strain curves from the FE simulations are compared with compression experiments. The purpose of this analysis is to study effect of the pore distribution on the mechanical properties through a comparison between monodisperse and polydisperse unit cells.

4.6 Analytical models

Due to the complex internal microstructure of composite materials, many authors have focused on finding upper and lower bounds of the Young's modulus, rather than an exact value. Although the estimates of the bounding methods are not exact, in certain cases may prove useful as they provide an indication of the magnitude of the Young's modulus of composite materials. The simplest 'bounding' models for assessing the average elastic moduli of composite materials are the Voigt [94] and Reuss [95] approximations, commonly known as the "rule of mixtures" and the "inverse rule of mixtures", respectively. The Voigt model assumes that the inclusions and the matrix have the same strain (iso-strain model). The Young's modulus, according to the Voigt model is calculated as

follows:

$$E = fE_m \tag{4.13}$$

where E_m is the Young's modulus of the matrix, E is the Young's modulus of the porous material and f is the porosity. The equation of the Reuss model will not be used in this thesis as it is not close to the experimental data.

The Voigt and Reuss bounds are the simplest models and are very conservative, but can be used as a first validation for the experimental data. Hashin and Shtrikman [100] extended the Voigt and Reuss models and provided closer upper and lower bounds for the elastic modulus. Their approach is based on the introduction of a homogeneous and isotropic reference material, known as the comparison material and evaluating the differences between the comparison material and the actual composite. The bulk, k_{HS}, and shear, μ_{HS}, moduli according to the Hashin-Shtrikman upper bounds are calculated as:

$$k_{HS} = \frac{4(1-f)\mu_m k_m}{4\mu_m + 3fk_m} \tag{4.14}$$

$$\mu_{HS} = \frac{(1-f)\,(8\mu_m + 9k_m)\,\mu_m}{4\mu_m(2+3f) + 3k_m(3+2f)} \tag{4.15}$$

where k_m and μ_m are the bulk and shear moduli of the matrix. The Young's modulus, E and the Poisson's ratio, ν are then calculated using the following equations:

$$E_{HS} = \frac{9k_{HS}\mu_{HS}}{3k + \mu_{HS}} \tag{4.16}$$

$$\nu_{HS} = \frac{3k_{HS} - 2\mu_{HS}}{6k + 2\mu_{HS}} \tag{4.17}$$

The two analytical models will be compared against the results from the micromechanical analysis and the experimental data.

4.7 Results and Discussion

Initially, the results for the prediction of the elastic modulus are presented, where simulations using both the monodisperse and the polydisperse distributions were conducted. The error bars, presented in the figures of this section, correspond to the maximum and minimum values calculated using five different RVE configurations. The differences between the monodisperse and the polydisperse analysis are similar and Figure 4.11 shows the results for a polydisperse microstructure with porosity $f = 15$vol%. In Figures 4.11a and 4.11b, the normalised bulk and shear moduli are presented. The PBC converge faster than the KUBC, as expected, and the dispersion of the calculations is smaller for the PBC. The bulk and shear moduli with PBC reach a constant value for unit cell with $N = 50$ pores, whereas the KUBC converge for a much larger unit cell of $N = 100$ pores. The

convergence criterion, introduced in section 4.3.3, is met for a unit cell with $N = 100$ pores, mean diameter size of $D = 45\,\mu m$ and edge size of $L = 0.31\,mm$. This is in agreement with the findings of Zerhouni et al. [118] who suggested that a ratio of $D/L \approx 0.1$ leads to converged RVEs. Figures 4.11c and 4.11d present the normalised Young's modulus and the Poisson's ratio, calculated using the values of the bulk and shear moduli. The same analysis was repeated for the $f = 15vol\%$ monodisperse samples and no difference was obtained neither for the converged RVE size nor for the value of the Young's modulus. The graphs for the monodisperse analysis of the $f = 15vol\%$ porosity are presented in appendix A.3. The $f = 10vol\%$ porosity microstructures were tested following the same methodology for both monodisperse and polydisperse distributions. The results showed that a unit cell with $N = 100$ pores and edge size $L = 0.36\,mm$ is considered as representative. The relevant graphs are presented in appendix A.4.

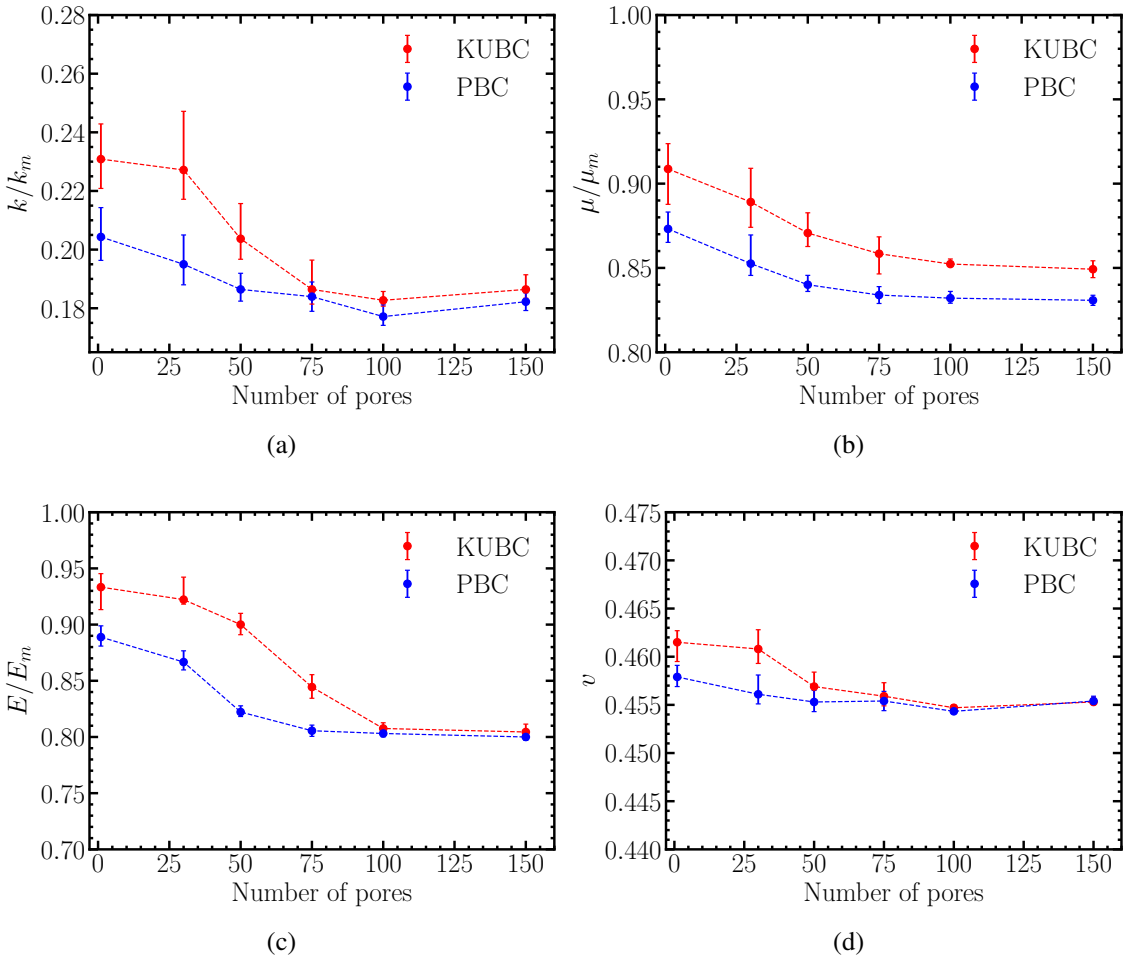

Figure 4.11: Comparison between different sizes of unit cells for KUBC and PBC (a) normalised bulk modulus, (b) normalised shear modulus, (c) normalised Young's modulus and (d) Poisson's ratio for $f = 15vol\%$ porosity and polydisperse microstructure. The bulk, shear and Young's moduli of the solid matrix are shown as k_m, μ_m and E_m respectively.

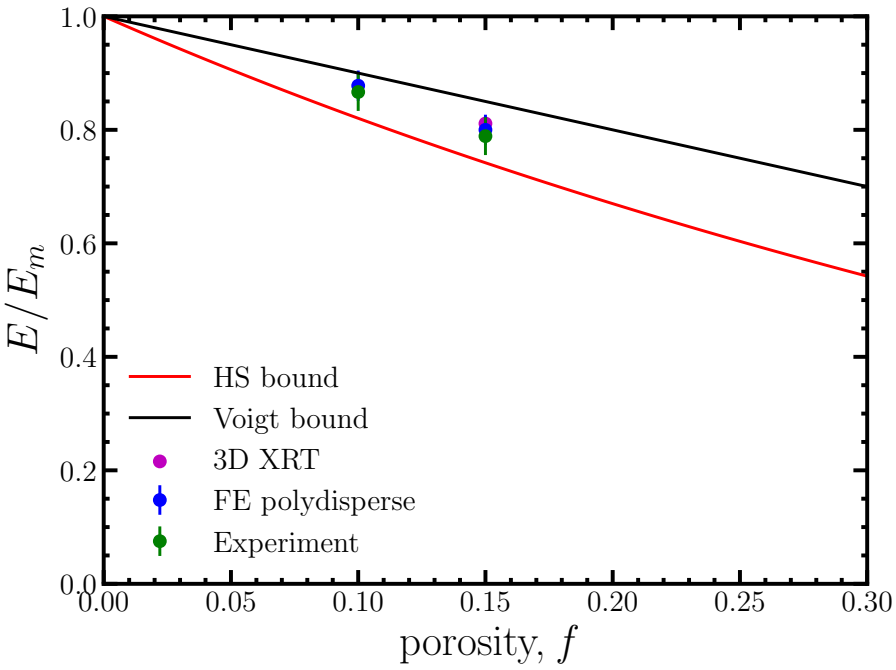

Figure 4.12: Normalised Young's modulus calculated from experiments [11], micromechanical FE simulations using microstructures generated with the RSA algorithm and micromechanical FE simulations with the 3D XRT geometry for porosity $f = 15$vol%. The upper Hashin and Shtrikman and Voigt bounds are also shown.

The normalised Young's modulus is also compared with the upper Hashin Shtrikman bound and Voigt model in Figure 4.12. The results from both porosities $f = 10$vol% and $f = 15$vol% are presented and there is a good agreement between the experiments and the FE simulation results. The XRT geometry for porosity $f = 15$vol%, was also analysed and the calculated Young's modulus lies between the error bars of both experiments and FE simulations using the MOTE3D generated geometries. It is worth mentioning that although KUBCs were used in the XRT, which overestimate the effective properties (as explained in section 4.3.3), the results agree with those of the converged RVEs, where PBC were used. This result is reasonable, since, as shown in Figure 4.3, the size of the XRT geometry ($L_{XRT} > 1$ mm) is greater than the size of the RVE ($L_{RVE} = 0.31$ mm), which was selected according to the criteria introduced in section 4.3.3, and the effective properties calculated with KUBC coincide with the PBC for large RVE sizes (see Figure 4.8).

The converged RVE microstructures, as calculated from the elastic analysis, were used for the calculation of plastic and fracture properties. Both monodisperse and polydisperse microstructures were investigated for both porosities. The stress-strain graph for porosity $f = 15$vol% with polydisperse distribution is presented in Figure 4.13a. The respective data of the monodisperse distribution of the same porosity is shown in Figure 4.13b. Comparing Figures 4.13a and 4.13b, initially the elastic region of the the FE simulations is in good agreement with the experimental data and no difference is observed

between monodisperse and polydisperse configurations. The FE simulations are also capable of capturing the yield stress for both distributions and lie in good agreement with the experimental data. Differences between polydisperse and monodisperse microstructures appear in the plastic region. The fracture initiation criterion is met in smaller strains for the monodisperse configuration resulting in softening to occur faster leading to failure in smaller strains. This is not present in the polydisperse configurations, where the stress-strain graph of Figure 4.13a reveals a more ductile behaviour resulting in a plastic region and final a fracture strain that is in good agreement with the compression experiments.

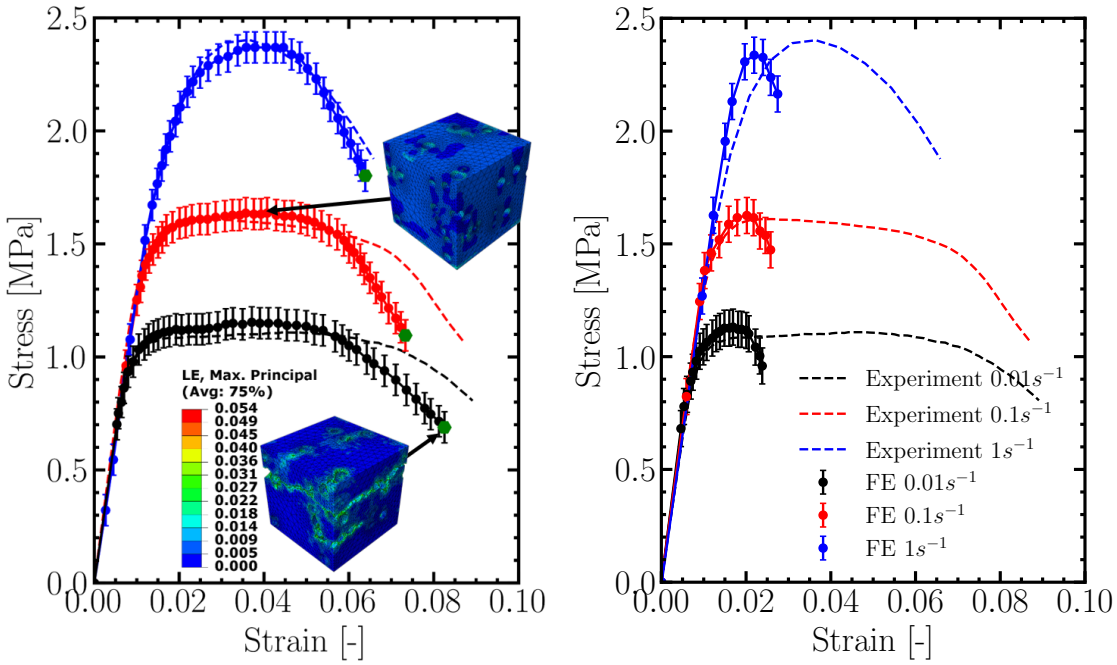

(a) (b)

Figure 4.13: Comparison between FE (solid lines) results and experimental results (dashed lines) for porosity $f = 15$vol% for different strain rates for (a) polydisperse and (b) monodisperse microstructure. Contour plots are also depicted in the plastic region and the fracture point for the polydisperse microstructure. The green hexagons mark the point where the plastic strain at fracture is calculated.

The same analysis was performed for the $f = 10$vol% for both monodisperse and polydisperse microstructures. A similar trend to the $f = 15$vol% is also present for the $f = 10$vol% as shown in Figure 4.14. The yield point is captured correctly for both polydisperse (Figure 4.14a) and monodisperse (Figure 4.14b) distributions, whereas the softening starts in smaller strain values for the monodisperse unit cells, similar to Figure 4.13

The bar chart of Figure 4.15a depicts the yield stress comparing experiments with monodisperse and polydisperse simulations for different strain rates for micro-aeration $f = 15$vol%. The yield stress is calculated as the first point when the linearity of the elastic region ends, following the methodology of Bikos et al. [11] to make possible the

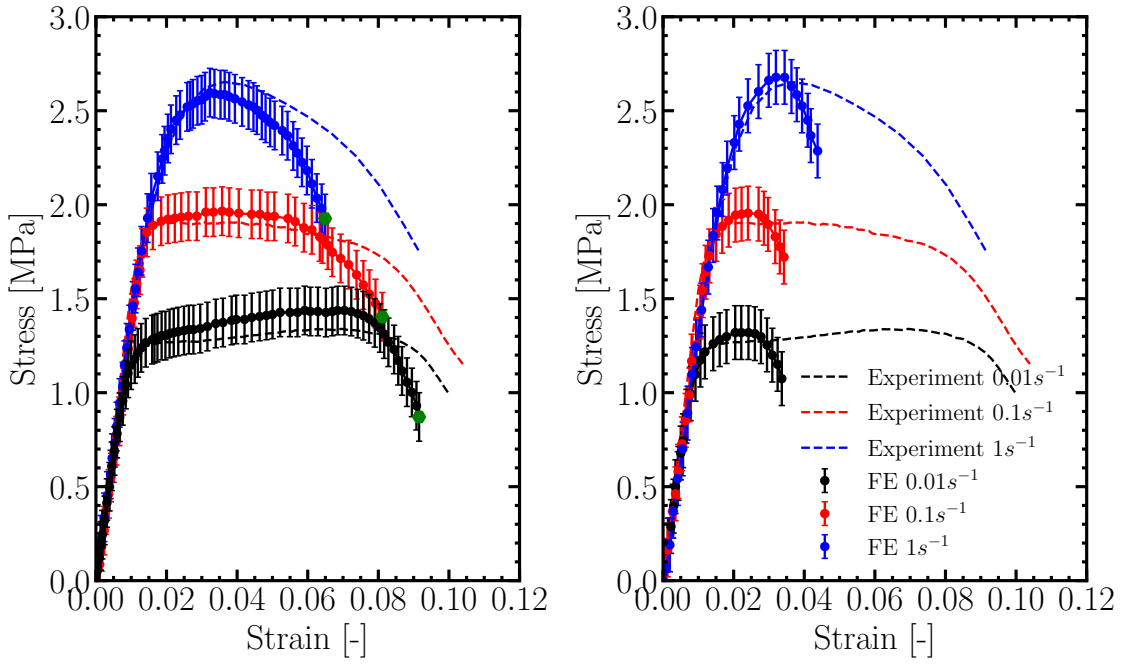

(a) (b)

Figure 4.14: Comparison between FE (solid lines) results and experimental results (dashed lines) for porosity $f = 10$vol% for different strain rates for (a) polydisperse and (b) monodisperse microstructure. Contour plots are also depicted in the plastic region and the fracture point for the polydisperse microstructure. The green hexagons mark the point where the plastic strain at fracture is calculated.

direct comparison between the FE calculations and the experimental results [11]. Figure 4.15b presents the equivalent plastic strain to failure for experiments and simulations in different strain rates for micro-aeration $f = 15$vol%. The values depicted in this bar chart corresponds to the green hexagons of Figure 4.13a. The respective data for the $f = 10$vol% porosity are presented in Figure 4.16.

Another important aspect that is calculated through the micromechanical simulations is the estimation of the equivalent plastic strain at the initiation of fracture. The equivalent plastic strain at fracture initiation is calculated from the strain that corresponds to the higher stress before softening. Then, the equivalent plastic strain is calculated through equation (3.21). Making use of the Figures 4.13a and 4.14a the equivalent plastic strain values at fracture initiation are calculated and the values are summarised in tables 4.2 and 4.3 for porosities $f = 15$vol% and $f = 10$vol% respectively. The calculated value corresponds to tension ($\eta = 1/3$) and by using the relation $\varepsilon^p_{eq,s} = \frac{2}{\sqrt{3}}\varepsilon^p_{eq,t}$ for the equivalent plastic strain in shear, that presented in section 3.4, the respective values for the equivalent plastic strain at the initiation of fracture were estimated.

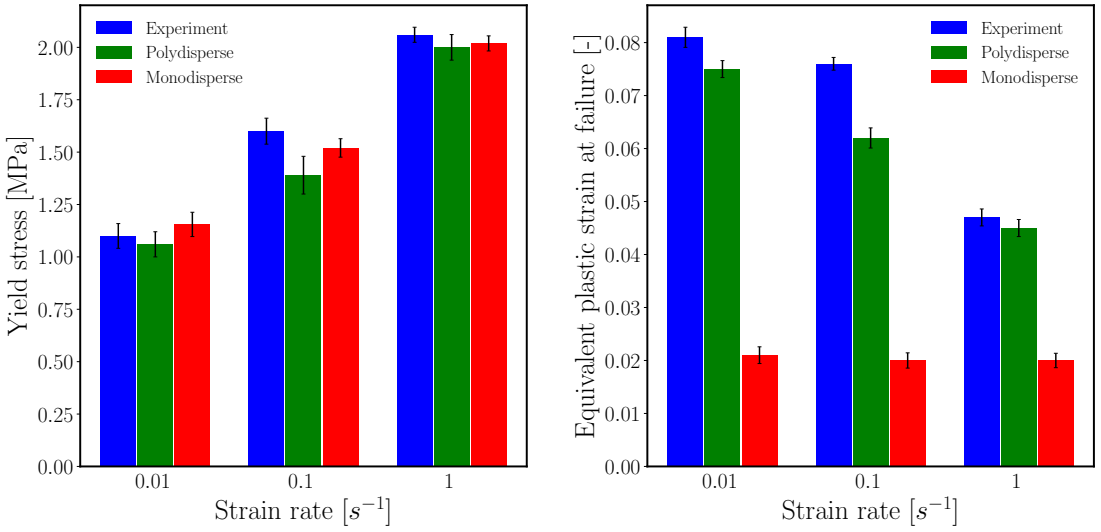

(a) (b)

Figure 4.15: (a)Yield stress comparison between experimental data and FE results from polydisperse and monodisperse microstructures in different strain rates for porosity $f =$ 15vol%, (b) plastic strain at failure comparison between experimental data and FE results from polydisperse and monodisperse microstructures in different strain rates for porosity $f = 15$vol%.

Table 4.2: Equivalent plastic strain at damage onset for different stress states and strain rates for micro-aerated chocolate with porosity $f = 15$vol%.

$\varepsilon^{p}_{eq,i}$	η	$\dot{\varepsilon}(\mathrm{s}^{-1})$
0.03	0	0.01
0.026	1/3	0.01
0.021	0	0.1
0.018	1/3	0.1
0.012	0	1
0.01	1/3	1

4.8 Conclusions

In this chapter the development of a micromechanical model for the prediction of elastic plastic and fracture properties due to the effect of micro-aeration was presented. Initially, the methodology for the generation of polydisperse and monodisperse unit cells was given and the RSA algorithm was presented. Afterwards, the KUBC and the PBC, employed for the estimation of a RVE and a unit cell with 100 voids was found to be representative for both the $f = 10$vol% and $f = 15$vol% porosities.

It is evident that there is good agreement between the experimental data and the micromechanical simulations in the elastic region using both monodisperse and polydisperse microstructures generated using the RSA algorithm and the 3D reconstructed XRT geom-

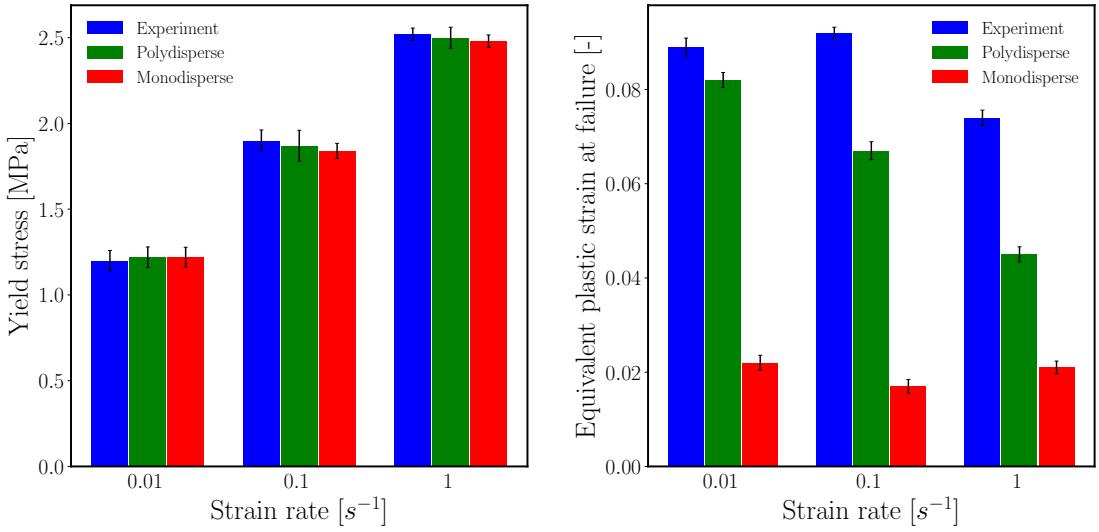

(a) (b)

Figure 4.16: (a)Yield stress comparison between experimental data and FE results from polydisperse and monodisperse microstructures in different strain rates for porosity $f =$ 10vol%, (b) plastic strain at failure comparison between experimental data and FE results from polydisperse and monodisperse microstructures in different strain rates for porosity $f = 15$vol%.

Table 4.3: Equivalent plastic strain at damage onset for different stress states and strain rates for micro-aerated chocolate with porosity $f = 10$vol%.

$\varepsilon^p_{eq,i}$	η	$\dot{\varepsilon}(\mathrm{s}^{-1})$
0.067	0	0.01
0.058	1/3	0.01
0.028	0	0.1
0.024	1/3	0.1
0.018	0	1
0.016	1/3	1

etry. Both experimental and computational results appear to be above the upper Hashin and Shtrikman bound and below the Voigt bound.

Regarding the yield stress calculations, there is a good agreement between the experimental data and the simulations for both monodisperse and polydisperse unit cells and the conclusion that the size size distribution does not affect the yield stress, can be drawn. On the other hand, the equivalent plastic strain in failure depends on the size distribution and the polydisperse microstructures provide a better agreement with the experimental data.

The findings of this micromechanical analysis will be used as an input for the macroscopic FE analysis, presented in chapter 5, were the chocolate specimen will be considered as homogeneous. The effect of porosity will be introduced through the change in the mechanical properties and especial the Young's modulus, the yield stress and the equiv-

alent plastic strain at fracture initiation, as those estimated from the micromechanical analysis presented in the current chapter.

5 Experimental and computational model for the simulation of the 1st bite

Topics

5.1 Introduction

First bite is the initial step of mastication or chewing and belongs in the general process of digestion. The first bite involves the structural breakdown of foods due to the interaction with teeth [14] and as a process is crucial since during breakdown the surface area that comes in contact with saliva increases allowing for further chemical degradation by the saliva enzymes [14].

Several attempts have been made to physically replicate the chewing process in a lab environment, through apparatus that simulates the movement of the teeth and measures the reaction force using strain gauges [128, 129]. Although the results obtained by such experimental set-ups are useful to characterise the food under investigation, it is difficult to derive safe conclusions that will allow an efficient food design [130]. For this reason, a reliable simulation tool is needed which can perform reliable virtual first bite simulations. A computational model allows for efficient product development and optimisation by providing a tool whose parameters can be easily changed and new configurations can be quickly and efficiently tested [74].

Harrison et al. [14, 13] used a coupled bio- mechanical-smoothed particle hydrodynamics (B-SPH) model that predicts the food breakdown due to the interaction of the food with saliva and anatomical structures of the mouth (tongue, teeth, cheeks). Although

this study takes into account a more accurate scenario where the food interacts with more surfaces in the mouth, the constitutive model used was a simple elastic-perfectly plastic model coupled with a simple fracture criterion. The SPH method is a numerical method that allows to model complex motions and large deformations by using a Lagrangian mesh free framework that uses particles to represent the volume under consideration [13, 131]. Dejak et al. [132] presented an FE model to analyse the stresses induced by the molar teeth during chewing of morsels using various elastic moduli. Skamniotis et al. [74] demonstrated an FE model in the ABAQUS/Explicit solver that simulates the first bite of pet food. In this model a more sophisticated viscoplastic material model was used coupled with a ductile damage evolution law that is driven by the fracture toughness. The results of this study were promising although a local damage model was used, making the simulation to be mesh dependent. This is the problem that the current thesis tries to improve by applying a non-local damage model.

The physiological conditions of the mouth during the first bite are important in creating a reliable FE model. Bite force is an important variable to investigate as it influences the fragmentation of the food. The most widely accepted recording device for measuring bite forces is the strain-gauge bite force transducer [133, 134, 135]. Biswas et al. [136] measured the bitting force of the molar teeth in a transduction device. The data obtained from the bitting forces showed that the axial forces can range between $77-2440\,\mathrm{N}$ and the lateral forces are less than $100\,\mathrm{N}$. Force measurement has been conducted to assess both the force required for mastication and maximum bite force. From measurements conducted in foods such as carrots and biscuits, forces were measured in the range $70-150\,\mathrm{N}$ [137]. Gibbs et al. [138] reported maximum bite forces within the range $500-700\,\mathrm{N}$. Hagbert [139] reported average maximum bite force between the molar teeth in the range $600-700\,\mathrm{N}$. It is also worth noting, that the bite force does not only depend on the material properties but also the geometry of the food, such as the width and the depth of the food [140]. Den et al. [140] reported that the maximum bite force increased with increasing thickness of two apple varieties.

The chewing speed is another parameter that plays an important role during the first bite [141, 142]. Meullenet et al. [143] reported chewing speed ranging between 26-35.1 $\mathrm{mm\,s^{-1}}$. Sánchez-Ayala et al. [144] used a cylindrical silicon test material similar to Buschang et al. [145] and the chewing speed measured was $26.2\,\mathrm{mm\,s^{-1}}$. These values are somewhat higher than those reported by Yoshiba et al. [146] ($19.4\,\mathrm{mm\,s^{-1}}$), Gomes et al. [147] ($16.8\,\mathrm{mm\,s^{-1}}$) and Throckmorton et al. [148] ($21.83\,\mathrm{mm\,s^{-1}}$). The differences in these chewing rate values can be related to the type of food used and also the shape of the specimens that the volunteers were asked to chew [144]. The study of Bates et al. [149] gives a wider range between $19.3\,\mathrm{mm\,s^{-1}}$ and $40\,\mathrm{mm\,s^{-1}}$. In the present study, the chewing speed used in the FE simulations is limited by the maximum speed ($15\,\mathrm{mm\,s^{-1}}$) that can be reached by INSTRON.

The chapter describes the FE model developed based on the explicit Johnson Cook constitutive model, presented in chapter 2, coupled with the non-local damage model presented in chapter 3. Although mastication can be characterised as a multiphysics phenomenon, which involves mechanical and thermal loads in addition to the degradation due to the interaction of the food with the saliva [150], in the current work the simulation of the first bite takes into account only the effect of the mechanical loads and the fracture of the food specimen is assumed to be caused by the contact of the teeth with the food. This is a reasonable assumption that has been adopted in the literature [73], since the fragmentation of the food during the first bite takes place in a very short time scale (~ 0.5 s [151]), not allowing the thermal loads and the enzymatic reaction to influence the process. In addition, the boundary conditions i.e. the jaw trajectories, were simplified by considering a linear vector of lower jaw against the upper jaw. The set-up of the chewing approach is presented first, including a physical chewing test which is replicated in FE as well as details on the simulation techniques employed. Furthermore, the fragmentation of the micro-aerated chocolate samples measured from the experimental set-up is compared against *in vivo* measurements.

5.2 Teeth geometry and boundary conditions

A digitised adult male 3D skull, generated using X-ray computed tomography, was used to extract a pair of the two last molar teeth for the FE simulations (Figure 5.1a). The data were provided by Nestlé as an STL format, which was processed in SOLIDWORKS and then imported as a STEP file in ABAQUS, as shown in Figure 5.1b. It is worth noting that the upper and lower jaw geometries are going to be used in both FE simulations and will be 3D printed for the experimental set-up. In order to aid the experimental procedure and simplify the model, the last two sets of molar teeth as shown in Figure 5.1a are extracted from the full jaw geometry and are tilted in order to become normal to the laboratory surface. To isolate the pair of the two molar teeth, the upper and lower jaws were cropped and the free edges were covered to create a closed surface that allowed the created volumes to be 3D printed.

In order to attach the pair of molar teeth, extracted from the full jaw model as described earlier, onto an Instron universal testing machine, adaptors were designed as shown in Figure 5.2. The adaptors were designed directly opposite to each other in order to provide the proper alignment with the load cell axis such that moment forces do not induce errors in the measurements. The adaptors were 3D printed together with the molar teeth as one continuous specimen using a Stratasys Dimension 1200es machine and were made of Acrylonitrile Butadiene Styrene (ABS).

In the present study, the assumption that the trajectory of the mandible remains linear during the duration of the first bite was adopted, similar to the study of Skamniotis et al.

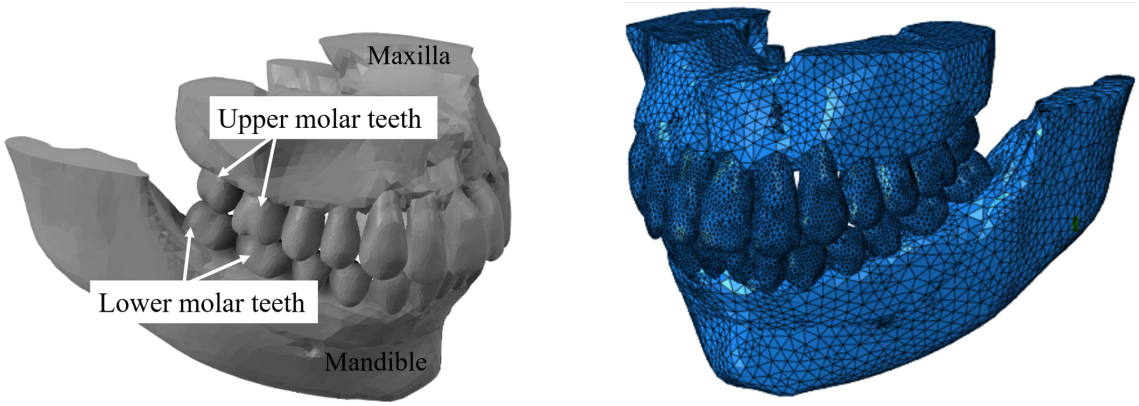

(a) (b)

Figure 5.1: (a) Representation of upper and lower molar teeth used in the FE simulation after segmented from the full jaw geometry.(b) Full jaw geometry after processing in SOLIDWORKS and before segmentation of the molar teeth.

[74] and Evans and Fortelius [152]. This approximation is adopted in order to simplify the model, since there already many parameters that are taken into account such as the non-local damage model and the strain rate dependent behaviour of the material. Some studies in the literature take into consideration more physical parameters that might influence the structural breakdown of food, but more simplified material and damage models were used [14, 13, 132]. Also this simplification allows the comparison of the FE model with an experimental set-up developed in a conventional uniaxial testing machine, without the need of a more sophisticated multiaxial testing machine.

5.3 First bite experiment

5.3.1 Experimental set-up of the first bite

The main purpose of the chewing experiment is to provide both qualitative and quantitative data. The qualitative data regard the influence that micro-aeration has on the fragmentation. These results will be compared with *in vivo* mastication results presented in detail by Bikos et al. [11] (shown in section 5.4) The quantitative data are the force-displacement test machine recordings that are used to validate the numerical results (shown in section 5.5).

The experimental set-up, shown in Figure 5.3, consists of an Instron universal testing machine with a 1 kN load cell, the 3D printed molar teeth and a camera to capture the different video frames during fragmentation. The chocolate specimens were cut using a razor blade in lengths of 10 mm. The width of 14 mm and height of 8 mm was provided from the manufacturing process of the specimens and overall the cross sectional area was 140 mm^2. These dimensions correspond to a mass of 1.5 g, which is consistent with the

Figure 5.2: The pair of the last two molar teeth was 3D printed as a continuous specimen with adaptors, allowing the proper alignment in the Instron universal machine.

study of Lucas and Luke [153] and in the range of the mouthful size [1, 154, 155]. The specimens were positioned as shown in Figure 5.3, having contact with both the two last molar teeth of the upper and lower jaw.

Three different speeds of, $\dot{\delta} = 8, 10, 15\,\mathrm{mm\,s^{-1}}$, were tested to examine the effect of rate dependency on the chocolate specimens. Although the mastication speed, recorded in the literature, is closer to the latter (higher) test speed, additional speeds were examined to test the repeatability of the results and verify the rate dependent behaviour of the material. The opening between the upper and lower teeth was specified by the height of the specimen ($\sim 8\,\mathrm{mm}$) and the initial position was adjusted before each test due to a slight variation in the height of the samples (due to the manufacturing process). The displacement, δ, was allowed to increase until $\delta = 7\,\mathrm{mm}$ allowing the test to terminate $1\,\mathrm{mm}$ before the upper and lower teeth come in contact to avoid damage to the load cell. The tests were repeated five times for each speed and both the non-aerated chocolate and the $f = 10\mathrm{vol}\%$ and $f = 15\mathrm{vol}\%$ micro-aerated chocolate samples were tested.

5.3.2 First bite experimental results

Figure 5.4 depicts the force-displacement data obtained for the three different speeds and the three micro-aeration levels. The error bars correspond to the maximum and minimum values across the five repeats of each test. There was a very good repeatability in all tests as shown in Figure 5.4. For all speeds and all micro-aeration levels, there is

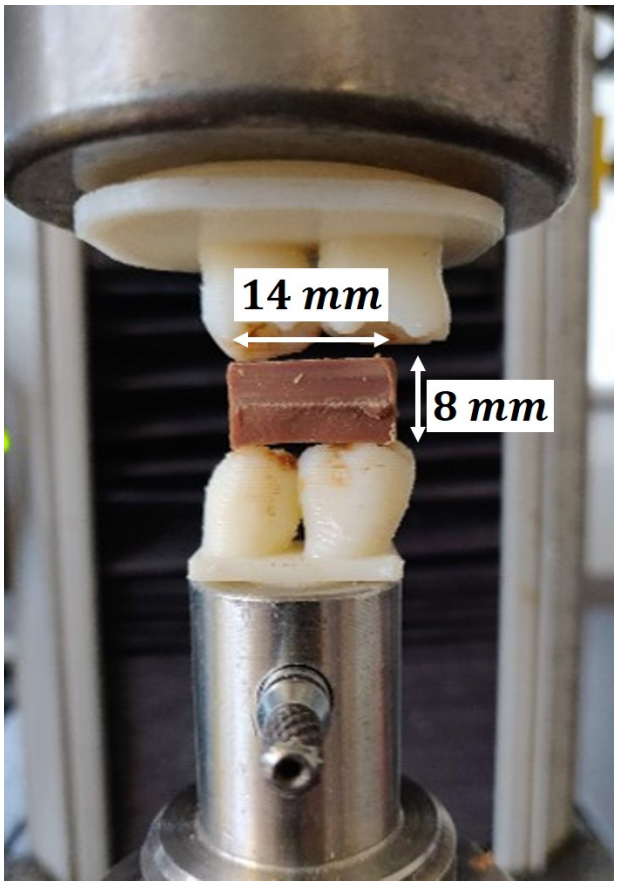

Figure 5.3: Experimental set-up consisting of the 3D printed upper and lower molar teeth with their adaptors, the Instron universal machine and the chocolate specimen placed between the teeth. The specimen dimensions are also shown. The horizontal line that is visible in the chocolate frames is due to the razor used to cut the specimens to the desired geometries.

an initial non-linear increase in force, followed by a sudden drop. The maximum force value corresponds to the fracture of the specimen due to the contact with the teeth. This force decrease is followed by another increase, which is a result of the compression of the already broken pieces in between the teeth. It is worth noting that the main interest of the current study is to capture the fragmentation of the specimen and for this reason the FE model will investigate only until when the specimen is considered as fully fractured, so until the sudden drop of the forces.

It is evident that increasing speed results in higher forces required for food breakdown, attributed to the rate dependent nature of the chocolate, as it has been already discussed in chapter 2. Focusing on the effect of micro-aeration on the bite forces, Figure 5.4 clearly shows that the higher the micro-aeration level, the lower the required bite forces for the fragmentation. This is a reasonable result, expected from the compression experiments, which showed that micro-aeration decreases the fracture strain for damage initiation. For the highest speed of, $\dot{\delta} = 15\,\mathrm{mm\,s^{-1}}$, which is as already stated the most appropriate to study, the maximum force drops from 59.8 N for the non-aerated to 49.3 N for $f = 10\mathrm{vol}\%$

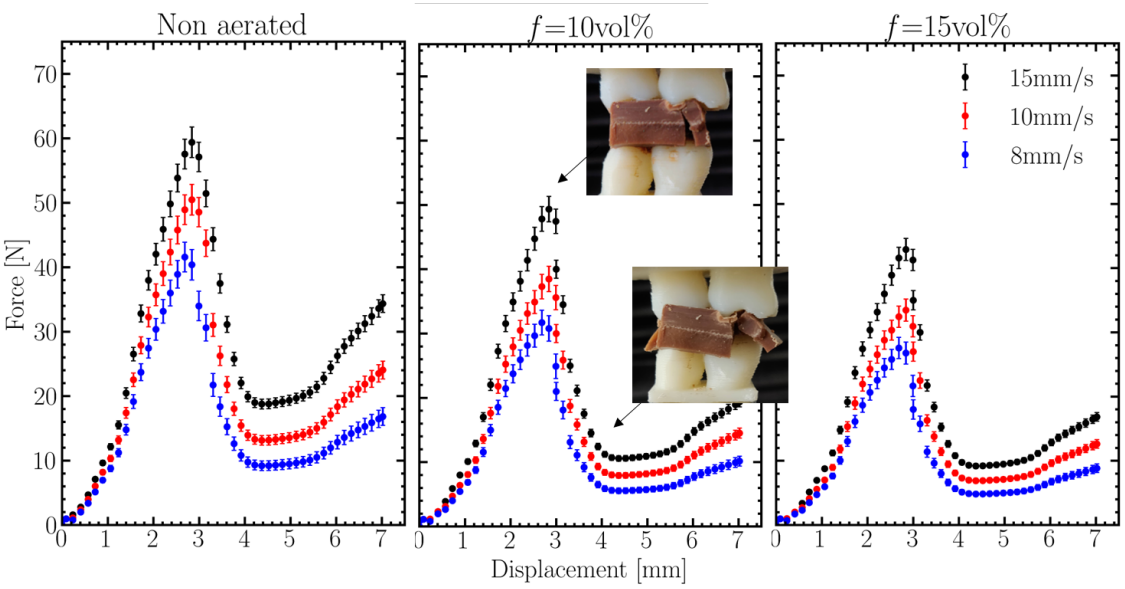

Figure 5.4: Force-displacement data obtained from the experimental set-up. Comparison between non-aerated samples, 10vol% and 15vol% micro-aerated samples. The results from three different chewing speeds are presented. The horizontal line that is visible in the chocolate frames is due to the razor used to cut the specimens to the desired geometries.

and to 42.9 N for $f = 15$vol%, resulting in 17.5% and 28.2% reductions respectively.

5.4 Fragmentation results

In this section the fragmentation results from the experimental set-up will be compared with *in vivo* mastication test results presented in the study of Bikos et al. [11]. For the *in vivo* tests, the chocolate specimens were placed in thin plastic sealed bags of 0.02 mm thickness, to avoid the contact of the specimens with the saliva and the inner mouth surfaces. Isolating the food specimen using sealed bags, allows for the study of fragmentation due to the interaction with the teeth without taking into account other effects, for example the chemical decomposition of the chocolate. The same procedure was also followed for the *in vitro* experiment where the experiment presented in section 5.3 was repeated with food specimens in silicon bags. The effect of the silicon bags on the force-displacement curves was investigated by comparing the force-displacement curves with the without the silicon bags present. It was found that the results are not influenced by the presence of the silicon bag and the force-displacement measurement with the silicon bag lie in the error bar range of the values obtained without the silicon bags. Although, saliva is not present in the experimental set-up and the fragmentation is caused only due to the interaction with the teeth, the chocolate specimens were placed in silicon bags to ease the collection of the fragments after the end of each experiment. The configuration of the teeth with the chocolate specimen in the silicon bag is shown in Figure 5.5.

The *in vivo* mastication tests were conducted by five volunteers, who were asked to

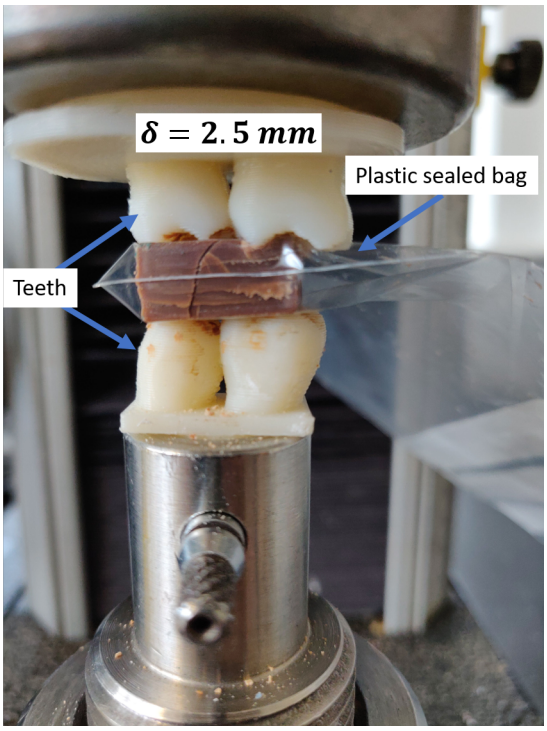

Figure 5.5: *In vitro* experimental set-up to study how fragmentation is influenced by micro-aeration. The samples were place in silicon bags to ease the collection of the fragments after the end of the test. Frame capture at a displacement $\delta = 2.5\,\text{mm}$ for a non-aerated sample at a speed of $\dot{\delta} = 15\,\text{mm}\,\text{s}^{-1}$.

chew the chocolate specimens for one cycle. The volunteers were asked to place the specimen between the molar teeth and chew naturally; no further instruction was given regarding the applied force or the speed that they would apply to perform the bite. Afterwards, the plastic sealed bags were collected and the fragments were studied through image analysis techniques [155] using the open source software ImageJ (v1.52 National Institutes of Health) [156]. The fragments were removed from the plastic sealed bags and a colour image was captured, as shown in Figure 5.6a. The colour images were imported into ImageJ, where the image contrast was changed in order to make the edges of the fragments more visible and the different fragments more distinct. The images were then turned into 8-bit format (black and white), as shown in Figure 5.6b, and the process for calculating the 2D area covered by the fragments was enabled. The methodology presented by Bikos et al. [11] was followed for the estimation of the fragmentation for the *in vitro* tests of this study. The surface area covered by the fragments was converted to an equivalent diameter which corresponds to the same area. Based on these diameters the size distribution was computed and averaged across the five volunteers. The methodology developed by Sahagian and Proussevitch [157] was applied to convert the 2D diameter distribution into a 3D size distribution . This approach takes into account any random cut plane and any shape of particles to convert the 2D size distribution into a 3D distribution and therefore to correct any errors associated with the naturally fractured 2D surfaces.

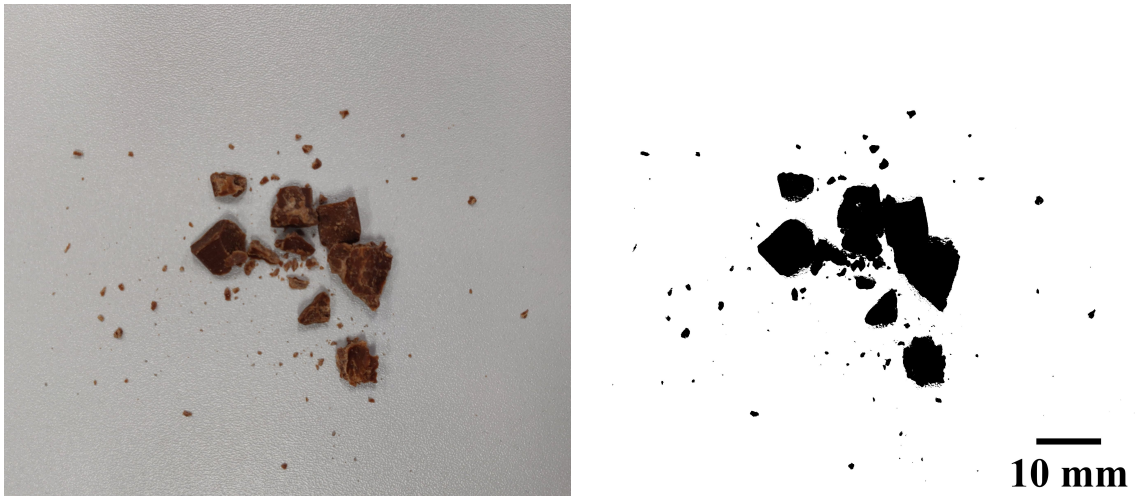

(a) (b)

Figure 5.6: (a) Representative example of chocolate fragments after the *in vitro* tests of non-aerated samples was examined; similar fragments are obtained from the *in vivo* tests, (b) binary image used to calculate the size distribution of the fragments.

The same methodology was followed for the estimation of the fragments from the *in vitro* experiment.

Figure 5.7a depicts the fragmentation results for the *in vivo* and *in vitro* non-aerated chocolate specimens. The blue scatter points are acquired from the study of Bikos et al. [11] and are compared with the *in vitro* experimental results for three different speeds. During the first bite, over 76% of the non-aerated fragments are smaller that 1.25 mm, compared to the respective value of 88% for $f = 15$vol% micro-aerated samples (Figure 5.7b). At this point, it is worth noting that the $f = 10$vol% chocolate samples were not included in the fragmentation study, since there were not available *in vivo* fragmentation results. Comparing Figures 5.7a and 5.7b it is evident that the micro-aerated chocolate specimens break into more smaller pieces comparing to the non-aerated samples, implying that the fragmentation is aided by micro-aeration.

As observed in Figures 5.7a and 5.7b, the fragmentation of the chocolate is influenced by the speed due to the rate dependent behaviour of the material. As the speed increases, the fragmentation distribution approaches the *in vivo* results for both the non-aerated and the $f = 15$vol% micro-aeration level. As already mentioned, the most relevant speed is the $\dot{\delta} = 15\,\mathrm{mm\,s^{-1}}$ since it is closer to the physiological conditions in the mouth.

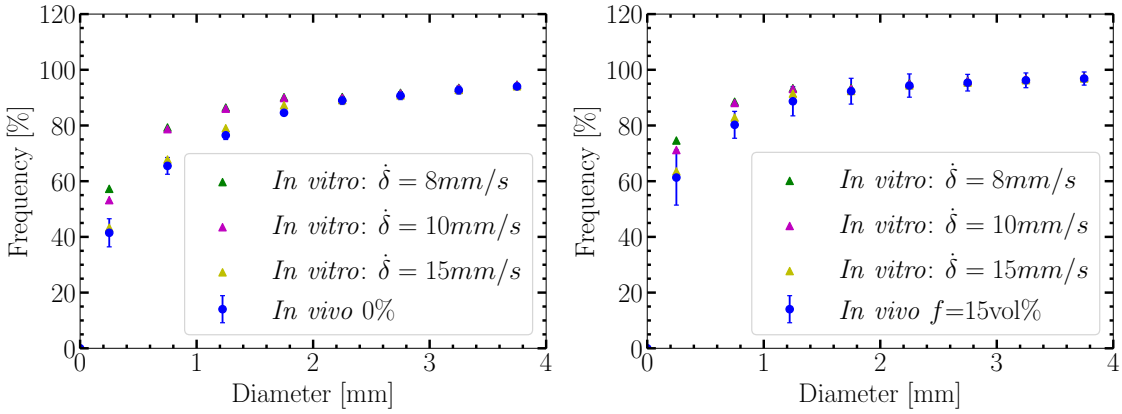

(a) (b)

Figure 5.7: Comparison of fragment diameter between *in vitro* and *in vivo* mastication tests conducted for (a) non-aerated samples and (b) $f = 15$vol% micro-aerated samples. The *in vivo* results were obtained from the study of Bikos et al. [11].

5.5 Finite element simulation of the first bite

5.5.1 FE simulation model

The same geometry of the 3D printed pair of molar teeth was imported in ABAQUS via using discrete rigid surfaces for the teeth and a deformable part for the food specimen, according to the dimensions used in the experimental set-up and the *in vivo* testing. (Figure 5.8). At this point, it is worth noting that the 3D printed teeth are considered as rigid, since the ABS is stiffer than the chocolate ($E_{ABS} \approx 1.9 - 2\,\text{GPa} > E_{ch} \approx 0.1\,\text{GPa}$ [158]). In addition to that, a compliance test was employed to eliminate any effects that a possible deformation of the ABS has due to interaction with the chocolate.

The upper and lower jaws were meshed with 23742 four-node 3D bilinear rigid quadrilateral elements (R3D4), whereas the food specimen was meshed with 140000 eight node thermally coupled bricks, trilinear displacement and temperature elements (C3D8T) [17]. A detailed discussion regarding the mesh sensitivity of the model will be provided in the following paragraphs. As already mentioned in chapter 3, a fully coupled thermal-stress analysis in ABAQUS/Explicit is chosen for the implementation of the non-local damage model, although there is no consideration of temperature in the model. The heat transfer equations are integrated for the calculation of the temperature that plays the role of the non-local equivalent plastic strain.

In ABAQUS/Explicit the heat transfer equations are integrated using the explicit forward-difference time integration rule, according to the following equation:

$$\theta^N_{(i+1)} = \theta^N_{(i)} + \Delta t_{(i+1)} \dot{\theta}^N_{(i)} \tag{5.1}$$

where θ_i^N is the temperature at node N at the time increment i of the explicit step. The already known value of $\dot{\theta}_{(i)}^N$ is used to calculate the temperature of the next increment and is obtained by:

$$\dot{\theta}_{(i)}^N = \left(C^{NJ}\right)^{-1}\left(R_{(i)}^J - F_{(i)}^J\right) \tag{5.2}$$

where C^{NJ} is the lamp capacitance matrix, R^J is the applied nodal source vector and F^J is the internal flux vector. This solution scheme is applied for the estimation of the temperature (non-local plastic strain in the current model), whereas the displacement is obtained using the central difference integration solution scheme to integrate the dynamic equilibrium equations explicitly. The dynamic equilibrium equations are satisfied at the beginning of the increment, t, and the accelerations calculated at time t are used for the estimation of velocities and displacements according to the following equations:

$$\dot{u}_{\left(i+\frac{1}{2}\right)}^N = \dot{u}_{\left(i-\frac{1}{2}\right)}^N + \frac{\Delta t_{(i+1)} + \Delta t_{(i)}}{2}\ddot{u}_{(i)}^N \tag{5.3}$$

$$u_{(i+1)}^N = u_{(i)}^N + \Delta t_{(i+1)}\dot{u}_{\left(i+\frac{1}{2}\right)}^N \tag{5.4}$$

where u^N is the displacement at node N and the subscript i is the increment number of the explicit step. The central difference integration scheme is quite simple since it uses the already known values $\dot{u}_{\left(i-\frac{1}{2}\right)}^N$ and $\ddot{u}_{(i)}^N$ from the previous increment to calculate the displacement of the next increment [17]. The accelerations are computed using the diagonal element mass matrices according to:

$$\ddot{u}_{(i)}^N = \left(M^{NJ}\right)^{-1}\left(P_{(i)}^J - I_{(i)}^J\right) \tag{5.5}$$

where M^{NJ} is the mass matrix, P^J is the applied load vector and I^J is the internal force vector. The explicit dynamics analysis performs a large number of small inexpensive time increments (compared to the direct integration dynamic analysis that is followed in ABAQUS/Implicit) since there is no solution for a set of simultaneous equations.

Another important parameter in the FE simulation of the first bite is the definition of contact between the teeth and the specimen. Following the study of Skamniotis et al. [74] the general contact option of ABAQUS/Explicit was used, which identifies surfaces in the 3D model assembly and generates contact forces to resist unreasonable penetrations. In the FE model, all the exterior and interior elements of the sample were assigned an element-based surface which was included in the contact domain. Thus, all the elements that consist the food specimen volume are allowed to be in contact between themselves (self-contact) as well as in contact with the teeth surface. The self contact parameter was necessary in this study since the final fragmentation of the specimen, driven by the element deletion, could cause some elements of the food specimen to come in contact

with each other.

The friction coefficient between the teeth and the food specimen plays an important role and influences significantly the results of the first bite simulation. Following the study of Skamniotis et al. [74] the tangential interaction behaviour available in ABAQUS was applied through the penalty contact option. Due to the lack of information regarding the coefficient of friction between the teeth and the chocolate, the tribology experiments (shown in chapter 6) were used as a guide in order to get a rough indication of the coefficient of friction. As will be presented in chapter 6 the coefficient of friction between the non-aerated chocolate and the PDMS (tongue substrate) was measured as $\mu = 0.42$ in dry conditions (no artificial saliva present). The same value drops to $\mu = 0.33$ and $\mu = 0.2$ for the $f = 10$vol% and $f = 15$vol% micro-aerated samples respectively. The ABS is noticeably rougher that the PDMS ($E_{PDMS} = 2$MPa[159]) so the coefficient of friction implemented in the FE models was assumed to be higher than $\mu = 0.42$ and following the study of Skamniotis et al. [74] in the mastication pet food, a parametric analysis for μ in the range $0.5 - 0.8$ will be conducted. It is worth noting that the measurement of the exact coefficient of friction between 3D printed molar teeth and chocolate was not possible due to the complex geometry of the teeth.

Regarding the boundary conditions of the chewing model, the maxilla was constrained in all translations and rotations, whereas the mandible was fixed in all translations and rotations besides the z-axis. It is worth noting to avoid confusion that in Figure 5.8 the maxilla appears on the top and the mandible at the bottom of the configuration. This was in order to have a direct comparison with the experimental set-up, where the mandible was attached on the top moving head of the Instron whereas the maxilla was placed at the bottom fixed head. This is the reason why the model appears rotated by 180°.

5.5.2 FE simulation Results & Discussion

In this section the force-displacement data computed from the simulations will be compared with the experimental results for all micro-aeration levels. Different coefficient of friction values will be examined and the FE model will be compared with video frames of the experiment to capture the fracture of the specimen due to the interaction with the molar teeth. In addition, the efficiency of the non-local damage model will be investigated, through a comparison between the local and the non-local damage model.

Different coefficient of friction values ranging between $\mu = 0.5$-0.8 for the non-aerated samples, were tested and the force-displacement results are shown in Figure 5.9. Increasing the coefficient of friction value resulted in higher forces for food fracture, as expected. In these simulations the non-local damage model was applied and the coefficient of friction $\mu = 0.8$ was found to agree with the experimental observations. Therefore, this value was kept constant for the rest of the simulations of the non-aerated

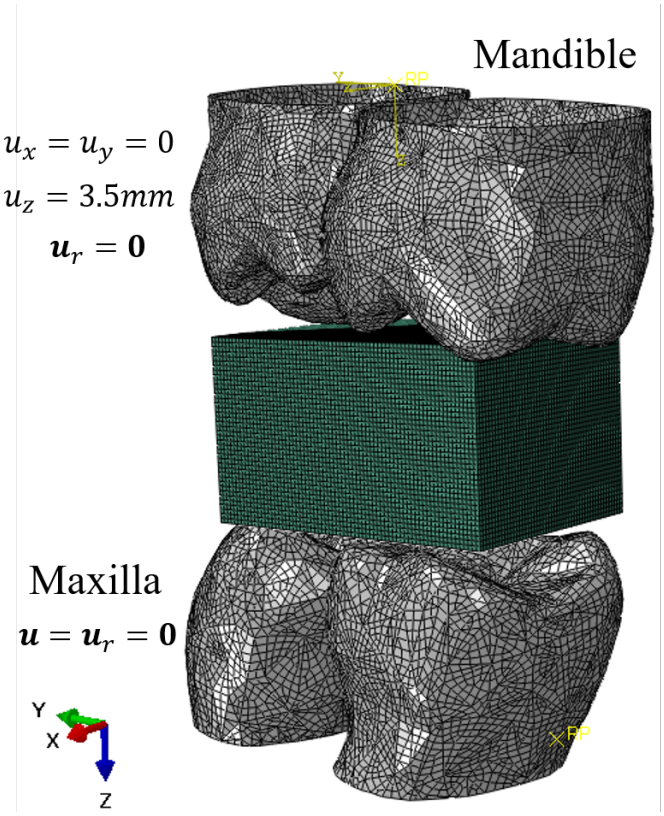

Figure 5.8: Chewing FE model assembly with the exact position of mandible, maxilla and food. The model appears 180° rotated to be consistent with the experimental set-up.

samples. The coefficient of friction values for the $f = 10$vol% and $f = 15$vol% were estimated based on the tribological experiments (shown in chapter 6) and the methodology followed will be presented in detail.

Mesh objectivity is crucial for the study of fragmentation. As already mentioned in chapter 3, damage laws based on the continuum damage mechanics theory suffer from mesh dependency. This is evident in Figure 5.10 where a coarse (100000 elements) and a dense (140000 elements) mesh discretisation of the food specimen are compared. The force-displacement data obtained from the local damage model follow a different behaviour, as the mesh becomes more dense, higher forces are obtained. This behaviour results in different fragmentation paths implying that the FE model with the local damage law is unreliable for predicting the fracture and furthermore the effect that micro-aeration has on the fragmentation. The mesh dependency is overcome by the implementation of the non-local damage law driven by the non-local equivalent plastic strain through the VDFLUX subroutine. The two blue scatter lines correspond to the same mesh densities, as the ones used with the local damage model, and a similar force-displacement trend is obtained, implying the mesh objectivity of the results. In this application the internal characteristic length, l_{ch}, which is a calibration parameter that depends on the size of the food specimen was chosen as $l_{ch} = 0.1$ mm and the rest of the calibrating parameters of the constitutive law remained the same (see Table 5.1). The l_{ch} is the same as in the

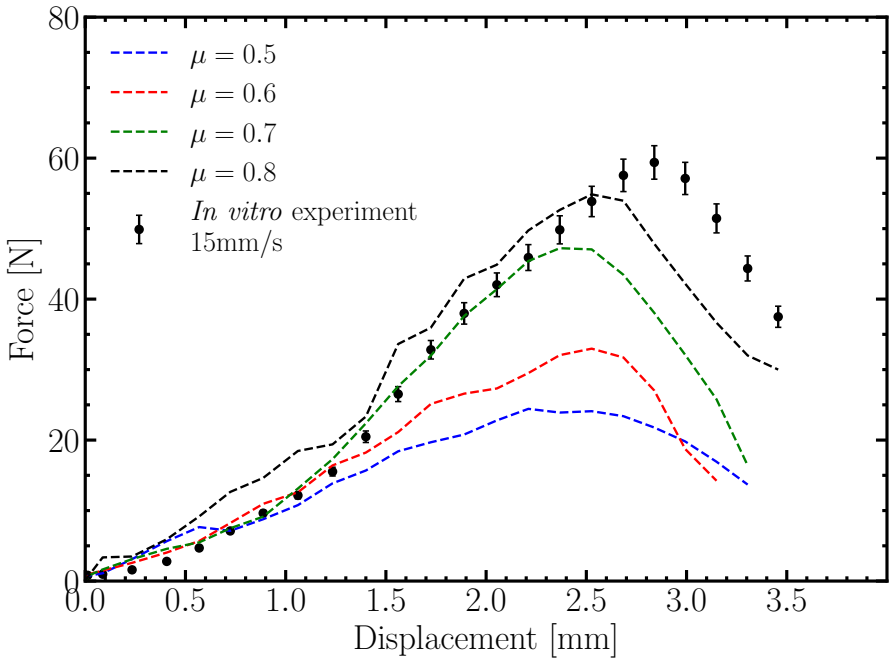

Figure 5.9: Comparison of the experimental and FE force-displacement data for different values of friction coefficient for the non-aerated chocolate. The non-local damage model and a mesh with 140000 elements were used for these simulations.

benchmark tests of section 3.6 as the size of the specimens used is in the same length scale range as the chocolate specimen of the first bite simulation.

The implementation of the non-local damage model ensures that the FE simulation results are mesh independent. This is a crucial aspect of the simulations since mesh dependent results would result in different fracture paths leading to unreliable fragmentation results. Figure 5.11 presents results of the first bite model for the non aerated chocolate where now only one mesh density is considered (140000 elements) and the simulations are repeated for different speeds according to the *in vitro* experiments. The results of Figure 5.11 show a good agreement between the *in vitro* experiments and the non-local FE simulations, fact that is attributed to the modified Johnson-Cook constitutive model that is used to capture the rate dependent mechanical properties of the chocolate.

At this point, special care should be taken on the time increment of the simulation. The time increment in the coupled temperature-displacement step is computed according to equation (3.30) and depends on the density, the element size, the thermal conductivity (replaced by the internal characteristic length) and the specific heat. From those parameters, only the specific heat does not have a physical meaning and is chosen according to equation (3.31) in order to have a reasonable time step that allows the model to converge in reasonable computational time. Table 5.1 summarises all the parameters used in the macroscopic first bite simulations.

Figure 5.12 depicts a comparison for the non-aerated chocolate between the FE model simulation and the experimental set-up for different time frames A, B, C and D for $\dot{\delta} =$

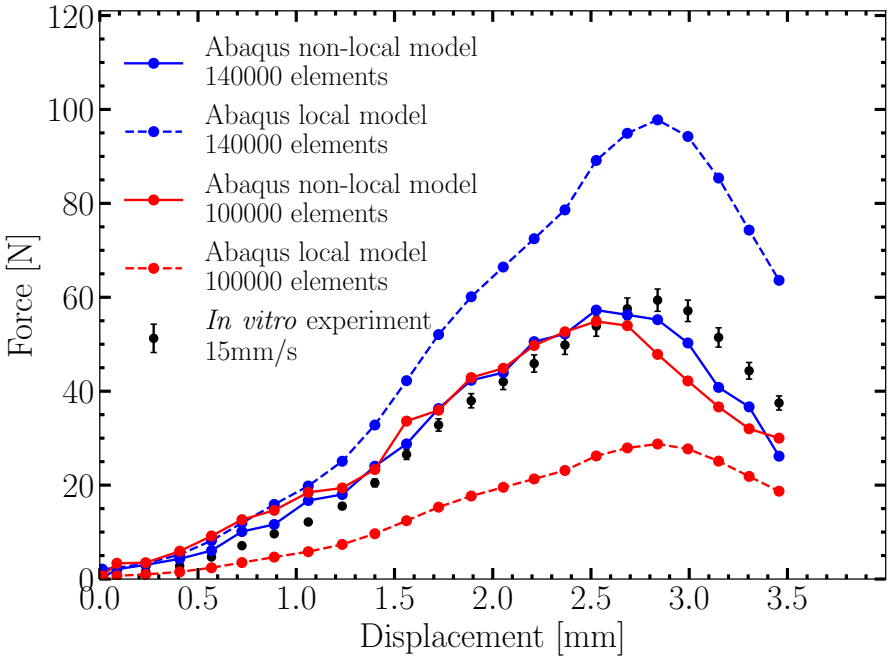

Figure 5.10: Comparison between *in vitro* experimental and FE force-displacement data for the non-aerated chocolate. The FE results include a comparison between the non-local and the local damage model for two different mesh densities. The coarse mesh has 100000 elements, whereas the dense mesh has 140000 elements. The coefficient of friction was $\mu = 0.8$ for these simulations.

$15\,\mathrm{mm\,s^{-1}}$. From Figure 5.12 (stage *B*) it is evident that, at the point of contact between the chocolate and the teeth the strain starts to increase leading to the crack initiation which is depicted at stage *C*. The strains increase even more as the displacement of the lower molar teeth increases (Figure 5.12 (stage C)) and the failure criterion is met and crack propagation initiates until complete fracture is occurred for a displacement of $\delta = 2.5\,\mathrm{mm}$ (Figure 5.12 (stage *D*)). The crack that is present in the chocolate sample in the experiment, shown in Figure 5.12 (stage *D*), it is captured well by the FE model. The methodology that is followed for the crack propagation through element removal is well depicted in Figure 5.13, where the equivalent plastic strain is compared with the triaxiality values that are present at each time step. It is worth reminding that the crack in the FE model is simulated by element removal when the damage criterion, based on the non-local equivalent plastic strain, is met. As already presented in section 3.4 the equivalent plastic strain for the initiation of failure, depends on the stress triaxiality. For the first bite simulation, and following the study of Skamniotis et al. [12], the elements that have been removed correspond to shear and tension states whereas the elements between the teeth that experience compression (negative triaxiality) can withstand higher stresses and remain in the model. This is demonstrated in Figure 5.13, where the contour plots of the triaxiality, η, that elements experience during the simulation is presented. By comparing the left and right column of Figure 5.13, it is evident that the elements with high

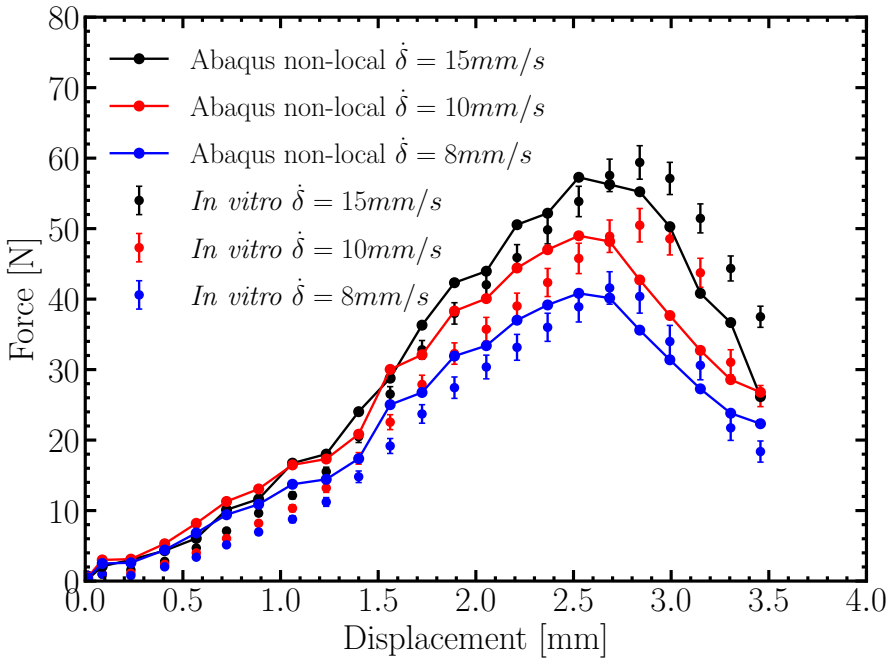

Figure 5.11: Comparison between *in vitro* experimental and FE force-displacement data for the non-aerated chocolate for different speeds. A mesh with 140000 elements and a coefficient of friction of $\mu = 0.8$ were used for these simulations.

equivalent plastic strains, that have not deleted from the model, are those that experience negative triaxiality, whereas those with triaxiality $\eta \geq 0$ have been deleted since the failure criterion has been met due to the high equivalent plastic strains at these triaxiality values. The same configuration presented in Figure 5.8 was used and the micro-aerated specimens were considered as homogeneous with the fracture properties that calculated in the micromechanical analysis of chapter 4. The contour plots of the $f = 10$vol% and $f = 15$vol% look similar to the non-aerated chocolate since in the FE simulations of the two micro-aerated samples, the chocolate is simulated as a homogeneous specimen using

Table 5.1: Material properties for the FE simulations of the first bite.

Parameter	**Value**
Density, ρ [kg m^{-3}]	1
Elastic modulus, E [MPa]	100
Poisson's ratio, ν [-]	0.49
A [MPa]	1.35
B [MPa]	3.5
C [-]	0.05
n [-]	0.8
$\dot{\varepsilon}$ [s^{-1}]	0.01
internal length, l [mm]	0.08
d_{cr}	0.1
specific heat, c [s/(kg/m^3)]	10^{-4}

the plastic and fracture properties as those calculated from the micromechanical analysis presented in chapter 4.

The implementation of the non-local damage model in the first bite simulation and the proven mesh independence of the force-displacement results (Figure 5.10) allows the implementation of the same model for the study that micro-aeration has on the fragmentation. As already mentioned, the same FE computational set up, presented in Figure 5.8, will be used for the simulation of the $f = 10$vol% and $f = 15$vol% micro-aerated samples and the chocolate specimen will be considered as homogeneous. Importing the chocolate specimen as a homogeneous part allows the simulation of the first bite in reasonable computational time, which would not be possible if the pores (in the micro-scale) were considered in the macroscopic simulation. This would restrict the minimum element size and subsequently increase the elements needed for the discretisation of the macroscopic chocolate geometry. Finally, since the results obtained by the simulations are mesh independent, due to the implementation of the non-local damage model, only mesh with 140000 elements will be considered in the following results. Initially, the $f = 10$vol% micro-aerated samples were simulated. The equivalent plastic strains at fracture initiation are implemented according to table 4.3 based on the micromechanical analysis, presented in chapter 4. In addition a lower coefficient of friction was used, since tribology experiments showed a drop of friction with the increase of micro-aeration level (as will be presented in chapter 6). For the $f = 10$vol% micro-aerated chocolates a coefficient of friction $\mu = 0.6$ was applied. This value was selected taking into account the 25% decrease, compared to the non-aerated samples, captured by the tribological experiments, shown in chapter 6. The assumption that the coefficient of friction due to micro-aeration between teeth and chocolate, reduces by the same percentage as in the tongue palate region, where the tribological experiments were conducted, is being made in this chapter. Figure 5.14 depicts the force-displacement data as obtained from the FE simulations in comparison to the experimental data for speeds of $\dot{\delta} = 8, 10$ and $15\,\mathrm{mm\,s^{-1}}$. The FE model is capable of capturing the force-displacement *in vitro* experimental data for three tested speeds. The rate dependent behaviour of the modified Johnson-Cook constitutive model used in the present thesis, allows the FE model to capture not only the trend of the force-displacement curve but also the rate dependency that is present due to the viscoplastic nature of the chocolate.

The same FE analysis was also applied for the $f = 15$vol% micro-aerated chocolate. The equivalent plastic strains at fracture initiation are implemented according to table 4.2 based on the micromechanical analysis, presented in chapter 4. Following the tribological results, which will be presented in chapter 6, where a 50% reduction compared to the non aerated coefficient of friction value was observed, the coefficient of friction between the teeth and the $f = 15$vol% micro-aerated chocolate was selected as $\mu = 0.4$ ($\mu = 0.8$ for the non-aerated). This coefficient of friction value was used for the FE simulations for the

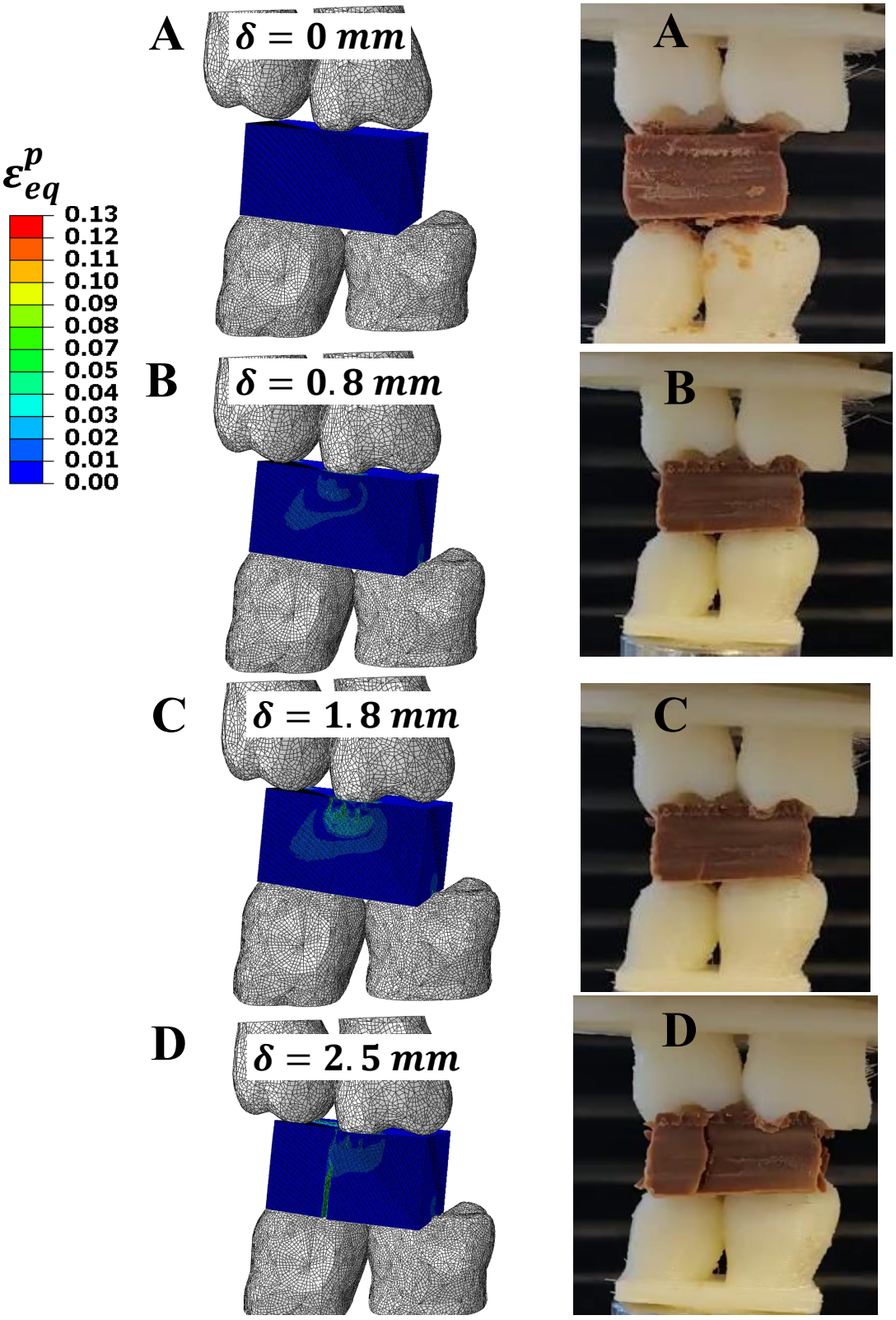

Figure 5.12: Comparison between the FE simulations (left) and video frames from the *in vitro* experiment of the first bite. The frames A, B, C and D correspond to the initiation of the experiment, two intermediate steps where the penetration of the teeth into the food has started and the final fracture respectively. These frames correspond to a non-aerated chocolate sample and the displacement, δ, for each frame is also depicted.

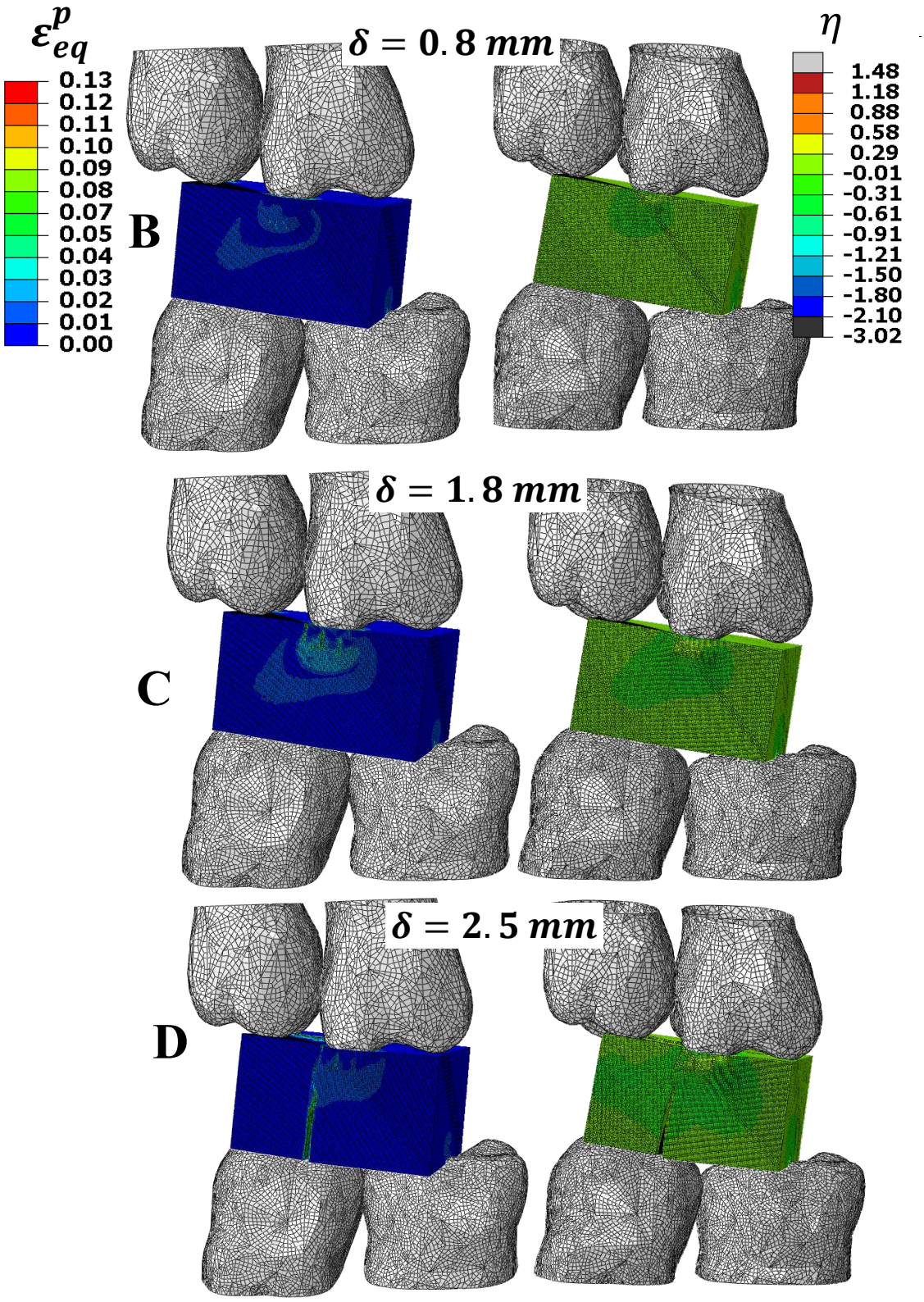

Figure 5.13: Comparison the equivalent plastic strain results (left) and the triaxiality (right) results calculated through the FE simulations. The frames B, C and D correspond to the respective notation of Figure 5.12 where point A has been omitted, since there are neither equivalent plastic strain nor triaxiality values recorded. These frames correspond to a non-aerated chocolate sample and the displacement, δ, for each frame is also depicted.

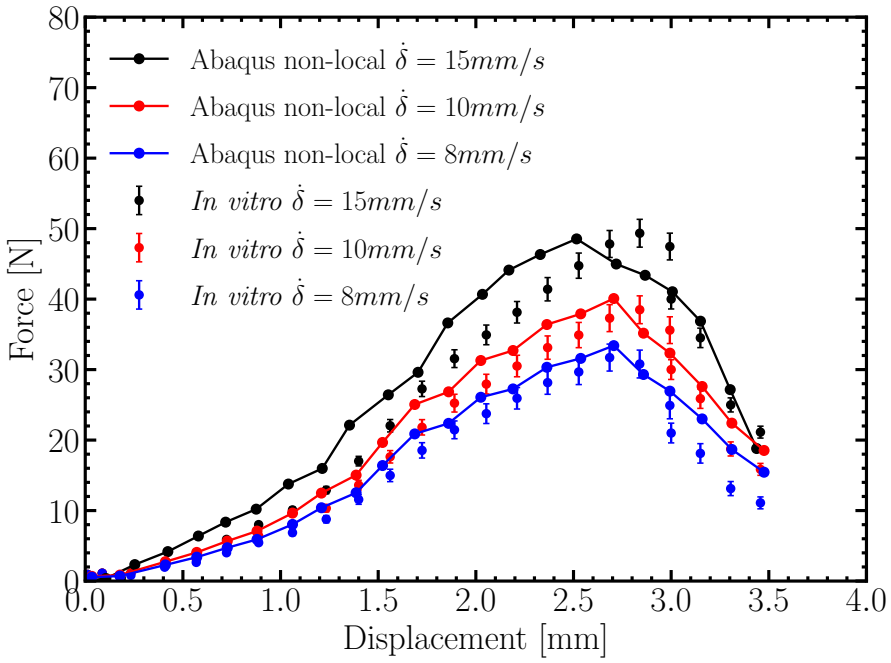

Figure 5.14: Comparison between experimental and FE force-displacement data for the $f = 10$vol% micro-aerated chocolate for different speeds. A mesh with 140000 elements and a friction coefficient of $\mu = 0.6$ were used for the FE simulations.

three different speeds $\dot{\delta} = 8, 10$ and $15\,\mathrm{mm\,s^{-1}}$ and the force-displacement data are shown in Figure 5.15. Similar to the non-aerated and the $f = 10$vol% micro-aerated chocolate simulations, the model is in good agreement with the *in vitro* experimental data for all the tested speeds, revealing the rate dependent properties of the constitutive model used.

5.6 Conclusions

In this chapter the FE configuration and the parameters applied for the simulation of the first bite were initially presented. The implementation of the non-local damage model in the FE simulation provided the desirable mesh objectivity in the model providing a reliable computational tool to study how fragmentation is influenced by the change in structure of the food i.e. micro-aeration.

In addition an experimental set-up for the *in vitro* study of the first bite was presented. The same pair of teeth was 3D printed and it was attached in a Instron machine to extract force-displacement data in order to validate the FE model. Different friction coefficients were tests for the non aerated chocolate and the respective values for the micro-aerated samples of 10vol% and 15vol% were estimated taking into consideration the friction decrease as measured from the tribology experiments. The results showed a good agreement between experiment and FE model and the efficiency of the non-local damage model in all micro-aeration levels was evident. The models were also capable of capturing the

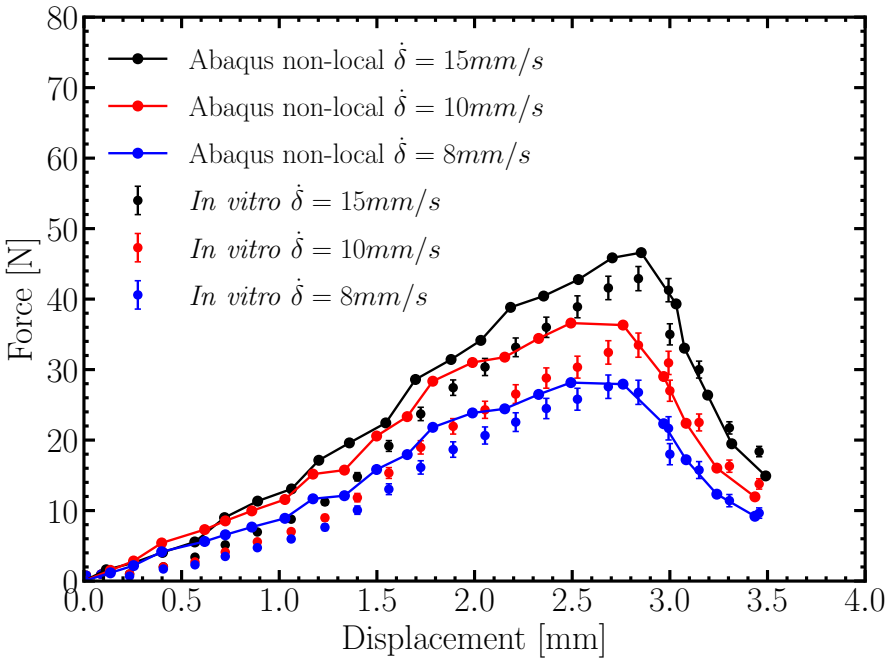

Figure 5.15: Comparison between experimental and FE force-displacement data for the $f = 15$vol% micro-aerated chocolate for different speeds. A mesh with 140000 elements and a friction coefficient of $\mu = 0.4$ were used for the FE simulations.

force-displacement data for different chewing speeds. This is attributed to the viscoplastic behaviour of the Johnson-Cook constitutive model.

Finally, the *in vitro* fragments were compared with *in vivo* mastication results provided by five volunteers. The different fragmentation results for different chewing speeds validated the strain rate dependent behaviour of the specimens and agreed with the *in vivo* results.

6 Measurement of molten chocolate friction under simulated tongue-palate kinematics: effect of cocoa solids content and micro-aeration

* Published in Current Research in Food Science [4]

Topics

6.1 Introduction

Food mastication is a complex dynamic procedure that involves multiple oral operations resulting in the breakdown of food in the mouth until swallowing. Throughout the food consumption, various interactions of the oral cavity, including the tooth-tooth and the tongue-palate contacts take part in the process. During mastication the structure of the foods changes and different components contribute to the texture and taste perception [160]. Texture perception, which includes aspects such as smoothness and slipperiness, is usually related to mechanical stimulation and hence friction experienced in the mouth [161].

Food texture is considered a multidimensional tactile sensation that is influenced by the composition, structure, rheology and surface properties of the food as it is sheared between the tongue and palate. Extensive research has already been conducted into the bulk properties of foods and the relationship to oral texture, mainly through rheological studies [162, 163]. However, this method does not quantify the mouth-feel sensation, which is mainly correlated with the thin film formation in the tongue palate contact zone [164]. According to Dresselhuis et al. [165, 166] "*an aspect that is not measured by rheology, but is probably sensorial relevant, is the process of rubbing and squeezing the*

product between tongue and palate during which the tongue and palate surfaces are in partial contact. In this process a frictional force is generated between palate and tongue, with the semi-solid food acting as a lubricant". Moreover, de Wijk et al. [167] suggested a link between the type of sensation and the time point processing in mouth, stating there is a transition from rheological to tribological properties depending on the oral processing time and the length scale of the food particles in the mouth.

Tribology, which is the science of wear, friction and lubrication, can be applied to food science and especially in the study of thin film formation between the tongue and palate. A review of oral tribology by Chen and Engelen [168] provided valuable background on tribology fundamentals in food science. Chen and Stokes [169] suggested tribology to be a contributing discipline for understanding oral processing, texture and mouthfeel of food. In the study of Pradal and Stokes [170] the importance of soft tribology as a characterization tool for sensory attributes was also highlighted. Sarkar and Krop [15] reviewed the applications of oral tribology in modelling food structures through correlating the coefficient of friction with sensory attributes. Thus, over the past few years, there has been increased research in the correlation between tribology and sensory perception. There is an increased interest from the food and beverage industry regarding tribology applications, since it is believed that the consumer's experience is influenced by the thin layer formation on the mouth surfaces. Prakash et al. [171] reviewed progress made in food tribology with a detailed presentation on how tribometers are modified and used to characterise the textural sensory properties of foods.

In this work, chocolate was studied as an example of a food where the consumer experience is influenced by the oral perception of creaminess and smoothness [172]. The global market for chocolate was valued at USD 103.28 billion in 2017 and is expected to grow 7% in revenue by 2024. However, there is considerable interest in the food industry in developing foods with reduced energy density, in the case of chocolate meaning less fat and sugar, but with the same mouthfeel. There are very few published papers reporting chocolate tribology [173, 174, 175, 176, 177, 178] and even fewer relating friction properties to sensory perception [173, 178]. A range of tribology test methods have been used including ball-on-flat [174, 179, 177] and modified rotational viscometer [173]. The studies usually compare friction/speed response for different chocolate manufacturing methods [173] or composition [173, 178]. In consumer sensory tests of chocolate texture, the smoothness is usually identified as a key characteristic [173] and might be linked to reduced friction in the low speed boundary regime. Friction coefficient varies with sliding speed [174, 173, 177, 178] and is in the range $\mu = 0.1 - 0.6$ depending on chocolate composition. Masen and Cann [178] used a reciprocating contact to measure friction with time of shear-degraded chocolate and reported friction coefficient range of $\mu = 0.18 - 0.32$ at $30\,\mathrm{mm\,s^{-1}}$ depending on composition. In tests where human saliva was present friction drops to $\mu = 0.06 - 0.09$ [175].

The cocoa solids content is thought to play a significant role in the oral friction experienced during mastication and this is studied in the current chapter. One possible way of maintaining or even improving mouthfeel may be the inclusion of micro-sized bubbles. In this chapter, micro-aerated chocolate will be tested and compared with commercial non-aerated chocolate samples. The development of a validated tongue-palate simulated test to measure the friction response of rubbed food samples could possibly replace the panel tests, which are currently used by the food industry. As will be presented below, the design of such a test is difficult when based on traditional tribology machines.

One of the aims of this work is to develop a new approach to designing tribology tests to measure friction in a simulated tongue-palate contact. This requires consideration of the "engineering" conditions in the mouth and the artificial models for biological tissue (tongue, palate, saliva), which will be used as test specimens.

The tongue palate environment is crucial for the perception of taste and texture. The palate is a relatively smooth and hard surface that does not have taste receptors and is used mainly to spread the already partially processed food from the teeth to the larger area in the mouth [179]. From there the food reaches the tongue where the receptors are placed that are responsible for the perception of different tastes and textures. The human tongue is a rough and flexible muscle and its surface is covered by conical papillae of order 100 µm in height [177]. Almost two-thirds of the human tongue is covered by filiform papillae that do not contribute to the taste perception but are sensitive to friction. Taste receptors are located at the fungiform and foliate papillae [159].

The tongue-palate contact is lubricated by saliva and according to Humphrey and Williamson [180] this plays a crucial role in the following processes: (1) lubrication and protection, (2) buffering action and clearance, (3) maintenance of tooth integrity, (4) antibacterial activity, and (5) taste and digestion. Saliva is a complex biological fluid which is mainly water (99%) but also contains a mixture of mucins, glyco-proteins, electrolytes and enzymes with a pH of 6-7 so that it is slightly acidic [180]. Lubrication is provided through the adsorption of saliva proteins, such as mucin, which account for 16% of the total proteins [181], onto the mouth surfaces [182, 183].

Saliva is involved in the perception of taste flavour and texture of foods and serves as a lubricant reducing the coefficient of friction and the shear stress on the surface of the tongue. Recent work by Upadhyay and Chen [184] highlighted the importance of the addition of saliva in tribology characterizations. He et al. [185] investigated the reduction of friction due to the presence of saliva, studying chocolate boluses composed of chocolate and human whole saliva. In order to have consistent results, in this study a simple artificial saliva recipe was used [186].

Eating starts with the first bite, where the food is mechanically broken down into smaller pieces. After a few chew cycles, while heat transfer may control the melting of fragments, the food enters the tongue-palate area, where it is sheared and forms a bolus,

before swallowing. When designing simulation tests the mechanical conditions occurring during the oral process must be considered. These include contact pressures, kinematics and the appropriate time-scale for friction measurements. The mechanical properties of the tongue change depending on the orientation of the muscle fibres [187], resulting in varying contact pressures for different relative tongue-palate positions. Nishinari et al. [188] measured the average maximum isometric tongue pressure, during food oral breaking, to be 50 ± 14 kPa which agrees with the findings published in the study of Alsanei et al. [189] who reported maximum isometric pressure ranging between 10 kPa to 70 kPa.

The relative speed between tongue and palate is another important physical factor related to mechanical processing. Hiiemae and Palmer [190] suggested a speed range between 2 and 35 mm s^{-1} depending on parameters, such as the stage of food oral processing, different speeds correspond to biting and to swallowing. The shear rate in the tongue palate region during mastication is a parameter that should be taken into consideration. Several studies have attempted to quantify the shear rates that occur in the tongue-palate interaction, and reported values range between 10 s^{-1} [191] to 50 s^{-1} [192].

In-mouth temperature is also important for the accurate design of the experiment. The values used in the literature vary depending on the stage of processing and the what is consumed. The reported values range between room temperature [165, 166] and 40 °C [173]. In this study the lower specimen is heated at 35 °C and the chocolate is allowed to melt before the start of the test. This value is believed to be representative as we expect to be less than 36.6 °C, but certainly higher than the room temperature. A summary of the mechanical conditions in the tongue-palate contact during food processing is provided in Table 6.1.

Table 6.1: Summary of the mechanical conditions in the tongue-palate contact.

Parameter	**Range Value**	**Test settings**
Contact pressure	3-36 kPa	35 kPa
Speed range	2-35 mm s^{-1}	120 mm s^{-1}
Time scale	5 s	5 s
Temperature	35 °C	35 °C

Several types of equipment have been used to measure friction in applications related to oral processing. Prakash et al. [171] provided a detailed overview of the various tribological instruments that have been used in food studies. Configurations used include pin-on-flat, ball-on-flat and flat-on-flat [171, 193, 194]. The most common technique used both in tribological and food science is the MTM tribometer [195], which consists of a ball in combined rolling and sliding motion against a rotating disk. The MTM test is usually employed to measure friction as a function of the changing speed (increasing or decreasing) to generate a Stribeck-type curve [15]. It measures a single friction value, averaged over several seconds, which is a relatively long time-scale compared to mastica-

tion times, which for chocolate range between 15 and 20 s [196]. Thus, these tests cannot be used to follow friction changes occurring during the first few seconds of mechanical breakdown in the tongue-palate region. In addition, the traditional test design requires a continued supply of fluid which is entrained through the inlet of the contact. Under these conditions, fluids experience shear rates of the order $10^5 - 10^7 s^{-1}$ in the inlet and contact regions, which is significantly higher than those reported for the tongue-palate contact region ($\sim 50 - 100 s^{-1}$) [192], and thus complex fluids may shear-degrade or suffer phase-changes. Thus, the composition of the film in the contact zone might differ from the average bulk [197]. To measure the mechanical breakdown of food over time, a single sample must be used which is subject to repeated rubbing, while reducing the effects of inlet shear.

Traditional tribometers that use a steel sample pair are not compatible with oral processing studies, since the pressure between the two surfaces is much higher than desired [198]. For this reason, tribological set-ups for food research use a combination of soft and hard surfaces in order to lower the contact pressures. Some of the most common soft surfaces used are teflon [199], polydimethylsiloxane (PDMS) [200] and rubber, and there are studies which used pig's tissue as a tongue substrate [193, 194, 165, 166]. The ideal material for lubrication studies would be the one that imitates the mechanical and chemical properties of the human palate and tongue [201]. PDMS is currently used as model tongue surface material for many food tribology studies [159, 15], although there are significant differences in the mechanical and chemical properties compared to the human tissue. The Young's modulus of PDMS ranges between $1 - 3$ MPa [202] which is higher than the human tongue ($46 - 150$ kPa) [159, 15]. Despite this difference it is usual to use a PDMS-glass combination as a soft-hard model of the tongue-palate [203, 204, 205]. One significant difference between the human tongue and the PDMS samples used is the surface texture. In some studies, the tongue texture has been replicated using surface-moulded PDMS [201] but this approach has not been adopted for the current work.

A new configuration is proposed, consisting of two flat surfaces to mimic the tongue-palate contact. The upper surface, a PDMS disk is loaded and reciprocates against the lower stationary surface, a glass microscope slide. This motion simulates the movement of the tongue against the palate [204]. In addition, due to the combination of a large contact area and a relatively short stroke length, the food under test is essentially isolated and new material is not continuously entrained. When eating semi-solid food is introduced into the mouth as individual samples which are mechanically degraded before swallowing. There are already studies that use flat on flat configurations [178] to successfully distinguish between confectionery products with different cocoa solids. In the current chapter, the experimental setup presented by Masen and Cann [178] is further developed by using a new device that is able to operate at the appropriate kinematics, a lower reciprocating frequency and by including the effect of artificial saliva in the system whilst recording

the friction forces and high temporal resolution. The test was used to assess friction for a range of chocolate compositions, since these are expected to show differences in oral perception.

6.2 Materials and methods

6.2.1 Tribology test device

The BTM (PCS Instruments, London) was used to measure the friction properties of lubricated and unlubricated contacts. In the setup, shown in Figure 6.1a, a model tongue comprising a flat cylindrical PDMS specimen (5 mm height, 6 mm diameter) is loaded against a stationary glass slide representing the palate. A load of 1 N was used, giving an approximate contact pressure of 30 kPa, which is comparable to reported pressures in the tongue/palate contact. The 6 mm diameter PDMS cylindrical specimen was punched from a 5 mm thick silicone sheet (Silex UK) using a biopsy punch, and the surface texture was measured using a White Light Interferometer. The PDMS disc was glued on the upper holder and reciprocates against the glass slide, imitating the movement of the tongue. The glass slide was attached to a temperature-controlled metal base, where the temperature was monitored through a thermocouple. The glass slide was preheated to 35 °C for 2 min before the start of the test. After the 2 min of preheating, a small amount (~ 0.2 g) of shaved chocolate was placed on the glass slide and allowed to melt for 30 s. Then, the PDMS flat disc was brought into a reciprocating sliding contact with the glass slide, with a specified load, stroke length and frequency. The BTM was specifically designed to mimic the physiological in-mouth conditions (Table 6.1) with an applied load of 1 N, a reciprocating frequency of 1 Hz and a stroke length of 5 mm, resulting in a mid-stroke sliding speed of 120 mm s^{-1}. The test conditions are summarised in Table 6.1. Friction data was recorded over 5 cycles at a temporal resolution of 100 Hz, continuously over the reciprocation cycle and was directly available in LabVIEW. Mean values were calculated averaging the 15 middle points of each stroke and data was plotted. The error bars in the graphs represent the entire range (minimum and maximum) of all the results. Ten different chocolate specimens of each type were used to collect samples from five different areas of each specimen. The significant difference between the samples was validated using a one way Analysis of Variance (ANOVA) at 95% confidence interval with a p-value < 0.05.

6.2.2 Cleaning procedure of the surfaces

As surface contaminants and thin films affect friction and wetting properties, all surfaces were cleaned before the friction measurements. After each test the PDMS cylinder was wiped and cleaned with isopropanol and it was replaced every five tests. The glass

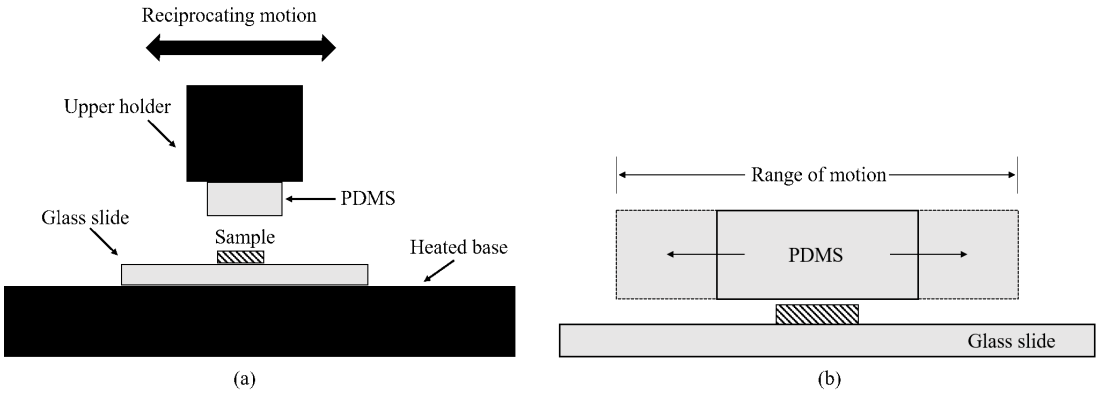

Figure 6.1: (a) Schematic representation of BTM test configuration, (b) Close-up of the interaction area between the PDMS and the sample, indicating the range of motion.

slide was cleaned with isopropanol after every test. Care was taken when handling the surfaces in order to reduce the risk of further contamination. Immediately after drying of the specimens the experimental procedure was started.

6.2.3 Artificial saliva

Human saliva is a complex fluid that contains several proteins and the design of an artificial saliva substrate is not straightforward. In the recent paper of Sarkar et al. [159, 15] the complexity of human saliva was presented and the difficulty of creating an exact human saliva substrate was also highlighted. In this study, in order to mainly focus on the material under test, a relatively simple artificial saliva recipe was used, consisting of 100 mL deionized water, 0.27 g mucin and half a tablet of phosphate buffered saline [206]. The chemicals were mixed in a magnetic stirrer at room temperature, stored at 5 °C and discarded after seven days [207]. The glass slide palate substrate was submerged in 10 mL of artificial saliva for 30 minutes, allowing the absorption of the proteins onto the glass slide. The glass slide was then carefully retracted leave a thin saliva film on the surface. It was then positioned on the heated base of the BTM and the chocolate sample was added. Table 6.2 summarizes the materials used in the experiment.

6.2.4 Chocolate specimens

Various commercially available chocolate specimens were selected to represent different levels of cocoa solids and micro-aeration level. The commercial chocolate samples with different cocoa solids are all made by the same manufacturer with cocoa solid amounts ranging from 30 wt% to 80 wt%. Further details of the commercial chocolate can be found in Masen and Cann [178].

Nestlé provided both non-aerated samples and micro-aerated samples with 10 vol%, 12 vol% and 15 vol% micro-aeration, with a bubble size of $\sim 45\,\mu m$. The chocolate was

Table 6.2: Summary of materials used in the experiment.

Material	Description
PDMS	- Silex Silicone Youngs modulus 2 MPa [159, 15] - 5 mm thickness, 6 mm diameter - Surface texture: array of dimples −10 µm deep, 0.4 mm diameter, 0.8 mm between dimples
Glass	- S8400 Sigma microscope slide
Artificial saliva	- 100 mL deionized water - 0.27 g mucin from porcine stomach Type II, (M2378 Sigma) - 0.5 PBS tablet (P4417)

prepared as shavings, using a razor blade and 25 g was placed on the heated glass slide (either clean, or with an absorbed saliva film) and allowed to melt for 120 s.

Table 6.3 summarizes the composition of the chocolate samples. Scanning electron microscopy (SEM) images from a non-aerated and a micro-aerated sample are depicted in Figure 6.2. A Hitachi S-3400 SEM was used at variable pressure mode and at a relatively low accelerating voltage of 10 kV to prevent the samples from melting.

Table 6.3: Composition of chocolate test samples.

Designation	Cocoa solid (wt%)	Fat content (wt%)	Sugar (wt%)	Micro-aeration (vol%)
85% Dark Chocolate	85	32	14	0
70% Dark Chocolate	70	25	29	0
37% Milk Chocolate	37	20	29	0
28% Milk Chocolate	28	27	44	0
28% Milk Chocolate	28	27	44	10
28% Milk Chocolate	28	27	44	12
28% Milk Chocolate	28	27	44	15

6.3 Results

6.3.1 Procedure for acquisition of experimental data

Friction tests were performed on the BTM using the configuration described above. Figure 6.3a depicts a typical measurement of the friction force during reciprocation. The positive and negative values correspond to left and right reciprocating motion of the upper holder, respectively. The data were processed, as shown in Figures 6.3b-6.3d. The first two strokes were eliminated from the data since the force becomes constant after the second stroke. The coefficient of friction is shown in Figure 6.3b as the absolute values of the friction force divided by the applied load of 1 N. Data measured at the reciprocation points was ignored and only the part of the motion that corresponds to sliding was

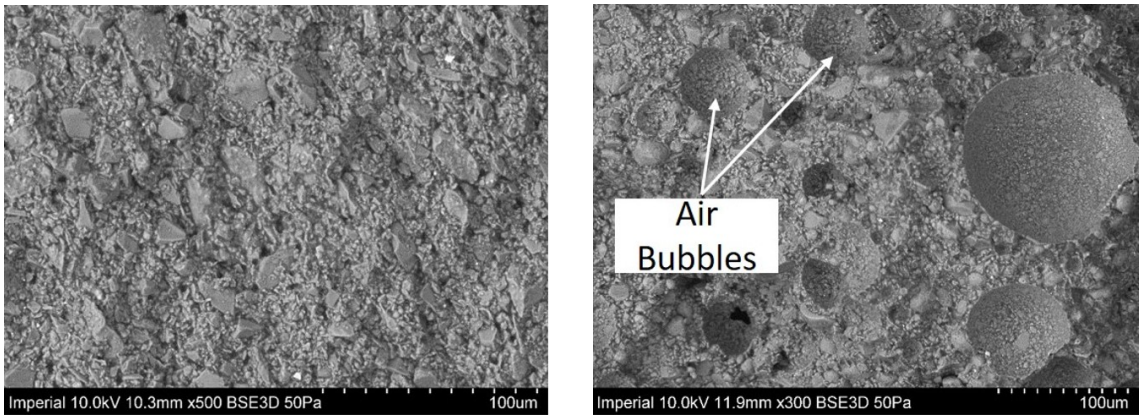

(a) (b)

Figure 6.2: SEM images from (a) non-aerated and (b) micro-aerated sample.

considered (Figure 6.3c). Each sample was tested once and discarded after the end of the test. The bar chart of Figure 6.3d can be calculated and used for comparison between the various conditions.

6.3.2 Repeatability of the friction results

Overall, the results were very repeatable, as shown in Figure 6.4, where three different tests are superimposed for dry conditions, i.e. PDMS against the glass slide, and for lubricated conditions PDMS - glass with artificial saliva. The coefficient of friction for the artificial saliva was measured to be $\mu = 0.23$, which lies in good agreement with results reported in literature [208].

6.3.3 Friction results for commercial chocolate samples with different cocoa solid content

Figure 6.5a shows a comparison for the friction coefficient between the commercially available chocolate samples tested without artificial saliva present. Differences were observed depending on the cocoa solids content. The high content samples ($\sim$ 85wt%) showed higher coefficient of friction during the first 5 strokes compared to the 70 wt% and 37 wt% cocoa solids samples. The tests were repeated with the artificial saliva and the results followed the same behaviour (Figure 6.5b), but the values of the friction coefficient were, as expected, lower. Statistical analysis through ANOVA indicated a clear difference between the samples in both cases.

6.3.4 Micro-aerated chocolate friction results

Figure 6.6a compares averaged coefficient of friction without artificial saliva for chocolate samples with levels of micro-aeration of 0, 10, 12, and 15 vol%. The friction trace

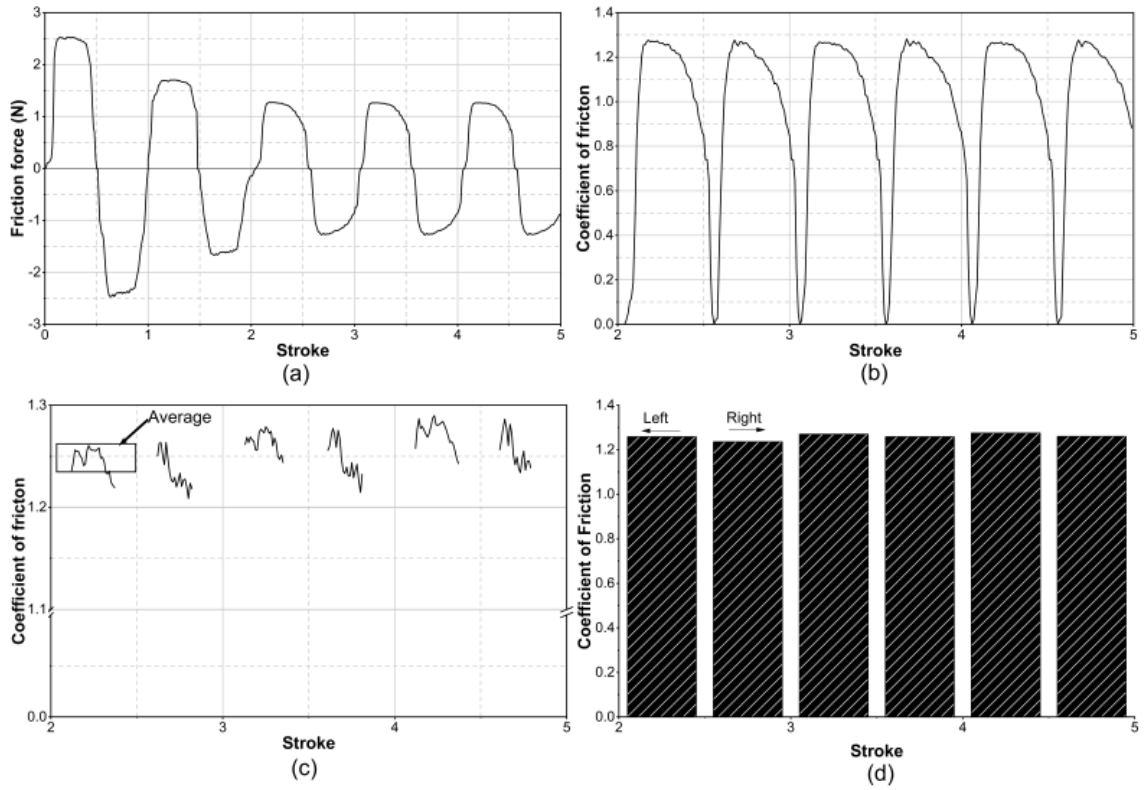

Figure 6.3: Measurement of friction force during reciprocating motion. (a) Typical friction force measurement during reciprocation, (b) coefficient of friction corresponding the absolute values of friction force with elimination of first two strokes, (c) data corresponding to the sliding, (d) bar chart by averaging the 15 middle points of each stroke.

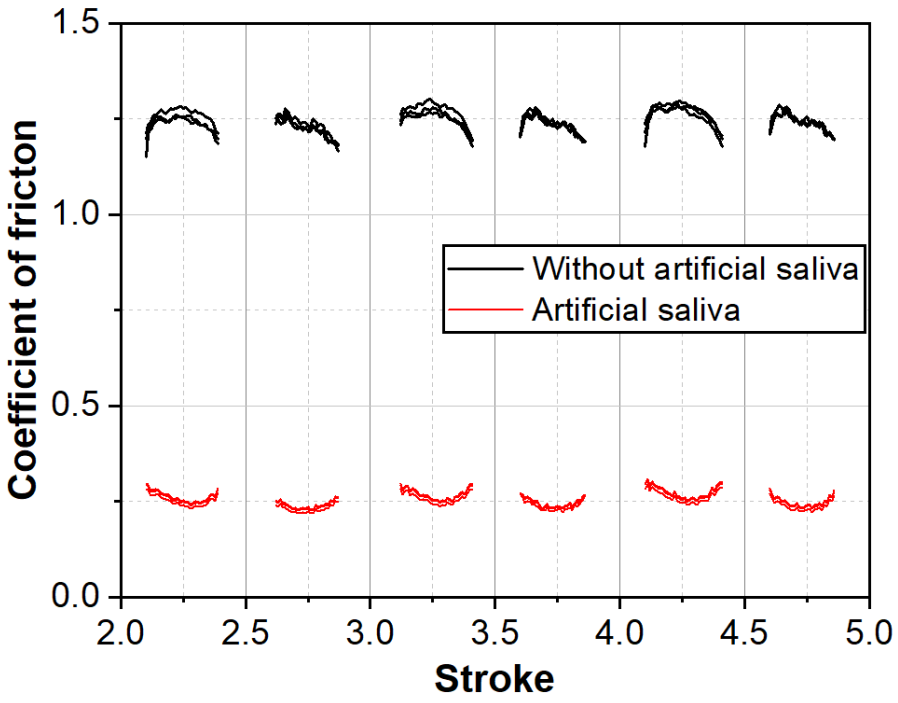

Figure 6.4: Measurement of coefficient of friction as a function of reciprocating motion. Repeatability for dry conditions (without artificial saliva) and artificial saliva

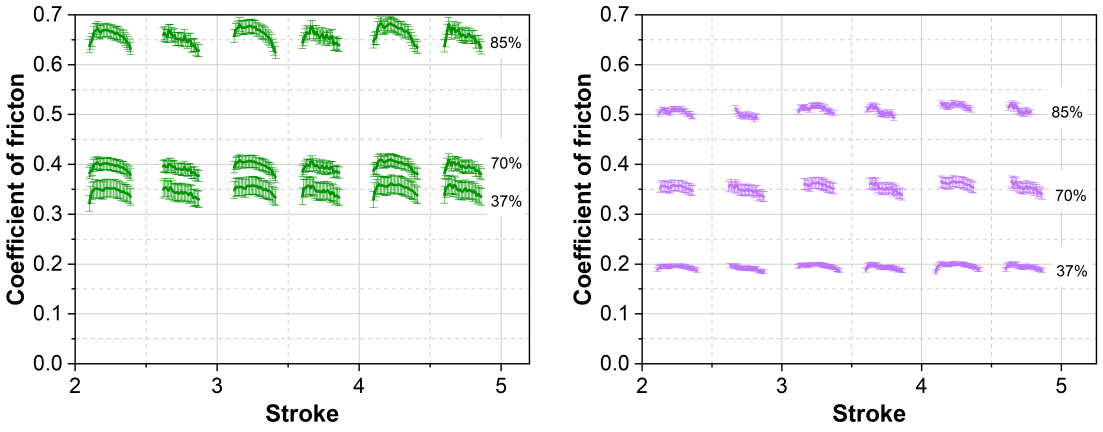

Figure 6.5: Measurement of coefficient of friction as a function of reciprocating motion. Comparison for samples with different cocoa solids content (a) without an artificial saliva film present and (b) with an artificial saliva film present.

changes over the stroke length. It is at a minimum at the reciprocation point and increases to a maximum in the middle of the stroke. The maximum friction coefficient deceased with micro-aeration level from $\mu = 0.4$-0.44 for the 0 vol% to $\mu = 0.2$-0.23 for the 15 vol% micro-aeration.

Figure 6.6b shows the results obtained for the various micro-aerated chocolates with artificial saliva present. Again, differences were recorded depending on micro-aeration level although overall the friction was much lower. The maximum friction coefficient deceased with micro-aeration level from $\mu = 0.16$-0.175 for the 0 vol% to $\mu = 0.07$-0.08 for the 15 vol% micro-aeration. Clear differences were observed in the friction coefficient values in both figures, which was also justified by the ANOVA analysis.

A major difference between the friction traces without (Figure 6.6a) and with (Figure 6.6b) artificial saliva is the shape of the curves. The results with artificial saliva are characterized by a convex curve, whereas non-lubricated conditions result in curves that are concave. For reference, Figure 6.8 also shows coefficient of friction measurements obtained for lubricated sliding of the PDMS against glass, when no chocolate was present. This friction is significantly higher than when chocolate is present in the contact.

These results show that the proposed experimental set-up can measure and identify differences in the coefficient of friction for different levels of micro-aeration. The test design aims to capture a single sample of chocolate and subject it to repeated shearing. The assumption is that no new material enters the contact during the reciprocating motion and although the chocolate is degraded, a thin layer remains intact on the glass surface without significant loss of the film. At the end of the test, the rubbed film on the glass slide was observed under a low power microscope (Figures 6.7a and 6.7b). Figure 6.7a shows the overall view of the chocolate sample with the rubbed portion in the middle.

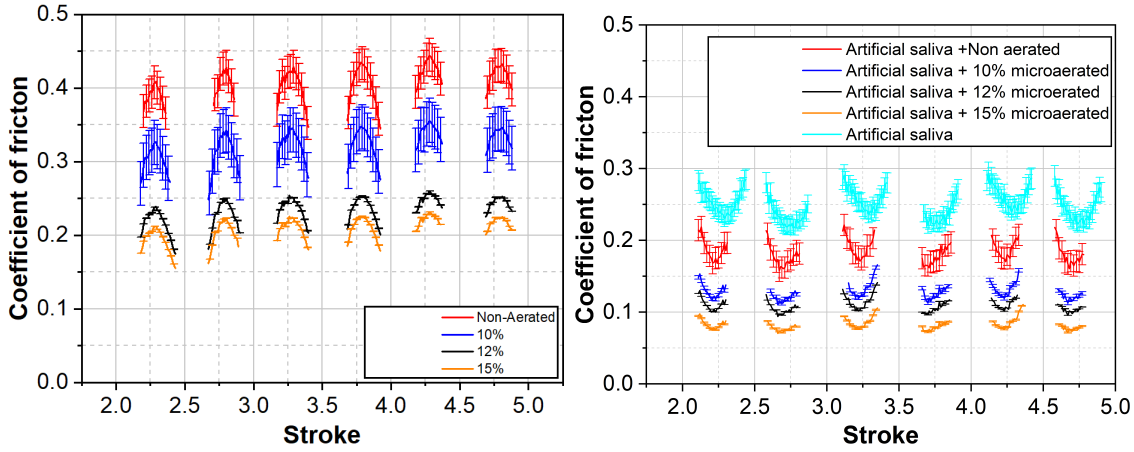

(a) (b)

Figure 6.6: Coefficient of Friction traces as a function of stroke position for chocolate samples with different micro-aeration levels (a) without an artificial saliva film present and (b) with an artificial saliva film present.

Figure 6.7b shows a DIC optical image from the rubbed region of non-aerated chocolate after the test. The image clearly shows that a macroscopic film remains in the contact and its structure is shear degraded. Immediately after the test, free fat droplets are present (these solidify on cooling) and discrete sugar/cocoa particles.

6.4 Discussion

A tribology test was developed to measure friction of different types of molten chocolate as it mechanically degraded. The test uses a reciprocating flat-on-flat configuration, which simulated the conditions and motion in the tongue-palate contact. In this arrangement the converging inlet, which is usually present in classical lubrication tests, is absent, thus the chocolate is not pre-sheared before friction is measured. Friction was measured over 10 strokes (5 reciprocating cycles at 1 Hz) to simulate in-mouth degradation over 5 seconds of mastication. The effect of the composition in terms of cocoa solid content and micro-aeration was studied in a series of tests with and without artificial saliva present.

The presence of artificial saliva decreased the friction coefficient from $\mu = 1.25$ (dry) to $\mu = 0.25$ (artificial saliva) which is similar to values reported in the literature [209]. The average mid-stroke friction coefficient is compared for the commercial samples in Figure 6.8. The results are plotted against cocoa, sugar and fat content for tests with and without artificial saliva present.

In all cases the friction coefficient decreased in the presence of the artificial saliva. It is difficult to draw concrete conclusions about the effect of composition on friction as the cocoa, fat and sugar content all change in the samples. However, some general trends may be identified. Friction coefficient decreased with decreasing cocoa, decreasing fat and

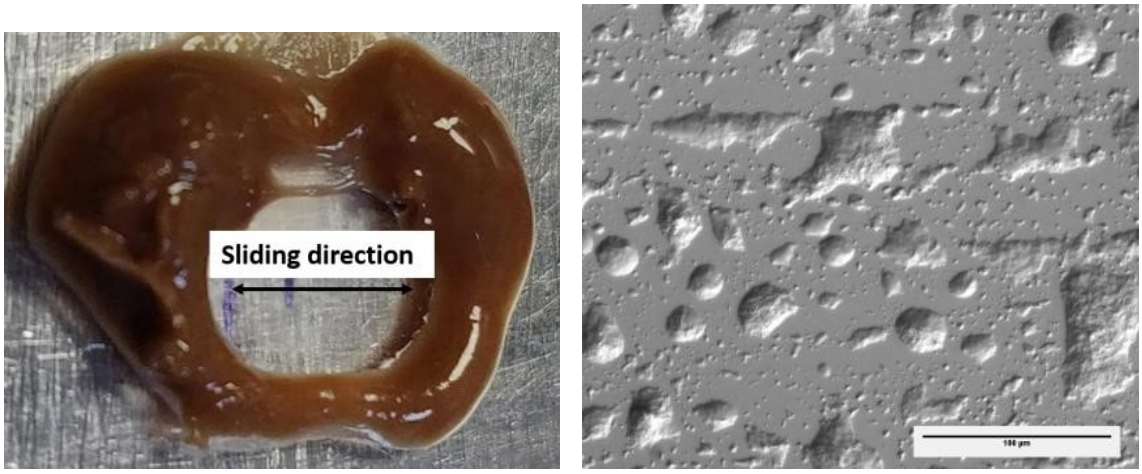

(a) (b)

Figure 6.7: (a) Sliding direction after the test, (b) microscope image of non-aerated chocolate in the sliding direction film after the test.

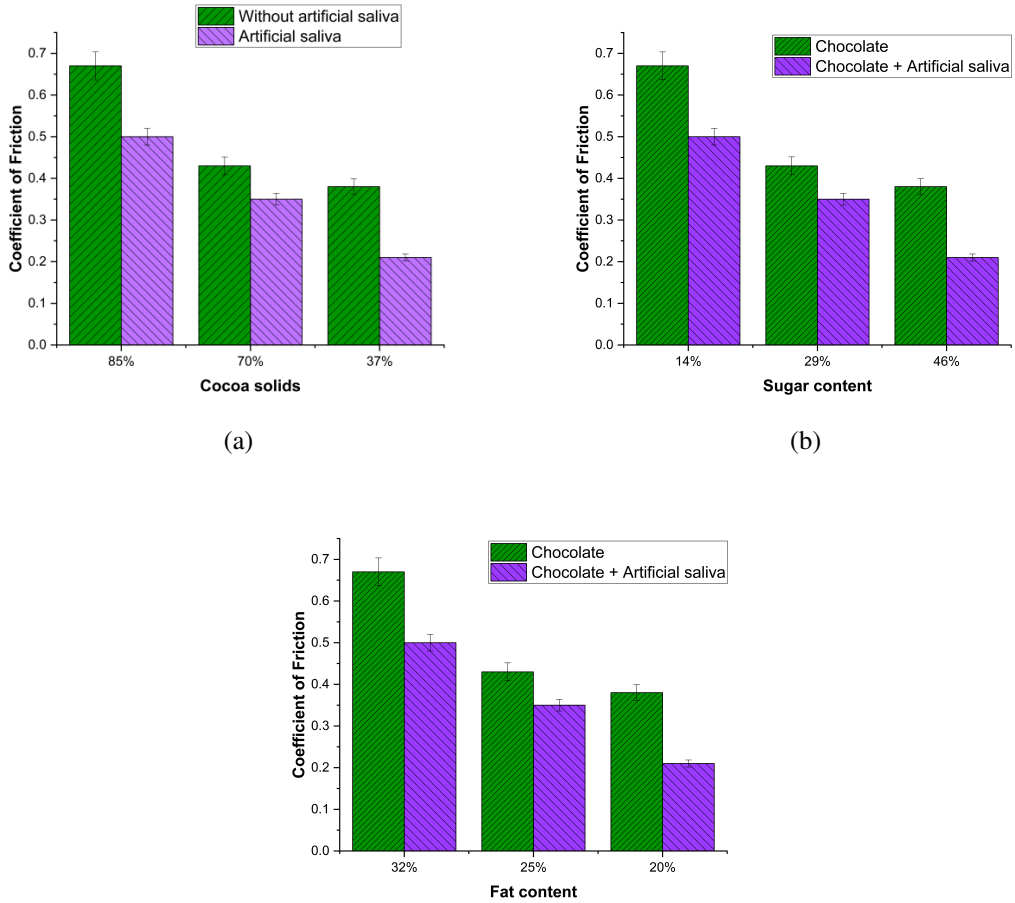

(a) (b)

(c)

Figure 6.8: Average mid-stroke coefficient of friction plotted for different chocolate composition for non-aerated samples with and without artificial saliva present. (a) cocoa solid content (b) sugar content (c) fat content.

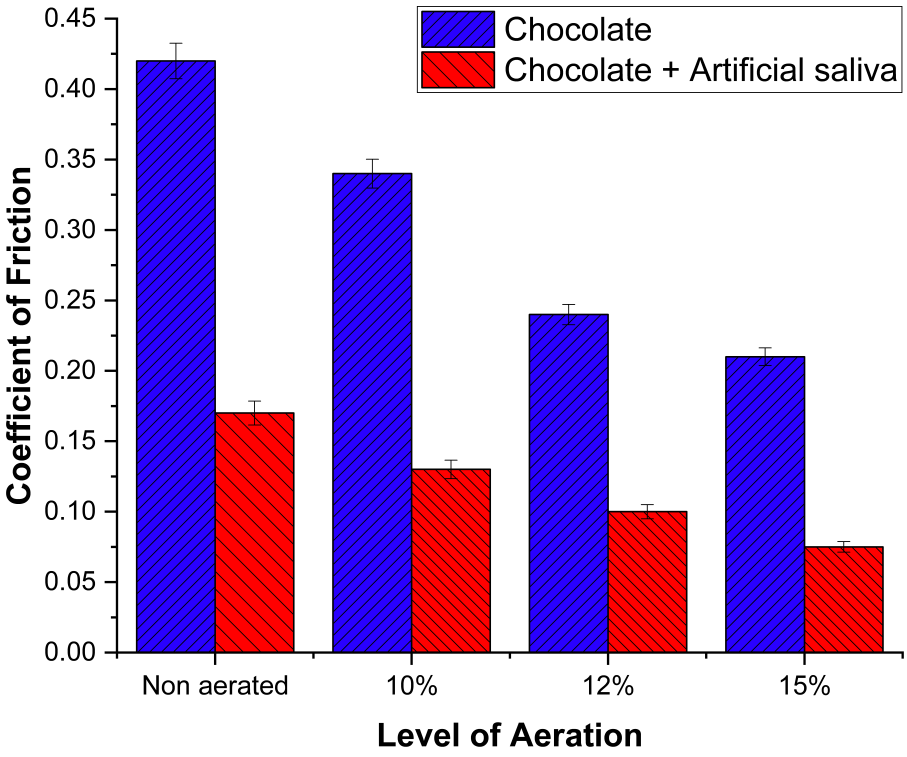

Figure 6.9: Comparison of coefficient of friction measurements for different micro-aeration levels with and without an artificial saliva film present.

increasing sugar content. Clearly it is difficult to isolate the effect of a single component on friction.

Figure 6.9 compares mid-stoke average friction for the micro-aerated samples with and without artificial saliva present. Again, friction reduces in the presence of the artificial saliva. The results for these chocolates are less ambiguous as the fat, sugar and cocoa solid content were all constant for all samples in this group. Friction coefficient decreases with increasing micro-aeration levels.

For both sets of chocolate samples, non-aerated and micro-aerated, the friction coefficient reduced in the case of artificial saliva being present in the contact. For the commercial chocolate samples, this decrease was in the range of 19-45%, depending on the cocoa-solid content. The reduction was much larger for the micro-aerated samples, where the largest decrease (65%) occurred for the 15 vol% micro-aerated samples.

Examination of the rubbed film post-test provides insights into structure degradation and component loss. The DIC image of the rubbed film in Figure 6.7b clearly shows the structure of chocolate has degraded and coalescence of fat. The amount of sample left in the track indicates the surfaces are separated by a lubricating film and that direct interaction of the glass and the silicone did not contribute to the measured friction. Chocolate is a complex material and the friction response will be influenced by the original composition, phase changes due to melting and mechanical degradation, and loss of some components during rubbing. The addition of saliva and the possible dissolution of some components,

for example sugar, will add to this complexity. To understand these processes, it will be necessary to test simpler, model systems with controlled compositions. Post-test analysis of the chemistry and distribution of the remaining film [175, 178] is also necessary.

Several chocolate studies [173, 175, 196, 210] have used a classical Stribeck-type analysis to explain their tribology results. Friction coefficient is plotted as a function of entrainment speed to identify different lubrication regimes. An idealised example is shown in Figure 6.10 where the boundary, mixed and hydrodynamic regimes are clearly delineated. The interpretation of Stribeck curves generated for chocolate have not been so clear cut. In some studies friction has been reported to increase with speed, typically over the range 0.01-100 $\mathrm{mm\,s^{-1}}$ for $\mu \sim 0.1$-0.6 [196, 210]. However, Rodrigues et al. [175] reported fairly constant friction coefficient of $\mu \sim 0.08$-0.1 over for a speed range of 1-100 $\mathrm{mm\,s^{-1}}$. Although there are doubts about this type of analysis, this method can be used to examine the chocolate friction response in the current work. In the BTM test the speed profile of the contact is sinusoidal, and the friction coefficient was measured over the entire stroke length, meaning the speed varied from 0 at the beginning and end of the stroke to 12 $\mathrm{mm\,s^{-1}}$ at the centre. The shape of the friction curve over the stroke differed between the various chocolate samples (commercial and micro-aerated) and with the addition of artificial saliva. The friction coefficient for the commercial chocolate was fairly constant over the stroke, both with and without artificial saliva. However, there was significantly different behaviour for the micro-aerated samples: without artificial saliva the friction coefficient increased with speed and the highest friction was recorded in the middle of the stroke. With added artificial saliva the friction coefficient decreased with speed and the lowest friction coefficient was in the middle of the stroke. Classical lubrication theory predicts that the thickness of the lubricating film will increase with speed due to increased entrainment of fluid and that the friction response will be described by a Stribeck-type curve. An example of a Stribeck curve, where the coefficient of friction is plotted as a function of the hydrodynamic film building parameter defined as viscosity x speed /load, is shown in Figure 6.10. For low speed and/or low viscosity the hydrodynamic component of the film is reduced, and friction is determined by the thin film chemistry of the contact. Increasing viscosity or speed increases the film thickness and shifts the friction response to the right-hand side of the diagram, where fluid-shear effects start to dominate.

The results for the chocolate with 10 vol% micro-aeration are superimposed onto the Stribeck curve for two positions in the stroke; (1) near the end of the stroke ($\sim 1\,\mathrm{mm\,s^{-1}}$) and (2) in the middle ($\sim 12\,\mathrm{mm\,s^{-1}}$) with and without artificial saliva. Although the applied speed ranges during the saliva and non-saliva experiments are identical, it is reasonable to assume that the addition of a thin artificial saliva layer reduces the chocolate viscosity and thus the friction response shifts towards the left-hand side of the curve. The same friction-speed response was measured for all the micro-aerated samples; however,

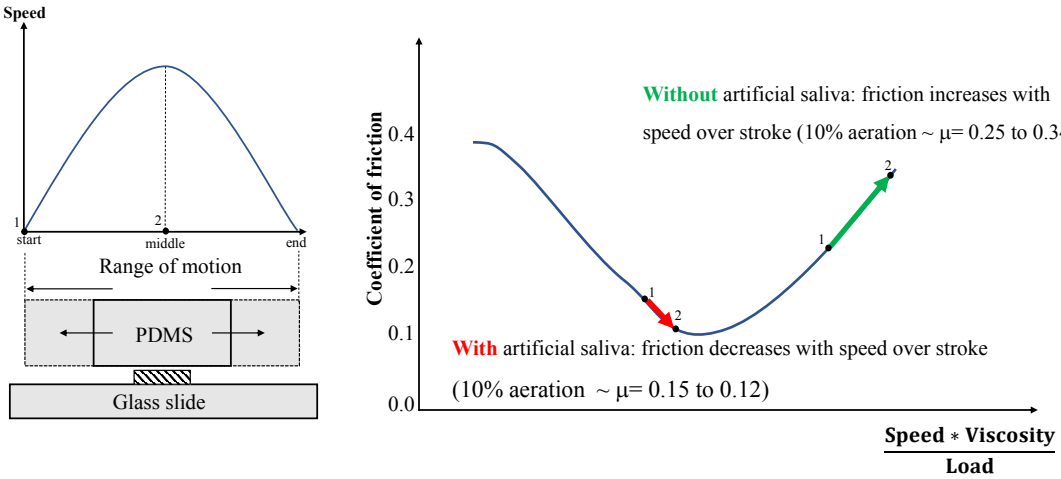

Figure 6.10: Idealised Stribeck curve, showing the friction to speed response for 10 vol% micro-aerated chocolate.

this was not seen for the commercial chocolate samples chocolate, where the friction coefficient was fairly constant over the speed range. Similar speed-independent friction response has been reported for commercial chocolate samples [175]. The friction coefficient was higher for the tests without artificial saliva, as expected, since the viscosity of the chocolate is expected to be higher.

Although a Stribeck-type analysis was used, it must be remembered that these curves were developed from friction tests on oils containing low concentrations of soluble additives, which behave quite different than chocolate. The validity of applying these models to complex multi-phase fluids with the inherent assumptions of film formation mechanisms and speed dependency is uncertain. This discussion uses a simple lubrication analysis to explain the effect of adding artificial saliva; however, it is likely the mechanism is more complex. For example, by adding an adsorbed/fluid mucin layer to the contact might also change the position of the shear plane It is possible that shearing occurs predominantly at the chocolate-mucin interface, which would have a much lower shear stress and thus friction.

The current chapter has reported a new approach to studying friction of mechanically degraded molten food samples. The advantage of the experimental setup is that it replicates the real timescale that food is rubbed between tongue and palate and that it measures transient friction changes rather than averages of longer timescales. The other improvement is the combination of a large contact area and a short reciprocation stroke, which is a better simulation of the tongue-palate contact and movement. This configuration also means that a single sample of food is captured in the contact and subjected to repeated rubbing rather than the continued entrainment of fresh material as it occurs in most other tribological tests.

The results have shown chocolate composition and structure influences friction. The individual roles of cocoa solids, fat, sugar, emulsifiers etc must be studied in a more methodical and controlled manner through model systems. The contribution of micro-

aeration is interesting and promising. Micro-aeration will affect many properties some of which will impact texture attributes for example bite, melting, rheology, mechanical breakdown, chocolate structure/cohesion. At present there is not enough information to propose a model for these complex processes and the relationship to friction and sensory perception. However, the results clearly show that micro-aeration can be used to control chocolate friction and thus is a promising method of altering the texture attributes in a controlled manner.

6.5 Conclusions

This work describes a novel experimental setup to measure the friction coefficient in reciprocating contact operating at low contact pressure and low speeds. The setup simulates the movement of the tongue and the palate using a combination of a large contact area and a relatively short stroke length. This means food under test is essentially isolated and new material is not continually entrained which is a closer simulation of oral processing. The test was used to distinguish between chocolate samples of different micro-aeration levels and cocoa-solid content. In commercial samples friction coefficient decreased with decreasing cocoa (85-37 wt%), decreasing fat (32-20 wt %) and increasing sugar (14-46 wt%). The friction coefficient decreased with increasing micro-aeration levels over the range of 0-15 vol% micro-aeration. For all chocolate samples the friction coefficient decreased with the presence of an artificial saliva film. In addition, different friction-speed response curves were observed depending on the nature of the chocolate and the presence of artificial saliva. The commercially available chocolate shows a friction coefficient that is constant over the stroke. For the micro-aerated chocolates the friction coefficient changes with speed. An increase with speed was observed when artificial saliva was not present. A decrease with speed was observed when the artificial saliva was present. These research challenges might be addressed by combining the results from the tribology experiments with rheology measurements with and without artificial saliva present.

7 Effect of cocoa solids and micro-aeration on the rheological properties of chocolate

Topics

7.1 Introduction

The rheological properties of foods play an important role in the quality of the final product [211, 212] and the measurement of the rheological properties of chocolate is important to ensure that the final product has the desired sensory and texture characteristics. Rheology is defined as "the study of the deformation and flow of matter" [213].

The rheological properties of foods (fluid or semisolid) has been extensively studied [214] and their properties range from Newtonian to viscoelastic. There are many studies classifying fluid foods depending on their rheological properties [215, 216, 217, 218]. Measurement and understanding of the rheological properties of foods can shed light into the design of foods with desired properties, such as sensory parameters [219]. Rheology studies have been conducted in different types of food and beverage products, ranging from soft drinks [220] to solids (sugar [221] or salt crystals [222]) although the majority of the foods studied belong to the soft matter category [223]. Lannes et al. [224] studied the flow behaviour of chocolate drinks at 25 °C and 40 °C and found that the Newton's, Power law and Bingham plastic models fit well with the experimental data. The rheological behaviour of coconut flavoured milk with varying fat content (15%-30%) was investigated in the study of Simuang et al. [225] at temperatures ranging between 70 °C and 90 °C. They reported a pseudoplastic behaviour and the effect of temperature on the apparent viscosity was explained by the Arrhenius equation.

Different factors, such as tempering, composition and particle size distribution can

influence the rheological properties of chocolate. Glicerina et al. [226] studied the effect that production process steps have on the rheological properties of dark chocolate. Servais et al. [211] proposed a methodology to measure the rheology of chocolate and related cocoa products using factory grade rheometers. Afoakwa et al. [172] provided a detailed review of factors influencing the rheological properties of chocolate, concluding that the processing technique, the ingredients and the particle size distribution are the most important. Afoakwa et al. [227] compared different rheological models for determining dark chocolate viscosity. Váscquez et al. [228] performed a rheological study on four commercial chocolate samples with similar microstructure and reported a shear thinning behaviour. According to Gonçalves and Lannes [229] yield stress and apparent viscosity are two values that are used to quantify the chocolate rheology during the manufacturing process. According to Windhab [230] melted chocolate is a non-Newtonian fluid as the viscosity depends on temperature, shear rate and time and the chocolate can be considered as "smooth" for viscosity values of 1.5-3.5 Pa s measured at a shear rate of $20\,s^{-1}$ and body temperature 37 °C. Melted chocolate contains sugar, cocoa and milk particles dissolved in the melted fat matrix. A number of mechanisms take place when the melted chocolate is sheared and the particles in the fat matrix deform. These mechanisms, illustrated in Figure 7.1 are the following: deformation, orientation, deagglomeration and agglomeration [230]. The structure decomposition is initiated for shear stress values $\tau_0 = 5\text{-}12$ MPa leading to deformation, orientation and deagglomeration [230]. The viscosity continues to reduce as the shear stress values increase, until a characteristic value, τ_1, which is in the range of $\tau_1 = 0.5\text{-}2$ MPa. After that point, the viscosity values remain constant until the shear stress reaches the characteristic value, τ_2, after which the structure collapses or new agglomerated structures are formed. The formation of the new agglomerated structures might lead to viscosity increase until shear stress reaches τ_3 where all the remaining in the system structures collapse and viscosity degrades for increasing shear stress.

Furthermore, Afoakwa et al. [231] concluded that the rheological properties are important in chocolate manufacturing for quality-control purposes and can be related to composition, processing strategy and solid particle size distribution. According to Ziegler et al. [232] viscosity influences the flavour attribute perception thus, rheological parameters often give information related to the sensory character in chocolate. For this reason, this chapter aims to elucidate how viscosity, storage and loss moduli are influenced by the composition and structure of melted chocolate. Both micro-aerated samples and samples with different fat content will be tested in frequency sweep and flow tests. The experimental data acquired from these rheological experiments are modeled using various semi-empirical models including the Carreau, Cross and Casson models. The characteristic equations of these models were fitted with the EXCEL solver using minimization of error-sum-of-squares for best fit. This study shows that micro-aeration and different fat content changes the rheological behaviour significantly and various models can represent

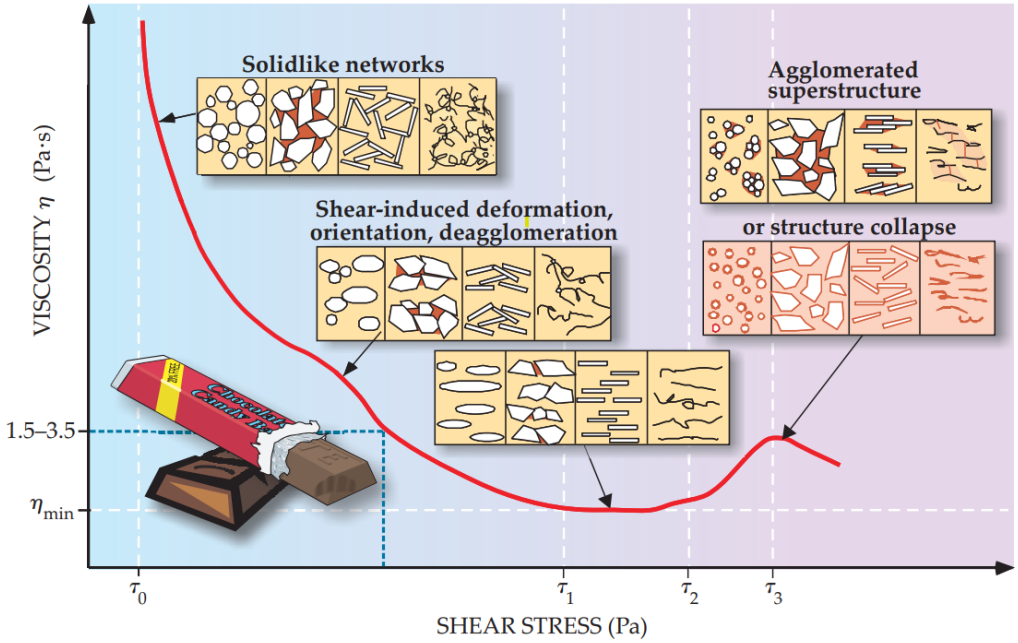

Figure 7.1: Representation of viscosity variation of melted chocolate with stress rate. The different mechanisms that take place in different shear rates are also depicted. Adapted from Windhab [230].

the observed change in the rheology. Furthermore, the effects of artificial saliva on the rheological properties is also examined.

7.2 Materials and Methods

7.2.1 Experimental set up

The rheological experiments were carried out using a Discovery Hybrid Rheometer, model HR–1 (TA instruments, USA), a schematic representation of which is given in Figure 7.2. Cross hatch parallel plates of 50 mm radius were used with a gap between the surfaces of 1000 µm in order to prevent the wall slip effects for steady state and frequency sweep measurements. The same geometry with the same gap was used for the measurement of the storage, G' and loss moduli, G''. The chocolate samples were pre-melted in an oven at 40 °C and then transferred to the plates. The rheometer plates were heated at 37 °C, to mimic the physiological conditions in the mouth, and kept constant for the duration of the tests. Initially, it was attempted to melt the chocolate specimens directly on the rheometer plates at 37 °C, but separation was observed implying that the chocolate was not fully melted. Flow sweep tests were performed with an increasing shear rate from $0.01 - 1000\,s^{-1}$. The flow curve was then obtained by plotting the viscosity as a function of the applied shear rate. Frequency sweep tests were performed in a low frequency range between 1 Hz and 20 Hz, in order to be consistent with the the physiological

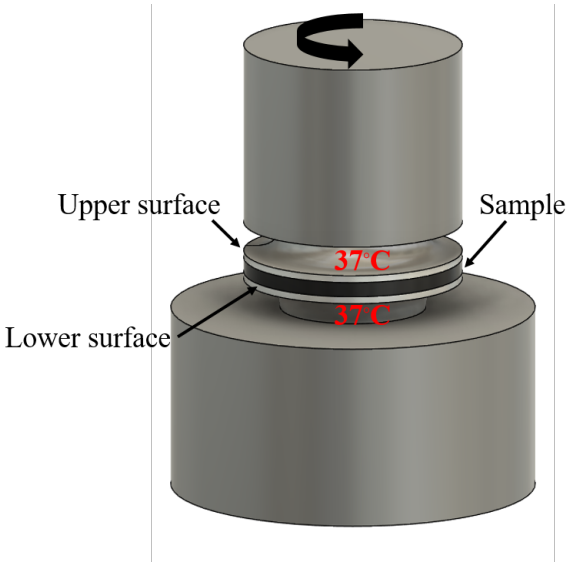

Figure 7.2: Schematic representation of the experimental set-up used for the rheology experiments.

conditions that exist in the mouth, as already presented in chapter 6. The mechanical parameters measured from the frequency sweep tests were the storage modulus, G', which gives an indication of the solid-like characteristics of the material; and the loss modulus, G'', which gives an indication of liquid like characteristics of the material and the applied stress was kept constant at 4 Pa. All measurements showed good repeatability and the error bars plotted correspond to the minimum and maximum measured values over three repeats. Before each test, the upper and lower plates were removed, cleaned and carefully placed onto the rheometer. Afterwards, the upper and lower plates were lowered slowly until they came in contact and a small normal force (~ 0.1 N) was recorded. The apparatus was then calibrated by setting the gap between the parallel plates to zero and the test was ready to start.

7.2.2 Chocolate samples and artificial saliva

The non aerated, the micro-aerated samples ($f = 10$vol% and $f = 15$vol%) and the commercial chocolate samples, presented in table 6.3 of section 6.2.4, were used for the rheology tests as well. The 12vol% micro-aerated samples were not tested as this micro-aeration level was not provided in the second batch of specimens received by Nestlé. The effect of saliva on the rheological properties of chocolate was also investigated. The flat plates were submerged in artificial saliva for 60 minutes allowing the proteins to be absorbed. The infused with artificial saliva parts were then heated to 37 °C and the tests were started. The same recipe and preparation methodology for artificial saliva, presented in section 6.2.3, is applied in the rheology experiments as well.

7.2.3 Flow models for fitting experimental results

A flow model is a mathematical equation that can describe rheological data, such as shear rate versus shear stress, or viscosity versus shear rate and provides a convenient and concise manner of describing the data. Rheological models are usually grouped in three categories: (1) empirical, (2) theoretical, and (3) structural [214]. The empirical models, like the power law (equation (7.1)) are derived from fitting experimental data.

$$\tau = K\dot{\gamma}^n \tag{7.1}$$

where, τ is the shear stress, K is a consistency coefficient, $\dot{\gamma}$ is the shear rate and n is the flow behaviour index indicating how close to the Newtonian flow is the behaviour of the examined fluid. However, the unbounded power law model has two drawbacks: first the model does not capture the constant viscosity for low and high shear rates, that are prevalent in most natural systems, and second the viscosity curve becomes singular in the limit of vanishing shear [214]. Consequently, constitutive models which combine a power law regime between a Newtonian behaviour at low and high shear rates, such as the Carreau model, have been proposed for real world applications [233]. Theoretical models are based on fundamental concepts and they provide valuable guidelines on understanding the role of structure on rheology.

A structural model is derived from considerations of the structure and often kinetics of changes in it. It may be used, together with experimental data, to estimate values of parameters that help characterise the rheological behaviour of a food sample. One such model is that of Casson [234] given by equation (7.2). The Casson model is one of the most widely used models to characterise the rheology of food suspensions.

$$\sqrt{\tau} = \sqrt{\tau_{CA}} + \sqrt{\eta_{CA}\dot{\gamma}} \tag{7.2}$$

where τ_{CA} is the Casson yield stress and η_{CA} is the Casson high shear viscosity. The International Office of Cocoa, Chocolate and Confectionery (IOCCC) has adopted the Casson model as the official method for interpretation of flow data of chocolate.

Other important models that have been used to characterise chocolate rheology include the Bingham model [235], given by equation (7.3), which is an example of a simple model of the flow of a suspension which exhibits a yield stress, τ_0, followed by Newtonian flow characterised by a high shear viscosity, η_{HS}.

$$\tau = \tau_0 + \eta_{HS}\dot{\gamma} \tag{7.3}$$

Quemada et al. [236] proposed a viscosity equation for dispersed systems based on zero-shear, η_0, and infinite-shear, η_∞, viscosities, and a structural parameter, λ, dependent

on the shear rate, that may be written as:

$$\frac{\eta}{\eta_\infty} = \frac{1}{\left\{1 - \left[1 - \left(\frac{\eta_\infty}{\eta_0}\right)^{0.5}\right]\lambda\right\}^2} \tag{7.4}$$

where:

$$\lambda = \frac{1}{\left[1 + (t_c\dot{\gamma})^{0.5}\right]} \tag{7.5}$$

The Casson and Quemada models have been used in the literature to study the role of cocoa solids and cocoa butter on cocoa dispersions [237, 238].

As it will be shown in the results section, the viscosity measurements from the chocolate samples tested in the current study are characterised by a three stage viscous response when sheared over a wide shear rate range. Figure 7.3 schematically shows the three stages of viscous response. More specifically, at low shear rates, the fluid behaves as Newtonian with a constant zero-shear viscosity (η_0) over a small shear range. Afterwards, a shear-thinning region is present where the viscosity decreases in accordance with the power law relationship; the reciprocal of the shear rate at which the transition from Newtonian to pseudoplastic behaviour occurs is the characteristic time or the time constant. Finally, at high shear rates, viscosity reaches a minimum constant infinite-shear-viscosity value (η_∞) [216].

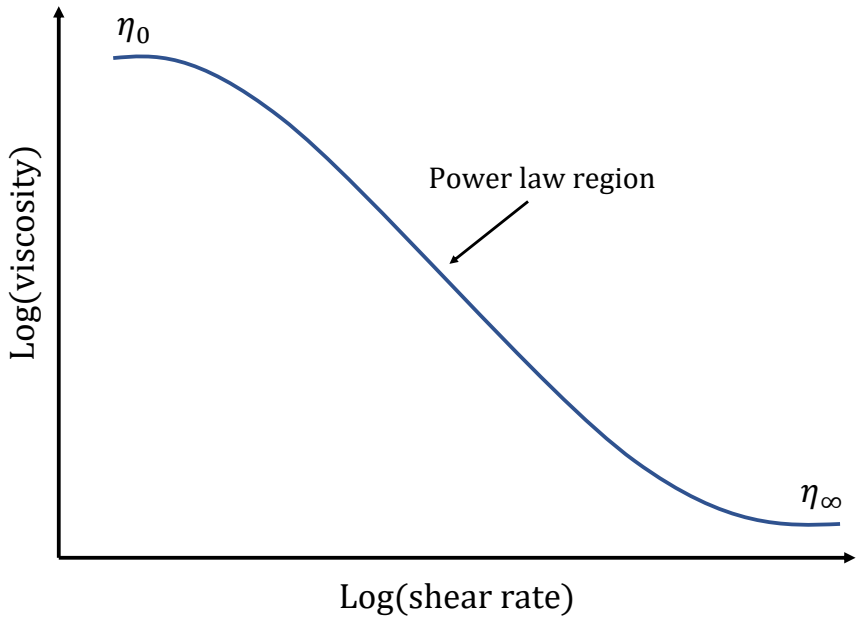

Figure 7.3: Qualitative plot of shear rate versus viscosity for shear thinning foods identifying three separate regions: a zero-shear viscosity at low shear rates, a power law region at intermediate shear rates, and an infinite-shear viscosity at high-shear rates [216]. Similar behaviour is obtained for the chocolate samples tested in the current study.

The models presented so far are not capable of capturing the shear thinning effect that is present in the samples tested (shown in section 7.3). For this reason the Cross [239] and Carreau [240] models, which can be used to model a fluid with a shear thinning behaviour as shown in Figure 7.3, are presented in equations (7.6) and (7.7) respectively.

$$\eta = \eta_\infty + \frac{\eta_0 - \eta_\infty}{1 + (\alpha_c \dot{\gamma})^m} \tag{7.6}$$

$$\eta = \eta_\infty + \frac{\eta_0 - \eta_\infty}{\left[1 + (\lambda_c \dot{\gamma})^2\right]^n} \tag{7.7}$$

where α_c and λ_c are time constants and m and n are dimensionless exponents. Table 7.1 summarises the flow models that exist in the literature. In this study only the Carreau and the Cross models were found to be applicable for characterising the rheology of the chocolate, as shown in section 7.3. The widely used Casson model was also examined and calibrated with the experimental data, but it was not found applicable for the specific chocolate samples.

7.3 Results and Discussion

7.3.1 Viscosity results for micro-aerated chocolate samples

The viscosity-strain rate plots without and with the artificial saliva present, as presented in Figures 7.4a and 7.4b respectively, show that viscosity decreases with increasing shear rate for all samples and increases with increasing micro-aeration level. Figure 7.4a compares viscosity values without artificial saliva for samples with porosities $f = 0, 10$ and 15vol%. The trend for all samples is the same, the viscosity is initially steady for low shear rates and reduces for shear rates between 0.2 and $600\,\mathrm{s}^{-1}$ as the shear rate increases until it reaches a constant value for shear rates above $\dot{\gamma} > 600\,\mathrm{s}^{-1}$.

Figure 7.4b shows results of viscosity for the different micro-aeration levels with the artificial saliva present. The same trend is observed, although there is no difference in viscosity values, for shear rates above $\dot{\gamma} > 600\,\mathrm{s}^{-1}$. Clear differences were observed in viscosity values for all micro-aeration levels with and without artificial saliva present in both figures, which was also justified by the ANOVA analysis. The Carreau and Cross models were fitted to the experimental results and both of them fit well as shown in Figures 7.4a and 7.4b. Tables 7.2 and 7.3 summarise the calibrated parameters of the two models without and with artificial saliva present respectively. The parameter n has a constant value of 0.72 whereas the parameter m ranges between 1.48 and 1.5. Both parameters are in good agreement with the study of Taylor et al. [244] who examined the rheology of molten crumb chocolate.

Table 7.1: Flow models found in the literature describing shear stress versus shear rate data [214].

Equation	Model	Parameters
$\tau = \eta\dot{\gamma}$	Newtonian [214]	τ : shear stress, η: viscosity, $\dot{\gamma}$: strain rate
$\tau = [\eta_\infty\dot{\gamma} + K_s\dot{\gamma}^{n_s}]$	Sisko [241]	η_∞ : infinite-shear viscosity K_s: time constant n_s: dimensionless exponent
$\eta = \eta_\infty + \frac{\eta_0-\eta_\infty}{1+(\alpha_c\dot{\gamma})^m}$	Cross [239]	η_0 : zero-shear viscosity α_c: time constant m: dimensionless exponent
$\eta = \eta_\infty + \frac{\eta_0-\eta_\infty}{\left[1+(\lambda_c\dot{\gamma})^2\right]^n}$	Carreau [240]	λ_c: time constant n: dimensionless exponent
$\tau = \mathrm{K}\dot{\gamma}^q$	Power law [214]	K: time constant q: dimensionless exponent
$\tau - \tau_{0\mathrm{H}} = K_H\dot{\gamma}^{n_\mathrm{H}}$	Herschel–Bulkley [242]	$\tau_{0\mathrm{H}}$: Herschel–Bulkley yield stress K_H: time constant q: dimensionless exponent
$\sqrt{\tau} = \sqrt{\tau_{CA}} + \sqrt{\eta_{CA}\dot{\gamma}}$	Casson [234]	τ_{CA}: Casson yield stress η_{CA}: Casson high shear viscosity
$\tau^{0.5} - \tau_{0\mathrm{M}} = K_\mathrm{M}\dot{\gamma}^{n_\mathrm{M}}$	Mizrahi and Berk [243]	$\tau_{0\mathrm{M}}$: Mizrahi yield stress K_M: Mizrahi time constant n_M: Mizrahi dimensionless exponent

As shown in the results presented so far, micro-aeration increases the viscosity of the chocolates while it reduces the coefficient of friction, as shown in chapter 6. The presence of micro-aeration modifies the rheology of the chocolate, and it has been observed to increase shear-thinning and viscoelastic behaviour [245]. Multiple studies on aerated liquids (honey, syrup, and guar gum) observed air bubbles resisting material deformation at a low shear rate, which results in a higher relative viscosity [246, 247]. According to Torres et al. [247] the pores that are present in the chocolate matrix influence the rheology behaviour leading to shear thinning. In low shear rates, the micro-pores act as a barrier to the deformation leading to viscosity increase with micro-aeration level. At higher shear rates, the micro-pores align with the material flow giving rise to shear-thinning. The capillary number, Ca, is used as a parameter to describe the deformation of micro-voids and is calculated as:

$$Ca = \frac{\eta_0 r\dot{\gamma}}{\Gamma} \tag{7.8}$$

where η_0 is the viscosity, r is the radius of the undeformed spherical pores, $\dot{\gamma}$ is the shear

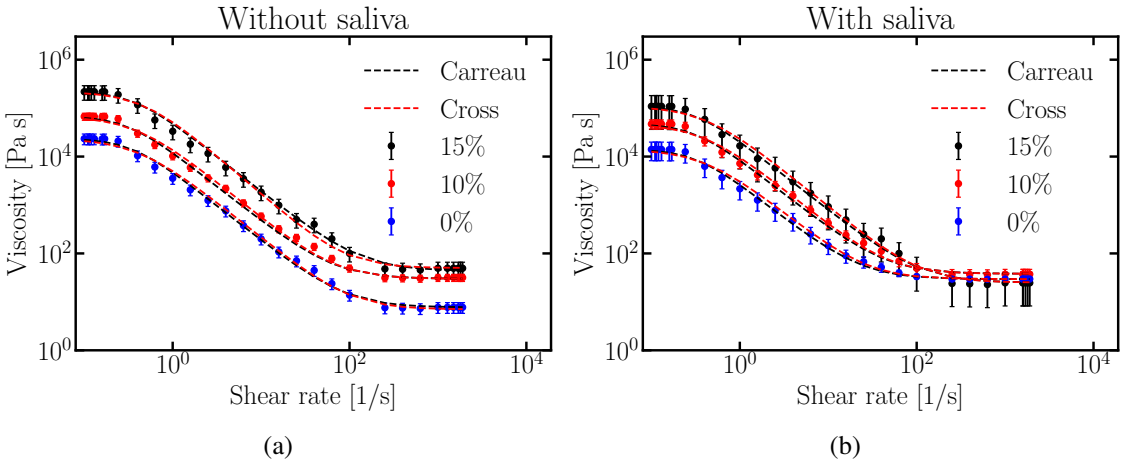

Figure 7.4: Flow behaviour of the three chocolate samples with different micro-aeration levels (a) without and (b) with artificial saliva present. The calibrated Carreau and Cross models are also depicted in both figures.

Table 7.2: Carreau and Cross calibrated parameters for different micro-aeration levels without artificial saliva present

Parameter	$f = 15$vol%	$f = 10$vol%	$f = 0$vol%
η_0 [Pa s]	218000	67191	23373
η_∞ [Pa s]	44	30	7.71
λ_c [s]	2.7	3.2	2.9
α_c [s]	2.1	2.5	2.4
n [-]	0.72	0.72	0.72
m [-]	1.6	1.5	1.48

rate and Γ is the surface tension at the pore-liquid interface. The equilibrium deformation is determined by the balance between the deforming, viscous stress $\eta_0\dot{\gamma}$ acting on a pore and the restoring stress supplied by surface tension (Γ/r). The shear thinning behaviour of aerated liquids has been reported in the literature initially in the study of Shaw et al. [248] who investigated the effect of bubbles in magma viscosity and the later study of Manga et al. [249] validated his findings. Figure 7.5 schematically illustrates the pore's shape changes for small Ca (left) and high Ca (right) values. The flow streamlines are more distorted in the case of the spherical pore which is associated to higher viscosity values. The additional viscous dissipation from the pores forces the liquid matrix to move around the pore's surface. Since the pore deformation produces an anisotropic microstructure, a scalar shear viscosity is not sufficient to describe the suspension viscosity. Theoretical [250, 251] and numerical [252] studies showed that large normal stress differences are generated by pore deformations. The viscosity reduction of micro-aerated chocolate follows the same trend as the bubble bearing magmas studied by Rust and Manga [247]. This theory can also be used to explain the similar viscosity values obtained for high strain rates

Table 7.3: Carreau and Cross calibrated parameters for different micro-aeration levels with artificial saliva present

Parameter	$f = 15$vol%	$f = 10$vol%	$f = 0$vol%
η_0 [Pa s]	109000	47048	14049
η_∞ [Pa s]	25	38	29.5
λ_c [s]	3.1	3.2	3.1
α_c [s]	2.4	2.5	2.4
n[-]	0.72	0.72	0.72
m[-]	1.6	1.5	1.48

when saliva is present in Figure 7.4b. The addition of saliva possibly enhances the flow of the melted chocolate around the deformed pores, reducing the effect that micro-aeration has on the viscosity.

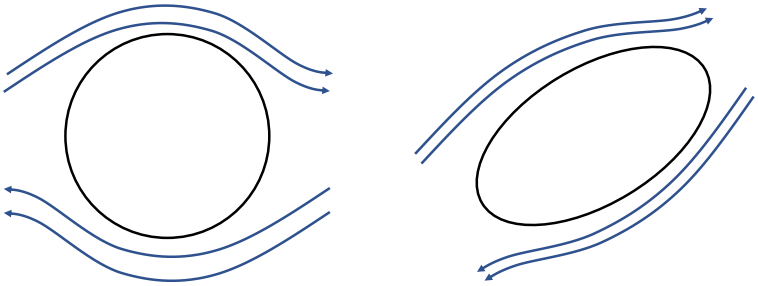

Figure 7.5: Illustration of bubble shapes and streamlines for small *Ca* (left) and high *Ca* (right). Deformed pores result in less deformed streamlines, and thus less viscous dissipation.

Another explanation can be attributed to effect of Fluid Immobilisation (FIM) that is a crucial aspect for the rheological characteristics of suspension systems. According to Windhab [253] the immobilization is related to the particle cavities and pores and will increase with increasing porosities. The FIM will lead to more viscous behaviour since the flow is restricted by the pores that exist in the matrix. Windhab [253] investigated the influence the porosity has on viscosity of starch particle/glucose syrup, and the findings agree with the trend presented in the current study.

7.3.2 Viscosity results for commercial chocolate samples with different cocoa solid content

Figure 7.6a shows a comparison for the viscosity values between the commercial chocolate samples without artificial saliva present. There is a clear difference for samples with different cocoa solids content. The highest cocoa solids content samples (85wt%) showed higher viscosity values for the entire range of tested shear rates compared to the 70wt% and 35wt% cocoa solid samples. The tests were repeated with artificial saliva

present and the results showed the same behaviour (Figure 7.6b), but in general the viscosity values are lower compared to the same tests without the artificial saliva present. Statistical analysis through ANOVA indicated a clear difference between the samples in both cases.

The viscosity curves followed the same trend as the micro-aerated samples. The shear thinning effect, present with and without the artificial saliva, was captured by both the Carrreu and the Casson models as shown with dashed lines in Figures 7.6a and 7.6b respectively. These two models have been frequently used in the literature to describe such suspensions [254]. The calibrated parameters of these models for the commercial samples with different cocoa solids content, without and with artificial saliva present are given in the Tables 7.4 and 7.5 respectively. The fitting parameters n and m have values in the range of 0.71-0.73 and 1.46-1.5 respectively, indicating strongly pseudoplastic behaviour, similar to the study of Taylor et al. [244].

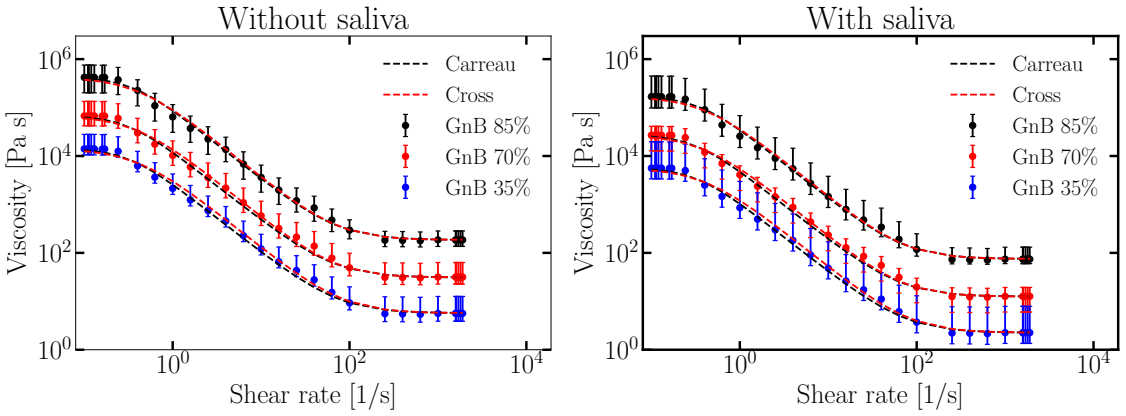

(a) (b)

Figure 7.6: Flow behaviour of the three commercial chocolate samples with different cocoa solid (a) without and (b) with artificial saliva present. The calibrated Carreau and Cross models are also depicted in both figures.

Table 7.4: Carreau and Cross calibrated parameters for the commercial chocolate samples for different fat content levels without artificial saliva present

Parameter	85%	70%	35%
η_0 [Pa s]	419932	67100	14025
η_∞ [Pa s]	185	31	5.7
λ_c [s]	2.8	3.2	3.1
α_c [s]	2.4	2.5	2.4
n [-]	0.73	0.72	0.71
m [-]	1.5	1.5	1.46

Table 7.5: Carreau and Cross calibrated parameters for the commercial chocolate samples for different fat content levels with artificial saliva present

Parameter	85%	70%	35%
η_0 [Pa s]	167972	26876	5610
η_∞ [Pa s]	75	12.5	2.25
λ_c [s]	2.7	3.15	3.1
α_c [s]	2.33	2.52	2.4
n [-]	0.72	0.73	0.71
m [-]	1.5	1.5	1.48

The Casson model is the most widely used model to describe the rheology of chocolate. The IOCCC has proposed the Cassson model as the standard method for determining chocolate rheology. In this study Casson model was implemented and calibrated for shear rates higher than $0.1\,s^{-1}$, since this is the recommended range to apply the Casson model. A representative result is shown in Figure 7.7 for the $f = 15$vol% micro-aerated chocolate sample without artificial saliva present, with calibrated parameters of $\tau_{CA} = 40\,000$ Pa and $\eta_{CA} = 4$ Pa s. It is evident that the Casson model is not appropriate for characterising the viscosity values of the chocolate samples under the conditions tested in the present study. The plot of Figure 7.7 also shows that, the data cannot be fitted to the Casson model over a limited shear rate range (similar to that specified in the IOCCC guidelines).

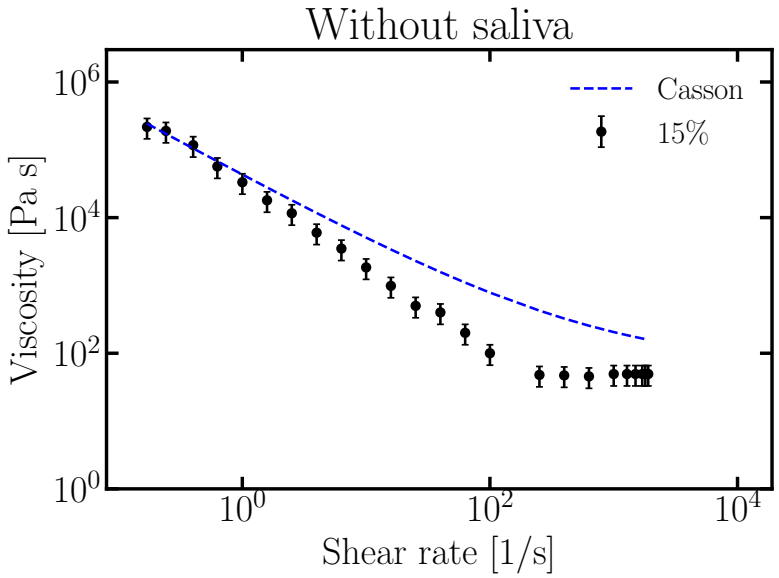

Figure 7.7: Fitting of Casson model to experimental data of micro-aerated samples with porosity $f = 15$vol% without artificial saliva present. The Casson calibrated parameters are $\tau_{CA} = 40\,000$ Pa and $\eta_{CA} = 4$ Pa s.

7.3.3 Frequency sweep results for micro-aerated samples

The dynamic rheological test provides a more direct correlation with microstructure than the steady shear rate rheological test since the materials can be examined in their at-rest state without causing any disruption of their underlying structures. Figures 7.8a and 7.8b illustrate the storage and loss moduli respectively obtained by frequency sweep tests without artificial saliva present. In both graphs the moduli decrease as micro-aeration increases and the loss modulus values are constantly higher than the storage modulus for all micro-aeration levels. The loss modulus tends to increase when frequency is increasing as shown in Figure 7.8b.

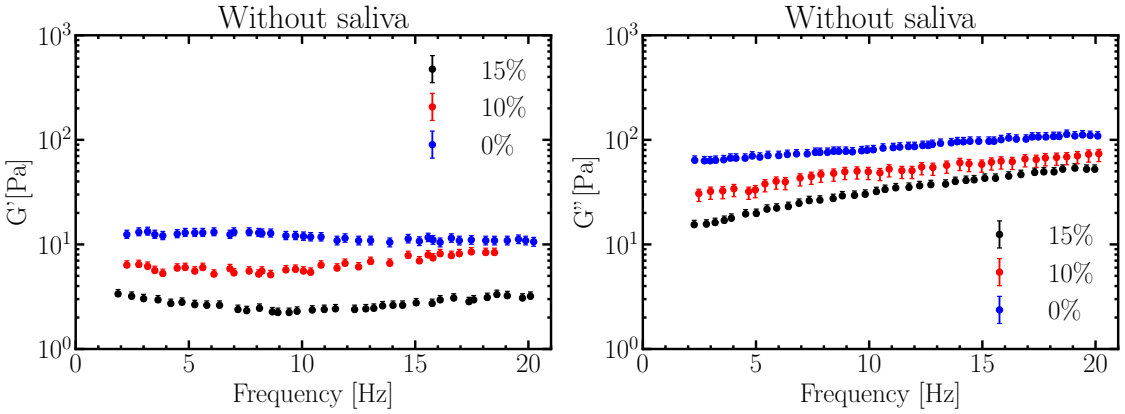

Figure 7.8: Frequency sweep test results for micro-aerated samples without artificial saliva present (a) storage modulus, G', (b) loss modulus G''. Error bars represent maximum and minimum values over five repeats.

A similar trend is obtained when artificial saliva is present in the experiment. Figures 7.9a and 7.9b represent the storage and loss moduli respectively, with artificial saliva present. The values are reduced, as expected, compared to the respective ones in Figure 7.8 due to the addition of artificial saliva. In both tests the values of loss modulus, G'', are higher than that of the storage modulus, G' implying that the chocolate has a more viscous than elastic behaviour. This type of behaviour is common in chocolate and lies in good agreement with results found in the literature [228]. The storage modulus, G', correlates with the stiffness of the structure and remains constant for all micro-aeration levels regardless whether artificial saliva in present or not. On the other hand the loss modulus tends to increase as the frequency increases.

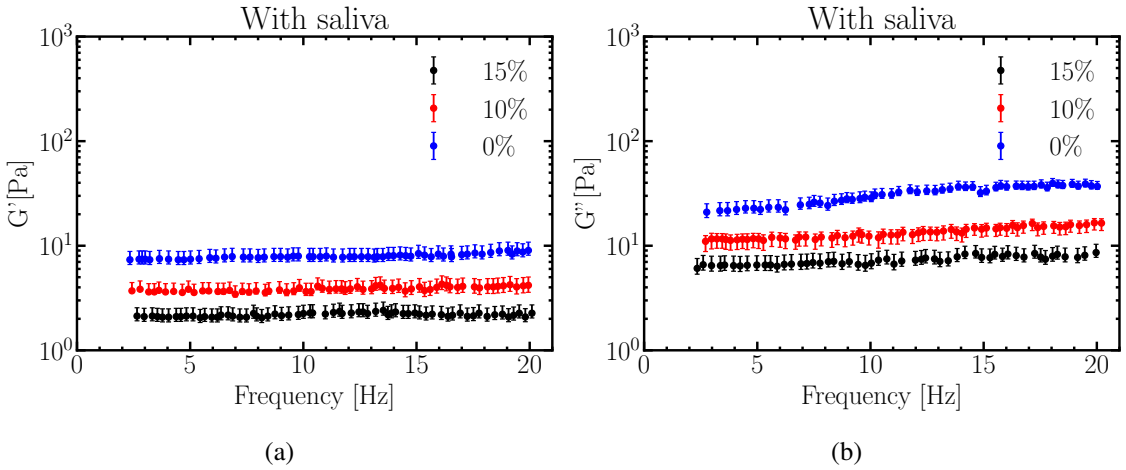

Figure 7.9: Frequency sweep test results for micro-aerated samples with artificial saliva present (a) storage modulus, G', (b) loss modulus G''. Error bars represent maximum and minimum values over five repeats.

7.4 Conclusions

Rheological tests were conducted to measure the viscosity and the storage and loss moduli of different types of molten chocolate. The test uses the parallel hashed plates configuration heated at 37 °C and the chocolate is pre-melted using an oven at 40 °C. The effect of cocoa content and micro-aeration was investigated with and without artificial saliva present. The presence of artificial saliva reduces the viscosity by approximately 40%. In all cases the viscosity values was characterized by shear thinning and the Carreau and Cross models were fitted to the experimental data. Although it is difficult to draw concrete conclusions regarding the effect of different components on the tested values, it is evident that viscosity *increased* with *increasing* micro-aeration and *increased* with *increasing* cocoa content.

The tribology results presented in Figure 6.6b (chapter 6) can be used in conjunction with the rheology findings of this chapter in order to explain how the lubricating properties are influenced by the micro-aeration. The coefficient of friction of the artificial saliva was relatively high, this decreased with the addition of chocolate to the contact. These plots (Figure 6.6b) show how friction changes during the reciprocating stroke: at the reciprocation point where the velocity is 0 the friction coefficient is high, but this reduces towards the middle of the stroke as the speed reaches a maximum of 30 mm s^{-1}. The lubricating film thickness increases with speed [255] and this contributes to a drop in friction in the middle of the stroke as the surfaces are separated. In addition, the coefficient of friction in the centre of the stroke reduced with increasing porosity from 0.175 for 0vol% aeration to 0.08 for 15vol% micro-aerated chocolate, i.e. a 54% reduction. This reduction is related to the increased viscosity of micro-aerated chocolate samples [256],

which also contributes to an increased lubrication film [257].

8 Discussion

* Part of this chapter has been published in Food Structure [257]

Topics

8.1 Sensory perception

The current chapter aims to link the findings presented so far in chapters 2 - 7 with sensory perception. Sensory perception is defined as the measurement of a product's quality based on the five senses: touching, hearing, sight, smell and taste [213]. The food industry is mainly using trained panels to evaluate the quality of a food product. The variability from person to person results in a large scatter in scores when the evaluation is based on sensory panels. This lack of precision comes from the way that sensory texture is perceived by an individual. Sensory texture is generated primarily by touch, followed by signals generated at the nerve endings which are transmitted through the central nervous system to the brain. There, the signals are combined with past experience of the consumer and a final opinion about the product is formed [258]. It is evident that texture measurement is a very complex but important factor that should be taken into consideration in food design. The goal of the current chapter is to provide an alternative methodology, based on experimental and computational methods, that is capable of providing an objective sensory evaluation. The mechanical, tribological and rheological results will be compared against a sensory evaluation from a trained sensory panel and a qualitative link between the findings and sensory properties will be provided.

Mastication is a complex procedure that includes processes like: food deformation and shear, flow, comminution and hydration and chemical degradation due to the interaction with artificial saliva which result in shape and size change of the food, and a transition

from solid to liquid phase (melting). The human senses are capable of recording each one of these processes and make a decision about texture perception. Unlike human body, there is no developed equipment that can mimic the entire mastication process, including the different mastication speeds and tongue motions and evaluate the sensory perception. In the current thesis, an attempt to break down the mastication process to individual components has been attempted and the connection of the findings presented in chapters 2-7 to the sensory panel results will be given in an attempt to proved a useful and objective tool in the sensory perception evaluation. Before that, it is important to understand how the sensory panels are being trained and what are the criteria with which they rank the food products.

According to Bourne [213] the major steps for establishing a sensory texture profile are listed below:

1. selection of sensory panel
2. training of the panel
3. establishing standard rating scales
4. establishing a basic Texture Profile Analysis (TPA) score sheet
5. developing a comparative TPA score sheet

The sensory panel is usually comprised by at least ten volunteers and is desired to have members of both genders. The recruitment process for the selection of the panel members includes the evaluation of four consecutive samples of different hardness scale presented in random order [259]. The participants who successfully rank the products according to their hardness, are used for further training and the rest are excluded from further participation. The successful candidates form the sensory panel test that is trained through a procedure which will be briefly presented here. The first step in the training is to familiarise the panel test with the standard scales that are used to rank the different food properties. When the panel is fully familiarised with the standard scales, they develop (as an exercise) a complete texture profile on a simple product such as soda crackers using the basic TPA score sheet. Afterwards, the panel uses a comparative texture profile from a different product, chosen randomly and repeats the rating until a similar texture perception is received and defined by all the panel members.

In the following section, two sensory study methods will be presented. Initially, the profile sensory test results are presented followed by the temporal dominance sensations (TDS) results.

8.1.1 Sensory profile results

Twelve expert panellists were asked, among others, to define in terms of mechanical characteristics the textural perception that they received. These mechanical characteristics

will be presented and will be used as the basis for the link between the findings of chapters 2-7 and the textural perception.

Hardness is defined as the force required to compress the food between the molar teeth for solid foods or between the tongue and the palate for semi-sold foods. Hardness is evaluated by the sensory panel, by placing the food between the molar teeth and evaluating the magnitude of the force needed to compress the food. Hardness can be related to experimental measurements such as the Young's modulus and the fracture stress [260, 1, 261, 262, 263]. Several studies have recommended a correlation between hardness and Young's modulus [264, 265, 266] while other studies suggest a link to the fracture stress [264, 260, 267]

Grittiness is defined as the force required for a food specimen in order to crack. The panelist is asked to place the specimen between the molar teeth and chew naturally until the food cracks. The grittiness is measured as the horizontal force with which the food moves away from the point where the vertical force is applied. Another criterion that helps determine grittiness is the suddenness with which the food breaks [213]. Grittiness can be related to the mechanical properties and particularly the fracture properties that influence the particle size distribution of the fragments [265]. Studies on gels showed that the rate of breakdown, fracture strain, and fracture toughness affect the grittiness/smoothness perception [268].

Stickiness is defined as the force required to remove food material that adheres to the oral cavity surfaces during the mastication. The technique the panel test follows for evaluating stickiness is to place the food in the mouth, press it against the palate, and evaluate the force required to remove it with the tongue [213]. These properties are associated with surface properties [262] and are greatly influenced by the presence of saliva. For this reason the panel test is asked to rinse their mouth with water before the evaluation begins [213]. Therefore, it is believed that the friction results in the presence of saliva could explain the changes in "stickiness". The tribology results indicated the chocolate structure influences the coefficient of friction, which decreases with increasing aeration, whereas the rheology experiments showed an increase in the viscosity due to micro-aeration.

Melting time is defined as the time that it takes for the food to melt in the oral cavity. Mongia and Ziegler [269] have already reported the link between fragmentation and melting time. Higher fragmentation, which is related to the mechanical properties, results in more surfaces exposed to the temperature of the oral cavity, leading to reducing melting time. The thermal characteristics of micro-aerated and non aerated chocolates samples is studied in detail in the PhD thesis of Bikos [10].

Dryness is related to the humidity levels that the sensory panelist experiences in the mouth. Dryness associated with the effect of saliva is mixed with the melted chocolate contributing to a higher level of moistness in the mouth.

The sensory profile results, presented in Figure 8.1, have been provided by Nestlé.

The sensory panel consisted of twelve experts asked to evaluate the non aerated and the $f = 10vol\%$ micro-aerated chocolate samples. An analysis of variance (ANOVA) using a 95% significance level was employed to identify significant differences between the two types of chocolate. The results are presented as averages in the form of bar charts and significant difference (p-value< 0.05) in attributes between the two chocolates were computed and are presented with grey stars in Figure 8.1. The red star refers to cocoa perception where a p-value close to the critical value of 0.05 was measured ($p = 0.06$). The methodology of ANOVA is described in Labbe et al. [270]. The panelists were allowed to consume a specific chocolate quantity ($\sim 1\,g$) as they needed to provide a reliable ranking.

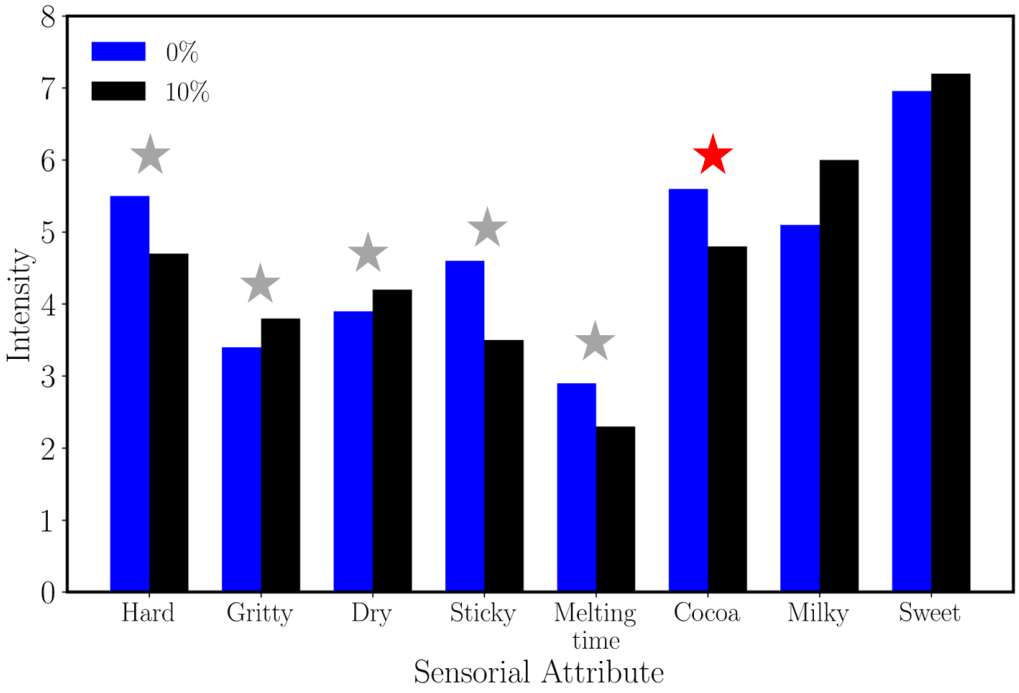

Figure 8.1: Sensory profile results of non aerated and $f = 10$vol% micro-aerated chocolate samples. Grey stars depict the attributes where significant differences have been based on ANOVA ($p < 0.05$), whilst the red star refers to cocoa perception where a p-value close to the critical value of 0.05 was measured ($p = 0.06$).

Table 8.1 summarises the attributes and the scale according to which the panel test assessed the two chocolate types.

Overall micro-aeration results in a softer, grittier, and less sticky product comparing to the non aerated chocolate. Interestingly, the sweetness perception remained roughly constant, although the mass of sugar particles per unit volume was lower for the micro-aerated samples.

Table 8.1: Sensory attributes and scale for assessing the chocolate types.

Attribute	Scale
Hardness	Soft (0) – Hard (10)
Crumbly	Not very (0) – Very (10)
Dry	Moist (0) – Dry (10)
Gritty	Smooth (<3) – Powdery (3-6) – Gritty (>6)
Sticky	Nil (0) – Strong (10)
Melting time	Short (0) – Long (10)

8.1.2 Temporal Dominance Sensations (TDS) results

The results of the Temporal Dominance Sensations (TDS) study were provided by Nestlé. The same group of panelists, as in the sensory profile tests, were asked to rank the two chocolate products according to their dominance. According to Pineau [271] the dominance of an attribute is not associated with its intensity but with the predominant sensorial attribute perceived by the panelists during a given time. The panelists consumed a square of 2 g per sample, and immediately after the sample was placed in the mouth, the time started. In TDS tests, the panelists assess the products using twelve textural attributes, soft/hard, dry/moist, crumbly, smooth/powdery, sticky, cooling, melting, powdery residue and mouth coating. During the tests, all twelve attributes were presented simultaneously on a computer monitor and the panellists had to choose the dominant attribute they perceived while consuming the product and after swallowing. When no more sensation was perceived, the assessment finished.

The data collected from this test are summarised as [270]:

- the time when an attribute is selected as dominant
- the name of the given attribute
- the intensity scored for attribute

It is worth noting that, the dominance of an attribute is not associated with its intensity but with the predominant sensorial attribute perceived during tasting by a panellist at a given time [271]. When with evolving time a new attribute is being sensed, the panellist would select this new attribute as the dominant one. It is possible to select the same attribute several times or not to select an attribute at all during the test. The attributes were scored in terms of the number of panellists who had selected a certain dominant attribute at a given time, i.e. dominance rate. The attributes, which were found to be significant, i.e. exceeded the significant line (shown as red dashed line in Figure 8.2), are presented. The methodology of constructing the significance line is described by Labbe et al. [270] and Pineau et al. [271].

Figure 8.2 shows the TDS results for both types of chocolate. The y-axis represents the dominance of each attribute which reflects the percentage of participants perceiving a certain attribute at a certain time interval. The x-axis the time normalised to the total test time is plotted. The red dashed line depicts the significance level above which an attribute is considered as significant. This significance level was selected to 16% dominance rate.

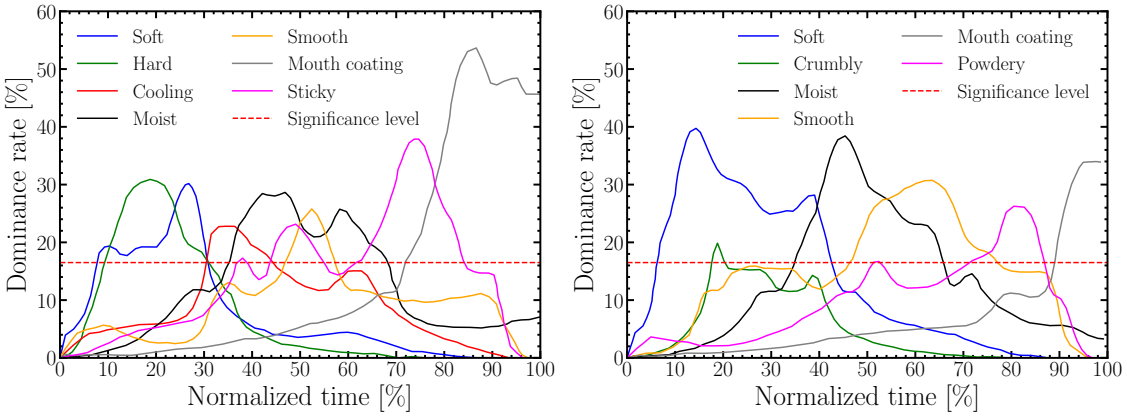

Figure 8.2: Comparison of Temporal Dominance Sensations (TDS) results between (a) non aerated and (b) $f = 10$vol% micro-aerated chocolate. The red dashed line represents the significance line

The TDS results of the non aerated chocolate samples, depicted in Figure 8.2a, show that initially softness and hardness are dominant. A maximum peak of 30% for hardness and softness was found at 20% and 28% of the total testing time respectively. Although hardness and softness are interpreted as opposite attributes and might be unclear how they can be simultaneously present, this can be attributed to the different chewing preference of the panelists which could create different textural perception as reported by other studies as well [143, 272]. Cooling is the next attribute that becomes dominant at a normalised time $\sim$ 30% and a duration of 15% of the total time. At this point it can be assumed that most of the chocolate mass has melted, since the cooling perception is associated with the latent heat during the phase change of the chocolate. Afterwards, between 40% and 60% normalised time, attributes such as moist, smooth and sticky become dominant with maximum dominance rate 28%, 25% and 38% respectively with a duration of 35%, 10%, and 40% of the total oral processing time respectively. Finally, mouth coating becomes dominant with a maximum value of 54% with a duration of 28% of the total time. Mouth coating is the last attribute that appears since it is perceived after swallowing and the initial perception of this attribute suggests the onset of swallowing.

Figure 8.2b summarises the TDS results for the $f = 10$vol% micro-aerated chocolate samples. Opposite to the non aerated samples, only softness was recorded initially for a duration of 40% of the total time with a maximum score of 40%. Crumbliness appears

in the same time period but becomes dominant for only 5% of the time with a maximum value of 20%. It is interesting that crumbliness was not recorded at any time in the non aerated samples of Figure 8.2a. Afterwards, the attributes of moist and smooth were recorded by the panelists in Figure 8.2b, with a score of 39% and 30% respectively. Powdery sensation becomes dominant later on with a peak value of 25% followed by the mouth coating, which 50% of the panelists found dominant and appears last similar to the results of the non aerated samples show in Figure 8.2a.

Overall, comparing the results of the two types of chocolate it is evident that the micro-aerated chocolate samples produce simpler TDS graphs with less recorded attributes. In addition, the higher dominant rate values observed for the micro-aerated chocolate for softness, moistness, and smoothness, depict the clear distinction of each attribute at each time. The common attributes between the two types are: soft, moist, smooth and mouth coating. Figure 8.3 depicts the difference between the $f = 10$vol% micro-aerated and the non aerated samples for these common attributes. Overall, it appears that micro-aeration increases the soft, moist and smooth attribute without influencing the time that they appear. On the other hand it is evident that mouth coating sensation decreases with micro-aeration.

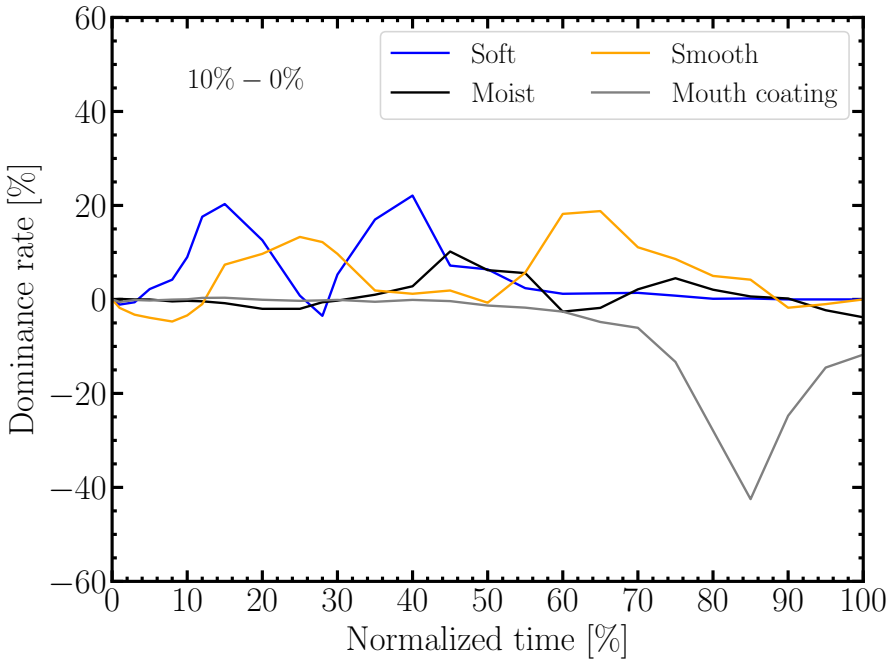

Figure 8.3: Difference between the $f = 10$vol% micro-aerated and non aerated chocolate samples for common sensorial attributes

8.2 Link of computational mechanics, tribology and rheology findings to the sensory study

The overall goal of the current thesis is to provide an alternative or additional computational and experimental tool that would act as complementary methodology of quantifying how the change in structure influences the sensory perception without the need of a sensory panel. In this section the findings presented in chapters 2-7, where the effect of micro-aeration on the mechanical, tribological and rheological properties were presented, will be linked and compared against the sensory panel test data provided by Nestlé. It is worth noting that, only the $f = 10$vol% was provided and it will be used for the comparison.

Starting with the mechanical properties, as those measured by experiments [11] and validated though computational models, micro-aeration decreases the Young's modulus, fracture stress and fracture toughness. These mechanical properties can be linked to textural properties such as softness, hardness and crumbliness which are present at the early stages of oral processing. The mechanical properties influence the fragmentation process during the initial chewing cycles. As the oral processing continues, more attributes appear in the mouth such as, moistness, dryness, cooling perception, smoothness, powdery and grittiness. These attributes can be related to the heat transfer properties of chocolate during the phase change. This topic was investigated in detail in the PhD dissertation of Bikos [10] and the main findings indicated that although the thermal conductivity of the micro-aerated chocolate decreases and slower heat transfer within the sample is expected, it melts faster due to the higher fragmentation compared to the solid chocolate. At the later stages of oral processing, stickiness and mouth coating are perceived which can be linked to the tribological and rheological results as a thin film is created between the rubbing surfaces. Figure 6.6b indicates that the lubricating film thickness increases with speed [255] and this contributes to a drop in friction in the middle of the stroke as the surfaces are separated. In addition, the coefficient of friction in the centre of the stroke reduced with increasing porosity. This reduction is related to the increased viscosity of micro-aerated chocolate samples [256], which also contributes to an decreased stickiness attribute [257].

The TDS results (Figure 8.2) can be used as a guide in terms of evolution of sensorial attributes happening in the mouth during the oral processing. Specifically, the softness/hardness attribute is perceived at the initial stages of the test, coinciding with the first bite [266]. Hardness values then decrease, since the food specimen is broken into smaller pieces easing the melting process. At the same time, the fragments interact with the oral cavity surfaces generating the attributes of grittiness (gritty-smooth) and dryness (dry-moist). The cooling attribute is accelerated as melting continues and the interaction

with saliva gives a moist and sticky sensation. Finally, after the fully melted chocolate is sheared between the tongue and the palate is swallowed leaving a smooth and mouth coating perception.

Comparing the TDS data for the micro-aerated chocolate (Figure 8.2a) to the ones of the non aerated (Figure 8.2b), it is evident that micro-aeration not only modifies the existence of certain sensorial attributes, for instance softness over hardness, but also the duration of dominance of certain sensorial attributes. Initially, the lower force required to fracture the micro-aerated sample (shown in Figure 5.4) creates a soft sensation as dominant, as opposed to the solid reference where a combination of softness and hardness was observed. The decrease in fracture toughness with micro-aeration releases a dominant crumbly sensation, which is perceived right after the peak in softness perception. The increase of fragmentation observed by the *in vivo* and *in vitro* mastication tests (shown in Figure 5.7), creates a moist sensation with a higher peak compared to the solid reference chocolate due to increase of surface area with fragmentation and the interaction of the fragments with saliva. For the micro-aerated chocolate, the increase of fragmentation reduces the melting time, creating a longer smooth perception compared to its solid counterpart. The reduction of the friction coefficient with micro-aeration suggests that a persistent thin film is developed in the tongue palate interface, which in turn, reduces the stickiness perception. This is also related to the increase in viscosity due to micro-aeration, which enhances the lubrication and reduces the coefficient of friction.

Overall, using engineering methods as a guide, the 17% reduction in the elastic modulus/fracture toughness values with $f = 10$vol% micro-aeration creates a drastic increase in the dominance peak and duration of softness, 33% and 40% respectively (Figure 8.2). In addition, a 28% decrease in friction coefficient for the $f = 10$vol% micro-aeration in combination with a 7% increase of viscosity eliminated the perception of stickiness as dominant for the $f = 10$vol% micro-aerated chocolate.

The instrumental results showed that small structural changes in chocolate's composition affect the respective material properties and, based on the sensory tests, such structural changes create significant changes in sensorial profile and the evolution of sensorial attributes during oral processing. It is believed that there is connection between material properties and sensorial attributes, but there is the need for conclusive statistical analysis to validate those findings

9 Conclusions

Topics

9.1 Summary and Concluding remarks

The aim of this thesis was to address the need for studying the initial stages of the oral processing of chocolate and examine the effect of micro-aeration. Micro-aeration was applied in chocolate and an experimental and computational study in mechanics, tribology and rheology was conducted. The computational mechanics study was firstly presented. This required the development of a material model, able to predict the strain rate dependent nature of chocolate and also capable of coupling with an appropriate damage model for the simulation of the first bite. Secondly, the effect that micro-aeration has on the mechanical properties of chocolate was studied through a micro-mechanical model the estimations of which were used in the macroscopic FE simulations of the first bite.

The strain rate dependence of chocolate that was observed by compression experiments [11] revealed the need for applying a viscoplastic constitutive model. Several viscoplastic constitutive models are provided in the built-in library of ABAQUS, including the Johnson-Cook and the two-layer viscoplastic model. Both of these models were calibrated against the experimental data, obtained by the parallel PhD study [10], and were both presented in chapter 2. The need of coupling the selected material model with an appropriate non-local damage model in the ABAQUS/Explicit solver, required the development of a VUMAT subroutine. A simplified version of the Johnson-Cook model, neglecting the temperature dependence, was written in a VUMAT subroutine, which was validated by comparing the stress-strain response of the VUMAT with the respective data obtained by a UMAT Johnson-Cook subroutine and the Johnson-Cook built-in model.

The damage criterion was introduced in the model by introducing a damage evolution

law. The damage criterion was calibrated against already available compression experiments from a parallel PhD study [10]. The equivalent plastic strain at fracture initiation and a stress triaxiality parameter were the main parameters of the damage evolution law. The fracture toughness, calculated from three point bending experiments [11], was used as a material parameter that drives the fracture evolution. An extension to the non-local damage model was applied by calculating the non-local equivalent plastic strain. This was done through coupling the VUMAT subroutine with a VDFLUX subroutine and by changing the step to temperature-displacement in ABAQUS/Explicit. The constitutive model coupled with the non-local damage law made it possible to predict fracture initiation and propagation in the form of element deletion, thus, without the common requirement of predefining the crack path; the latter was desirable in the micromechanical FE models and the chewing FE model.

After establishing the constitutive and the damage laws, a micromechanical study was conducted in order to estimate the effect that micro-aeration has on the mechanical properties. Initially, an RSA algorithm was used to generate porous unit cells in both monodisperse and polydisperse configurations. The size of the unit cells that could be considered as representative was examined by applying KUBC and PBC. A unit cell with 100 pores was considered as representative of the entire volume and was used for the subsequent mechanical simulations. The Young's modulus was found to agree well with the experimental data for both micro-aeration levels $f = 10\text{vol}\%$ and $f = 15\text{vol}\%$ for both monodisperse and polydisperse pore diameter distributions. The results were compared with analytical models and found to lie between the Voigt model and and the upper bound Hashin-Shtrikman model. The same RVEs were used for the plastic and fracture properties. In both examined porosities the yield point was found to be in good agreement with the experimental data for both monodisperse and polydisperse microstructures. However, only the polydisperse RVEs predicted well the strain at failure, whereas the monodisperse configurations underestimated the failure strain for both micro-aeration levels of 10vol% and 15vol%. The estimated values were used in the macroscopic FE simulations of the first bite, where the food specimen is introduced as a homogeneous part with mechanical properties calculated from the micromechanical analysis.

The computational mechanics study was completed with the macroscopic FE simulation of the first bite. For this study, a digitised adult male 3D skull, generated using X-ray computed tomography, was used to extract a pair of the two last molar teeth for the FE simulations and the same pair of molar teeth was 3D printed for the experimental set up. The FE simulations were conducted in the ABAQUS/Explicit solver and the VUMAT subroutine coupled with the VDFLUX subroutine. The force-displacement curves from the FE simulations were examined with the respective ones from the experiments conducted with the same 3D printed geometry and same food specimen size. The results obtained from the FE simulations found to agree well with the experimental data for all

tested speeds and the mesh independency was shown. The food fragments from the experiment were also compared against *in vivo* experiments and it was found that higher chewing speeds in the experiment result in fragments that are closer to the *in-vivo* results.

A novel tribology experimental set-up was developed, in chapter 6, to measure the changes in the friction coefficient due to composition and structure. The test consisted of a flat PDMS disk, representing the tongue loaded and reciprocating against a stationary lower glass surface representing the palate. The test was applied to molten chocolate samples with and without artificial saliva. Friction was measured over the first few rubbing cycles, simulating mechanical degradation of chocolate in the tongue-palate region. Samples of different micro-aeration levels and cocoa-solid content were tested in order to quantify the influence that each parameter has on the friction properties. In commercial samples, friction coefficient decreased with decreasing cocoa (85-37 wt%), decreasing fat (32-20 wt%) and increasing sugar (14-46 wt%). The friction coefficient decreased with increasing micro-aeration levels over the range of 0-15 vol% micro-aeration and for all chocolate samples the friction coefficient decreased with the presence of an artificial saliva film. In addition, different friction-speed response curves were observed depending on the nature of the chocolate and the presence of artificial saliva. The commercially available chocolate showed a friction coefficient that is constant over the stroke. For the micro-aerated chocolate samples the friction coefficient changed with speed. An increase with speed was observed when artificial saliva was not present, whereas a decrease with speed was observed when the artificial saliva was present.

The rheological experimental set-up was presented in chapter 7. A parallel hatched plate geometry configuration was used and the same chocolate samples of the tribology study were used to measure the viscosity and the storage and loss moduli. All the tests were conducted at 37 °C and the chocolate samples were pre-melted using an oven at 37 °C. The presence of artificial saliva reduced the viscosity by approximately 40% and in all cases the viscosity was characterized by shear thinning and the Carreau and Cross model were fitted to the experimental data. It is evident that viscosity *increased* with *increasing* micro-aeration and increased with *increasing* cocoa content. In addition, the loss modulus was consistently higher than the storage, regardless of whether the artificial saliva was present or not, revealing the viscoplastic nature of chocolate.

Finally in chapter 8 a link between the findings presented in chapters 2-7 and the data available from a sensory study on the $f = 10$vol% was provided. The reduction to the mechanical properties due to micro-aeration has a significant effect on the dominance peak and duration of softness. In particular, a 17% reduction to the elastic modulus and fracture toughness values, due to $f = 10$vol% micro-aeration, leads to an increase in the dominance peak (by 33%) and duration (by 40%) of softness. In addition, the 28% decrease in friction coefficient and the 7% increase of viscosity for the $f = 10$vol% micro-aeration, eliminated the perception of stickiness as dominant for the $f = 10$vol% micro-

aerated chocolate.

9.2 Future work

Several novel computational and experimental methodologies developed during this study. This section highlights limitations and assumptions that were applied in chapters 2-8 based on which future work is proposed.

In chapter 5 the first bite was studied from both an experimental and computational point of view. A pair of molar teeth was 3D printed and was attached at an Instron universal machine. The outcome of this experiment was twofold. The recorded force-displacement data were used to validate the FE simulations, whereas the fragmented chocolate parts were compared against *in vivo* experiments. A proposed improvement of this experimental set-up would be to run the experiment in a controlled temperature and humidity environment in order to better replicate the physiological conditions that exist in the mouth. The effect of saliva was not considered since the chocolate specimens were placed in silicon bags in both *in vitro* and *in vivo* experiments. Future studies could include a small amount of artificial saliva in the experimental procedure.

The theory and the findings of chapters 2-4, led to the development of a FE simulation that can reliably predict both the force-displacement response but also the crack pattern due to the interaction of the food with the teeth. The FE simulations revealed the influence that the coefficient of friction has on the simulation results. Higher force-displacement responses were obtained for increasing coefficient of friction values. The models were initial calibrated for the non-aerated samples and the coefficient of friction valued was reduced, in an analogy to the data available from the tribology experiments, for the $f = 10$vol% and $f = 15$vol% micro-aeration levels. While a simple contact ABAQUS law and was used here, a more sophisticated frictional law is suggested for future studies. In addition, the assumption of the coefficient of friction analogy between the tribology experiments, contacted in the tongue-palate region, and friction between teeth and chocolate can be further studied in future studies.

Regarding the damage onset criterion, this was set to occur when the critical equivalent plastic strain is exceeded in the shear or tensile states. This was chosen in order to avoid unreasonable and unphysical removal of material (element deletion). Therefore, future research is recommended on developing damage laws that take into account anisotropic stress degradation.

Another important aspect that needs to be further investigated is the strain rates that exist during the first bite. The available experimental data provided information for strain rates between $0.01\,\mathrm{s}^{-1}$ and $1\,\mathrm{s}^{-1}$, values that are lower than those developed between teeth and food during the oral process. This leads to the assumption that the chocolate behaves in a similar way for higher strain values, an assumption that is applied by extrapolation

through ABAQUS. This could be further investigated in a future study, by performing experiments in apparatus that allows testing in higher strain values.

Finally, regarding further improvements in the tribological and rheological experimental set ups, a chamber could be designed to provide temperature and humidity controls. Also a more sophisticated artificial saliva recipe could be used that could include more ingredients of saliva than only mucin that was used in the present thesis.

A Appendices

A.1 Jacobian derivation for the Johnson-Cook consitutive model

The methodology for the calculation of the Jacobian for the modified Johnson-Cook constitutive model is based on the work of Achour et al. [26] and is an extension of the elastic-plastic approach presented by Simo and Hughes [273]. Initially the constitutive model pf equation (2.21) is expressed in terms of gradients as:

$$\begin{aligned}\Delta\sigma_{ij}^{(n+1)} &= 2G\Delta\varepsilon_{ij}^{(n+1)} + \lambda\Delta\varepsilon_{kk}^{(n+1)}\delta_{ij} - 2G\Delta\varepsilon_{ij}^{p(n+1)} \\ &\overset{eq.(2.16)}{=} 2G\Delta\varepsilon_{ij}^{(n+1)} + \lambda\Delta\varepsilon_{kk}^{(n+1)}\delta_{ij} - 2G\left[\frac{3}{2}\Delta\varepsilon_{eq}^{p(n+1)}\frac{S_{ij}^{(n+1)}}{\sigma_{eq}^{(n+1)}}\right] \\ &= 2G\Delta\varepsilon_{ij}^{(n+1)} + \lambda\Delta\varepsilon_{kk}^{(n+1)}\delta_{ij} - 3G\Delta\varepsilon_{eq}^{p(n+1)}\frac{S_{ij}^{(n+1)}}{\sigma_{eq}^{(n+1)}}\end{aligned} \tag{A.1}$$

Derivation with respect to $\Delta\varepsilon_{ij}^{(n+1)}$ leads to:

$$\begin{aligned}\frac{\partial\Delta\sigma_{ij}^{(n+1)}}{\partial\Delta\varepsilon_{kl}^{(n+1)}} = 2G\frac{1}{2}\left[\delta_{il}\delta_{jk}+\delta_{ik}\delta_{jl}\right] + \lambda\,\delta_{ij}\delta_{kl} - 3G\Delta\varepsilon_{eq}^{p(n+1)}\frac{1}{\sigma_{eq}^{(n+1)}}\frac{\partial S_{ij}^{(n+1)}}{\partial\Delta\varepsilon_{kl}^{(n+1)}} \\ -3G\frac{\partial\Delta\varepsilon_{eq}^{p(n+1)}}{\partial\Delta\varepsilon_{kl}^{(n+1)}}\frac{S_{ij}^{(n+1)}}{\sigma_{eq}^{(n+1)}}\end{aligned} \tag{A.2}$$

The calculation of the derivative $\frac{1}{\sigma_{eq}^{(n+1)}}\frac{\partial S_{ij}^{(n+1)}}{\partial\Delta\varepsilon_{kl}^{(n+1)}}$ in not straight forward and further investigation is needed. The deviatoric parts of the stress and strain are written as:

$$\boldsymbol{S} = \boldsymbol{\sigma} - \frac{1}{3}\mathrm{tr}[\boldsymbol{\sigma}]\boldsymbol{I}, \quad \boldsymbol{e} = \boldsymbol{\varepsilon} - \frac{1}{3}\mathrm{tr}[\boldsymbol{\varepsilon}]\boldsymbol{I} \tag{A.3}$$

It can be shown that:

$$\boldsymbol{S}^{tr(n+1)} = \boldsymbol{S}^{(n)} + 2G\Delta\boldsymbol{e}^{(n+1)} = \boldsymbol{S}^{(n+1)} + 2G\Delta\boldsymbol{\varepsilon}^{p(n+1)} \tag{A.4}$$

Therefore, the following can be derived:

$$\frac{1}{\sigma_{eq}^{(n+1)}}\frac{\partial S_{ij}^{(n+1)}}{\partial \Delta\varepsilon_{kl}^{(n+1)}} = \frac{\partial S_{ij}^{(n+1)}}{\partial S_{pq}^{tr(n+1)}}\frac{\partial S_{pq}^{tr(n+1)}}{\partial \Delta\varepsilon_{kl}^{(n+1)}} = \frac{2G}{\sigma_{eq}^{(n+1)}}\frac{\partial S_{ij}^{(n+1)}}{\partial S_{pq}^{tr(n+1)}}\frac{\partial \Delta e_{pq}^{(n+1)}}{\partial \Delta\varepsilon_{kl}^{(n+1)}} \tag{A.5}$$

where:

$$\frac{\partial \Delta e_{pq}^{(n+1)}}{\partial \Delta\varepsilon_{kl}^{(n+1)}} = \frac{\partial \Delta\varepsilon_{pq}^{(n+1)}}{\partial \Delta\varepsilon_{kl}^{(n+1)}} - \frac{1}{3}\frac{\partial \Delta\varepsilon_{ii}^{(n+1)}}{\partial \Delta\varepsilon_{kl}^{(n+1)}}\delta_{pq} = \frac{1}{2}\left[\delta_{pl}\delta_{qk} + \delta_{pk}\delta_{ql}\right] - \frac{1}{3}\delta_{pq}\delta_{kl} \tag{A.6}$$

In addition:

$$\begin{aligned}
\frac{1}{\sigma_{eq}^{(n+1)}}\frac{\partial S_{ij}^{(n+1)}}{\partial S_{pq}^{tr(n+1)}} &= \frac{\partial}{\partial S_{pq}^{tr(n+1)}}\left(\frac{S_{ij}^{tr(n+1)}}{\sigma_{eq}^{tr(n+1)}}\right) \\
&= \frac{\frac{1}{2}\left[\delta_{ip}\delta_{jq} + \delta_{iq}\delta_{jp}\right]}{\sigma_{eq}^{tr(n+1)}} - \frac{3}{2}S_{ij}^{tr(n+1)}\frac{S_{kl}^{tr(n+1)}\frac{1}{2}\left[\delta_{kp}\delta_{lq} + \delta_{kq}\delta_{lp}\right]}{\left[\sigma_{eq}^{tr(n+1)}\right]^3} \\
&= \frac{1}{\sigma_{eq}^{tr(n+1)}}\left\{\frac{1}{2}\left[\delta_{ip}\delta_{jq} + \delta_{iq}\delta_{jp}\right] - \frac{3}{2}\frac{S_{ij}^{(n+1)}}{\sigma_{eq}^{tr(n+1)}}\frac{S_{pq}^{(n+1)}}{\sigma_{eq}^{tr(n+1)}}\right\}
\end{aligned} \tag{A.7}$$

Substituting equations (A.6) and (A.7) into equation (A.5), the following is obtained:

$$\begin{aligned}
\frac{\partial}{\partial \Delta\varepsilon_{kl}^{(n+1)}}\left(\frac{S_{ij}^{(n+1)}}{\sigma_{eq}^{tr(n+1)}}\right) &= \frac{2G}{\sigma_{eq}^{tr(n+1)}}\left\{\frac{1}{2}\left[\delta_{pl}\delta_{qk} + \delta_{pk}\delta_{ql}\right] - \frac{1}{3}\delta_{pq}\delta_{kl}\right\}\cdot \\
&\quad \left\{\frac{1}{2}\left[\delta_{ip}\delta_{jq} + \delta_{iq}\delta_{jp}\right] - \frac{3}{2}\frac{S_{ij}^{(n+1)}}{\sigma_{eq}^{tr(n+1)}}\frac{S_{pq}^{(n+1)}}{\sigma_{eq}^{tr(n+1)}}\right\} \\
&= \frac{2G\left\{\frac{1}{2}\left[\delta_{il}\delta_{jk} + \delta_{ik}\delta_{jl}\right] - \frac{1}{3}\delta_{ij}\delta_{kl}\right\} - 3G\frac{S_{ij}^{(n+1)}}{\sigma_{eq}^{tr(n+1)}}\frac{S_{pq}^{(n+1)}}{\sigma_{eq}^{tr(n+1)}}}{\sigma_{eq}^{tr(n+1)}}
\end{aligned} \tag{A.8}$$

Differentiating the equation (2.30) with respect to the total strain increment, yields to:

$$\begin{aligned}
\frac{\partial \sigma_{eq}^{tr(n+1)}}{\partial \Delta\varepsilon_{kl}^{(n+1)}} - 3G\frac{\partial \Delta\varepsilon_{eq}^{p(n+1)}}{\partial \Delta\varepsilon_{kl}^{(n+1)}} - \frac{\partial \sigma_y^{(n+1)}}{\partial \Delta\varepsilon_{eq}^{p(n+1)}}\frac{\partial \Delta\varepsilon_{eq}^{p(n+1)}}{\partial \Delta\varepsilon_{kl}^{(n+1)}} - \\
\frac{\partial \sigma_y^{(n+1)}}{\partial \Delta\varepsilon_{eq}^{p(n+1)}}\frac{\partial \Delta\varepsilon_{eq}^{p(n+1)}}{\partial \Delta\varepsilon_{kl}^{(n+1)}} = 0
\end{aligned} \tag{A.9}$$

Moreover:

$$\frac{\partial \sigma_{eq}^{tr(n+1)}}{\partial \Delta \varepsilon_{kl}^{(n+1)}} = \frac{2\frac{3}{2} S_{pq}^{tr(n+1)} \frac{\partial S_{pq}^{tr(n+1)}}{\partial \Delta \varepsilon_{kl}^{(n+1)}}}{2\sigma_{eq}^{tr(n+1)}} = 3G \frac{S_{kl}^{tr(n+1)}}{\sigma_{eq}^{tr(n+1)}} \tag{A.10}$$

Now, using equation (A.10), equation (A.9) is rewritten as:

$$\frac{\partial \Delta \dot{\varepsilon}_{eq}^{p(n+1)}}{\partial \Delta \varepsilon_{kl}^{(n+1)}} = \frac{\frac{S_{kl}^{(n+1)}}{\sigma_{eq}^{tr}}}{\left[1 + \frac{1}{3G} \frac{\partial \sigma_y^{(n+1)}}{\partial \Delta \varepsilon^{p(n+1)_{eq}}}\right] \Delta t + \frac{1}{3G} \frac{\partial \sigma_y^{(n+1)}}{\partial \Delta \dot{\varepsilon}_{eq}^{p(n+1)}}} \tag{A.11}$$

where it was applied that:

$$\frac{\partial \Delta \varepsilon_{eq}^{p(n+1)}}{\partial \Delta \varepsilon_{kl}^{(n+1)}} = \frac{\partial \dot{\varepsilon}_{eq}^{p(n+1)}}{\partial \Delta \varepsilon_{kl}^{(n+1)}} \Delta t \tag{A.12}$$

Finally, combining equations (A.8) and (A.11) the Jacobian is written as:

$$\begin{aligned} \frac{\partial \Delta \sigma_{ij}^{(n+1)}}{\partial \Delta \varepsilon_{kl}^{(n+1)}} &= K \delta_{ij} \delta_{kl} + 2\mu \left[1 - \frac{3G \Delta \dot{\varepsilon}_{eq}^{p(n+1)} \Delta t}{\sigma_{eq}^{tr(n+1)}}\right] \left[\frac{1}{2}\left[\delta_{il}\delta_{jk} + \delta_{ik}\delta_{jl}\right] - \frac{1}{3}\delta_{ij}\delta_{kl}\right] \\ &- 3G \left[\frac{\Delta t}{\left[1 + \frac{1}{3\mu} \frac{\partial \sigma_y^{(n+1)}}{\partial \Delta \varepsilon_{eq}^{p(n+1)}}\right] \Delta t + \frac{1}{3\mu} \frac{\partial \sigma_y^{(n+1)}}{\partial \Delta \dot{\varepsilon}_{eq}^{p(n+1)}}} - \frac{3\mu \Delta \dot{\varepsilon}_{eq}^{p(n+1)} \Delta t}{\sigma_{eq}^{tr(n+1)}}\right]^{(n+1)} \frac{S_{kl}^{n+1}}{\sigma_{eq}^{n+1}} \end{aligned} \tag{A.13}$$

A.2 VDFLUX subroutine

```
      subroutine VDFLUX(
     C Read only -
     1 nblock, ndim, kStep, kIncr, stepTime, totalTime, jUid,
     2 amplitude, temp, curCoords, velocity, dirCos, jltyp, sname,
     C Write only -
     3 value)
     C
           include 'vaba_param.inc'
     C
           dimension curCoords(nblock,ndim), velocity(nblock,ndim),
     1   jUid(nblock), dirCos(nblock,ndim,ndim), temp(nblock),
     2         value(nblock)
               DIMENSION GAMMABAR(nblock)
               dimension epsp(1000000)
           character*80 sname
     C
             common /myCB/ epsp
             do 100 km = 1, nblock
              GAMMABAR(km) = epsp(km)
              value(km) =  GAMMABAR(km) - temp(km)
       100 continue
           return
             end
```

A.3 Results for monodisperse RVEs with porosity f=0.15

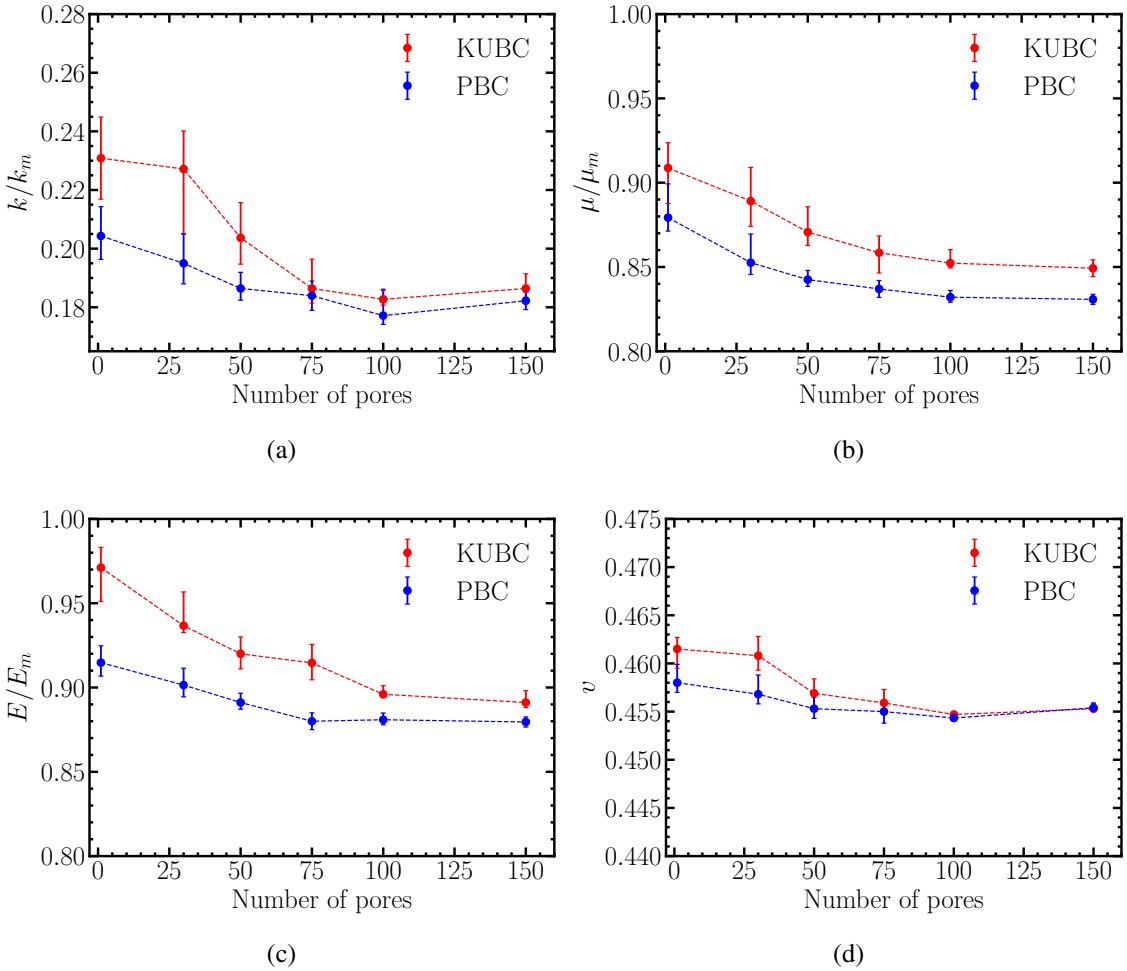

Figure A.1: Comparison between different sizes of unit cells for KUBC and PBC (a) normalised bulk modulus, (b) normalised shear modulus, (c) normalised Young's modulus and (d) Poisson's ratio for $f = 15$vol% porosity and monodisperse microstructure. The bulk, shear and Young's moduli of the solid matrix are shown as k_m, μ_m and E_m respectively.

A.4 Results for monodisperse and polydisperse analysis in RVEs with porosity f=0.1

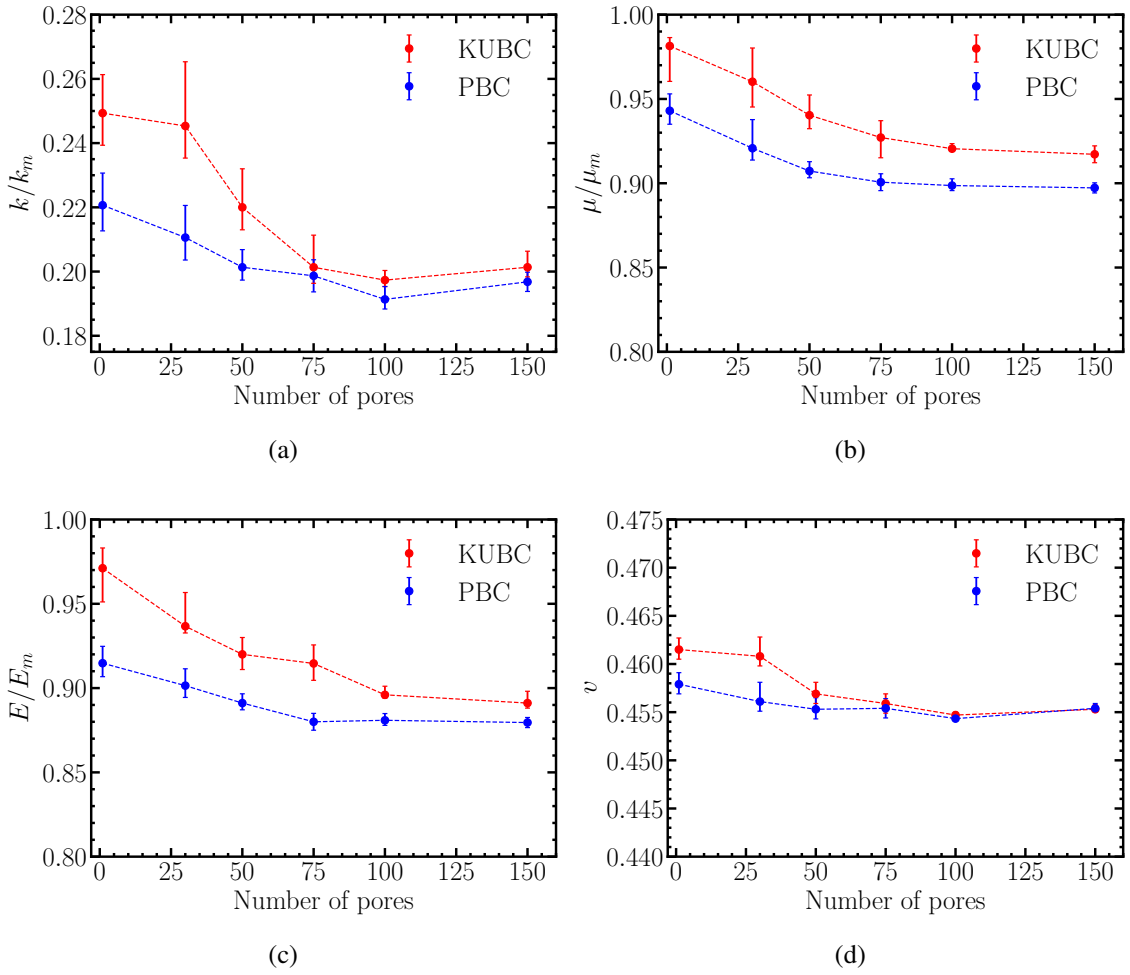

Figure A.2: Comparison between different sizes of unit cells for KUBC and PBC (a) normalised bulk modulus, (b) normalised shear modulus, (c) normalised Young's modulus and (d) Poisson's ratio for $f = 10$vol% porosity and monodisperse microstructure. The bulk, shear and Young's moduli of the solid matrix are shown as k_m, μ_m and E_m respectively.

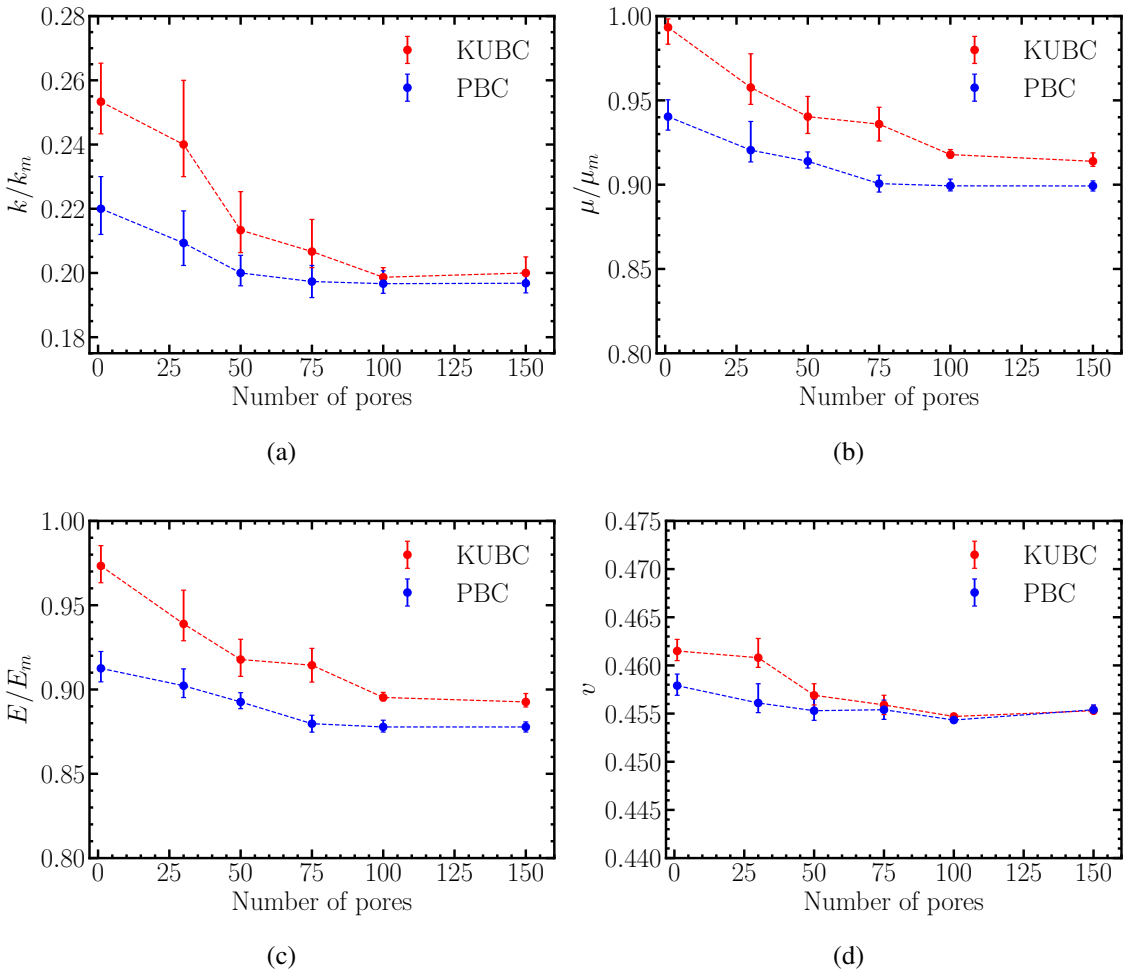

Figure A.3: Comparison between different sizes of unit cells for KUBC and PBC (a) normalised bulk modulus, (b) normalised shear modulus, (c) normalised Young's modulus and (d) Poisson's ratio for $f = 10$vol% porosity and polydisperse microstructure. The bulk, shear and Young's moduli of the solid matrix are shown as k_m, μ_m and E_m respectively.

Bibliography

[1] J Chen. Food oral processing-A review, jan 2009.

[2] LJ Gibson. Cellular solids. *Mrs Bulletin*, 28(4):270–274, 2003.

[3] ST Beckett. *The science of chocolate*. Royal Society of Chemistry, 2019.

[4] G Samaras, D Bikos, J Vieira, C Hartmann, M Charalambides, Y Hardalupas, M Masen, and P Cann. Measurement of molten chocolate friction under simulated tongue-palate kinematics: effect of cocoa solids content and aeration. *Curr. Res. Food Sci.*, 3:304–313, 2020.

[5] V Ranawana, CJK Henry, and M Pratt. Degree of habitual mastication seems to contribute to interindividual variations in the glycemic response to rice but not to spaghetti. *Nutrition Research*, 30(6):382–391, 2010.

[6] WE Brown and D Braxton. Dynamics of food breakdown during eating in relation to perceptions of texture and preference: a study on biscuits. *Food Quality and Preference*, 11(4):259–267, 2000.

[7] M Alfonso, E Neyraud, O Blanc, MA Peyron, and E Dransfield. Relationship between taste and chewing patterns of visco-elastic model foods. *Journal of sensory studies*, 17(2):193–206, 2002.

[8] A Woda, K Foster, A Mishellany, and M Peyron. Adaptation of healthy mastication to factors pertaining to the individual or to the food. *Physiology & Behavior*, 89(1):28–35, 2006.

[9] J Chen and L Engelen. Bolus formation and swallowing. *Food oral processing: Fundamentals of eating and sensory perception*, pages 139–156, 2012.

[10] D Bikos. *Effect of Micro-aeration on Mechanical and Thermal Properties of Chocolate and Correlation to Oral Processing*. PhD thesis, Imperial College London, 2021.

[11] D Bikos, G Samaras, P Cann, M Masen, Y Hardalupas, C Hartmann, J Vieira, and MN Charalambides. Effect of micro-aeration on the mechanical behaviour of chocolates and implications for oral processing. *Food Funct.*, 12(11):4864, 2021.

[12] C Skamniotis, M Elliott, and MN Charalambides. On modelling the constitutive and damage behaviour of highly non-linear bio-composites–mesh sensitivity of the viscoplastic-damage law computations. *International Journal of Plasticity*, 114:40–62, 2019.

[13] SM Harrison, G Eyres, PW Cleary, MD Sinnott, C Delahunty, and L Lundin. Computational modeling of food oral breakdown using smoothed particle hydrodynamics. *J. Texture Stud.*, 45(2):97–109, 2014.

[14] Simon M Harrison and Paul W Cleary. Towards modelling of fluid flow and food breakage by the teeth in the oral cavity using smoothed particle hydrodynamics (sph). *European Food Research and Technology*, 238(2):185–215, 2014.

[15] A Sarkar and EM Krop. Marrying oral tribology to sensory perception: a systematic review. *Current opinion in food science*, 27:64–73, 2019.

[16] G Tabilo-Munizaga and GV Barbosa-Cánovas. Rheology for the food industry. *J. Food Eng.*, 67(1-2):147–156, 2005.

[17] Michael S. *ABAQUS/Standard User's Manual, Version 6.17*. Dassault Systèmes Simulia Corp, United States, 2017.

[18] V Tømmernes. Implementation of the arruda-boyce material model for polymers in abaqus. Master's thesis, Institutt for konstruksjonsteknikk, 2014.

[19] MSH Fatt and X Ouyang. Integral-based constitutive equation for rubber at high strain rates. *International Journal of Solids and structures*, 44(20):6491–6506, 2007.

[20] JC Simo and RL Taylor. Consistent tangent operators for rate-independent elastoplasticity. *Comput. Methods Appl. Mech. Eng.*, 48(1):101–118, 1985.

[21] F Dunne and N Petrinic. *Introduction to computational plasticity*. Oxford University Press on Demand, 2005.

[22] L Ming and O Pantalé. An efficient and robust VUMAT implementation of elastoplastic constitutive laws in Abaqus/Explicit finite element code. *Mech. Ind.*, 19(3), 2018.

[23] R Zaera and J Fernández-Sáez. An implicit consistent algorithm for the integration of thermoviscoplastic constitutive equations in adiabatic conditions and finite deformations. *Int. J. Solids Struct.*, 43(6):1594–1612, 2006.

[24] AF Bower. *Applied mechanics of solids*. CRC press, 2009.

[25] I Doghri and A Ouaar. Homogenization of two-phase elasto-plastic composite materials and structures: Study of tangent operators, cyclic plasticity and numerical algorithms. *International Journal of Solids and structures*, 40(7):1681–1712, 2003.

[26] N Achour, G Chatzigeorgiou, F Meraghni, Y Chemisky, and J Fitoussi. Implicit implementation and consistent tangent modulus of a viscoplastic model for polymers. *International Journal of Mechanical Sciences*, 103:297–305, 2015.

[27] C Skamniotis. *Characterising and modelling fracture in functional pet foods*. PhD thesis, Imperial College London, 2017.

[28] S Murakami. *Continuum damage mechanics: a continuum mechanics approach to the analysis of damage and fracture*, volume 185. Springer Science & Business Media, 2012.

[29] GZ Voyiadjis and PI Kattan. *Damage mechanics*. CRC Press, 2005.

[30] J Lemaitre. *A course on damage mechanics*. Springer Science & Business Media, 2012.

[31] D Krajcinovic. Damage mechanics, applied mathematics and mechanics vol. 41, 1996.

[32] J Kestin and JR Rice. *Paradoxes in the application of thermodynamics to strained solids*. Citeseer, 1969.

[33] RJ Dorgan. *A nonlocal model for coupled damage-plasticity incorporating gradients of internal state variables at multiscales*. Louisiana State University and Agricultural & Mechanical College, 2006.

[34] N Aravas and I Papadioti. A non-local plasticity model for porous metals with deformation-induced anisotropy: Mathematical and computational issues. *Journal of the Mechanics and Physics of Solids*, 146:104190, 2021.

[35] EC Aifantis. On the microstructural origin of certain inelastic models. *J. Eng. Mater. Technol. Trans. ASME*, 106(4):326–330, 1984.

[36] E Kröner. Elasticity theory of materials with long range cohesive forces. *International Journal of Solids and Structures*, 3(5):731–742, 1967.

[37] AC Eringen and DGB Edelen. On nonlocal elasticity. *International Journal of Engineering Science*, 10(3):233–248, 1972.

[38] G Pijaudier-Cabot and ZP Bažant. Nonlocal damage theory. *Journal of engineering mechanics*, 113(10):1512–1533, 1987.

[39] GZ Voyiadjis and RJ Dorgan. A gradient enhanced, generalized plasticity/damage model: Rigorous mathematical formulation and finite element implementation. *Journal of the Mechanical Behavior of Materials*, 15(4-5):309–340, 2004.

[40] DJ Bammann and EC Aifantis. On the perfect lattice-dislocated state interaction. *Mechanics of structured media*, pages 79–91, 1981.

[41] DJ Bammann and EC Aifantis. On a proposal for a continuum with microstructure. *Acta Mechanica*, 45(1):91–121, 1982.

[42] EC Aifantis. On the Microstructural Origin of Certain Inelastic Models. *Journal of Engineering Materials and Technology*, 106(4):326–330, 1984.

[43] EC Aifantis. Remarks on media with microstructures. *International Journal of Engineering Science*, 22(8-10):961–968, 1984.

[44] D Walgraef and EC Aifantis. Dislocation patterning in fatigued metals as a result of dynamical instabilities. *Journal of applied physics*, 58(2):688–691, 1985.

[45] EC Aifantis. The physics of plastic deformation. *International journal of plasticity*, 3(3):211–247, 1987.

[46] I Vardoulakis and EC Aifantis. Gradient dependent dilatancy and its implications in shear banding and liquefaction. *Ingenieur-Archiv*, 59(3):197–208, 1989.

[47] HB Muhlhaus and EC Aifantis. The influence of microstructure-induced gradients on the localization of deformation in viscoplastic materials. *Acta mechanica*, 89(1):217–231, 1991.

[48] GZ Voyiadjis, B Deliktas, and EC Aifantis. Multiscale analysis of multiple damage mechanisms coupled with inelastic behavior of composite materials. *Journal of Engineering Mechanics*, 127(7):636–645, 2001.

[49] NA Fleck and JW Hutchinson. A phenomenological theory for strain gradient effects in plasticity. *Journal of the Mechanics and Physics of Solids*, 41(12):1825–1857, 1993.

[50] John Y Shu and Norman A Fleck. Strain gradient crystal plasticity: size-dependentdeformation of bicrystals. *Journal of the Mechanics and Physics of Solids*, 47(2):297–324, 1999.

[51] DJ Bammann, D Mosher, DA Hughes, NR Moody, and PR Dawson. Using spatial gradients to model localization phenomena. Technical report, Sandia National Labs., Albuquerque, NM (US); Sandia National Labs ..., 1999.

[52] JS Stölken and AG Evans. A microbend test method for measuring the plasticity length scale. *Acta Materialia*, 46(14):5109–5115, 1998.

[53] NA Fleck, GM Muller, MF Ashby, and JW Hutchinson. Strain gradient plasticity: theory and experiment. *Acta Metallurgica et materialia*, 42(2):475–487, 1994.

[54] HB Mühlhaus and EC Alfantis. A variational principle for gradient plasticity. *International Journal of Solids and Structures*, 28(7):845–857, 1991.

[55] S Ramaswamy and N Aravas. Finite element implementation of gradient plasticity models part i: Gradient-dependent yield functions. *Computer Methods in Applied Mechanics and Engineering*, 163(1-4):11–32, 1998.

[56] GZ Voyiadjis and RJ Dorgan. Bridging of length scales through gradient theory and diffusion equations of dislocations. *Computer methods in applied mechanics and engineering*, 193(17-20):1671–1692, 2004.

[57] RHJ Peerlings, R de Borst, WAM Brekelmans, and JHP De Vree. Gradient enhanced damage for quasi-brittle materials. *International Journal for numerical methods in engineering*, 39(19):3391–3403, 1996.

[58] E Kuhl, E Ramm, and R de Borst. An anisotropic gradient damage model for quasi-brittle materials. *Computer Methods in Applied Mechanics and Engineering*, 183(1-2):87–103, 2000.

[59] GZ Voyiadjis and RJ Dorgan. Gradient formulation in coupled damage-plasticity. *Archives of Mechanics*, 53(4-5):565–597, 2001.

[60] J Besson. Continuum models of ductile fracture: a review. *International Journal of Damage Mechanics*, 19(1):3–52, 2010.

[61] LM Kachanov. Rupture time under creep conditions. *Int. J. Fract.*, 97(1-4):11–18, 1999.

[62] ZF Zhang, J Eckert, and L Schultz. Difference in compressive and tensile fracture mechanisms of $Zr_{59}Cu_{20}Al_{10}Ni_8Ti_3$ bulk metallic glass. *Acta Materialia*, 51(4):1167–1179, 2003.

[63] B Wu, X Li, Y Di, V Brinnel, J Lian, and S Münstermann. Extension of the modified bai-wierzbicki model for predicting ductile fracture under complex loading conditions. *Fatigue & Fracture of Engineering Materials & Structures*, 40(12):2152–2168, 2017.

[64] JR Rice and DM Tracey. On the ductile enlargement of voids in triaxial stress fields. *Journal of the Mechanics and Physics of Solids*, 17(3):201–217, 1969.

[65] V Tvergaard and A Needleman. Analysis of the cup-cone fracture in a round tensile bar. *Acta metallurgica*, 32(1):157–169, 1984.

[66] L Xue. Constitutive modeling of void shearing effect in ductile fracture of porous materials. *Engineering Fracture Mechanics*, 75(11):3343–3366, 2008.

[67] K Nahshon and JW Hutchinson. Modification of the Gurson Model for shear failure. *European Journal of Mechanics-A/Solids*, 27(1):1–17, 2008.

[68] J Lemaitre. A continuous damage mechanics model for ductile fracture. *J. Eng. Mater. Technol. Trans. ASME*, 107(1):83–89, 1985.

[69] GR Johnson and WH Cook. Fracture characteristics of three metals subjected to various strains, strain rates, temperatures and pressures. *Eng. Fract. Mech.*, 21(1):31–48, 1985.

[70] Y Bao and T Wierzbicki. On the cut-off value of negative triaxiality for fracture. *Engineering fracture mechanics*, 72(7):1049–1069, 2005.

[71] Y Bai and T Wierzbicki. A new model of metal plasticity and fracture with pressure and Lode dependence. *Int. J. Plast.*, 24(6):1071–1096, 2008.

[72] J Lian, M Sharaf, F Archie, and S. Münstermann. A hybrid approach for modelling of plasticity and failure behaviour of advanced high-strength steel sheets. *Int. J. Damage Mech.*, 22(2):188–218, 2013.

[73] C Skamniotis, M Elliott, and MN Charalambides. Computer simulations of food oral processing to engineer teeth cleaning. *Nature communications*, 10(1):1–12, 2019.

[74] C Skamniotis, Y Patel, MN Charalambides, and M Elliott. Fracture investigation in starch-based foods. *Interface Focus*, 6(3), 2016.

[75] I Papadioti, N Aravas, J Lian, and S Münstermann. A strain-gradient isotropic elastoplastic damage model with j3 dependence. *International Journal of Solids and Structures*, 174:98–127, 2019.

[76] RHJ Peerlings, MGD Geers, R De Borst, and WAM Brekelmans. A critical comparison of nonlocal and gradient-enhanced softening continua. *International Journal of solids and Structures*, 38(44-45):7723–7746, 2001.

[77] RAB Engelen, MGD Geers, and FPT Baaijens. Nonlocal implicit gradient-enhanced elasto-plasticity for the modelling of softening behaviour. *International journal of Plasticity*, 19(4):403–433, 2002.

[78] D Lasry and T Belytschko. Localization limiters in transient problems. *International Journal of Solids and Structures*, 24(6):581–597, 1988.

[79] X Zhang and K Aifantis. Interpreting the internal length scale in strain gradient plasticity. *Reviews on Advanced Materials Science*, 41(1):72–83, 2015.

[80] EM Pañeda. *Strain gradient plasticity-based modeling of damage and fracture*. Springer, 2017.

[81] WD Nix and H Gao. Indentation size effects in crystalline materials: A law for strain gradient plasticity. *J. Mech. Phys. Solids*, 46(3):411–425, 1998.

[82] P Shrotriya, SM Allameh, J Lou, T Buchheit, and WO Soboyejo. On the measurement of the plasticity length scale parameter in LIGA nickel foils. *Mech. Mater.*, 35(3-6):233–243, 2003.

[83] YJ Ro, MR Begley, RP Gangloff, and SR Agnew. Effect of aging on scale-dependent plasticity in aluminum alloy 2024. *Mater. Sci. Eng. A*, 435-436:333–342, 2006.

[84] S Guo, Y He, J Lei, Z Li, and D Liu. Individual strain gradient effect on torsional strength of electropolished microscale copper wires. *Scr. Mater.*, 130:124–127, 2017.

[85] SP Iliev, X Chen, MV Pathan, and VL Tagarielli. Measurements of the mechanical response of Indium and of its size dependence in bending and indentation. *Mater. Sci. Eng. A*, 683:244–251, 2017.

[86] J Mediavilla, RHJ Peerlings, and MGD Geers. A nonlocal triaxiality-dependent ductile damage model for finite strain plasticity. *Comput. Methods Appl. Mech. Eng.*, 195(33-36):4617–4634, 2006.

[87] A Seupel, G Hütter, and M Kuna. An efficient FE-implementation of implicit gradient-enhanced damage models to simulate ductile failure. *Eng. Fract. Mech.*, 199:41–60, 2018.

[88] AM Korsunsky. Eigenstrain analysis of residual strains and stresses. *The Journal of Strain Analysis for Engineering Design*, 44(1):29–43, 2009.

[89] A Benallal and V Tvergaard. Nonlocal continuum effects on bifurcation in the plane strain tension-compression test. *Journal of the Mechanics and Physics of Solids*, 43(5):741–770, 1995.

[90] JC Michel and P Suquet. The constitutive law of nonlinear viscous and porous materials. *Journal of the Mechanics and Physics of Solids*, 40(4):783–812, 1992.

[91] PP Castañeda. The effective mechanical properties of nonlinear isotropic composites. *Journal of the Mechanics and Physics of Solids*, 39(1):45–71, 1991.

[92] PP Castaneda. Second-order homogenization estimates for nonlinear composites incorporating field fluctuations: I—theory. *Journal of the Mechanics and Physics of Solids*, 50(4):737–757, 2002.

[93] MD Rintoul and S Torquato. Reconstruction of the structure of dispersions. *J. Colloid Interface Sci.*, 186(2):467–476, 1997.

[94] W Voigt. Ueber die Beziehung zwischen den beiden Elasticitätsconstanten isotroper Körper. *Ann. Phys.*, 274(12):573–587, 1889.

[95] A Reuss. Berechnung der Fließgrenze von Mischkristallen auf Grund der Plastizitätsbedingung für Einkristalle . *ZAMM - J. Appl. Math. Mech. / Zeitschrift für Angew. Math. und Mech.*, 9(1):49–58, 1929.

[96] JD Eshelby. The determination of the elastic field of an ellipsoidal inclusion, and related problems. *Proceedings of the royal society of London. Series A. Mathematical and physical sciences*, 241(1226):376–396, 1957.

[97] Zvi Hashin. The elastic moduli of heterogeneous materials. Technical report, HARVARD UNIV CAMBRIDGE MA, 1960.

[98] Z am Hashin and S Shtrikman. On some variational principles in anisotropic and nonhomogeneous elasticity. *Journal of the Mechanics and Physics of Solids*, 10(4):335–342, 1962.

[99] ZSHTR Hashin and S Shtrikman. A variational approach to the theory of the elastic behaviour of polycrystals. *Journal of the Mechanics and Physics of Solids*, 10(4):343–352, 1962.

[100] Z Hashin and S Shtrikman. A variational approach to the theory of the elastic behaviour of multiphase materials. *J. Mech. Phys. Solids*, 11(2):127–140, 1963.

[101] AV Hershey. The Elasticity of an Isotropic Aggregate of Anisotropic Cubic Crystals. *J. Appl. Mech.*, 21(3):236–240, 1954.

[102] E Kröner. Bounds for effective elastic moduli of disordered materials. *Journal of the Mechanics and Physics of Solids*, 25(2):137–155, 1977.

[103] JR Willis and JW Provan. Variational principles and bounds for the overall properties of composites. *Continuum models for discrete systems*, pages 185–215, 1978.

[104] JR Willis. Variational and related methods for the overall properties of composites. In *Advances in applied mechanics*, volume 21, pages 1–78. Elsevier, 1981.

[105] JR Willis. On methods for bounding the overall properties of nonlinear composites. *Journal of the Mechanics and Physics of Solids*, 39(1):73–86, 1991.

[106] SK Reinke, F Wilde, S Kozhar, F Beckmann, J Vieira, S Heinrich, and S Palzer. Synchrotron X-Ray microtomography reveals interior microstructure of multicomponent food materials such as chocolate. *J. Food Eng.*, 174:37–46, 2016.

[107] R Hill. Elastic properties of reinforced solids: Some theoretical principles. *J. Mech. Phys. Solids*, 11(5):357–372, 1963.

[108] T Kanit, S Forest, I Galliet, V Mounoury, and D Jeulin. Determination of the size of the representative volume element for random composites: Statistical and numerical approach. *Int. J. Solids Struct.*, 40(13-14):3647–3679, 2003.

[109] Z Hashin. Analysis of composite materials: A survey. *J. Appl. Mech. Trans. ASME*, 50(3):481–505, 1983.

[110] WJ Drugan and JR Willis. A micromechanics-based nonlocal constitutive equation and estimates of representative volume element size for elastic composites. *J. Mech. Phys. Solids*, 44(4):497–524, 1996.

[111] IM Gitman, H Askes, and LJ Sluys. Representative volume: Existence and size determination. *Eng. Fract. Mech.*, 74(16):2518–2534, 2007.

[112] M Ostoja-Starzewski. Random field models of heterogeneous materials. *Int. J. Solids Struct.*, 35(19):2429–2455, 1998.

[113] S Saeb, P Steinmann, and A Javili. Aspects of computational homogenization at finite deformations: A unifying review from Reuss' to Voigt's Bound, 2016.

[114] C Huet. Application of variational concepts to size effects in elastic heterogeneous bodies. *J. Mech. Phys. Solids*, 38(6):813–841, 1990.

[115] A Mbiakop, A Constantinescu, and K Danas. An analytical model for porous single crystals with ellipsoidal voids. *J. Mech. Phys. Solids*, 84:436–467, 2015.

[116] J Schöberl. An advancing front 2D/3D-mesh generator based on abstract rules. *Comput. Vis. Sci.*, 1(1):41–52, 1997.

[117] M Ostoja-Starzewski. Microstructural randomness versus representative volume element in thermomechanics. *J. Appl. Mech. Trans. ASME*, 69(1):25–35, 2002.

[118] O Zerhouni, MG Tarantino, and K Danas. Numerically-aided 3d printed random isotropic porous materials approaching the hashin-shtrikman bounds. *Composites Part B: Engineering*, 156:344–354, 2019.

[119] C Huet. Coupled size and boundary-condition effects in viscoelastic heterogeneous and composite bodies. *Mechanics of Materials*, 31(12):787–829, 1999.

[120] M Ostoja-Starzewski. Scale effects in materials with random distributions of needles and cracks. *Mechanics of Materials*, 31(12):883–893, 1999.

[121] S Pecullan, LV Gibiansky, and S Torquato. Scale effects on the elastic behavior of periodic andhierarchical two-dimensional composites. *Journal of the Mechanics and Physics of Solids*, 47(7):1509–1542, 1999.

[122] K Terada, M Hori, T Kyoya, and N Kikuchi. Simulation of the multi-scale convergence in computational homogenization approaches. *International Journal of Solids and Structures*, 37(16):2285–2311, 2000.

[123] F Fritzen, S Forest, T Böhlke, D Kondo, and T Kanit. Computational homogenization of elasto-plastic porous metals. *Int. J. Plast.*, 29(1):102–119, 2012.

[124] DW Cooper. Random-sequential-packing simulations in three dimensions for spheres. *Phys. Rev. A*, 38(1):522–524, 1988.

[125] G Zhang and S Torquato. Precise algorithm to generate random sequential addition of hard hyperspheres at saturation. *Phys. Rev. E - Stat. Nonlinear, Soft Matter Phys.*, 88(5), 2013.

[126] H Richter. Mote3D: An open-source toolbox for modelling periodic random particulate microstructures. *Model. Simul. Mater. Sci. Eng.*, 25(3), 2017.

[127] K Anoukou, R Brenner, F Hong, M Pellerin, and K Danas. Random distribution of polydisperse ellipsoidal inclusions and homogenization estimates for porous elastic materials. *Comput. Struct.*, 210:87–101, 2018.

[128] E Conserva, M Menini, T Tealdo, M Bevilacqua, F Pera, G Ravera, and P Pera. Robotic chewing simulator for dental materials testing on a sensor-equipped implant setup. *International Journal of Prosthodontics*, 21(6), 2008.

[129] P Morell, I Hernando, and SM Fiszman. Understanding the relevance of in-mouth food processing. a review of in vitro techniques. *Trends in food science & technology*, 35(1):18–31, 2014.

[130] M Devezeaux De Lavergne, AK Young, J Engmann, and C Hartmann. Food oral processing-an industry perspective. *Frontiers in Nutrition*, 8:24, 2021.

[131] I Mohagheghian, Y Wang, J Zhou, L Yu, X Guo, Y Yan, MN Charalambides, and JP Dear. Deformation and damage mechanisms of laminated glass windows subjected to high velocity soft impact. *International Journal of Solids and Structures*, 109:46–62, 2017.

[132] B Dejak, A Młotkowski, and M Romanowicz. Finite element analysis of stresses in molars during clenching and mastication. *J. Prosthet. Dent.*, 90(6):591–597, 2003.

[133] J Paphangkorakit and JW Osborn. Effect of jaw opening on the direction and magnitude of human incisal bite forces. *Journal of dental research*, 76(1):561–567, 1997.

[134] M Kikuchi, TWP Korioth, and AG Hannam. The association among occlusal contacts, clenching effort, and bite force distribution in man. *Journal of dental research*, 76(6):1316–1325, 1997.

[135] D Tortopidis, MF Lyons, and RH Baxendale. Bite force, endurance and masseter muscle fatigue in healthy edentulous subjects and those with tmd 1. *Journal of oral rehabilitation*, 26(4):321–328, 1999.

[136] BK Biswas, S Bag, and S Pal. Biomechanical analysis of normal and implanted tooth using biting force measurement. *International Journal of Engineering*, 4(2):8269, 2013.

[137] DJ Anderson. Measurement of stress in mastication. i. *Journal of Dental Research*, 35(5):664–670, 1956.

[138] CH Gibbs, PE Mahan, HC Lundeen, K Brehnan, EK Walsh, SL Sinkewiz, and SB Ginsberg. Occlusal forces during chewing-influences of biting strength and food consistency. *J Prosthet Dent*, 46(5):561–567, 1981.

[139] C Hagberg. Assessments of bite force: a review. *Journal of Craniomandibular Disorders*, 1(3), 1987.

[140] H Dan, H Watanabe, and K Kohyama. Effect of sample thickness on the bite force for apples. *J. Texture Stud.*, 34(3):287–302, aug 2003.

[141] S Panda, J Chen, and O Benjamin. Development of model mouth for food oral processing studies: Present challenges and scopes. *Innovative Food Science & Emerging Technologies*, page 102524, 2020.

[142] AM Carvalho-da Silva, I Van Damme, B Wolf, and J Hort. Characterisation of chocolate eating behaviour. *Physiology & behavior*, 104(5):929–933, 2011.

[143] JF Meullenet, ML Finney, and M Gaud. Measurement of biting velocities, and predetermined and individual crosshead speed instrumental imitative tests for predicting cheese hardness. *Journal of texture studies*, 33(1):45–58, 2002.

[144] A Sánchez-Ayala, A Farias-Neto, Hellen CN, and RC Matheus Rodrigues Garcia. Relationship between chewing rate and masticatory performance. *CRANIO®*, 31(2):118–122, 2013.

[145] PH Buschang, GS Throckmorton, KH Travers, and G Johnson. The effects of bolus size and chewing rate on masticatory performance with artificial test foods. *Journal of Oral Rehabilitation*, 24(7):522–526, 1997.

[146] E Yoshida, K Fueki, and Y Igarashi. Association between food mixing ability and mandibular movements during chewing of a wax cube. *Journal of oral rehabilitation*, 34(11):791–799, 2007.

[147] SG Farias Gomes, W Custodio, F Faot, AA Del Bel Cury, and RCM Rodrigues Garcia. Masticatory features, emg activity and muscle effort of subjects with different facial patterns. *Journal of oral rehabilitation*, 37(11):813–819, 2010.

[148] GS Throckmorton, BH Buschang, H Hayasaki, and T Phelan. The effects of chewing rates on mandibular kinematics. *Journal of Oral Rehabilitation*, 28(4):328–334, 2001.

[149] JF Bates, GD Stafford, and A Harrison. Masticatory function—a review of the literature: Iii. masticatory performance and efficiency. *Journal of Oral Rehabilitation*, 3(1):57–67, 1976.

[150] X Wang and J Chen. Food oral processing: Recent developments and challenges, mar 2017.

[151] H Dan and K Kohyama. Interactive relationship between the mechanical properties of food and the human response during the first bite. *Archives of Oral Biology*, 52(5):455–464, 2007.

[152] AR Evans and M Fortelius. Three-dimensional reconstruction of tooth relationships during carnivoran chewing. *Palaeontologia Electronica*, 11(2):1–11, 2008.

[153] PW Lucas and DA Luke. Methods for analysing the breakdown of food in human mastication. *Arch. Oral Biol.*, 28(9):813–819, 1983.

[154] PW Lucas and DA Luke. Optimum mouthful for food comminution in human mastication. *Arch. Oral Biol.*, 29(3):205–210, 1984.

[155] C Yven, S Guessasma, L Chaunier, G Della Valle, and C Salles. The role of mechanical properties of brittle airy foods on the masticatory performance. *J. Food Eng.*, 101(1):85–91, nov 2010.

[156] CA Schneider, WS Rasband, and KW Eliceiri. Nih image to imagej: 25 years of image analysis. *Nature methods*, 9(7):671–675, 2012.

[157] DL Sahagian and AA Proussevitch. 3D particle size distributions from 2D observations: Stereology for natural applications. *J. Volcanol. Geotherm. Res.*, 84(3-4):173–196, sep 1998.

[158] O Meincke, D Kaempfer, H Weickmann, C Friedrich, M Vathauer, and H Warth. Mechanical properties and electrical conductivity of carbon-nanotube filled polyamide-6 and its blends with acrylonitrile/butadiene/styrene. *Polymer*, 45(3):739–748, 2004.

[159] A Sarkar, E Andablo-Reyes, M Bryant, D Dowson, and A Neville. Lubrication of soft oral surfaces. *Curr. Opin. Colloid Interface Sci.*, 39:61–75, 2019.

[160] D Liu, Y Deng, L Sha, A Hashem, and S Gai. Impact of oral processing on texture attributes and taste perception. *Journal of food science and technology*, 54(8):2585–2593, 2017.

[161] E Stribiţcaia, EM Krop, R Lewin, M Holmes, and A Sarkar. Tribology and rheology of bead-layered hydrogels: Influence of bead size on sensory perception. *Food Hydrocoll.*, 104, 2020.

[162] AM Janssen, MEJ Terpstra, RA De Wijk, and JF Prinz. Relations between rheological properties, saliva-induced structure breakdown and sensory texture attributes of custards. *J. Texture Stud.*, 38(1):42–69, 2007.

[163] RA de Wijk, LJ van Gemert, MEJ Terpstra, and CL Wilkinson. Texture of semi-solids; sensory and instrumental measurements on vanilla custard desserts. *Food Qual. Prefer.*, 14(4):305–317, 2003.

[164] ME Malone, IAM Appelqvist, and IT Norton. Oral behaviour of food hydrocolloids and emulsions. part 2. taste and aroma release. *Food hydrocolloids*, 17(6):775–784, 2003.

[165] DM Dresselhuis, MAC Stuart, GA van Aken, RG Schipper, and EHA de Hoog. Fat retention at the tongue and the role of saliva: Adhesion and spreading of 'protein-poor' versus 'protein-rich' emulsions. *J. Colloid Interface Sci.*, 321(1):21–29, 2008.

[166] DM Dresselhuis, EHA de Hoog, MA Cohen Stuart, MH Vingerhoeds, and GA van Aken. The occurrence of in-mouth coalescence of emulsion droplets in relation to perception of fat. *Food Hydrocoll.*, 22(6):1170–1183, 2008.

[167] RA De Wijk, AM Janssen, and JF Prinz. Oral movements and the perception of semi-solid foods. *Physiol. Behav.*, 104(3):423–428, 2011.

[168] J Chen and L Engelen. *Food oral processing: fundamentals of eating and sensory perception*. John Wiley & Sons, 2012.

[169] J Chen and JR Stokes. Rheology and tribology: Two distinctive regimes of food texture sensation, 2012.

[170] C Pradal and JR Stokes. Oral tribology: Bridging the gap between physical measurements and sensory experience. *Current Opinion in Food Science*, 9:34–41, 2016.

[171] S Prakash, DDY Tan, and J Chen. Applications of tribology in studying food oral processing and texture perception. *Food Research International*, 54(2):1627–1635, 2013.

[172] EO Afoakwa, A Paterson, and M Fowler. Factors influencing rheological and textural qualities in chocolate - a review. *Trends Food Sci. Technol.*, 18(6):290–298, 2007.

[173] S Lee, M Heuberger, P Rousset, and ND Spencer. A tribological model for chocolate in the mouth: General implications for slurry-lubricated hard/soft sliding counterfaces. *Tribology Letters*, 16(3):239–249, 2004.

[174] S Lee, M Heuberger, P Rousset, and ND Spencer. Chocolate at a sliding interface. *Journal of food science*, 67(7):2712–2717, 2002.

[175] SA Rodrigues, N Selway, MP Morgenstern, L Motoi, JR Stokes, and BJ James. Lubrication of chocolate during oral processing. *Food & function*, 8(2):533–544, 2017.

[176] PAS Breslin. An evolutionary perspective on food and human taste. *Current Biology*, 23(9):R409–R418, 2013.

[177] GA van Aken, MH Vingerhoeds, and EHA de Hoog. Colloidal behaviour of food emulsions under oral conditions. *Food colloids: interactions, microstructure and Processing*, pages 356–366, 2005.

[178] M Masen and PME Cann. Friction measurements with molten chocolate. *Tribology Letters*, 66(1):24, 2018.

[179] PAS Breslin. An evolutionary perspective on food and human taste, 2013.

[180] SP Humphrey and RT Williamson. A review of saliva: normal composition, flow, and function. *The Journal of prosthetic dentistry*, 85(2):162–169, 2001.

[181] SA Payment, B Liu, GD Offner, FG Oppenheim, and RF Troxler. Immunoquantification of human salivary mucins mg1 and mg2 in stimulated whole saliva: factors influencing mucin levels. *Journal of Dental Research*, 79(10):1765–1772, 2000.

[182] L Shi and KD Caldwell. Mucin adsorption to hydrophobic surfaces. *Journal of colloid and interface science*, 224(2):372–381, 2000.

[183] Hahn BI, MW Rutland, and T Arnebrant. Lubricating properties of the initial salivary pellicle—an afm study. *Biofouling*, 19(6):365–369, 2003.

[184] R Upadhyay and J Chen. Smoothness as a tactile percept: Correlating 'oral'tribology with sensory measurements. *Food Hydrocolloids*, 87:38–47, 2019.

[185] Q He, F Bramante, A Davies, C Elleman, K Fourtouni, and B Wolf. Material properties of ex vivo milk chocolate boluses examined in relation to texture perception. *Food & function*, 9(6):3532–3546, 2018.

[186] FQ Ionta, FL Mendonça, GC de Oliveira, CRB de Alencar, HM Honorio, and D Magalhaes, ACand Rios. In vitro assessment of artificial saliva formulations on initial enamel erosion remineralization. *Journal of dentistry*, 42(2):175–179, 2014.

[187] VJ Napadow, Q Chen, VJ Wedeen, and RJ Gilbert. Intramural mechanics of the human tongue in association with physiological deformations. *Journal of biomechanics*, 32(1):1–12, 1999.

[188] K Nishinari, S Ishihara, K Hori, and Y Fang. Tongue-palate squeezing of soft gels in food oral processing. *Trends in Food Science & Technology*, 99:117–132, 2020.

[189] WA Alsanei and J Chen. Studies of the oral capabilities in relation to bolus manipulations and the ease of initiating bolus flow. *Journal of Texture Studies*, 45(1):1–12, 2014.

[190] KM Hiiemae and JB Palmer. Tongue movements in feeding and speech. *Critical Reviews in Oral Biology & Medicine*, 14(6):413–429, 2003.

[191] An Cutler, Edwin R Morris, and LJ Taylor. Oral perception of viscosity in fluid foods and model systems. *Journal of texture studies*, 14(4):377–395, 1983.

[192] M Akhtar, J Stenzel, BS Murray, and E Dickinson. Factors affecting the perception of creaminess of oil-in-water emulsions. *Food hydrocolloids*, 19(3):521–526, 2005.

[193] J Chen, Z Liu, and S Prakash. Lubrication studies of fluid food using a simple experimental set up. *Food Hydrocolloids*, 42:100–105, 2014.

[194] HS Joyner, CW Pernell, and CR Daubert. Impact of formulation and saliva on acid milk gel friction behavior. *Journal of food science*, 79(5):E867–E880, 2014.

[195] HM Shewan, C Pradal, and JR Stokes. Tribology and its growing use toward the study of food oral processing and sensory perception. *Journal of texture studies*, 51(1):7–22, 2020.

[196] AM Carvalho-Da-Silva, I Van Damme, W Taylor, J Hort, and B Wolf. Oral processing of two milk chocolate samples. *Food Funct.*, 4(3):461–469, 2013.

[197] C Myant, R Underwood, J Fan, and PM Cann. Lubrication of metal-on-metal hip joints: The effect of protein content and load on film formation and wear. *J. Mech. Behav. Biomed. Mater.*, 6:30–40, 2012.

[198] E Scholten. Composite foods: from structure to sensory perception. *Food & function*, 8(2):481–497, 2017.

[199] A Chojnicka-Paszun and HHJ de Jongh. Friction properties of oral surface analogs and their interaction with polysaccharide/mcc particle dispersions. *Food research international*, 62:1020–1028, 2014.

[200] JHH Bongaerts, K Fourtouni, and JR Stokes. Soft-tribology: lubrication in a compliant pdms–pdms contact. *Tribology International*, 40(10-12):1531–1542, 2007.

[201] H Ranc, A Elkhyat, C Servais, S Mac-Mary, B Launay, and Ph Humbert. Friction coefficient and wettability of oral mucosal tissue: Changes induced by a salivary layer. *Colloids and Surfaces A: Physicochemical and Engineering Aspects*, 276(1-3):155–161, 2006.

[202] Y Payan and P Perrier. Synthesis of vv sequences with a 2d biomechanical tongue model controlled by the equilibrium point hypothesis. *Speech communication*, 22(2-3):185–205, 1997.

[203] M Devezeaux de Lavergne, VMG Strijbosch, AWM Van den Broek, F Van de Velde, and M Stieger. Uncoupling the Impact of Fracture Properties and Composition on Sensory Perception of Emulsion-Filled Gels. *J. Texture Stud.*, 47(2):92–111, 2016.

[204] K Liu, M Stieger, E van der Linden, and F van de Velde. Effect of microparticulated whey protein on sensory properties of liquid and semi-solid model foods. *Food Hydrocoll.*, 60:186–198, 2016.

[205] TAM Rovers, G Sala, E Van der Linden, and MBJ Meinders. Potential of Microbubbles as Fat Replacer: Effect on Rheological, Tribological and Sensorial Properties of Model Food Systems. *J. Texture Stud.*, 47(3):220–230, 2016.

[206] FQ Ionta, FL Mendonça, GC De Oliveira, CRB De Alencar, HM Honório, AC Magalhães, and D Rios. In vitro assessment of artificial saliva formulations on initial enamel erosion remineralization. *J. Dent.*, 42(2):175–179, 2014.

[207] M Sumarokova, J Iturri, A Weber, M Maares, C Keil, H Haase, and J Toca-Herrera. Influencing the adhesion properties and wettability of mucin protein films by variation of the environmental pH. *Sci. Rep.*, 8(1), 2018.

[208] F Xu, E Liamas, M Bryant, A Feyisara Adedeji, E Andablo-Reyes, M Castronovo, R Ettelaie, TVJ Charpentier, and A Sarkar. A Self-Assembled Binary Protein Model Explains High-Performance Salivary Lubrication from Macro to Nanoscale. *Adv. Mater. Interfaces*, 7(1):1901549, 2020.

[209] E Andrysewicz, J Mystkowska, JR Dabrowski, and R Olchowik. Influence of self-made saliva substitutes on tribological characteristics of human enamel. *Acta Bioeng. Biomech.*, 16(2):67–74, 2014.

[210] S Mantihal, S Prakash, FC Godoi, and B Bhandari. Effect of additives on thermal, rheological and tribological properties of 3D printed dark chocolate. *Food Res. Int.*, 119:161–169, 2019.

[211] C Servais, H Ranc, and ID Roberts. Determination of chocolate viscosity. *Journal of Texture Studies*, 34(5-6):467–497, 2003.

[212] RP Borwankar. Food texture and rheology: a tutorial review. *Rheology of foods*, pages 1–16, 1992.

[213] Malcolm Bourne. *Food texture and viscosity: concept and measurement*. Elsevier, 2002.

[214] MA Rao. *Rheology of fluid and semisolid foods: principles and applications*. Springer Science & Business Media, 2010.

[215] MA Rao. Measurement of flow properties of fluid foods-developments, limitations, and interpretation of phenomena. *Journal of Texture Studies*, 8(3):257–282, 1977.

[216] MA Rao. Rheology of liquid foods- a review 1. *Journal of Texture Studies*, 8(2):135–168, 1977.

[217] JF Steffe. *Rheological methods in food process engineering*. Freeman press, 1996.

[218] P Sherman. Industrial rheology with particular reference to foods, pharmaceuticals, and cosmetics. *Industrial rheology with particular reference to foods, pharmaceuticals, and cosmetics.*, 1970.

[219] TM Deboni, M Bündchen, CV Junior, D Hotza, R Piletti, and MGN Quadri. Effect of the processing steps on cactus juice production. *Food and bioprocess technology*, 7(4):990–1000, 2014.

[220] AR Taherian, P Fustier, M Britten, and HS Ramaswamy. Rheology and stability of beverage emulsions in the presence and absence of weighting agents: a review. *Food Biophysics*, 3(3):279–286, 2008.

[221] YH Chang, Seung Taik Lim, and B Yoo. Dynamic rheology of corn starch–sugar composites. *Journal of Food Engineering*, 64(4):521–527, 2004.

[222] NL Carter, ST Horseman, JE Russell, and J Handin. Rheology of rocksalt. *Journal of Structural Geology*, 15(9-10):1257–1271, 1993.

[223] P Fischer, M Pollard, P Erni, I Marti, and S Padar. Rheological approaches to food systems. *Comptes Rendus Physique*, 10(8):740–750, 2009.

[224] SC da Silva Lannes and ML Medeiros. Rheological properties of chocolate drink from cupuassu. *International Journal of food engineering*, 4(1), 2008.

[225] J Simuang, N Chiewchan, and A Tansakul. Effects of fat content and temperature on the apparent viscosity of coconut milk. *Journal of Food Engineering*, 64(2):193–197, 2004.

[226] V Glicerina, F Balestra, M Dalla Rosa, and S Romani. Rheological, textural and calorimetric modifications of dark chocolate during process. *Journal of Food Engineering*, 119(1):173–179, 2013.

[227] EO Afoakwa, A Paterson, M Fowler, and J Vieira. Comparison of rheological models for determining dark chocolate viscosity. *Int. J. Food Sci. Technol.*, 44(1):162–167, jan 2009.

[228] C Vásquez, G Henríquez, JV López, EK Penott-Chang, AJ Sandoval, and AJ Müller. The effect of composition on the rheological behavior of commercial chocolates. *LWT*, 111:744–750, 2019.

[229] EV Gonçalves and SC Lannes. Chocolate rheology. *Food Science and Technology*, 30:845–851, 2010.

[230] EJ Windhab. What makes for smooth, creamy chocolate? *Physics today*, 59(6):82, 2006.

[231] EO Afoakwa, A Paterson, and M Fowler. Effects of particle size distribution and composition on rheological properties of dark chocolate. *European Food Research and Technology*, 226(6):1259–1268, 2008.

[232] GR Ziegler, G Mongia, and R Hollender. The role of particle size distribution of suspended solids in defining the sensory properties of milk chocolate. *International Journal of Food Properties*, 4(2):353–370, 2001.

[233] U Eberhard, HJ Seybold, M Floriancic, P Bertsch, J Jiménez-Martínez, JS Andrade, and M Holzner. Determination of the effective viscosity of non-Newtonian fluids flowing through porous media. *Front. Phys.*, 7(MAY):1–9, 2019.

[234] B Metz, NWF Kossen, and JC Van Suijdam. The rheology of mould suspensions. In *Advances in Biochemical Engineering, Volume 11*, pages 103–156. Springer, 1979.

[235] EC Bingham. *Fluidity and plasticity*, volume 2. McGraw-Hill, 1922.

[236] D Quemada, P Flaud, and PH Jezequel. Rheological properties and flow of concentrated disperse media i-modelling of steady and unsteady behavior. *Chemical Engineering Communications*, 32(1-5):61–83, 1985.

[237] TN Fang, C Tiu, X Wu, and S Dong. Rheological behaviour of cocoa dispersions. *Journal of texture studies*, 26(2):203–215, 1995.

[238] T Fang, H Zhang, T Hsieh, and C Tiu. Rheological behavior of cocoa dispersions with cocoa butter replacers. *Journal of texture studies*, 28(1):11–26, 1997.

[239] MM Cross. Relation between viscoelasticity and shear-thinning behaviour in liquids. *Rheologica Acta*, 18(5):609–614, 1979.

[240] PJ Carreau and D De Kee. Review of some useful rheological equations. *The Canadian Journal of Chemical Engineering*, 57(1):3–15, 1979.

[241] KhS Mekheimer and MA El Kot. Mathematical modelling of unsteady flow of a sisko fluid through an anisotropically tapered elastic arteries with time-variant overlapping stenosis. *Applied Mathematical Modelling*, 36(11):5393–5407, 2012.

[242] WH Herschel and R Bulkley. Measurement of consistency as applied to rubber-benzene solutions. In *Am. Soc. Test Proc*, volume 26, pages 621–633, 1926.

[243] S Mizrahi and Z Berk. Flow behaviour of concentrated orange juice: mathematical treatment. *Journal of Texture Studies*, 3(1):69–79, 1972.

[244] JE Taylor, I Van Damme, ML Johns, AF Routh, and DI Wilson. Shear rheology of molten crumb chocolate. *J. Food Sci.*, 74(2), 2009.

[245] MD Torres, F Gadala-Maria, and DI Wilson. Comparison of the rheology of bubbly liquids prepared by whisking air into a viscous liquid (honey) and a shear-thinning liquid (guar gum solutions). *Journal of Food Engineering*, 118(2):213–228, 2013.

[246] HM Mader, EW Llewellin, and SP Mueller. The rheology of two-phase magmas: A review and analysis. *Journal of Volcanology and Geothermal Research*, 257:135–158, 2013.

[247] AC Rust and M Manga. Bubble shapes and orientations in low re simple shear flow. *Journal of colloid and interface science*, 249(2):476–480, 2002.

[248] HR Shaw, TL Wright, DL Peck, and R Okamura. The viscosity of basaltic magma; an analysis of field measurements in makaopuhi lava lake, hawaii. *American Journal of Science*, 266(4):225–264, 1968.

[249] M Manga, J Castro, KV Cashman, and M Loewenberg. Rheology of bubble-bearing magmas. *Journal of Volcanology and Geothermal Research*, 87(1-4):15–28, 1998.

[250] WR Schowalter, CE Chaffey, and H Brenner. Rheological behavior of a dilute emulsion. *Journal of colloid and interface science*, 26(2):152–160, 1968.

[251] D Barthes-Biesel and A Acrivos. Deformation and burst of a liquid droplet freely suspended in a linear shear field. *Journal of Fluid Mechanics*, 61(1):1–22, 1973.

[252] M Loewenberg and EJ Hinch. Numerical simulation of a concentrated emulsion in shear flow. *Journal of Fluid Mechanics*, 321:395–419, 1996.

[253] EJ Windhab. Fluid immobilization–a structure-related key mechanism for the viscous flow behavior of concentrated suspension systems. *Applied Rheology*, 10(3):134–144, 2000.

[254] DA Barker and DI Wilson. Rheology of a thermoplastic paste through the mushy state transition. *Chemical engineering science*, 63(6):1438–1448, 2008.

[255] D Dowson and GR Higginson. *Elasto-hydrodynamic lubrication: international series on materials science and technology*. Elsevier, 2014.

[256] ABJ Kroezen, J Groot Wassink, and CAC Schipper. The flow properties of foam. *Journal of the Society of Dyers and Colourists*, 104(10):393–400, 1988.

[257] D Bikos, G Samaras, P Cann, M Masen, Y Hardalupas, M N Charalambides, C Hartmann, J German, and J Vieira. Effect of structure on the mechanical and physical properties of chocolate considering time scale phenomena occurring during oral processing. *Food Struct.*, 31:100244, 2021.

[258] E Larmond. Methods for sensory evaluation of foods. pub. 1284. *Food Res. Inst., Central Exp. Farm, Ottawa, Canada*, 1970.

[259] C Loret, M Walter, N Pineau, Marie-Agnès Peyron, C Hartmann, and N Martin. Physical and related sensory properties of a swallowable bolus. *Physiology & behavior*, 104(5):855–864, 2011.

[260] JFV Vincent, DEJ Saunders, and P Beyts. The use of critical stress intensity factor to quantify "hardness" and "crunchiness" objectively. *Journal of Texture Studies*, 33(2):149–159, 2002.

[261] ESTHER H-J Kim, Virginia K Corrigan, Arran J Wilson, Ian R Waters, Duncan I Hedderley, and Marco P Morgenstern. Fundamental fracture properties associated with sensory hardness of brittle solid foods. *Journal of Texture Studies*, 43(1):49–62, 2012.

[262] Yvette Pascua, Hicran Koç, and E Allen Foegeding. Food structure: Roles of mechanical properties and oral processing in determining sensory texture of soft materials. *Current Opinion in Colloid & Interface Science*, 18(4):324–333, 2013.

[263] Torsten Witt and Jason R Stokes. Physics of food structure breakdown and bolus formation during oral processing of hard and soft solids. *Current opinion in food science*, 3:110–117, 2015.

[264] Marine Devezeaux de Lavergne, Fred van de Velde, and Markus Stieger. Bolus matters: The influence of food oral breakdown on dynamic texture perception. *Food & function*, 8(2):464–480, 2017.

[265] Hicran Koç, CJ Vinyard, GK Essick, and EA Foegeding. Food oral processing: conversion of food structure to textural perception. *Annual review of food science and technology*, 4:237–266, 2013.

[266] E Çakır, CR Daubert, MA Drake, CJ Vinyard, G Essick, and E A Foegeding. The effect of microstructure on the sensory perception and textural characteristics of whey protein/κ-carrageenan mixed gels. *Food Hydrocolloids*, 26(1):33–43, 2012.

[267] EA Foegeding, CR Daubert, MA Drake, G Essick, M Trulsson, CJ Vinyard, and F Van de Velde. A comprehensive approach to understanding textural properties of semi-and soft-solid foods. *Journal of Texture Studies*, 42(2):103–129, 2011.

[268] EA Gwartney, DK Larick, and EA Foegeding. Sensory texture and mechanical properties of stranded and particulate whey protein emulsion gels. *Journal of food science*, 69(9):S333–S339, 2004.

[269] G Mongia and GR Ziegler. The role of particle size distribution of suspended solids in defining the flow properties of milk chocolate. *International Journal of Food Properties*, 3(1):137–147, 2000.

[270] D Labbe, Pascal Schlich, Nicolas Pineau, Franck Gilbert, and N Martin. Temporal dominance of sensations and sensory profiling: A comparative study. *Food Quality and Preference*, 20(3):216–221, 2009.

[271] N Pineau, P Schlich, S Cordelle, C Mathonnière, S Issanchou, A Imbert, M Rogeaux, P Etiévant, and E Köster. Temporal dominance of sensations: Construction of the tds curves and comparison with time–intensity. *Food Quality and Preference*, 20(6):450–455, 2009.

[272] AM Carvalho-da Silva, I Van Damme, B Wolf, and J Hort. Characterisation of chocolate eating behaviour. *Physiol. Behav.*, 104(5):929–933, 2011.

[273] JC Simo and TJR Hughes. *Computational inelasticity*, volume 7. Springer Science & Business Media, 2006.